Investigation on Thermocatalytic CO_2 Hydrogenation by High Surface Area Silica Supported Transition Metal Catalysts

A Thesis Submitted for the Degree of

Doctor of Philosophy

As a part of

Ph.D. Programme (Chemical Science)

by

Mr. Arjun Cherevotan

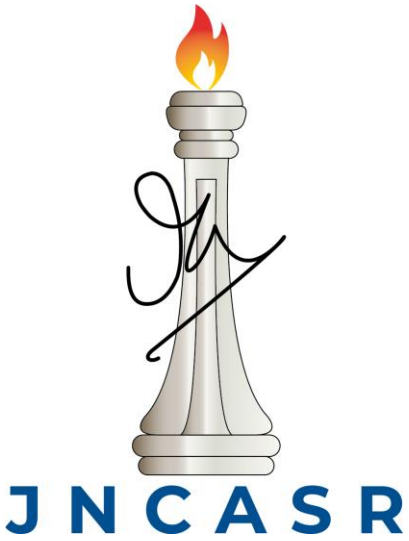

New Chemistry Unit

Jawaharlal Nehru Centre for Advanced Scientific Research

(A Deemed University)

Bangalore-560064 (INDIA)

January 2022

"*It is right that we should stand by and act on our principles; but not right to hold them in obstinate blindness or retain them when proved to be erroneous.*"

-Michael Faraday

Dedicated to Amma Achan and All my Gurus

Declaration

I hereby declare that the matter embodied in the thesis entitled ***"Investigation on Thermocatalytic CO_2 Hydrogenation by High Surface Area Silica Supported Transition Metal Catalysts"*** is the result of investigations carried out by me at the New Chemistry Unit, Jawaharlal Nehru Centre for Advanced Scientific Research, Bengaluru, India under the supervision of Prof. Sebastian C. Peter and that it has not been submitted elsewhere for the award of any degree or diploma. In keeping with the general practice in reporting scientific investigations, due acknowledgement has been made wherever the work described is based on findings of other investigators. Any omission that might have occurred by oversight or error of judgement is regretted.

Date: 19 January 2022 Arjun Cherevotan

Bengaluru, India

Certificate

I hereby declare that the matter embodied in the thesis entitled "***Investigation on Thermocatalytic CO_2 Hydrogenation by High Surface Area Silica Supported Transition Metal Catalysts***" has been carried out by Mr. Arjun Cherevotan at the New Chemistry Unit, Jawaharlal Nehru Centre for Advanced Scientific Research, Bengaluru, India under my supervision and that it has not been submitted elsewhere for the award of any degree or diploma.

Date: 19 January 2022

Bengaluru, India

Prof. Sebastian C. Peter
Associate Professor
New Chemistry Unit, JNCASR
(Research Supervisor)

Acknowledgement

"*A grateful heart is a magnet of miracles*"

The successful accomplishment of my Ph.D. thesis includes immense contribution from various people for their constant help, support and enthusiasm that motivated me to move ahead however, difficult the path be. The thesis would be incomplete without me expressing my gratitude towards them.

First and foremost, with deepest gratitude and great humility I would like to extend my sincere thanks and gratitude to my mentor, supervisor and guide, ***Prof. Sebastian C. Peter*** for his contribution in shaping the foundation of my research career. His persistent support, advice, criticism and wisdom not only inspired me to do better work each day but also helped me grow as an individual. Apart from him being an excellent scientist I have known him as one the most extraordinary human beings. Not only I have learnt science from him but also each of his words stimulated optimism and confidence in me. He taught me perseverance and most importantly how to remain calm and composed in every situation. Whenever a paper got rejected and most of us would be dejected, he is the one to always remain hopeful and positive. He has been like an umbrella for our SCP lab family. I am always indebted to him more than he knows. Today words are too less to express my gratefulness to him. Thank you, sir, for being so kind, gracious and for everything that helped me to improve myself each day.

I would like to express my sincere thanks to **Prof. C. N. R. Rao, FRS,** for being the epitome of inspiration, generous support and encouragement throughout my JNC life. I also thank him for providing the infrastructure and necessary facilities to carry out my research work.

I would like thank **Prof. Subi J. George**, the Chairman, **New Chemistry Unit, Jawaharlal Nehru Centre for Advanced Scientific Research** for an excellent and world class research environment provided in the centre.

I would like to thank all my course instructors Prof. Sebastian C. Peter, Prof. Chandrabhas Narayana, Prof. A. Sundaresan, Prof. Kanishka Biswas, Dr. Sarit Agasti, Prof. Shobhana Narasimhan and Prof. Amitabh Joshi for their excellent courses.

I take this opportunity to thank my collaborators: Prof. Umesh V. Waghmare, Prof. Peter Wells (University of Southampton), Dr. Chathakudath. P. Vinod (NCL Pune), Dr. Shaujon Xu (Cardiff University), Dr. Ujjal K. Gautam (IISER Mohali), Dr. Lakshay Dheer & Komalpreet Kaur (IISER Mohali).

My sincere thanks to all the technical staff of JNCASR: Mr. Sreenivas, Mrs. Usha, Mr. Anil, Ms. Selvi, Mr. Mahesh, Mr. Vasu, Mr. Deepak, Mr. Shivakumar, Mr. Rahul and Ms. Meenakshi for their help with the various characterization techniques. I would like to thank Melissa, Naveen, JNCASR Administration and Academic Sections, Complab, Students' Residence, Library, Dhanvantari and Security.

I would like to thank University for Grants Commission (UGC) for research fellowship. I would like to thank JNCASR, DST and DESY-Germany for various fundings.

I would like to express my gratitude to my Lab Family to whom I will always remain indebted: **Present members**: Dr. Shreya Sarkar, Dr. Sathyapal R. Churipard, Dr. Kousik Das, Dr. Veenu Mishra, Debabrata Bagchi, Ashutosh Kumar Singh, Risov Das, Bitan Ray, Devender Goud, Soumi Mondal, Subhajit Chakraborty, Nilutpal Dutta, Anish Yadav, Rahul Naskar and Jyoti Vashist.

Breathe Members: Rahul K. Ravindran, Shan Royson and Manjunath Doddamani

Past members: Dr. Saurav Chandra Sarma, Dr. Soumyabrata Roy, Dr. Sumanta Sarkar, Dr. Udumula Subbarao, Abhishek Rawat, Dr. Raghu Vamsy, Dr. Nithi Phukan, Jithu Raj, Vinay Naral, Kajol Tonk, Dundappa Mumbaraddi, Vamseedhara Vemuri, Md Javed Hossain, Jayesh Krishamoorthy, Dr. Tapas Paramanik, Dr. Vijaykumar Marakkatti, Vidyanshu Mishra, Dr. M. Kanagaraj, Dr. Subba Reddy Mari, Manoj Kaja Sai, Dr. A. R. Rajamani, Merin Vargheese, Chanachal; **Summer Student who worked with me:** Aswathy Mechoor, Atul Arware; **Visiting faculties:** Dr. Sudhakara Prasad and Dr. C. K. Sumesh.

I take this opportunity to thank Jithu Raj, Anish, Bitan, Debabrata and Ashutosh for rendering their unconditional support that helped me accomplish few works.

I extend my gratitude to Dr. Ashly P. C. for being an overwhelming host and for constant enthusiasm for lab trips and parties. She has always been encouraging and positive. I extend my love to the beautiful angels Caitlyn and Angelyn whose presence made all our activities more fun filled and memorable.

I express my thanks to all my JNCASR friends and batchmates: Arka Som, Biswanath, Suman, Monis, Momin, Brinta, Yogender, Laha, Resmi, Rajarshi, Manjushree, Smitha, Nijitha, Surishi, Shashank, Brijesh. Specially I would thank Soumita Chakraborty and Suchismita for always having them by my side.

I extend my gratitude and love to friends outside JNCASR: Vijil ATV, Anand K N, Ashwini, Shilpa, Sanoop, Binoy, Pranav, Mani, Uday, Naveenetan, Saraswati, Ambu, Maitreya, Dr. Jayashree for their gracious support throughout my life.

I am grateful to my Alma Mater Kendriya Vidyalaya Payyannur, GASC Mathil & Chemistry Department NITK Surathkal.

Most importantly, I am grateful to my Parents and Madhu Maman

Arjun

Preface

The thesis is majorly divided into five chapters.

Chapter 1. gives an introduction about the current climate changes caused by CO_2 emissions and over dependence on fossil fuels for meeting worlds hiking energy demands. The chapter describes how selective capture and conversion of CO_2 to various value-added products serve as a solution for both climate change and hiking energy demands. Further, different catalytic routes to hydrogenate CO_2 back to fuels are discussed in brief with more emphasis on thermocatalytic with its advantages over the others. The chapter gives more focus on the ways utilized to design the thermocatalyst which is divided into oxide support and active metals, or metal system loaded. The strategies to improve the surface area and textural properties of supports are described deeply. Finally, the chapter discuss in depth, the ways utilized for tuning electronic and structural properties active metal nanoparticles loaded such as intermetallic and bimetallic formations.

Chapter 2. describes how the physical textural properties of the supports can influence catalytic activity of CO_2 hydrogenation. Ni on silica support is well known for CO_2 methanation, we impregnated more than 20% of Ni on various high surface area silica supports (SBA-15, MCM-41 & non-mesoporous silica(nMPS)) with different textural properties. The TEM analysis and textural property analysis shows that the Ni NPs are highly dispersed inside the channels of SBA with vacant space while in case of MCM-41 the pores are blocked completely by 8 nm particles. The catalytic screening results revealed that Ni/SBA-15 gave the best CO_2 conversion (X_{CO_2}) with 100 % methane selectivity (S_{CH_4}) followed by Ni/MCM-41 (X_{CO_2} =79 % & S_{CH_4} = 85%) and least by Ni/nMPS. The Diffused Reflectance Infra-Red Spectroscopy (DRIFTS) experiments were conducted to understand the pathway and the

intermediates during the methanation which reveals that a faster methanation pathway involving CO_2 decomposition to CO and O, and hydrogenation to methane occurs over Ni/SBA-15, while in case of Ni/MCM-41 the pores are completely filled blocked by Ni nanoparticles and the methanation reaction proceeds through formate pathway generated on dangling -OH group which can be decomposed to CO and are relatively slower pathway. In case of Ni/nMPS the CO formed get stabilized and poisons the surface of Ni nanoparticles by forming Ni3-CO bridged intermediate reducing the conversion highly. Hence in this chapter we provide insight on how physical textural properties of support dictates metal particle distribution on them and affect the pathway CO_2 methanation reaction.

Chapter 3. In this chapter we describe how the CO_2 methanation activity of Ni gets optimized to yield methanol (MeOH) on formation of an operando generated metastable kinetic Ni_3In intermetallic phase. Here we synthesized different ratio of Ni-In intermetallics on SBA-15 support which all ended up in thermodynamically stable Ni_7In_3 triclinic phase. The catalytic screening of Ni_7In_3 at 573 K and 20 bar gave best activity towards methanol, and the spent catalyst XRD revealed an operando phase transition of Ni_7In_3 to Ni_3In which is identified as the active species for CO_2 to methanol conversion. Further, the XPS and XANES spectra revealed a In to Ni charge transfer on Ni_3In formation affecting the electronic properties of Ni to optimize its reduction towards MeOH formation. The first principle calculations and DRIFTS studies revealed that the CO_2 to MeOH conversion follows bidendate formate pathway. Hence, we designed a new CO_2 to methanol catalyst by modifying Ni with Indium to generate an operando intermetallic catalyst with enhanced CO_2 to methanol activity.

Chapter 4. describes about the promotional effect of non-coinage methanation catalyst in generating higher surface oxygen deficiency over In_2O_3 which acts as sites to activate CO_2. Here we impregnated 10% In_2O_3 on SBA-15 along with different ratio of non-coinage methanation catalyst Ni & Co (3:1, 2:1, 1:1, 1:2 &1:3). The In 3d XPS revealed that the oxygen

vacancy on In_2O_3 is highest on Ni:Co (1:1)/In_2O_3/SBA-15 which yielded highest MeOH activity of 10.2 $\mu mol_{MeOH}/g_{cat}$.s surpassing all the reported Ni/In_2O_3 catalyst towards CO_2 to MeOH. Also, a NiIn *P*6*mmm* intermetallic (IMC) phase was formed, it was concluded that the NiIn IMC along with Co helps in spill-over of incoming hydrogen molecule to yield higher surface oxygen vacancies over the In_2O_3. This was further confirmed by the DRIFTS studies since the CO_2 to MeOH intermediates such as bidendate formate and carbonates were present with higher intensity on Ni:Co(1:1)/In_2O_3/SBA-15 compared with Ni/In_2O_3/SBA-15 and Co/In_2O_3/SBA-15. Thus, we found novel strategy to improve the surface oxygen vacancies of In_2O_3 by using non-coinage metals.

In **Chapter 5**, Pd containing bimetallic systems are dispersed over Schiff base functionalized silica and employed as catalyst for CO_2 hydrogenation to formic acid (FA) in $KHCO_3$ solution by batch technique**.** By condensing 3-aminpropyltriethoxysilane (APTES) with two different types of aldehydes, butyraldehyde (BUT) and glutaraldehyde (GLU), we were able to make four different types of Schiff bases functionalized SBA-15 with the help of two different synthetic route. The catalyst performance towards CO_2 reduction to FA identified to have linear dependence on CO_2 capture ability of support and charge polarization in the bimetallic system dispersed over them.

List of Abbreviations

BET	Brunauer, Emmett & Teller equation
BPR	Back Pressure Regulator
CAMERE	Carbon dioxide hydrogenation to form Methanol via the Reverse water-gas shift reaction
CCU	Carbon capture and utilization
CZ	Cu/ZnO
CZA	$Cu/ZnO/Al_2O_3$
DFT	Density Functional Theory
DME	Dimethyl ether
DRIFTS	Diffused reflectance infra-red Fourier transform spectroscopy
EM	Electron microscopy
FA	Formic Acid
GC	Gas chromatography
HPLC	High performance liquid chromatography
IM	Intermetallic
IPCC	Intergovernmental panel on climate change
IWI	Incipient wetness impregnation
MeOH	Methanol
MFC	Mass flow controller
NRV	Non-return valve
Ov	Oxygen vacancy
RDS	Rate determining step
RWGS	Reverse water gas shift reaction
SEM	Scanning electron microscopy
TEM	Transmission electron microscopy
TPD	Temperature programmed desorption
TPR	Temperature programmed reduction
WGS	Water gas shift reaction
XAS	X-ray absorption spectroscopy
XPS	X-ray photoelectron spectroscopy
XRD	X-ray Diffraction

Table of Contents

Chapter 1

Introduction

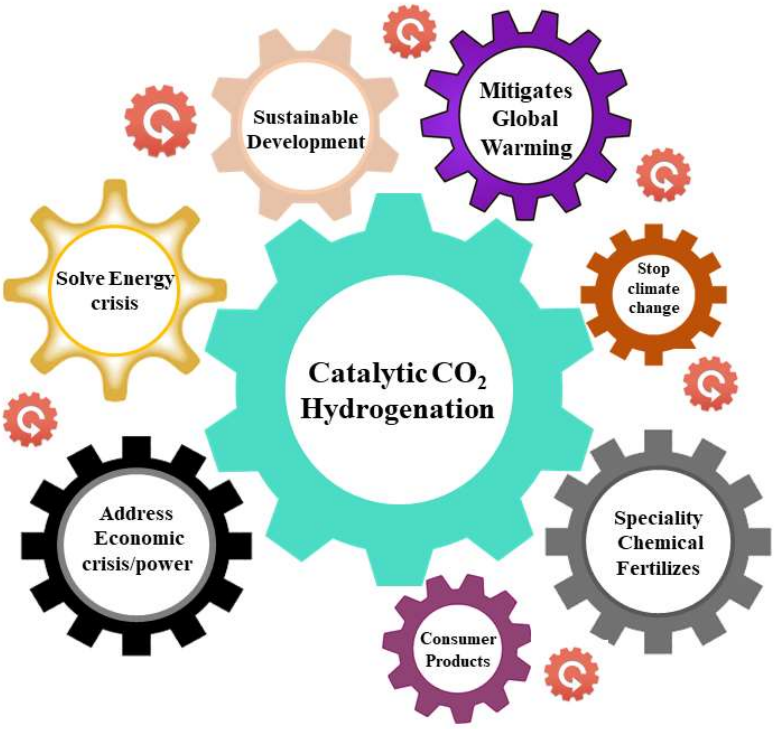

Part of this chapter is taken from

Thermochemical CO_2 Hydrogenation to Single Carbon Products: Scientific and Technological Challenges. **Arjun Cherevotan**, Soumyabrata Roy, and Sebastian C. Peter. *ACS Energy Lett*., 2018, 3(8), 1938-1966.

Table of Contents

1.1. Background

This thesis focusses on the development of cheap, efficient, and stable catalyst for sustainable carbon dioxide hydrogenation to value added products such as fuels and chemicals. Since industrial revolution there has been an exponential improvement in the living standard of human beings fueled by carbonaceous fuels causing anthropogenic CO_2 emission into atmosphere. Carbon dioxide being an infra-red active molecule, enhanced the heat trapping ability of earth's atmosphere causing unprecedented hike in global temperature and associated climate changes in cryosphere and low-lying coastal areas. The catalytic conversion of CO_2 to fuels can ameliorate the global warming and parallelly solve shortage of fuel issue making the linear trend of carbonaceous fuel usage to a circular trend. The development of an efficient scalable process for CO_2 valorization is being bottle necked chiefly by the stability of CO_2 compared to their reduced product and green sustainable hydrogen production from sustainable energy sources. This thesis completely focusses on designing better catalyst to activate the stable CO_2 and improve its hydrogenation reactivity to ease the overall process of CO_2 hydrogenation to fuels.

1.1.1. Energy Crisis and Global Warming

Last three centuries witnessed huge exponential growth in science, technology, human population and living standards of human beings leading to unprecedented exploitation of carbonaceous fuels for energy production affecting adversely the natural carbon cycle. The growing energy demand by increased dependence on fossil fuel and consequent global temperature hike is the major challenge to the scientific community in the current century. The global consumption of energy per hour is expected to reach 1.1×10^{21} J by the mid of 21st century. This is 80% higher than what can be derived from fossil fuel resources.[1] However, the recent discovery of shale gas oil resources and the idea of utilizing methane hydrates, it is evident that running out of fossil fuels is a definite but is a distant possibility.[2-4] Due to its abundance and low emission, the demand for natural gas is expected to increase 55% by 2030 as compared to the early 2000s. Being a highly populated and developing country, India is the 3rd largest producer (1,560,900 GWh) and consumer of energy in the world behind China and the United States, of which 75.4% is contributed currently by fossil fuels.[5-7] All other developing countries exhibit similar scenarios and considering the current energy demand rate, it is expected that the overdependence on coal will continue for coming several decades.[6, 7]

The annual CO_2 emission rate started rising from industrialization period and reached around 36.4 billion metric ton by 2021 (Source: Global Carbon Project) as shown in **Figure 1.1** causing an increase in CO_2 concentration of atmosphere from 270 ppm to nearly 420 ppm in 2021 (last 60 years saw 100 ppm increment).[8] To address the rapidly escalating energy demands and global warming, various initiatives such as the Intergovernmental Panel on Climate Change (IPCC) and United Nations Climate Change Conference have emphasized on the urgency to depend on renewable energy sources to mitigate the GHG emissions. In 2015, Paris Climate Accords considered that a global temperature increments closer to 2 °C above the pre-industrial levels is not safe. IPCC also warned that without an urgent mitigation drive in the coming years leading to a sharp decline in GHG emissions by 2030, the global warming will surpass 1.5 °C in the upcoming decades. This leads to irreversible damage in ecosystems, which includes the changes in the oceanography and cryosphere such as melting of ice caps, sea level rise, sea water temperature rise, sea water acidification and ultimately impact human existence on the planet earth **(Figure 1.2)**. Unfortunately, limited scientific, technological, and practical solution to exploit renewable energy, the target to limit average global temperature to 2 °C seems to be an eminent challenge.

1.1.2. Scientific Solution

The CO_2 emission can be mitigated via three possible strategies: (a) extensive shift of the global energy base from fossil to renewable energy and greener fuels like hydrogen, (b) CO_2 sequestration, and (c) CO_2 utilization by hydrogenation.[9] The first strategy, though very important, has serious disadvantages since it requires major changes in the energy infrastructure of the transportation sector and may also cause political issues of implementing these changes in large geographical areas with abundant fossil fuel deposits. Storage of CO_2 (strategy b) has limitations of high cost, intensive energy requirements for separation and pumping, and is a carbon negative economically unviable process. Thus, strategy (c) of carbon utilization through CO_2 hydrogenation, produces gaseous and liquid fuels such as carbon monoxide, methane, methanol, formic acid, dimethyl ether and other higher alcohols and hydrocarbons **(Table 1.1)**.

Carbon dioxide hydrogenation if done with green hydrogen produced by renewable energy sources can shift the linear trend of carbon fuel utilization to circular cyclic trend addressing both GHG emission and energy acting as a single stone two bird approach. Any energy conversion and production of fuels or chemicals involves overcoming thermodynamic and kinetic barriers by the catalyst material. Thus, the success rate of the chemical process depends on the innovative development of the catalytic process and material design.

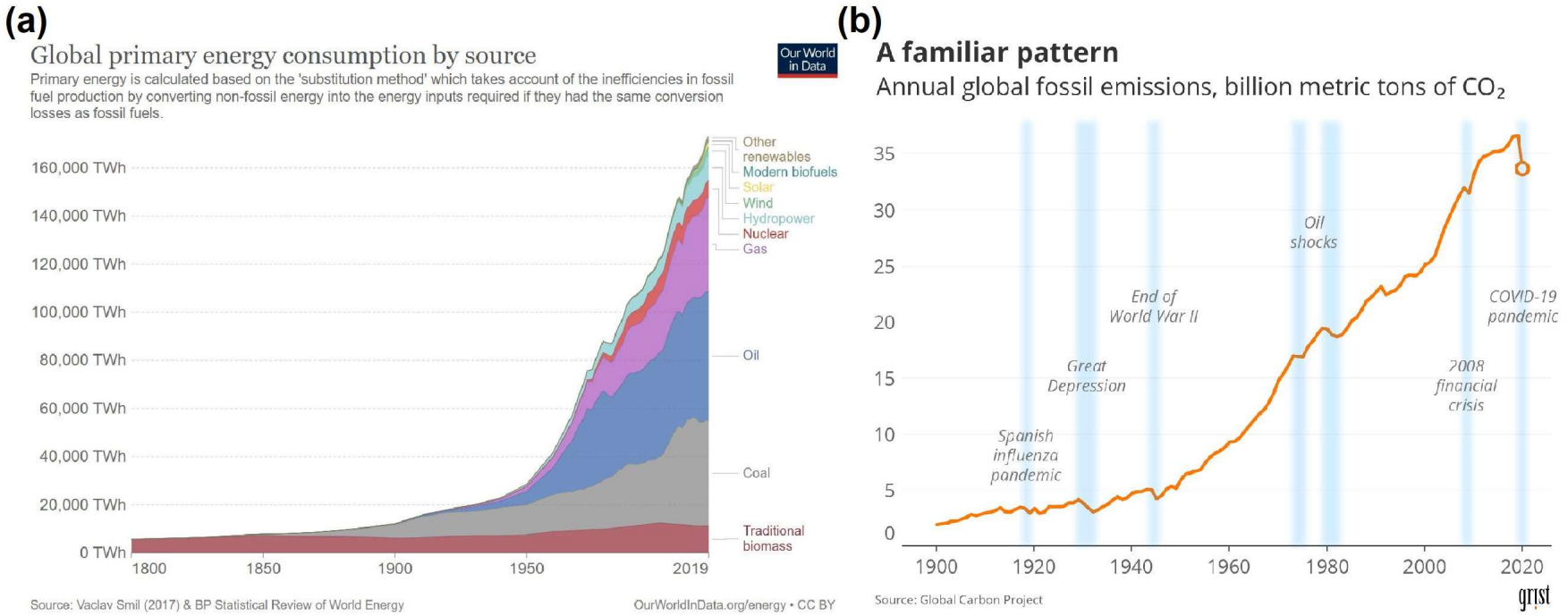

Figure 1.1. (a) Global energy consumption by source, (b) annual global fossil emission for last 30 years (Source: Global Carbon Project).

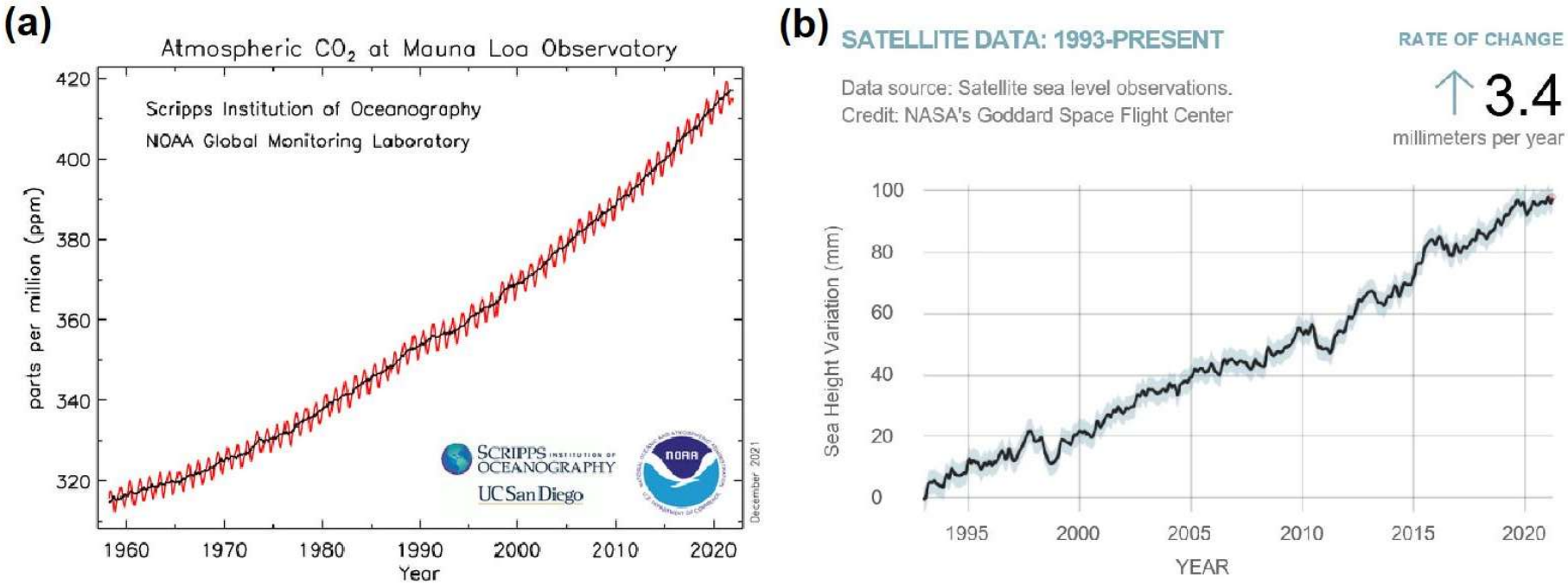

Figure 1.2. (a) Change in atmospheric CO_2 concentration for last 60 years and (b) rate of sea level increase in last 30 years.

Understanding the reactivity, physicochemical nature of both reactant and products are also crucial, which are discussed in upcoming sections. This thesis primarily focuses on microscopic problems of design and development of sustainable cost-effective catalysts for carbon dioxide hydrogenation.

Table 1.1. List of compounds produced via CO_2 hydrogenation process.

1	Carbon monoxide	7	Allyl alcohol	13	Glycolaldehyde
2	Formate	8	Acetaldehyde	14	Hydroxyacetins
3	Methane	9	Propinaldehyde	15	Acetone
4	Ethylene	10	Acetate	16	Glycerol
5	Ethanol	11	Methanol	17	Dimethyl ether
6	n-Propanol	12	Ethylene Glycol		

1.2. Carbon Dioxide Molecule – The Facts

Carbon dioxide (CO_2) is the highest oxidized form of carbon with 44 g/mol molecular weight and exists as gas at room temperature and ambient pressure. In earth's atmosphere, CO_2 naturally emits by volcanic eruptions, forest fires and animal respiration. The only major sink for CO_2 is photosynthesis by green plants, which use solar energy to convert CO_2 and water into carbohydrates with release of oxygen. This natural CO_2 cycle controls and optimize the CO_2 levels in atmosphere. CO_2 being highest oxidized form of carbon is thermodynamically stable linear molecule with highly negative Gibb's energy change ($\Delta G^o = -394$ kJ/mol), this makes its catalytic activation process a major challenge **(Figure 1.3)**. All the reduced forms of CO_2 have less negative Gibb's free energy making the catalytic conversion tedious.[10] Overcoming the thermodynamic barrier of CO_2 activation requires large energy input making the economic and energy efficient utilization a formidable challenge for scientific community.

1.3. Carbon Dioxide Hydrogenation

Recycling CO_2 as a renewable carbon source for the generation of high-value fuels and chemicals has recently acquired huge attention as a viable way to reduce over reliance on fossil fuels and combat climate change. If the hydrogen is produced using a renewable energy source, catalytic CO_2 hydrogenation is the most viable and appealing alternative among the existing CO_2 recycling solutions. Hydrogenation of CO_2 has many chemical paths depending on the catalyst, and multiple value-added hydrocarbons can be generated. In recent years, intensive study has resulted in the development of high-performance catalysts, identified complex reaction pathways, intermediates and gained deeper knowledge about the reaction mechanisms.

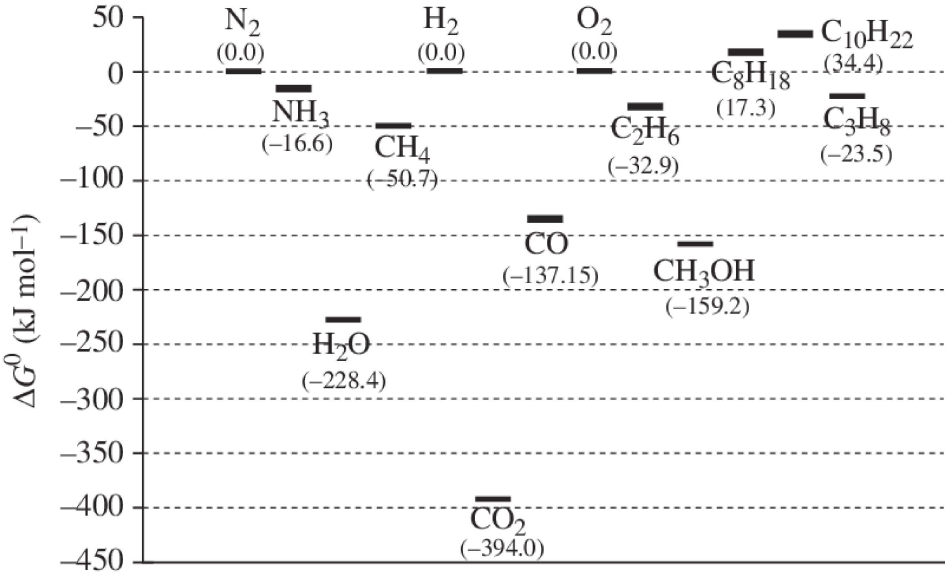

Figure 1.3. Gibbs free energy of formation for selected chemicals.[10] Reproduced with permission from ref. 10 (Copyright 2010 Royal Society).

1.3.1. Catalysts

Catalysts are the materials that alters the rate of a reaction without appearing in any of the products of that reaction. A catalyst may increase the rate or slow down a reaction (negative catalyst). In case of a reversible reaction, a catalyst alters the rate at which equilibrium is attained without altering the position of equilibrium. Catalysts alters the rate of a reaction by guiding the reaction through an alternative low activation energy pathway or intermediate formation as shown in **Figure 1.4**.

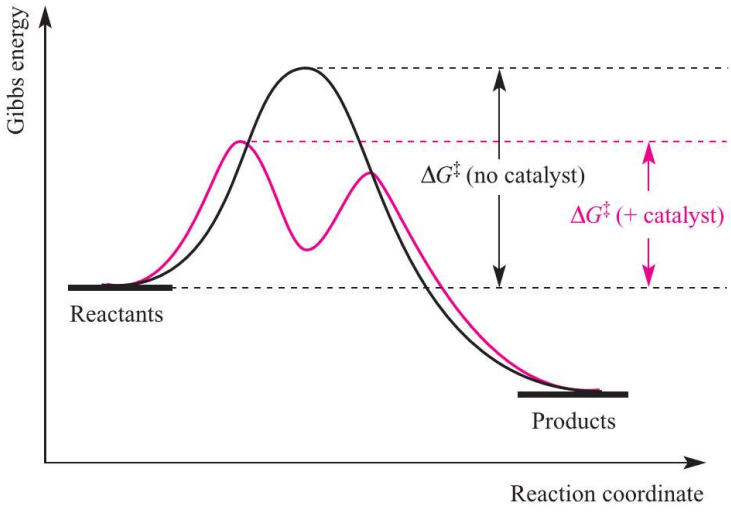

Figure 1.4. A schematic representation of the reaction profile of a reaction with and without a catalyst. The pathway for the catalyzed reaction has two steps, and the first step is rate determining (RDS).

The type of catalysis is broadly divided into homogeneous and heterogenous based on the reaction phase. In homogeneous catalysis all reactants and catalysts are in the same phase while in heterogenous they are in different phase. In heterogenous catalysis, the catalyst (mostly solids) and reactant molecule interact with each other via various adsorption process. Since both catalyst and reactants are in same phase (homogeneous catalysis), typically it is a low temperature process while heterogenous catalysis requires harsh reaction conditions and this cause a concern about the catalyst stability. Both diffusivity and heat transfer might be difficult for heterogeneous catalysts with low surface area. When compared with homogenous catalysis, understanding the active sites, intermediates and reaction pathway are tedious in heterogenous catalysis and mostly require *operando*-spectroscopic, electron microscopic and X-ray absorption techniques along with computational models making the analysis complex and expensive. Major differences between homogenous catalysis and heterogenous catalysis are provided in **Table 1.2.** Based on the type of energy input, catalysis can be further classified as electrocatalysis, photocatalysis and thermocatalysis. As evident from the names they use electricity, light and thermal, respectively, or the combination for the chemical catalytic transformations. Out of these, electrocatalysis is having the highest energy efficiency but is constrained by its high cost and large overpotential. Photocatalysis if done by solar light harvesting is the greenest process but limited by low light harvesting and sensitization capability in visible region. Heterogenous thermo-catalysis based on solid catalyst is the most established process in industry with extensive applications in the field of petrochemical and chemical manufacturing and thus commercially established. But the thermo-catalytic process is energy inefficient in most case due to large heat losses in reactors.

Table 1.2. Difference between homogenous and heterogenous catalysis.

Homogenous Catalyst	**Heterogeneous Catalyst**
Liquid Phase	Liquid/Gas/Solid Phase
Low Temperature Process	High Temperature Process
High Selectivity	Low Selectivity
High Diffusivity	Low Diffusivity
Easy Heat Transfer	Heat Transfer Can be an Issue
Catalyst Separation Difficult	Easy Catalyst Separation
Expensive Recycling	Simple Recycling
Well Defined Active Sites	Poorly Defined Active Sites
Easy Catalyst Modification	Difficult Catalyst Modification
Reaction Mechanism Well Understood	Reaction Mechanism Poorly Understood

1.3.2. Chemical Reaction of CO_2 Hydrogenation

The hydrogenation reaction has been identified as the most important one among various chemical conversions of CO_2 as it offers a good opportunity for sustainable development in the energy and environmental sectors.[9] Additionally, the products of CO_2 conversion are value-added and can be used as fuels or precursors to produce more complex chemicals and fuels.[11] The "Sabatier reaction", discovered in the 1910s,[12] was the first industrially developed CO_2 hydrogenation to methane, which has been a pivotal discovery in understanding the basic underlying principles of modern-day catalysis. However, with the discovery of the Fischer-Tropsch (FT) process for synthesizing hydrocarbons from syngas (CO, H_2, CO_2 mix), the Sabatier reaction became less industrially relevant.[12] Methane, the easiest C_1 hydrocarbon of CO_2 conversion, however, is much more stable and less reactive than methanol in forming further derivatives and chemicals.[12] Methanol, one of the most important products of CO_2 reduction, is industrially synthesized from syngas (with CO and H_2 in a ratio of 1:2), which is also called the metgas.[12, 13] Several industrial or industrially relevant downstream processes from methanol have been well studied, e.g., conversion to HCHO (formaldehyde) and HCOOH (formic acid) and their further conversions to formamide, sugars, nucleic acid bases, amino acids, and even peptides.[12] Methanol also has extensive applications in producing higher hydrocarbons and derivatives or gasoline through the MTO (methanol to olefins) and MTG (methanol to gasoline) reactions.[14] Methanol is considered as one of the future transportation fuel since it can be independently used or can be used as an additives to gasoline for the existing internal combustion engines. The methanol economy is a future in which methanol and dimethyl ether replace fossil fuels as a source of energy, ground transportation fuel, and raw material for synthetic hydrocarbons and their derivatives. It also predicted to offer a substitute to hydrogen and ethanol economy and this was advocated by Prof. George A. Olah in 1990s to mitigate Global warming and energy issues.[15] Carbon monoxide, on the other hand, has immense applications in chemical and fuel industries through the FT process and as a major syngas component. Moreover, it has wide applications in the steel industry, in the metal fabrication industry, and in the field of pharmaceuticals. It is important to note that the process of CO_2 hydrogenation to various products like Methane, MeOH, CO, DME (dimethyl ether), etc. is now being widely practiced industrially in many countries, with the first industrial plant being put up in Iceland by Carbon Recycling International to produce methanol from CO_2 using a geothermal energy source. Other notable endeavors include the methanol plant in Osaka, Japan by Mitsui Chemicals, DME production by KOGAS Corporation in Korea, methanol production at the

Lünen power plant, CO production by Haldor Topsoe in La Porte Texas and Mitsubishi Hitachi Power Systems Europe (MHPSE).

Despite all these efforts, it is rather apparent that CO_2 hydrogenation technology is still far away from extensive commercialization, which is necessary to bring the intended environmental change. This is primarily because of insufficient conversion and product selectivity, which are the effects of competitive and unfavorable kinetic and thermodynamic factors. The only way to address these issues is to develop more efficient and selective catalysts and integrated reactor systems that can form targeted products at high conversion rates with minimum energy expense over industrial time scales. Designing better catalysts demands thorough understanding of the reaction mechanisms. However, determining reaction mechanisms in the case of thermochemical hydrogenation of CO_2 is complicated and challenging because of the lack of in-situ probing techniques, complexities of extreme reaction conditions, and spectroscopically opaque reactor designs. This thesis focuses on the development of highly active, selective, and stable catalysts for thermochemical CO_2 reduction based on mechanistic understanding of the catalytic processes.[11] In future, the catalytic conversion can be integrated with CO_2 capture to reduce CO_2 by the hydrogen produced by greener routes **(Figure 1.5)**, neutralizing growing energy demand and mitigating CO_2 emissions.

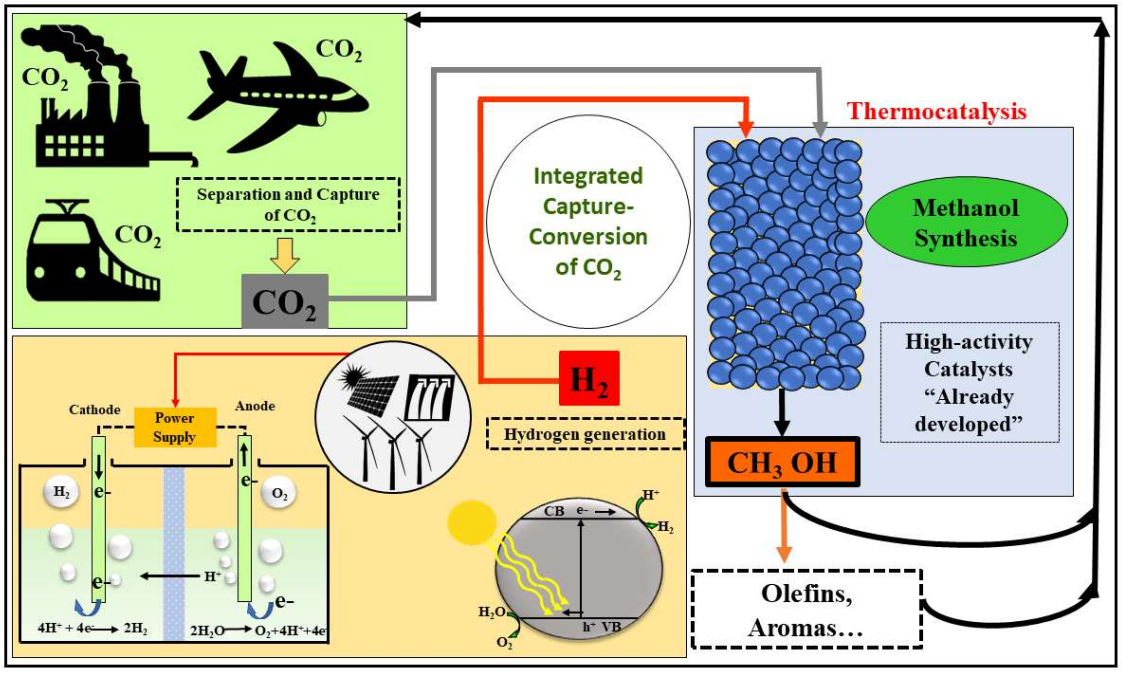

Figure 1.5. Schematic illustration of thermocatalytic CO_2 hydrogenation integrated with CO_2 capture and sustainable hydrogen production.

1.3.3. CO_2 to C_1 Hydrocarbons

Carbon dioxide hydrogenation into various C_1 products **(Figure 1.6)** such as CH_4, CO, HCOOH, and CH_3OH has been a hot study topic for several decades and warrants further investigation. Both CO and CH_4 are commonly utilized as low calorific gaseous fuels, while CH_3OH and HCOOH are commonly used as liquid fuels. Carbon monoxide is employed as a formylation source in the manufacturing of a range of formylated products,[16] while HCOOH is used widely in reduction, carboxylation, or reductive formylation as an H_2 and CO source.[17] Interesting properties like high latent heat, fast-burning velocity, no carbon-to-carbon bonds, and high-octane rating makes methanol a better fuel compared to other conventional fuels in internal combustion engines including ethanol.[18, 19] Most importantly, higher hydrocarbons, paints, synthetic textiles forming the basis of chemical industry uses C_1 fuel methanol as the precursor since compared to ethanol it has the highest number of non-food sources making it relatively cheap. In this thesis we study different thermocatalytic CO_2 to C_1 hydrogenation process with more focus on the catalyst design and understanding the reaction mechanism.

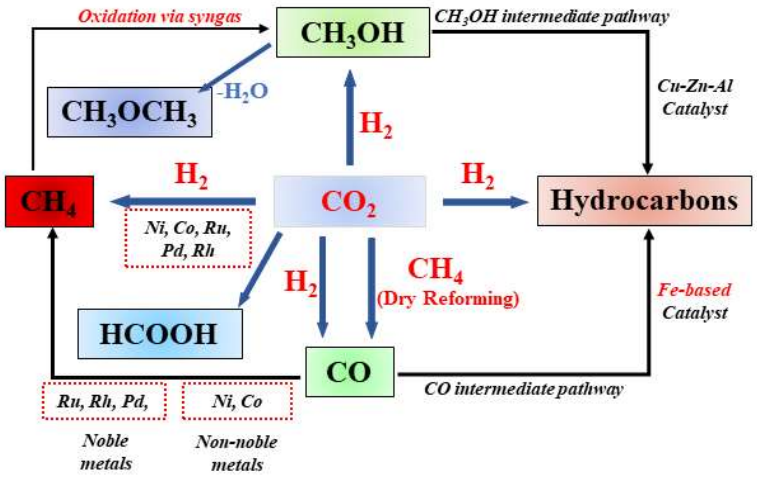

Figure 1.6. Different C_1 obtained by CO_2 hydrogenation via thermocatalytic routes.

1.3.3.1. Forward and Reverse Water Gas Shift Reaction (WGS & RWGS)

Water gas shift reaction is a highly celebrated industrial process employed for H_2 production and was reported in 1888. It is an exothermic and ambient pressure reaction in which CO combines with H_2O yielding CO_2 and H_2.[20] Due to its ability to supply pure hydrogen the WGS reaction has become increasingly important in industrial applications. Since the WGS reaction provides the ideal means for CO (harmful for Pt electrode) removal from the hydrogen required as a fuel, it finds application also in fuel cell power generation.[21] WGS reaction being

an exothermic equilibrium reaction, at slightly higher temperature the process changes to endothermic RWGS **(eqn. 1.1)**.

$$H_2 + CO_2 \leftrightarrow CO + H_2O \qquad \Delta H\ (298\ K) = 41.2\ kJ\ mol^{-1} \qquad (1.1)$$

Earlier, the RWGS reaction has been considered as an unfavorable reaction since it produces highly poisonous CO. The RWGS reaction when identified as a key reaction for CO_2 utilization began to attract increasing attention. CO_2 hydrogenation to CO process is now regarded as the first step in the production of a wide range of commercially important chemicals. For instance, the CAMERE process (Carbon dioxide hydrogenation to form Methanol via the Reverse water-gas shift reaction), which is of current interest commences with the RWGS reaction to produce CO first, then subsequently hydrogenate to MeOH (methanol).[22, 23] The formation of syngas (CO/H_2) from CO_2 via RWGS reaction also opens the door to a whole range of useful hydrocarbon synthesis and mitigates CO_2 related climate changes.[24]

As discussed earlier, the higher stability of CO_2 demands a large amount of energy input for its hydrogenation to CO and H_2O. The reaction being endothermic is favored thermodynamically at higher temperatures. The equilibrium of RWGS can also be forced to shift to the right by increasing the concentration of either reactant. The timely removal of products upon formation can also help shift the equilibrium to the right. A bifunctional catalyst active for both the RWGS reaction and then consumption of CO/H_2 to the final product to methanol would be beneficial since as soon as CO is formed it could be consumed forcing the further conversion of CO_2. Another alternative would be the removal of water which can be achieved by desiccant bed usage.[25]

Typically, heterogeneous catalysts suitable to produce good rates of reaction in the forward process also shows a higher reaction rate in the reverse process.[26] This is also true for the WGS reaction and RWGS reaction, in which most catalysts active in the direct WGS process is also effective in the reverse reaction. Catalysts used for the RWGS can be classified mainly as (i) Cu-based, (ii) noble metals supported on metal oxides, and (iii) reducible oxide supported ones. The RWGS on all these classes of catalysts goes through either the redox mechanism or the formate dissociation pathway. The redox mechanism occurs primarily in Cu-based catalysts where CO_2 oxidizes Cu^0 to Cu^+ and generates CO while H_2 reduces Cu^+ back and forms water.[27-29] In the formate dissociation mechanism, CO_2 gets hydrogenated into formate followed by subsequent cleaving of C=O, which requires bifunctionality in the catalyst.[11] In metal nanoparticles supported on metal oxide systems, the metals dissociatively adsorb H_2 and spill it

over to the M-O sites where CO_2 is adsorbed.[30] In view of all of the catalysts reported to date, it could be concluded that both the mechanisms are prevalent in any reaction, with relative dominance of one pathway over the other, depending on the catalysts. The state of art material used for RWGS is $Cu/ZnO/Al_2O_3$ (CZA), where ZnO act as structure directing agent, stabilizer and promoter.[31] Cu/ZnO is supported on Al_2O_3 which improves the dispersivity of the Cu-Zn active center but Al_2O_3 itself is an inert material towards the reaction. The activity and stability of CZA can be improved by alkali metal[32] and manganese addition.[33] CZA systems are highly susceptible towards poisoning[34] and are also pyrophoric.[25]

One of the main challenges of using metal nanoparticles at metal oxides for the RWGS is the role of metal doping percentages in determining the balance between conversion and selectivity. For instance, in the case of Pd/Al_2O_3, the CO_2 conversion increased with active metal loading, but a higher Pd loading on Al_2O_3 (i.e. 5% Pd) led to 2 to 3-fold increase in methane selectivity compared to 0.5% Pd/Al_2O_3.[35] Formate mechanism involves spilling of the formed CO back to Pd and then gets adsorbed. The subsequent desorption of CO depends upon the strength of adsorbed CO. Higher Pd loading led to more active terrace sites with multiple CO-Pd bonds, which upon subsequent hydrogenation yielded CH_4. The catalysts with 0.5% Pd loading, although less active, showed higher stability as there was no deactivation due to CO adsorption on metal sites. Non-noble metals like Ni[36, 37] and Cu[38] loaded on SiO_2 are also reported with better RWGS activity.

Reports using reducible supports like CeO_2 started appearing in the early 2000s, which easily outperformed the inert nonreducible supports like alumina and silica.[39] In TiO_2, as the support, presence of a strong metal support interaction was evidenced due to reducibility of TiO_2 to form $Pt–Ov–Ti^{3+}$ (Ov: O vacancy) sites that have high potential to donate electrons and activate CO_2 by trapping O of CO_2 in their vacancies.[40] In case of CeO_2, the mechanism starts with the exchange of O of CO_2 with CeO_2 to give CO (direct dissociation of CO_2 to CO),[41, 42] which necessitated the ceria surface to be reduced prior to the reaction. This was followed by subsequent reaction of spilled over hydrogen from the metal with O of CeO_2 to regenerate the O vacancy as shown in **Figure 1.7** (RWGS via redox reaction).

1.3.3.2. Carbon Dioxide Methanation

CO_2 methanation better known as Sabatier process is an interesting catalytic process in CCU. Methane is extensively used as fuel in LNG (liquefied natural gas) and rocket fuel, and feedstock for many value-added chemicals.

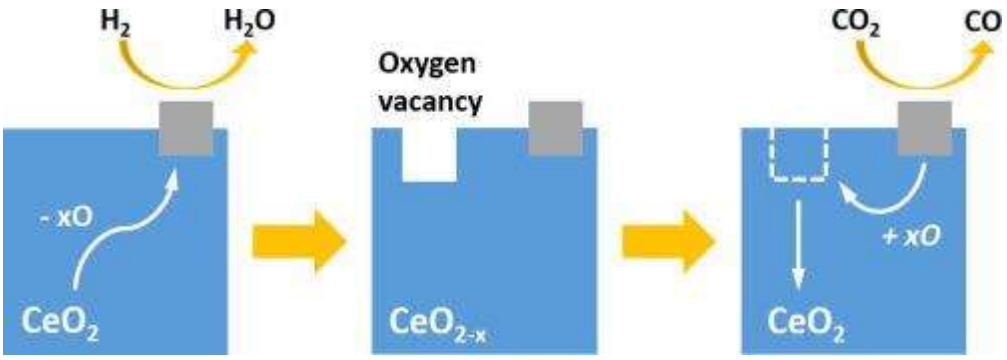

Figure 1.7. Schematic illustration of direct dissociation of CO_2 to CO and O over CeO_2 catalyst surface.[43] Reproduced with permission from ref. 43 (Copyright 2020 Elsevier).

Apart from CO_2 mitigation, the major application of methane is also in fuel cells.[44] The whole fuel cell industry is interested in CO free methane as the former poisons the catalyst. Even the Mars mission of NASA studied how to convert the CO_2 of Mars to fuel and water for energy and life support.[45] In view of thermodynamics, the CO_2 methanation/Sabatier process is a highly favorable process with large negative values of enthalpy and Gibbs free energy **(eqn. 1.2)**. At the same time, the involvement of eight electrons in the process makes it highly kinetically limited.[46]

$$4H_2 + CO_2 \leftrightarrow CH_4 + 2H_2O \qquad \Delta H\ (298\ K) = -252.9\ kJ\ mol^{-1} \qquad (1.2)$$
$$\Delta G\ (298\ K) = -130.8\ kJ\ mol^{-1}$$

Ni metals with various supports are the most widely studied catalysts for the methanation reaction.[45, 47-49] Both reducible and inert oxide supports are commonly used which includes SiO_2,[45] Al_2O_3,[47, 49, 50] TiO_2,[51] CeO_2,[52, 53] and ZrO_2.[54] The catalysts based on Rh[55] and Ru[56, 57] are the next classes that widely for this reaction. The stability and regenerating ability of Ru/γ-alumina were exceptionally high along with low operation temperature.[57] Also, a combination of Ru on reducible supports (Ru/CeO_2) gave similar stability and regeneration of the catalytically active surface.[58]

The 100% methanation selectivity at lower temperature was the highlight for Rh on TiO_2.[51] However, Ru and Rh cannot be compared to Ni in terms of cost and practical applicability. The methanation process can primarily be classified as (1) the mechanism involving CO as the intermediate and (2) the mechanism that does not involve CO. The majority of recent reports highlight the absence of CO, particularly on CeO_2-ZrO_2. The mechanism involving CO can be further classified into two ways. (a) The first pathway proceeds through the direct dissociation of CO_2 to CO* and O* with further dissociation of the CO* to C* and

O*, the former of which gets hydrogenated to methane. This mechanism was confirmed on a Ni(111) surface by DFT.[59] The pathway involving CO_2 dissociation to CO has the lowest-energy rate determining step (RDS), which involves CO* dissociation to C* and O* and subsequent hydrogenation of C to yield CH_4.[59, 60] The second pathway (b) through the CO mechanism proceeds through a consecutive RWGS and CO hydrogenation. In this mechanism, CO is formed via the RWGS and then undergoes hydrogenation through C-O bond scission via HCOH, H_2COH, and H_3CO, which results in a CH_x species giving methane at last.[61, 62] Though, by definition, process (a) can also be termed as the RWGS, it can be distinctly differentiated as CO formation via direct CO_2 dissociation. Mixed oxide supports, especially CeO_2-ZrO_2, have been widely studied in the past decade for methanation. Ni supported on CeO_2-ZrO_2 gave good activity and stability due to high Ni dispersion, weak basic sites, and low coke formation.[63] The mechanism of methanation on Ni/CeO_2-ZrO_2 was determined by IR as a formate pathway without any CO involvement **(Figure 1.8)**. Comparative experiments done on bare CeO_2-ZrO_2 and Ni/CeO_2-ZrO_2 revealed that formate bands arose exclusively in the case of Ni/CeO_2-ZrO_2, while both surfaces showed the formation of mono- and bicarbonates at 150 °C under gas flow.[64]

1.3.3.3. Carbon Dioxide Hydrogenation to Methanol

CO_2 to methanol (CTM) conversion is one of the primary processes of industrial relevance in the current scenario, where global warming is threatening the existence of human civilization. With an annual global market demand of 70-80 million metric tons, it is expected to increase at a very fast rate and reach 90 million tons by the year 2026. Methanol (MeOH) is primarily used for important downstream processes of formaldehyde, acetic acid, dimethyl ether (DME), and methyl tertbuthyl ether (MTBE) syntheses. Methanol is also projected as a future transportation fuel, or at least a major fuel substituent.[66]

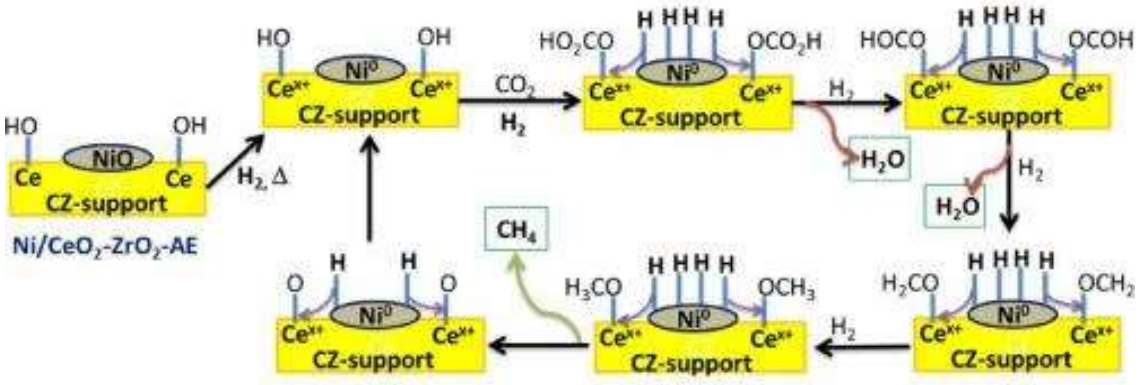

Figure 1.8. Formate mechanism of CO_2 to methane over Ni/CeO_2-ZrO_2 support.[65] Reproduced with permission from ref. 65. (Copyright 2017 Elsevier).

This thermochemical process is a combined outcome of three reactions, as shown below, where the preferred direct methanol formation **(eqn. 1.1)** from CO_2 may often be accompanied by a combination of the RWGS **(eqn. 1.3)** followed by subsequent hydrogenation of CO **(eqn. 1.4)** to methanol.[67, 68] The relative occurrences of these parallel or consecutive reactions are difficult to quantify under the operational conditions and are generally functions of thermodynamic process conditions and the chemical nature of the catalyst. Commercially, methanol is produced by a catalytic process by reacting syngas, which is an optimum mixture of CO, H_2, and CO_2.

$$H_2 + CO_2 \leftrightarrow CO + H_2O \qquad \Delta H\ (298\ K) = 41.2\ kJ\ mol^{-1} \qquad (1.1)$$

$$3H_2 + CO_2 \leftrightarrow CH_3OH + H_2O \qquad \Delta H\ (298\ K) = -49.5\ kJ\ mol^{-1} \qquad (1.3)$$

$$2H_2 + CO \leftrightarrow CH_3OH \qquad \Delta H\ (298\ K) = -90.6\ kJ\ mol^{-1} \qquad (1.4)$$

From a thermodynamic point of view of the above reactions **(eqns. 1.1, 1.3** and **1.4)** in terms of enthalpy and entropy considerations, it can be concluded that low temperature and high pressure are favorable for direct CTM conversion (**eqn. 1.3)** is endothermic, but its subsequent hydrogenation to methanol **(eqn. 1.4)** is highly exothermic with decreasing entropy, in contrast to the RWGS where the number of moles remains constant. Thus, the overall process becomes an equilibrium limited one, where thermodynamics and equilibrium shifts interplay to control the conversion and selectivity of the products. One common way adapted for shifting the equilibrium is to remove the products, in-situ, either in the form of water or methanol by dehydrating it to DME through an exothermic ($\Delta H = -23.4$ kJ/mol) process.[68]

To date, the majority of the catalysts reported for CTM are also used to reduce CO to methanol. More than 75% of the catalysts reported over the last 10-15 years are primarily Cu based systems.[69] Among those, CZ motif is at the core of the industrial catalysts used for CO_2 conversion to MeOH. CZA catalyst, the most extensively used industrial catalyst, is most conveniently prepared by coprecipitation technique using sodium carbonate as the precipitant and metal nitrates as the precursors. With the classical CTM catalysts, CZ or CZA, also being active for the RWGS, the main factors governing the reaction pathway to CO or methanol mostly happen to be the CO_2:H_2 ratio and the reaction temperatures and pressures, owing to opposing enthalpy and entropy requirements.

The exact mechanism of CTM is an elusive one. There are no conclusive inferences about the nature of the activity of Cu (Cu^0 or Cu^+) present at the interface.[70, 71] The basic step

starts with CO_2 adsorption on the oxide surface followed by H_2 spilling over from Cu sites.[71] The critical catalytic process is said to take place at the interface of Cu and metal-oxide. However, the identity of the exact active site and the role of ZnO are still debatable in the catalysis community.[72, 73] The sites consisting of Cu-steps decorated by Zn species have been identified as the most probable active site. According to the report by Behrens *et al*.,[73] Cu-steps act as the active site, with nearby Zn serving as the adsorption site for O-bound intermediates (**Figure 1.9)**. Kateel *et al*., while providing a different view of the CZA catalytic mechanism, reported CuZn alloy, which undergoes oxidation to give ZnO by O* due to dissociation of CO_2. This is attributed to the homogeneous dispersion of Zn on top of Cu leading to easy oxidation of Zn. The synergy between Cu and ZnO enhances the methanol productivity through the formate mechanism, which is discussed later.[74] Employing supports like TiO_2, ZrO_2, or TiO_2-ZrO_2 increased the dispersion of Cu and the adsorption capacity of CO_2 and H_2 due to increased basicity, which showed a direct linear relationship with the methanol yield.[75] The increase in surface area of Cu was in the order of ZnO < ZnO-TiO_2 < ZnO-ZrO_2 < ZnO-ZrO_2-TiO_2. "Dual site mechanism" is a rightly coined term here to explain the spillover from Cu and the reduction of carbonate or bicarbonate on the support.

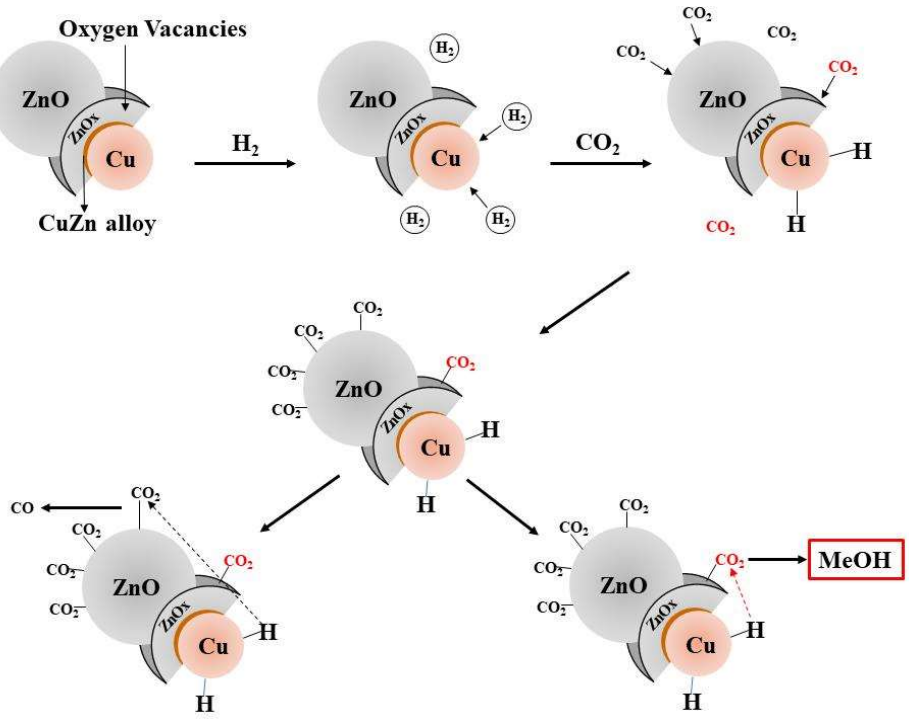

Figure 1.9. Schematic illustration of CO_2 hydrogenation to methanol at Cu/ZnO catalyst surface.[76]

Methanol production if accomplished from CO_2 can undoubtedly address both energy and global warming issues, but CZA catalyst exhibits only limited activity due to inhibition by release of water as by-product causing Cu sintering and the parasitic RWGS reaction.[77-79] However, last decade saw the reports on In_2O_3 based systems activating CO_2 by the surface O vacancies.[80] The C=O cleavage of the stable CO_2 takes place at the O vacancy of the In_2O_3 surface, giving 100% methanol selectivity through the formate pathway in contrast to other M/M-O systems.[81] Here there is a shuttle between repairing of the surface O vacancy of In_2O_3 during methanol formation and regeneration of the O vacancy to form water by H.[81] Ye *et. al*.[81] highlighted the ability of this O vacancy of In_2O_3 to trap CO_2 and cleave C=O, which was followed by regeneration of the O vacancy by H as shown in **Figure 1.10**. This was proved experimentally later in 2016 by loading In_2O_3 on ZrO_2, which exhibited 1000 h of consistent and continuous activity with 100% selectivity toward methanol.[80, 81] The lower conversion of CO_2 owing to a smaller number of oxygen vacancies on indium oxide limits its total MeOH activity. Various strategies have been adopted to improve the catalytic performance by facilitating the enhancement of surface oxygen vacancies (Ov) (In_2O_{3-x}) as active sites.[82] Predominantly the Ov over In_2O_3 is improved by zero valent transition metals[83-85] over In_2O_3 which under reducing environment creates surface Ov by H_2 spill over and also by mixing In_2O_3 with ZrO_2 and creating Ov.[86-88]

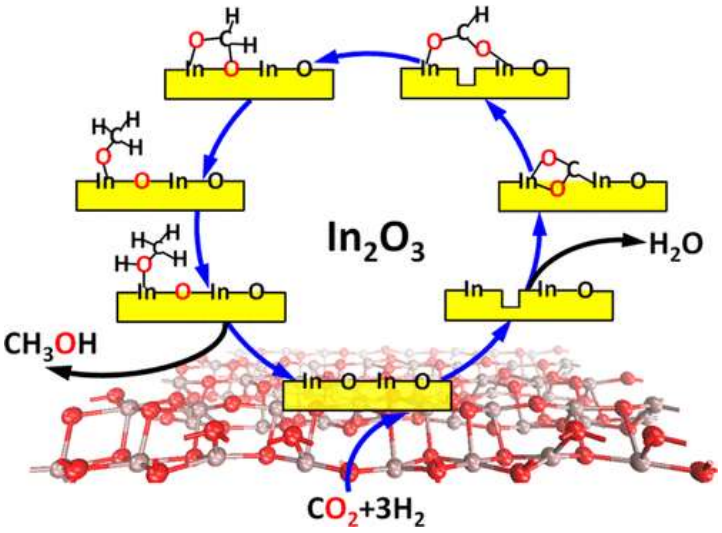

Figure 1.10. Schematic representation of MeOH formation from CO_2 over vacancy defects of Indium oxide catalyst.[81] Reproduced with permission from ref. 81. (Copyright 2013 American Chemical Society).

Last decade have also seen the modification of transition metal-based CO_2 methanation catalyst with gallium or indium yielding methanol.[89, 90] Mostly gallium or indium-based transition metal intermetallics are synthesized by impregnating inert mesoporous supports. Some of these intermetallics show unique catalytic property of CO_2 hydrogenation at lower pressures providing a potential scope to reduce the complexity associated with the CTM process.

1.3.3.4. Carbon Dioxide Hydrogenation to Formic Acid (FA)

Formic acid or methanoic acid is the simplest acid which is soluble in both water and most of organic solvents.[91] Formic acid is primarily used in antiseptics and as an antibacterial agent in animal feed.[91, 92] Because of its low toxicity, formic acid and formate can be utilized as food additives. It has a volumetric hydrogen capacity of 53 g/L, which is higher than the 20-40 g/L of different hydrides and compressed hydrogen.[93-96] Formic acid finds its most important application as a fuel in the direct formic acid fuel cell (DFAC).[97, 98] DFAC has a higher theoretical efficiency than a direct methanol fuel cell, which has been widely studied recently.

Like other CO_2 hydrogenation reactions, FA formation from CO_2 by reduction is also thermodynamically un-favorable ($\Delta G = 32.9$ kJ mol^{-1}) due to higher CO_2 stability. The reactivity can be improved much by improving the dissolution of CO_2 in the reaction medium with help of basic additives such as NaOH, $NaHCO_3$, imidazole, quinoline, and other heterocyclic nitrogen compounds.[99, 100] But these additives necessitate an additional separation of FA after the reaction from these solvents. CO_2 hydrogenation to formic acid or formates has been studied since the early 1900s, with previous investigations relying on homogeneous catalysts with poor activity. CO_2 is usually activated by a base or electron donor since it is an electrophile or Lewis acid. For homogeneous catalysts, the rational design of electron donating ligands on metal active sites is critical. Homogenous catalysis of CO_2 to FA mainly revolves around phosphine, pincer and pincer like ligands with Fe, Co, Ni, Ru, Rh, Pd, and Ir metal systems.[101-106] In this thesis we focused on developing heterogenous catalyst for FA production from CO_2 owing to the fact that usage homogenous catalyst causes high impurity in the FA formed and requires complex separation of FA and catalyst which resists the large-scale application of ligand based homogenous catalyst.

Adkins et al. produced the first heterogeneous Raney Ni catalyst in 1935 for the hydrogenation of CO_2 to formic acid at 10-20 MPa in the presence of different amines.[107] Since then, a variety of heterogeneous catalysts based on Ru, Pd, Pt, Rh, Ir, and Au metals supported on various organic or inorganic supports (such as polymers, ionic liquids, silica, clay, and

zeolites) have been utilised to catalytically hydrogenate CO_2 to create formic acid. Petri et al. employed an Au/TiO_2 catalyst to generate $HCOOH/NEt_3$ adducts from CO_2 hydrogenation in the presence of NEt_3, and the continuous reaction could be performed for 37 days without noticeable deactivation.[108] The role of the support in Au-catalyzed CO_2 hydrogenation was also explored. The supported and unsupported Au catalyst were compared for CO_2 to FA to understand the metal-support interaction and reaction mechanism by Filonenko et al.[109] The Au/Al_2O_3 interface facilitated the heterolytic dissociation of H_2 to form surface hydroxyl and metal hydride species. The CO_2 then interacted with the alumina's surface OH groups to generate a carbonate species. The Au-hydride attack on the bicarbonate resulted in adsorbed formate species that moved to the alumina surface to produce formates. However, the unsupported Au nanoparticles were catalytically inert. Park et al. investigated the effects of graphitic carbon nitride ($g\text{-}C_3N_4$) as a support for Pd catalyzed HCOOH production under neutral circumstances.[110] The numerous lone pair electrons in $g\text{-}C_3N_4$ provide basic sites for CO_2 adsorption during the reaction, therefore no additional basic additive in solution is required. The total Pd time yield (PTY, mmol of HCOOH produced/(mol of total Pd/second)) of 1.4 mol $Pd/g\text{-}C_3N_4$ catalyst was 306.7, which is 12 times greater than Pd/carbon nanotubes (CNT) with a similar Pd particle size. The HCOOH production reaction is thought to take place at the $Pd/g\text{-}C_3N_4$ interface, where CO_2 is activated while H_2 is activated on the Pd surface. The influence of Pd particle size was also examined using $Pd/g\text{-}C_3N_4$ catalysts with varying Pd loadings: when the Pd particle size was reduced from 7.2 to 3.4 nm, the TOF (number of HCOOH molecules produced/(number of surface Pd atoms/second)) increased. This is because the smaller Pd particles have larger interfacial area with $g\text{-}C_3N_4$, and thus the TOF for HCOOH production is higher.

Nguyen et al. demonstrated that a bifunctional PdNi alloy outperformed a monometallic Pd catalyst in terms of catalytic activity.[111] Under mild reaction conditions of 40°C and 5.0 MPa, the highest formic acid yield of 1.92 mmol with a TON of 6.4 and a TOF of 1.2×10^4 s^{-1} was produced when the PdNi alloy on a CNT-graphene support was reacted in water without a base addition. The H_2 molecules are dissociatively adsorbed on the Pd surface because Pd is electron-rich, and Ni is electron-deficient in the alloy. Meanwhile, the oxygen atoms of CO_2 adsorb independently on Ni as shown in **(Figure 1.11a)**. They also discovered that the catalyst with the best catalytic activity had a Pd/Ni molar ratio of 3/7. Liu et al.[112] recently reported on the direct hydrogenation of CO_2 to formates utilising Schiff-base-meditated Au nanoparticles on SiO_2.

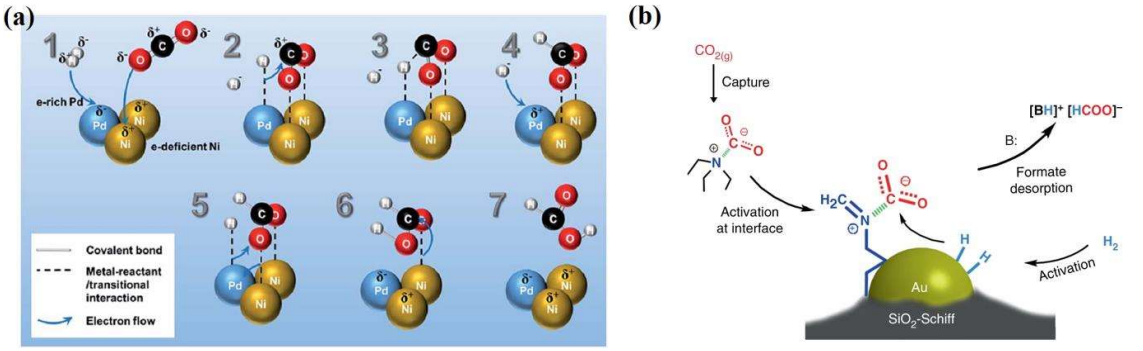

Figure 1.11. Reaction mechanism of FA formation over (a) PdNi bimetallic catalyst.[111] Reproduced with permission from ref. 111 (Copyright 2008 Royal Society of Chemistry) and (b) Au/SiO_2-Schiff Base catalyst.[112] Reproduced with permission from ref. 112. (Copyright 2017 Springer Nature).

The authors discovered that CO_2 was activated at the Au Schiff base contact by a weakly bound carbamate zwitterion intermediate, which was critical in the transformation of CO_2 to formate with a high TON of 14470 as shown in **Figure 1.11b.**

1.4. Catalyst Design

The heterogenous solid catalysts used for the CO_2 reduction in this thesis has two components: an inert mesoporous silica (SiO_2) support and an active metal nanoparticle (M-NPs). The high surface area mesoporous support ensures uniform distribution of metal nanoparticles without sintering during harsh catalytic reactions and helps in better diffusion of both reactants and products through their mesopores. Additionally, the hydroxyl groups on them activates CO_2 and stabilizes intermediates to contribute towards the hydrogenation reaction. There are many different family of mesoporous silica, mobile crystalline material (MCM),[113] Santa Barbara Amorphous (SBA)[114] and Michigan State University (MSU)[115] with different pore morphology and characteristics owing to the surfactants used in their synthesis. The main synthesis steps start with usage of an organic surfactants to form micelles in aqueous solution, followed by addition of a silica precursor (an alkoxide such as tetraethyl orthosilicate sodium metasilicate) and subsequent hydrothermal treatments. Finally, the organic surfactants are removed by oxidation or calcination, leaving the free mesopores **(Figure 1.12)**.[116] The pore size and textural properties of the mesopores can be tuned by altering the hydrothermal treatment temperature and heat treatment period.

Transition metals of group 8, 9, 10 and 11 of periodic table are reported to show excellent catalytic activity towards thermocatalytic CO_2 hydrogenation. Precisely the

noble/coinage metals of these groups are superior catalyst for all CO_2 hydrogenation reactions owing to their ability to dissociate CO_2 to CO and O, and most of the noble metals shows the property of splitting H_2 and distributing it to the intermediates for easy hydrogenation termed as hydrogen spill over.[30, 39, 45] On the other hand, the non-noble metals easily degrade during the catalytic operation affecting the stability of the catalyst. However, commercialization of coinage metal-based catalysts is limited due to their higher cost. The cost related problems of catalysts can be overcome by two methods: (a) dilution of noble metal in the catalyst by active non-noble metals (b) by designing stable non-noble metal catalyst. Both these strategies can be easily realized by mixing two metals to form stable structurally ordered phase called intermetallics (IM).[117] The major drawback of using single metal catalyst is higher activity with lower selectivity. This drawback is surpassed in intermetallics by forming reduced cluster of several noble active metal atoms separated by the secondary metal, this leads to a limited number of adsorption configurations for the reactants and intermediates enhancing the selectivity. The phenomenon of limiting active noble metal sites by a secondary metal is known as site isolation. In some cases, the activity of the reaction may decrease drastically depending upon the second metal selection. Besides site isolation the structurally ordered IMs shows several unique features in the field of catalysis such as electronic effect (ligand effect), geometric effect (ensemble effect or active site isolation), ordering and high stability.[118] The co-metal addition alters the electronic properties of the parent metal in IM, which is referred as "ligand effect".[119]

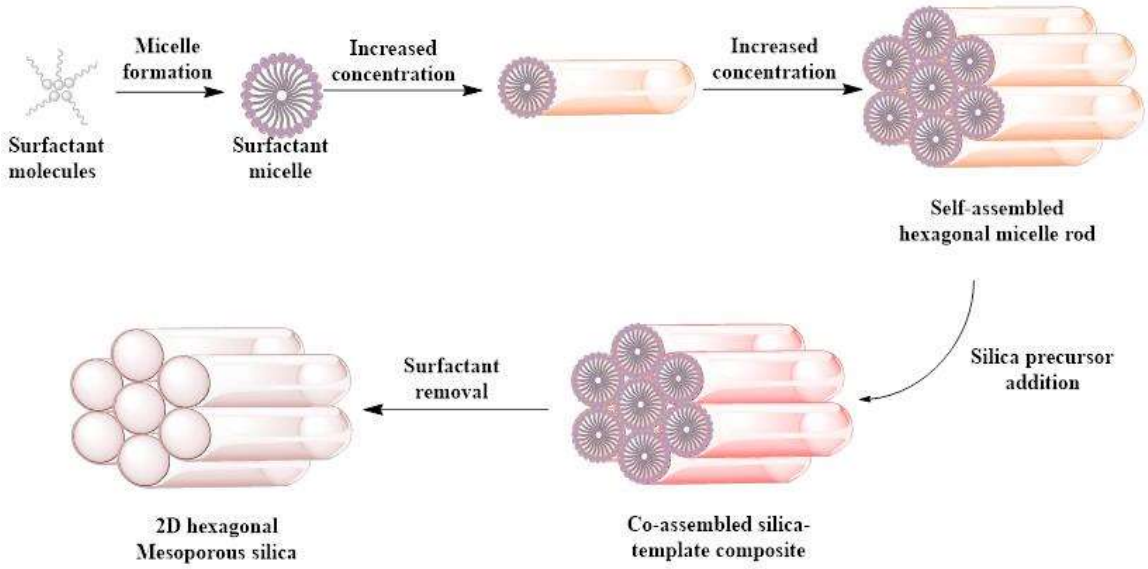

Figure 1.12. Schematic illustration of various steps involved in synthesis of mesoporous silica material.

Proper selection of metals on the basis of electronegative difference can tune the electronic properties of IM formed, which will have a crucial influence on the sorption properties of reactants, intermediates, and products in a specific catalytic study.[120, 121]

In this thesis, both single metal and IMs are loaded on the silica support to act as hydrogenation catalyst. The activity, selectivity and stability of the single metal is modified by indium-based IM formation. In some cases, indium oxide along with IM act as the activation sites for CO_2. Both single active metal NPs and IM-NPs are nestled inside the mesopores of silica by incipient wetness impregnation (IWI). This thesis basically revolves around usage of silica supported Ni based catalyst for CO_2 hydrogenation owing to the fact that it is a cheaper non-coinage transition metal with outstanding catalytic hydrogenation property. Nickel metal over silica or alumina can directly catalyze kinetically difficult 8 e^- reduction of CO_2 to methane under thermally mild operating conditions. The kinetically challenging 8 e^- reduction of CO_2 to methane over Ni metal is directly a consequence of superior hydrogen spill over property of Ni in reducing environment. The Ni clusters are known to split the H_2 gas over them and supply it to the carbon intermediates adsorbed over the catalyst known as hydrogen spill-over in literature.[122-124] This spilled hydrogen can also create surface Ov (oxygen vacancy) over reducible metal oxides creating activation sites for the stable CO_2 by trapping its oxygen in them.[125] Also, the Ni 8 e^- reduction property can be optimized by forming alloys, intermetallics or bi-metallics resulting in 6 e^- reduction or lower electron reduction products such as methanol.[89, 90] Both the concepts of IM and creation of surface Ov are used through-out this thesis in different chapters.

Incipient wetness impregnation (IWI) is also well known as dry impregnation or capillary impregnation. IWI is typical facile technique used to synthesize heterogeneous catalysts with porous support. The active metal precursor is dissolved in aqueous or organic solution. The metal-containing solution of the same or less volume (incipient wetness amount) was added on the support containing pore volume. The pore volume of the support is typically verified by adding deionized water dropwise to the support until they had a glistening appearance. The appearance indicates that the pores are fully filled, and the measuring was done by the volume of water used. Excess solution is always avoided since this excess solution causes the solution transport to change from a capillary action process to a diffusion process, which is significantly slower. The capillary action is substantially faster than liquid diffusion, which draws the solution into the pores. Then the catalysts are dried and calcined to deposit the metal on the catalyst surface **(Figure 1.13)**. The concentration profile of the impregnated compound

depends on the solubility of the precursor in the solution and mass transfer conditions within the pores during the impregnation and drying process. There are plenty of results reported in the literature for the synthesis of heterogeneous metal catalysts using IWI technique.[89, 90, 126]

The basic steps involved in are,

a) Preparation of known volume and concentration of metal precursor solution.
b) Introduction of this to the porous support.
c) Evaporating excess solution in slightly high temperature.
d) Calcination at higher temperatures.

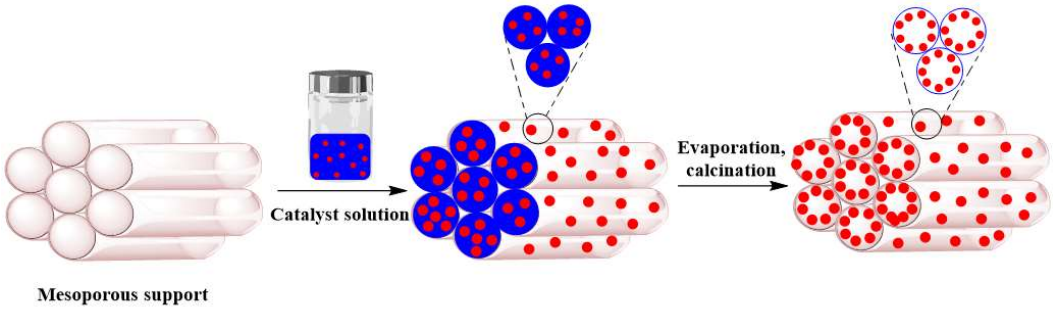

Figure 1.13. Schematic Illustration of different steps involved in Incipient Wetness impregnation.

1.5. Catalyst Characterizations and Catalyst Screening

1.5.1. Powder X-ray Diffraction (XRD)

Powder X-ray diffraction is used in determining the atomic structure and phase formed on the amorphous support material. In 1912, Bragg demonstrated that the constructive interference from a set of consecutive parallel planes can only occur for certain angles θ, and that angle θ is related to the X-ray wavelength and the interplanar spacing of the material **(Figure 1.14)**. This relation can be written as Bragg's law **(eqn. 1.5)**. Note that the fraction of the X-ray photons that is not scattered passes through to the next layer of atoms, where another portion of the X-rays are scattered. XRD was extensively used in this thesis to characterize the structure of the catalysts in this thesis. XRD patterns are compared with the reported phases available in the Pearson Crystallographic database to identify the phases formed.

$$n\lambda = 2d(hkl)\sin\theta \qquad (1.5)$$

θ: angle of incidence of the X-ray, n: an integer, λ is the wavelength, and *d(hkl)* is the spacing between atomic layers

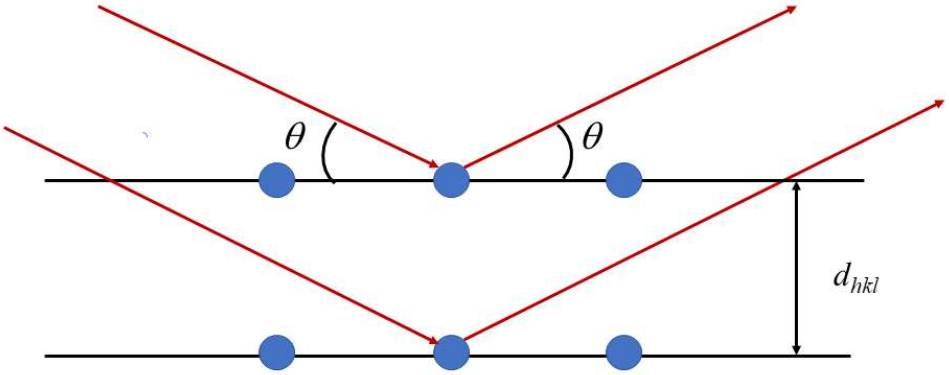

Figure 1.14. Schematic illustration of the beams diffracted by two different layers.

1.5.2. Electron Microscopy

Scanning electronic microscopy (SEM) and transmission electron microscopy (TEM) play an inevitable role in the characterization of catalysts. EM uses electron beams generated from the cathode (a tungsten filament or lanthanum hexaboride). When the beams are focused on the sample, the primary beam interacts with the atoms of the material causing scattering with various emissions, including secondary electrons (SE), backscattered electrons (BSE), and characteristic X-rays.[127] All these three radiations are usually significant for SEM analysis. These signals are associated with various types of information from the microscopy. The volume of electron beams interacting with the material depends on the energy of the incident beam, the type of material, and the atomic number of the elements.[128] The secondary electrons are very important in SEM while TEM uses the transmitted electrons. The number of secondary electrons emitted depends on other factors, like the acceleration and the characteristic voltage of the material (e.g., topography of the sample). These signals are responsible for information about the surface of the sample like morphology and topography. The basic distinction between SEM and TEM is closely related to the intensity of the beam and how it is controlled and optimized by optical electronic column. The inelastic scattered electrons, secondary electrons are excluded from analysis through the lens objective. In addition, the speed with which the electrons pass through the electron optic column in TEM is typically much larger compared to SEM. Here the SEM is employed to understand the morphology of solid materials and characterize them in nanoscale. SEM technique commonly offers the image on the nanometre (nm) to micrometre (μm) scale and were specially employed in non-crystalline catalysts to observe distribution and sizes of mesopores. Similarly, TEM is also employed to understand the active metal nanoparticle distribution over the mesoporous solids. For TEM, a grid laden with sample was prepared before measurements. A small amount of each powder sample was dispersed into 500 μL ethanol and

sonicated for 30 minutes. 5 to 10 µL from the dispersion was dropped on a carbon- coated grid and dried at for 8 hours before imaging. TEM images and selected area electron diffraction (SAED) patterns were collected using a JEOL JEM-2010 TEM instrument.

1.5.3. X-ray Photoelectron Spectroscopy (XPS)

Since heterogenous catalysis is a surface phenomenon, XPS is employed to understand the surface composition (<~ 10 nm of the surface) and oxidation state of the elements in the material. The principle of XPS is originated from the photoelectric effect proposed by Einstein and the photoemission used as an analytical tool was proposed by Kai Siegbahn.[129] In brief, an atom or molecule is excited with a photon causing an electron ejection. The kinetic energy (K.E.) of the ejected electron depends upon the photon energy (hν) and the binding energy (B.E.) of the electron (energy required to remove the electron from the surface). XPS is a quantitative technique in the sense that the number of electrons recorded for a given transition is proportional to the number of atoms at the surface. A relation between hν, K.E., and B.E. can be expressed as **eqn. 1.6**. The value of binding energy and chemical shift (difference from the elemental state) are utilized for identification of an element and estimation of its chemical bonding state in the specimen.[130] The XPS data is fitted with the help of CasaXPS in this thesis.

$$h\nu = \text{Kinetic Energy} + \text{Binding Energy} + \varphi \qquad (1.6)$$

φ : Work Function

1.5.4. X-ray Absorption Spectroscopy (XAS)

This technique is used to understand the local geometry and electronic structure of the material. High intensity X-rays generated by a synchrotron source are used to excite the core-level electrons (K, L or M shell) of a particular element from the ground state to an excited electronic state. This excitation leaves an empty core-level, within a short span of 10^{-15} secs is filled by an electron from the higher energy shell. Fluorescence occurs during the return of this electron to a lower energy state from the higher one. This energy released is equal to the energy difference between the two orbitals and hence, the absorption energy is specific for each element. The incident X-ray is also partly absorbed by the sample while the remaining is transmitted by the sample. The probability of X-ray absorption is defined by the X-ray absorption coefficient. This absorption coefficient being element specific increases with binding energy of the core-level electrons and depends on the atomic number of the elements. In a typical XAS measurement incident X-ray beam passes through an ionization chamber which measures

the initial intensity (I_0). The fluorescence detector kept at angle of 45° from the sample detects the photoelectrons that are produced upon interaction of the incident radiation with the sample surface. The remaining radiation enters a second ionization chamber where the transmitted radiation (I_t) is measured. A reference foil is placed after the second ionization chamber and intensity of the transmitted X-rays through the reference is determined in a third ionization chamber (I_r). The X-ray absorption coefficient can be determined based on measured intensity of incident and transmitted radiation. When the incident radiation has an energy equal to that of the energy required to excite a core-level electron a sharp increase of μ is expected which is defined as the absorption edge in a typical XAS spectrum. This absorption edge is element specific. Typically, XAS spectra comprises of two regions: X-ray near edge structure (XANES) and Extended X-ray absorption fine structure (EXAFS). XANES gives information about the oxidation state and charge transfer of the absorbing atoms. EXAFS gives important information about the local structure of the element i.e., bonding environment and coordination number. XANES region ranges from – 50 to +100 eV of the absorption edge whereas EXAFS region begins after 50 eV from the absorption edge. A Fourier transform of the data expressed in k-space (momentum space) leads to expression of data in R-space where, R is the radial distance of the neighboring atom from the absorbing atom.

1.5.5. Temperature Programmed Reduction/ Desorption (TPR/TPD)

TPR as a catalyst characterization technique mainly gives information about the degree of reduction of the active sites in heterogeneous catalysts. The apparatus consists of a quartz reactor with temperature controller, gas mass flow controllers (MFC) to provide a mixture of gases of a given reducing gas along with the carrier gas, and a TCD (thermal conductivity detector) or mass spectrometer to detect the gas flow composition after the reaction. The procedure involves reduction of the catalyst by passing reducing gas mixture of known concentration. The temperature is raised with a certain ramping rate while continuous monitoring of the reduction by hydrogen consumption is done using the TCD, which is pre-calibrated by the reduction of pure metal oxides (e.g. Fe_2O_3, Co_3O_4, CuO, NiO).[131]

TPD analysis provides an in-depth insight on the number of adsorption sites, the degree of dispersion, surface desorption temperature, rate of desorption, kinetic order of desorption, and the energy of desorption. During TPD, the catalyst samples are pre-treated with desired reactant gases such as CO_2 (understanding interaction with catalyst surface) or ammonia (for identifying basic sites), pre-treatments are done in corresponding gas environment of increasing temperature with constant ramping rate. Then during desorption, it is purged by an inert gas

such as helium, argon, or nitrogen again with ramping temperature. The sample surface desorbs the gas that has been previously chemisorbed, and a TCD or mass spectrometer monitors the process. The Langmuir adsorption model may be used as well for the TPD spectra interpretation as it describes both gas adsorption and desorption in both the cases of associative and dissociative adsorption.[132] Apart from being a powerful technique TPD has two major limitations: it is a sample destructive technique and also there is no way to "visually observe" what is on the surface but just what comes off the surface. Further, the binding sites, structures, and absolute coverage cannot be identified by TPD itself.

1.5.6. BET Surface Area and Textural Properties

N_2 adsorption-desorption isotherm characterization were crucial in understanding the surface area, pore size distribution and other textural properties of mesoporous supports and catalysts used in the thesis. The surface area was measured by N_2 adsorption over the surface at 77K, with the help of BET (Brunauer, Emmett & Teller) equation by BelCat Instrument (BELSORP max II).

$$\frac{1}{v\left[\left(\frac{1}{P/P_0}\right)-1\right]} = \frac{c-1}{v_m c}\left(\frac{P}{P_0}\right)+\frac{1}{v_m c} \tag{1.7}$$

Where P is the equilibrium pressure and P_0 is the saturation pressure of the adsorbate at the time of adsorption. P/P_0 is the relative pressure, v is the volume of the total adsorbed gas, v_m is the volume of adsorbed gas for monolayer formation and c is the BET constant. From this equation Adsorbed gas volume is plotted against the relative pressure. Based on the above BET equation, specific surface area can be calculated as,

$$S_{BET} = \frac{v_m\, N\, s}{a\, V} \tag{1.8}$$

N is the avogadro no. (6.023×10^{23}), *s* is cross-section of adsorbing species (16.2Å^2 for Nitrogen), V is molar volume of adsorbate gas and a is the mass of the adsorbent, v_m is the volume of adsorbed gas for monolayer formation which can be obtained from BET equation.

1.6. Catalyst Screening

In this thesis two types of heterogenous catalytic processes are used to screen the catalysts discussed. One catalytic process used is vapor phase continous flow reaction process, here the catalyst is loaded in tubular reactor over the inert bed and reactants are being

continously passed over them. The tubular reactor are heated and pressurized by furnace and back pressure regulator to achieve desired reaction conditions. The vent of the reactor is continously monitored for different products and the product is also collected. The second type of catalytic process used is Batch process in which catalyst is dispersed in a solvent medium pressurized with reactant gases (CO_2 and H_2), the whole set-up of catalyst and solvent medium is enclosed in autoclave reactor and heated by an oil bath. Here the products are analyzed after completion of reaction. The details of the process and their pre-requirements are explained in the two upcoming sections.

1.6.1. Flow Reactor

An example of the flow reactor system configuration used in this thesis is schematically illustrated in **Figure 1.15**. This specific setup was designed for atmospheric pressure to high pressure (1 to 50 Bar) CO_2 hydrogenation to $C_{1\text{-}2}$ gaseous and liquid fuels (mainly methane, CO, methanol and DME). For C_1 liquid fuels requiring high pressure the reactor pressure is built by the manual back pressure regulator (BPR) with the help of non-return valves (NRV). For RWGS reaction and methanation reaction the manual BPR are turned to minimum to avoid any pressure building inside the reactor. The gases (H_2, CO_2 & N_2) can be fed into the vertically positioned stainless steel flow reactor via mass flow controllers (MFCs) which records and controls the flow speed. To avoid any pressure drop and to ensure smooth flow of reactants and products the synthesized catalyst powders are extruded into wire-like structures and supported at the middle of the stainless steel (SS) reactor between catalytically inert alumina beads. The extrudate synthetic scheme of catalyst powder is depicted in **Figure 1.16**. The reactor was heated by a tubular furnace connected with a PID controller, and all the heated parts were controlled at the same temperature to ensure an isothermal condition. A pressure relieve valve was installed to prevent the system from over pressurization. Finally, the products are collected and analyzed with an online GC equipped with TCD and/or FID. The sealing, safety, and thermodynamics of the high-pressure reactor system need extra consideration to achieve a reliable and consistent evaluation of catalysts. The leak test and maintenance of fitting parts and filters should be done regularly.

1.6.2. Batch Reactor

The batch process of CO_2 hydrogenation was studied by a high pressure reactor of Parr make. In this process, previously weighed catalysts were dispersed in 0.5 M $KHCO_3$ solution in vials with magnetic rice beads and kept inside the parr autoclave as shown in **Figure 1.17**.

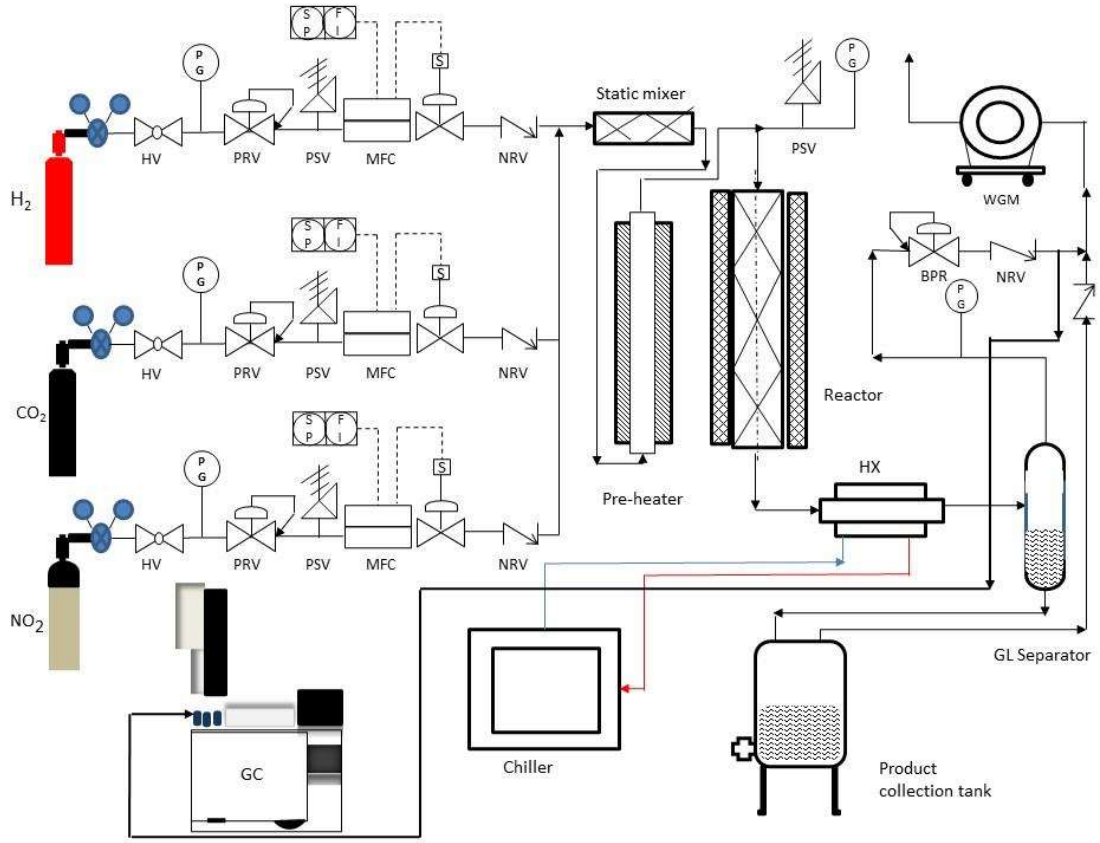

Figure 1.15. Process flow diagram of the semi-industrial scale CO_2 hydrogenation flow reactor used in this thesis.

The vial is kept firm by using glass wools and the temperature inside the autoclave were monitored by a thermocouple. The parr reactor is heated in oil bath and pressurized with different ratios of CO_2 and H_2 by the respective MFCs. The pressure inside the autoclave will be displayed by the pressure gauge on the reactor. Before the reaction, the autoclave is flushed 3 times using the feed gas mixture to flush out the oxygen gas from vessel.

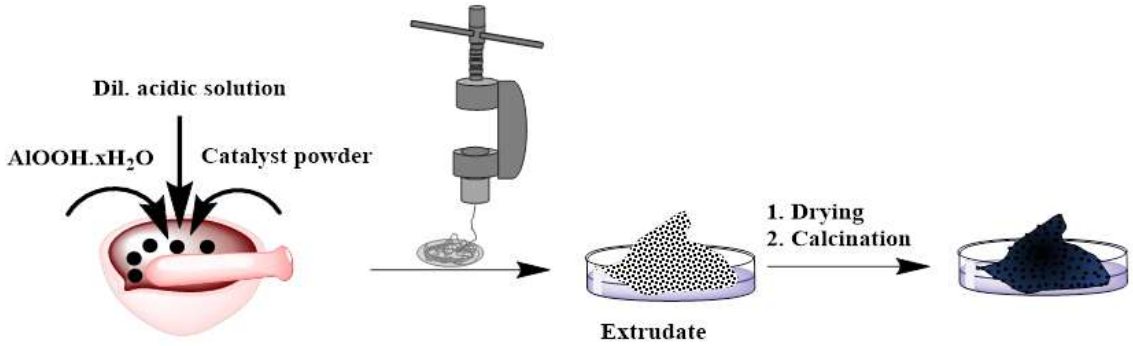

Figure 1.16. Schematic illustration of different steps involved in catalytic powder extrusion into wire type extrudate.

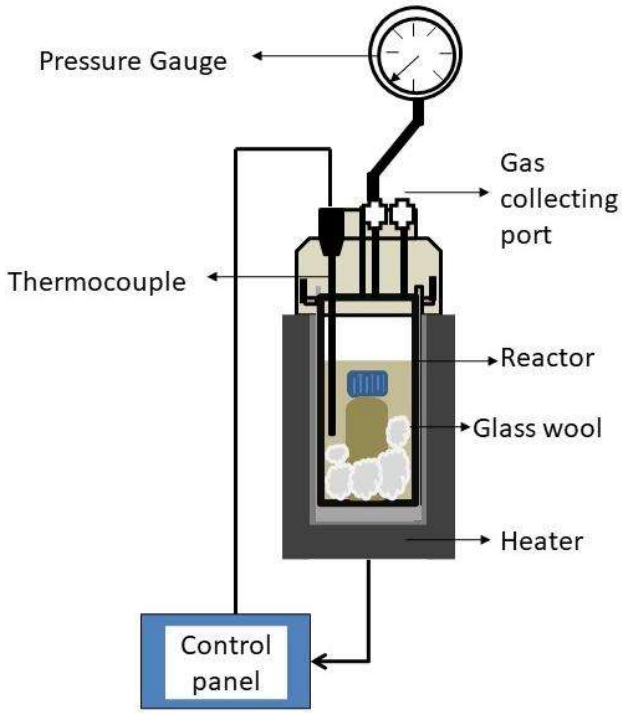

Figure 1.17. Schematic representation of batch reactor used in the thesis.

The vessel was pressurized till 40 bar and put inside the preheated oil bath at 40 °C. Upon completion of experiment the product solution was removed from vials and centrifuged to remove catalyst. The products solution was analyzed by Agilent HPLC, with RID and VWD1 as the detector.

1.7. Product Analysis

1.7.1. Gas chromatography (GC)

Chromatography is one of the powerful analytical techniques used to separate and analyze quantitatively and qualitatively the chemical compounds in a gas or liquid sample, or in a feed stream if equipped with an on-line sampling device. In the experimental setup we used for continuous flow reactor, the gas stream from sampler of reactor is continuously analyzed by the gas chromatograph (GC). This type of analysis is commonly known as online analysis. The GC employed here is Agilent 7890A equipped with both thermocouple detectors (TCD) and flame ionization detector (FID). The former is a universal detector while the latter is specialized detector for all hydrocarbons. Thus hydrogen, nitrogen, CO_2 and CO are detected by TCD while FID are used for methane, methanol and dimethyl ether (DME). The software ChemStation 7890A used to analyze the chromatograph were provided by Agilent. The gas and liquid calibration of GCs were done by standard calibration gas mixture.

1.7.2. High-Performance Liquid Chromatography (HPLC)

The liquid products were analyzed by HPLC (Agilent 1220 Infinity II LC system). The HPLC compartment contains autosampler, quaternary pump, column, refractive index detector (RID), and variable wavelength detector (VWD). Hi-Plex H column has been used to detect the organic liquid products like acids and alcohols. The flow rate through the Hi-Plex H column is kept at 0.5 ml/min while analyzing samples. Five mM H_2SO_4 is used as the mobile phase during analysis. The column temperature was kept at 50 °C. VWD uses a light signal to detect chromophores in the analytes. It can be used the products include ketones/carboxylic acids/aldehydes. Acquisition frequency is given as 10 Hz with a peak width of 0.05 min. It is good enough to record sufficient data points. RID is the primary detector in this HPLC configuration. It is a highly sensitive detector which works based on the difference in refractive index of the sample and analyte.

1.8. Mechanistic Studies

1.8.1. Diffused Reflectance Infrared Fourier Transform Spectroscopy (DRIFTS)

The understanding about pathway and intermediate of catalytic reactions are crucial in designing better catalytic system. Powerful in-situ techniques only can give insights about the intermediates formed over the catalytic surface during the reaction, DRIFT is one such technique. The schematic of DRIFT set up is shown in Figure **1.18**.

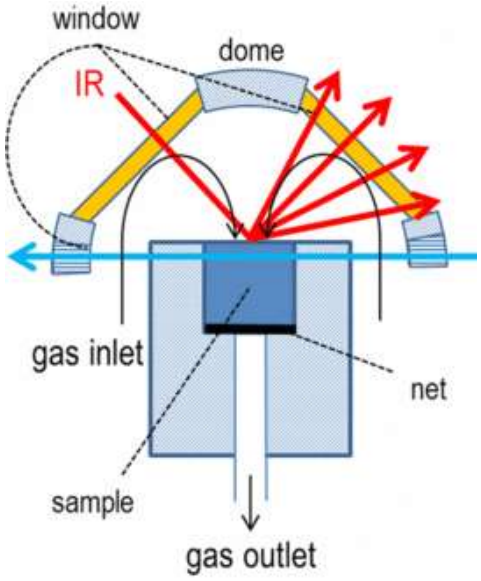

Figure 1.18. Schematic illustration of DRIFTS set-up for catalyst evaluation.[133] Reproduced with permission from ref. 133 (Copyright 2014 AIP Publishing)

Diffuse reflectance measures the energy that diffuse after interaction with electromagnetic radiation in the infrared region with a discontinuous matrix (powder, solid, or film-type samples) and reflects by charging spectral information that is dependent on the concentration of the sample. Thus, analyses performed by DRIFTS have the major advantage of minimum sample preparation (no pellet preparation). It can be easily employed to analyze samples in powder form or those deposited in a matrix. This technique has proven to be a valuable tool for characterizing catalysts since it enables the acquisition of information about the modifications occurring at surface of catalysts during chemical reactions and providing insights about the intermediate species formed and most importantly reaction pathways.[134, 135]

1.8.2. Density Functional Theory Calculations (DFT)

Combining in-situ vibrational spectroscopic techniques with DFT simulations can reveal the reaction pathways and its interaction with structure of catalytic surfaces at the molecular level. The calculations were carried out on systems with a large number of atoms, which necessitated the optimization of the electronic/geometric structures before any property calculations could be carried out.

Electronic Optimization: It's a single-point energy calculation in which atoms are held in a fixed position and the energy associated with that arrangement is calculated.

Geometric Optimization: Since the system travels through numerous configurations driven by lowest energy and investigates the most stable ground state configuration, this computation aids in perceiving the most stable configuration.

Adsorption energy: The first step in any catalytic process is the interaction of reactant with catalyst surface by adsorption. The total energy of binding of a catalytic system (catalyst and reactants) can be calculated as

$$E_b = E_{(ads/slab)} - E_{(slab)} - E_{(ads)} \quad (1.9)$$

where, $E_{(ads/slab)}$; energy of the final optimized adsorption configuration on the slab, $E_{(ads)}$: is the energy of the adsorbed molecule and $E_{(slab)}$; is the energy of the catalyst surface.

Free energy diagram: The free energy diagram can provide the account of thermodynamics of reaction intermediates without considering the kinetics. It considers the kinetic barrier between each stage as well as the thermodynamics associated with each intermediate's adsorption energy. The adsorption energy calculation is the cornerstone of the free-energy diagram. Here we simulated adsorption of various intermediates occurring during the CO_2 reduction reaction

(CO_2RR) and calculated their adsorption energies to obtain thermodynamically most feasible pathway to identify the mechanism and intermediates.

1.9. Thesis Outlook

The first chapter of the thesis starts with introducing briefly the problems related to the upsurging energy crisis and global warming. It briefly discusses the motivation to develop a CO_2 capture-conversion technology and integrating them with greener hydrogen source for energy and environmental application. A literature overview of already reported catalyst and mechanism are presented along with different material characterization, spectroscopic techniques and catalyst screening techniques adopted in the thesis. Introduction mainly highlights the development of transition metal-based mesoporous silica supported catalyst and their synthesis.

Chapter 2 investigates how inert silica supports with different physicochemical textural properties influences the activity of transition metal catalyst towards CO_2 hydrogenation. The difference in activity, selectivity, mechanism, and intermediates formed with change of textural properties of silica were deeply studied with help of operando spectroscopic studies. This may provide better insight about selection of support material for CO_2 conversion as well as other catalysis. The best mesoporous silica support from the study were used in chapter 3-5 for transition metal loading for CO_2 hydrogenation.

In chapter 3 the hydrogenation of Ni was modified by alloying with indium to obtain IM systems on mesoporous support. For this Ni-In IMs of different ratios were targeted and the selective CO_2 hydrogenation to methanol were studied by changing the ratio of Ni and In. The remarkable shift of product selectivity from methane to methanol upon IM formation were mapped by operando diffuse reflectance infrared Fourier transform spectroscopy analysis, corroborated by first-principles calculations.

Chapter 4 explores the enhancement of number of Ov on indium oxide to improve the activation and selective hydrogenation of CO_2 to MeOH non-noble transition metals. The surface Ov in In_2O_3 rationally improved by co-impregnating two non-noble metals, Ni and Co, onto the mesoporous silica and the improvement in methanol activity were correlated with the quantity of surface Ov. These enhancements were studied and discussed with the help of XPS and XAS characterization respectively.

Chapter 5 discusses about Pd containing bimetallic systems distributed over Schiff base functionalized silica as superior catalyst for CO_2 hydrogenation to formic acid (FA) in $KHCO_3$

solution by batch process. Here we synthesized four different types of Schiff base over inside SBA-15 by condensing 3-aminpropyltriethoxysilane (APTES) with two different types of aldehydes such a Butyraldehyde (BUT) and Glutaraldehyde (GLU). Pd based bimetallic systems loaded on SBA-15/APTES-GLU show the highest CO_2 to FA activity compared to other Schiff base functionalized silica. Further, the higher activity of the catalyst was correlated with both dynamic and static CO_2 capture experiments conducted on the Schiff base support.

In overall, this thesis aimed to discover several non-noble metal for the efficient conversion of CO_2 to chemicals and fuels.

1.10. References

1. Zhao, G.; Huang, X.; Wang, X.; Wang, X., Progress in Catalyst Exploration for Heterogeneous CO_2 Reduction and Utilization: A Critical Review. *J. Mater. Chem. A* **2017,** *5* (41), 21625-21649.
2. Yuqiang, J.; Dazhong, D.; Lin, Q.; Yanfei, S.; Chan, J.; Fuwei, H., Basic Features and Evaluation of Shale Gas Reservoirs. *Nat. Gas Ind.* **2010,** *30* (10), 7-12.
3. Cipolla, C. L.; Lolon, E. P.; Erdle, J. C.; Rubin, B., Reservoir Modeling in Shale-Gas Reservoirs. *SPE Reservoir Eval. Eng.* **2010,** *13* (04), 638-653.
4. Lee, S.-Y.; Holder, G. D., Methane Hydrates Potential as a Future Energy Source. *Fuel Process. Technol.* **2001,** *71* (1), 181-186.
5. Eren, B. M.; Taspinar, N.; Gokmenoglu, K. K., The Impact of Financial Development and Economic Growth on Renewable Energy Consumption: Empirical Analysis of India. *Sci. Total Environ.* **2019,** *663*, 189-197.
6. Wang, Q.; Li, R., Drivers for Energy Consumption: A Comparative Analysis of China and India. *Renewable Sustainable Energy Rev.* **2016,** *62*, 954-962.
7. Wang, Q.; Jiang, X.-t.; Yang, X.; Ge, S., Comparative Analysis of Drivers of Energy Consumption in China, the USA and India – A Perspective from Stratified Heterogeneity. *Sci. Total Environ.* **2020,** *698*, 134117.
8. Stoddard, I.; Anderson, K.; Capstick, S.; Carton, W.; Depledge, J.; Facer, K.; Gough, C.; Hache, F.; Hoolohan, C.; Hultman, M., Three Decades of Climate Mitigation: Why Haven't We Bent the Global Emissions Curve? *Annual Rev. Environ. Resources* **2021,** *46*, 653-689.
9. Saeidi, S.; Amin, N. A. S.; Rahimpour, M. R., Hydrogenation of CO_2 to Value-Added Products—A Review and Potential Future Developments. *J. CO_2 Util.* **2014,** *5*, 66-81.
10. Jiang, Z.; Xiao, T.; Kuznetsov, V. á.; Edwards, P. P., Turning Carbon Dioxide into Fuel. *Philos. Trans. R. Soc. A* **2010,** *368* (1923), 3343-3364.
11. Porosoff, M. D.; Yan, B.; Chen, J. G., Catalytic Reduction of CO_2 by H_2 for Synthesis of CO, Methanol and Hydrocarbons: Challenges and Opportunities. *Energy Environ. Sci.* **2016,** *9* (1), 62-73.
12. Olah, G. A.; Mathew, T.; Prakash, G. K. S., Chemical Formation of Methanol and Hydrocarbon ("Organic") Derivatives from CO_2 and H_2-Carbon Sources for Subsequent Biological Cell Evolution and Life's Origin. *J. Am. Chem. Soc.* **2017,** *139* (2), 566-570.

13. Olah, G. A.; Prakash, G. K. S.; Goeppert, A.; Czaun, M.; Mathew, T., Self-Sufficient and Exclusive Oxygenation of Methane and Its Source Materials with Oxygen to Methanol via Metgas Using Oxidative Bi-reforming. *J. Am. Chem. Soc.* **2013,** *135* (27), 10030-10031.
14. Tsiao, C.; Corbin, D. R.; Dybowski, C., Investigation of Methanol Adsorbed on Zeolite H-ZSM-5 by Carbon-13 NMR Spectrometry. *J. Am. Chem. Soc.* **1990,** *112* (20), 7140-7144.
15. Olah, G. A., Beyond Oil and Gas: The Methanol Economy. *Angew. Chem. Int. Ed.* **2005,** *44* (18), 2636-2639.
16. Ulmer, U.; Dingle, T.; Duchesne, P. N.; Morris, R. H.; Tavasoli, A.; Wood, T.; Ozin, G. A., Fundamentals and Applications of Photocatalytic CO_2 Methanation. *Nat. Commun.* **2019,** *10* (1), 3169.
17. Behra, A.; Kar, A. K.; Srivastava, R., Challenges and Prospects in the Selective Photoreduction of CO_2 to C_1 and C_2 Products with Nanostructured Materials: A Review. *Mater. Horiz.* **2021**.
18. Zhen, X.; Wang, Y., An Overview of Methanol as an Internal Combustion Engine Fuel. *Renewable Sustainable Energy Rev.* **2015,** *52*, 477-493.
19. Murthy, P. S.; Liang, W.; Jiang, Y.; Huang, J., Cu-Based Nanocatalysts for CO_2 Hydrogenation to Methanol. *Energy & Fuels* **2021,** *35* (10), 8558-8584.
20. Ratnasamy, C.; Wagner, J. P., Water Gas Shift Catalysis. *J. Catal. Rev.* **2009,** *51* (3), 325-440.
21. Faur Ghenciu, A., Review of Fuel Processing Catalysts for Hydrogen Production in PEM Fuel Cell Systems. *Curr. Opin. Solid State Mater. Sci.* **2002,** *6* (5), 389-399.
22. Takht Ravanchi, M.; Sahebdelfar, S., Catalytic Conversions of CO_2 to Help Mitigate Climate Change: Recent Process Developments. *Process Saf. Environ. Prot.* **2021,** *145*, 172-194.
23. Joo, O.-S.; Jung, K.-D.; Moon, I.; Rozovskii, A. Y.; Lin, G. I.; Han, S.-H.; Uhm, S.-J., Carbon Dioxide Hydrogenation To Form Methanol via a Reverse-Water-Gas-Shift Reaction (the CAMERE Process). *Ind. Eng. Chem. Res.* **1999,** *38* (5), 1808-1812.
24. Espinoza, R. L.; Steynberg, A. P.; Jager, B.; Vosloo, A. C., Low Temperature Fischer–Tropsch Synthesis from a Sasol Perspective. *Appl. Catal. A* **1999,** *186* (1), 13-26.
25. Centi, G.; Perathoner, S., Opportunities and Prospects in the Chemical Recycling of Carbon Dioxide to Fuels. *Catal. Today* **2009,** *148* (3), 191-205.

26. Kim, S. S.; Park, K. H.; Hong, S. C., A Study of the Selectivity of the Reverse Water–Gas-Shift Reaction over Pt/TiO_2 Catalysts. *Fuel Process. Technol.* **2013,** *108*, 47-54.
27. Chen, C.-S.; Cheng, W.-H.; Lin, S.-S., Study of Iron-Promoted Cu/SiO_2 Catalyst on High Temperature Reverse Water Gas Shift Reaction. *Appl. Catal. A* **2004,** *257* (1), 97-106.
28. Ginés, M. J. L.; Marchi, A. J.; Apesteguía, C. R., Kinetic Study of the Reverse Water-Gas Shift Reaction over CuO/ZnO/Al_2O_3 Catalysts. *Appl. Catal. A* **1997,** *154* (1), 155-171.
29. Shen, G. C.; Fujita, S.-I.; Takezawa, N., Preparation of Precursors for the Cu/ZnO Methanol Synthesis Catalysts by Coprecipitation Methods: Effects of the Preparation Conditions Upon the Structures of the Precursors. *J. Catal.* **1992,** *138* (2), 754-758.
30. Conner Jr, W. C.; Falconer, J. L., Spillover in Heterogeneous Catalysis. *Chem. Rev.* **1995,** *95* (3), 759-788.
31. Spencer, M. S., The Role of Zinc Oxide in Cu/ZnO Catalysts for Methanol Synthesis and the Water-Gas Shift Reaction. *Top. Catal.* **1999,** *8* (3), 259.
32. Klier, K.; Young, C. W.; Nunan, J. G., Promotion of the Water Gas Shift Reaction by Cesium Surface Doping of the Model Binary Copper/Zinc Oxide Catalyst. *Ind. Eng. Chem. Res.* **1986,** *25* (1), 36-42.
33. Li, Y.; Fu, Q.; Flytzani-Stephanopoulos, M., Low-Temperature Water-Gas Shift Reaction Over Cu- and Ni-Loaded Cerium Oxide Catalysts. *Appl. Catal. B* **2000,** *27* (3), 179-191.
34. Rhodes, C.; Hutchings, G. J.; Ward, A. M., Water-Gas Shift Reaction: Finding the Mechanistic Boundary. *Catal. Today* **1995,** *23* (1), 43-58.
35. Wang, X.; Shi, H.; Kwak, J. H.; Szanyi, J., Mechanism of CO_2 Hydrogenation on Pd/Al_2O_3 Catalysts: Kinetics and Transient DRIFTS-MS Studies. *ACS Catal.* **2015,** *5* (11), 6337-6349.
36. Lu, B.; Kawamoto, K., Direct Synthesis of Highly Loaded and Well-Dispersed NiO/SBA-15 for Producer Gas Conversion. *RSC Adv.* **2012,** *2* (17), 6800-6805.
37. Lu, B.; Ju, Y.; Abe, T.; Kawamoto, K., Dispersion and Distribution of Bimetallic Oxides in SBA-15, and Their Enhanced Activity for Reverse Water Gas Shift Reaction. *Inorg. Chem. Front.* **2015,** *2* (8), 741-748.
38. Fujita, S.-I.; Usui, M.; Takezawa, N., Mechanism of the Reverse Water Gas Shift Reaction Over Cu/ZnO Catalyst. *J. Catal.* **1992,** *134* (1), 220-225.

39. Goguet, A.; Meunier, F. C.; Tibiletti, D.; Breen, J. P.; Burch, R., Spectrokinetic Investigation of Reverse Water-Gas-Shift Reaction Intermediates over a Pt/CeO_2 Catalyst. *J. Phys. Chem. B* **2004,** *108* (52), 20240-20246.
40. Kim, S. S.; Lee, H. H.; Hong, S. C., A Study on the Effect of Support's Reducibility on the Reverse Water-Gas Shift Reaction Over Pt catalysts. *Appl. Catal. A* **2012,** *423-424*, 100-107.
41. Laosiripojana, N.; Assabumrungrat, S., Catalytic Dry Reforming of Methane Over High Surface Area Ceria. *Appl. Catal. B* **2005,** *60* (1), 107-116.
42. Bueno-López, A.; Krishna, K.; Makkee, M., Oxygen Exchange Mechanism Between Isotopic CO_2 and Pt/CeO_2. *Appl. Catal. A* **2008,** *342* (1), 144-149.
43. Yamaguchi, D.; Tang, L.; Scarlett, N.; Chiang, K., The Activation and Conversion of Carbon Dioxide on the Surface of Zirconia-Promoted Ceria Oxides. *Chem. Eng. Sci.* **2020,** *217*, 115520.
44. Galletti, C.; Specchia, S.; Saracco, G.; Specchia, V., CO Selective Methanation Over Ru–γAl_2O_3 Catalysts in H_2-Rrich Gas for PEM FC Applications. *Chem. Eng. Sci.* **2010,** *65* (1), 590-596.
45. Aziz, M. A. A.; Jalil, A. A.; Triwahyono, S.; Mukti, R. R.; Taufiq-Yap, Y. H.; Sazegar, M. R., Highly Active Ni-Promoted Mesostructured Silica Nanoparticles for CO_2 Methanation. *Appl. Catal. B* **2014,** *147*, 359-368.
46. Park, J.-N.; McFarland, E. W., A Highly Dispersed Pd–Mg/SiO_2 Catalyst Active for Methanation of CO_2. *J. Catal.* **2009,** *266* (1), 92-97.
47. Danaci, S.; Protasova, L.; Lefevere, J.; Bedel, L.; Guilet, R.; Marty, P., Efficient CO_2 Methanation Over Ni/Al_2O_3 Coated Structured Catalysts. *Catal. Today* **2016,** *273*, 234-243.
48. Wu, H.; Chang, Y.; Wu, J.; Lin, J.; Lin, I.; Chen, C. C. S.; Technology, Methanation of CO_2 and Reverse Water Gas Shift Reactions on Ni/SiO_2 Catalysts: The Influence of Particle Size on Selectivity and Reaction Pathway. *Catal. Sci.* **2015,** *5* (8), 4154-4163.
49. Yang Lim, J.; McGregor, J.; Sederman, A. J.; Dennis, J. S., Kinetic Studies of CO_2 Methanation Over a Ni/γ-Al_2O_3 Catalyst Using a Batch Reactor. *Chem. Eng. Sci.* **2016,** *141*, 28-45.
50. Rahmani, S.; Rezaei, M.; Meshkani, F., Preparation of Promoted Nickel Catalysts Supported on Mesoporous Nanocrystalline Gamma Alumina for Carbon Dioxide Methanation Reaction. *J Ind. Eng. Chem.* **2014,** *20* (6), 4176-4182.

51. Akamaru, S.; Shimazaki, T.; Kubo, M.; Abe, T., Density Functional Theory Analysis of Methanation Reaction of CO_2 on Ru Nanoparticle Supported on TiO_2 (101). *Appl. Catal. A* **2014,** *470*, 405-411.
52. Zhou, G.; Liu, H.; Cui, K.; Jia, A.; Hu, G.; Jiao, Z.; Liu, Y.; Zhang, X., Role of Surface Ni and Ce Species of Ni/CeO_2 Catalyst in CO_2 Methanation. *Appl. Surf. Sci.* **2016,** *383*, 248-252.
53. Tada, S.; Shimizu, T.; Kameyama, H.; Haneda, T.; Kikuchi, R., Ni/CeO_2 Catalysts with High CO_2 Methanation Activity and High CH_4 Selectivity at Low Temperatures. *Int. J. Hydrogen Energy* **2012,** *37* (7), 5527-5531.
54. da Silva, D. C.; Letichevsky, S.; Borges, L. E.; Appel, L. G., The Ni/ZrO_2 Catalyst and the Methanation of CO and CO_2. *Int. J. Hydrogen Energy* **2012,** *37* (11), 8923-8928.
55. Matsubu, J. C.; Yang, V. N.; Christopher, P., Isolated Metal Active Site Concentration and Stability Control Catalytic CO_2 Reduction Selectivity. *J. Am. Chem. Soc.* **2015,** *137* (8), 3076-3084.
56. Abe, T.; Tanizawa, M.; Watanabe, K.; Taguchi, A., CO_2 Methanation Property of Ru Nanoparticle-loaded TiO_2 Prepared by a Polygonal Barrel-Sputtering Method. *Energy Environ. Sci.* **2009,** *2* (3), 315-321.
57. Janke, C.; Duyar, M.; Hoskins, M.; Farrauto, R., Catalytic and Adsorption Studies for the Hydrogenation of CO_2 to Methane. *Appl. Catal. B* **2014,** *152*, 184-191.
58. Upham, D. C.; Derk, A. R.; Sharma, S.; Metiu, H.; McFarland, E. W., CO_2 Methanation by Ru-Doped Ceria: The Role of the Oxidation State of the Surface. *Catal. Sci. Technol.* **2015,** *5* (3), 1783-1791.
59. Ren, J.; Guo, H.; Yang, J.; Qin, Z.; Lin, J.; Li, Z., Insights into the Mechanisms of CO_2 Methanation on Ni(111) Surfaces by Density Functional Theory. *Appl. Surf. Sci.* **2015,** *351*, 504-516.
60. Qiao, J.; Liu, Y.; Hong, F.; Zhang, J., A Review of Catalysts for the Electroreduction of Carbon Dioxide to Produce Low-Carbon Fuels. *Chem. Soc. Rev.* **2014,** *43* (2), 631-675.
61. Kattel, S.; Yu, W.; Yang, X.; Yan, B.; Huang, Y.; Wan, W.; Liu, P.; Chen, J. G., CO_2 Hydrogenation Over Oxide-Supported PtCo Catalysts: The Role of the Oxide Support in Determining the Product Selectivity. *Angew. Chem. Int. Ed.* **2016,** *55* (28), 7968-7973.

62. Marwood, M.; Doepper, R.; Renken, A., In-situ Surface and Gas Phase Analysis for Kinetic Studies Under Transient Conditions The Catalytic Hydrogenation of CO_2. *Appl. Catal. A* **1997,** *151* (1), 223-246.

63. Ocampo, F.; Louis, B.; Kiwi-Minsker, L.; Roger, A.-C., Effect of Ce/Zr Composition and Noble Metal Promotion on Nickel Based $Ce_xZr_{1-x}O_2$ Catalysts for Carbon Dioxide Methanation. *Appl. Catal. A* **2011,** *392* (1), 36-44.

64. Aldana, P. A. U.; Ocampo, F.; Kobl, K.; Louis, B.; Thibault-Starzyk, F.; Daturi, M.; Bazin, P.; Thomas, S.; Roger, A. C., Catalytic CO_2 Valorization into CH_4 on Ni-based Ceria-Zirconia. Reaction Mechanism by Operando IR Spectroscopy. *Catal. Today* **2013,** *215*, 201-207.

65. Ashok, J.; Ang, M. L.; Kawi, S., Enhanced Activity of CO_2 Methanation over Ni/CeO_2-ZrO_2 Catalysts: Influence of Preparation Methods. *Catal. Today* **2017,** *281*, 304-311.

66. Artz, J.; Müller, T. E.; Thenert, K.; Kleinekorte, J.; Meys, R.; Sternberg, A.; Bardow, A.; Leitner, W., Sustainable Conversion of Carbon Dioxide: An Integrated Review of Catalysis and Life Cycle Assessment. *Chem. Rev.* **2018,** *118* (2), 434-504.

67. Chen, W.-H.; Lin, B.-J.; Lee, H.-M.; Huang, M.-H., One-step Synthesis of Dimethyl Ether from the Gas Mixture Containing CO_2 with High Space Velocity. *Appl. Energy* **2012,** *98*, 92-101.

68. Dubois, J.-L.; Sayama, K.; Arakawa, H., Conversion of CO_2 to Dimethylether and Methanol Over Hybrid Catalysts. *Chem. Lett.* **1992,** *21* (7), 1115-1118.

69. Álvarez, A.; Bansode, A.; Urakawa, A.; Bavykina, A. V.; Wezendonk, T. A.; Makkee, M.; Gascon, J.; Kapteijn, F., Challenges in the Greener Production of Formates/Formic Acid, Methanol, and DME by Heterogeneously Catalyzed CO_2 Hydrogenation Processes. *Chem. Rev.* **2017,** *117* (14), 9804-9838.

70. Koeppel, R. A.; Baiker, A.; Wokaun, A., Copper/Zirconia Catalysts for the Synthesis of Methanol from Carbon Dioxide: Influence of Preparation Variables on Structural and Catalytic Properties of Catalysts. *Appl. Catal. A* **1992,** *84* (1), 77-102.

71. Jansen, W. P. A.; Beckers, J.; v. d. Heuvel, J. C.; Denier v. d. Gon, A. W.; Bliek, A.; Brongersma, H. H., Dynamic Behavior of the Surface Structure of Cu/ZnO/SiO_2 Catalysts. *J. Catal.* **2002,** *210* (1), 229-236.

72. Kuld, S.; Conradsen, C.; Moses, P. G.; Chorkendorff, I.; Sehested, J., Quantification of Zinc Atoms in a Surface Alloy on Copper in an Industrial-type Methanol Synthesis Catalyst. *Angew. Chem. Int. Ed.* **2014,** *126* (23), 6051-6055.

73. Behrens, M.; Studt, F.; Kasatkin, I.; Kühl, S.; Hävecker, M.; Abild-Pedersen, F.; Zander, S.; Girgsdies, F.; Kurr, P.; Kniep, B.-L., The Active Site of Methanol Synthesis Over Cu/ZnO/Al_2O_3 Industrial Catalysts. *Science* **2012,** *336* (6083), 893-897.

74. Kattel, S.; Ramírez, P. J.; Chen, J. G.; Rodriguez, J. A.; Liu, P., Active Sites for CO_2 Hydrogenation to Methanol on Cu/ZnO Catalysts. *Science* **2017,** *355* (6331), 1296-1299.

75. Xiao, J.; Mao, D.; Guo, X.; Yu, J., Effect of TiO_2, ZrO_2, and TiO_2–ZrO_2 on the Performance of CuO-ZnO Catalyst for CO_2 Hydrogenation to Methanol. *Appl. Surf. Sci.* **2015,** *338*, 146-153.

76. Dalena, F.; Senatore, A.; Basile, M.; Knani, S.; Basile, A.; Iulianelli, A., Advances in Methanol Production and Utilization, with Particular Emphasis Toward Hydrogen Generation via Membrane Reactor Technology. *Membranes* **2018,** *8* (4), 98.

77. Studt, F.; Behrens, M.; Kunkes, E. L.; Thomas, N.; Zander, S.; Tarasov, A.; Schumann, J.; Frei, E.; Varley, J. B.; Abild-Pedersen, F., The Mechanism of CO and CO_2 Hydrogenation to Methanol over Cu-Based Catalysts. *ChemCatChem* **2015,** *7* (7), 1105-1111.

78. Nakamura, J.; Choi, Y.; Fujitani, T., On the Issue of the Active Site and the Role of ZnO in Cu/ZnO Methanol Synthesis Catalysts. *Top. Catal.* **2003,** *22* (3), 277-285.

79. Fichtl, M. B.; Schlereth, D.; Jacobsen, N.; Kasatkin, I.; Schumann, J.; Behrens, M.; Schlögl, R.; Hinrichsen, O., Kinetics of Deactivation on Cu/ZnO/Al_2O_3 Methanol Synthesis Catalysts. *Appl. Catal. A* **2015,** *502*, 262-270.

80. Martin, O.; Martín, A. J.; Mondelli, C.; Mitchell, S.; Segawa, T. F.; Hauert, R.; Drouilly, C.; Curulla-Ferré, D.; Pérez-Ramírez, J., Indium Oxide as a Superior Catalyst for Methanol Synthesis by CO_2 Hydrogenation. *Angew. Chem. Int. Ed.* **2016,** *55* (21), 6261-6265.

81. Ye, J.; Liu, C.; Mei, D.; Ge, Q., Active Oxygen Vacancy Site for Methanol Synthesis from CO_2 Hydrogenation on In_2O_3(110): A DFT Study. *ACS Catal.* **2013,** *3* (6), 1296-1306.

82. Wang, J.; Zhang, G.; Zhu, J.; Zhang, X.; Ding, F.; Zhang, A.; Guo, X.; Song, C., CO_2 Hydrogenation to Methanol over In_2O_3-Based Catalysts: From Mechanism to Catalyst Development. *ACS Catal.* **2021,** *11* (3), 1406-1423.

83. Jiang, H.; Lin, J.; Wu, X.; Wang, W.; Chen, Y.; Zhang, M., Efficient Hydrogenation of CO_2 to Methanol Over Pd/In_2O_3/SBA-15 Catalysts. *J. CO_2 Util.* **2020,** *36*, 33-39.

84. Rui, N.; Wang, Z.; Sun, K.; Ye, J.; Ge, Q.; Liu, C.-j., CO_2 Hydrogenation to Methanol over Pd/In_2O_3: Effects of Pd and Oxygen Vacancy. *Appl. Catal. B* **2017,** *218*, 488-497.

85. Snider, J. L.; Streibel, V.; Hubert, M. A.; Choksi, T. S.; Valle, E.; Upham, D. C.; Schumann, J.; Duyar, M. S.; Gallo, A.; Abild-Pedersen, F.; Jaramillo, T. F., Revealing the Synergy between Oxide and Alloy Phases on the Performance of Bimetallic In–Pd Catalysts for CO2 Hydrogenation to Methanol. *ACS Catal.* **2019,** *9* (4), 3399-3412.

86. Dang, S.; Gao, P.; Liu, Z.; Chen, X.; Yang, C.; Wang, H.; Zhong, L.; Li, S.; Sun, Y., Role of Zirconium in Direct CO_2 Hydrogenation to Lower Olefins on Oxide/Zeolite Bifunctional Catalysts. *J. Catal.* **2018,** *364*, 382-393.

87. Dou, M.; Zhang, M.; Chen, Y.; Yu, Y., Theoretical Study of Methanol Synthesis from CO_2 and CO Hydrogenation on the Surface of ZrO_2 Supported In_2O_3 Catalyst. *Surf. Sci.* **2018,** *672-673*, 7-12.

88. Gao, P.; Dang, S.; Li, S.; Bu, X.; Liu, Z.; Qiu, M.; Yang, C.; Wang, H.; Zhong, L.; Han, Y.; Liu, Q.; Wei, W.; Sun, Y., Direct Production of Lower Olefins from CO_2 Conversion via Bifunctional Catalysis. *ACS Catal.* **2018,** *8* (1), 571-578.

89. Studt, F.; Sharafutdinov, I.; Abild-Pedersen, F.; Elkjær, C. F.; Hummelshøj, J. S.; Dahl, S.; Chorkendorff, I.; Nørskov, J. K., Discovery of a Ni-Ga Catalyst for Carbon Dioxide Reduction to Methanol. *Nat. Chem.* **2014,** *6* (4), 320-324.

90. Cherevotan, A.; Raj, J.; Dheer, L.; Roy, S.; Sarkar, S.; Das, R.; Vinod, C. P.; Xu, S.; Wells, P.; Waghmare, U. V.; Peter, S. C., Operando Generated Ordered Heterogeneous Catalyst for the Selective Conversion of CO_2 to Methanol. *ACS Energy Lett.* **2021,** *6* (2), 509-516.

91. Coffey, R., The Decomposition of Formic Acid Catalysed by Soluble Metal Complexes. *Chem. Commun.* **1967,** (18), 923b-924.

92. Aresta, M.; Dibenedetto, A.; Angelini, A., Catalysis for the Valorization of Exhaust Carbon: from CO_2 to Chemicals, Materials, and Fuels. Technological Use of CO_2. *Chem. Rev.* **2014,** *114* (3), 1709-1742.

93. Centi, G.; Quadrelli, E. A.; Perathoner, S., Catalysis for CO_2 Conversion: A Key Technology for Rapid Introduction of Renewable Energy in the Value Chain of Chemical Industries. *Energy Environ. Sci.* **2013,** *6* (6), 1711-1731.

94. Wang, W.-H.; Himeda, Y.; Muckerman, J. T.; Manbeck, G. F.; Fujita, E., CO_2 Hydrogenation to Formate and Methanol as an Alternative to Photo- and Electrochemical CO_2 Reduction. *Chem. Rev.* **2015,** *115* (23), 12936-12973.

95. He, M.; Sun, Y.; Han, B., Green Carbon Science: Scientific Basis for Integrating Carbon Resource Processing, Utilization, and Recycling. *Angew. Chem. Int. Ed.* **2013,** *52* (37), 9620-9633.

96. Yu, K. M. K.; Curcic, I.; Gabriel, J.; Tsang, S. C. E., Recent Advances in CO_2 Capture and Utilization. *ChemSusChem* **2008,** *1* (11), 893-899.

97. Duchesne, P. N.; Li, Z. Y.; Deming, C. P.; Fung, V.; Zhao, X.; Yuan, J.; Regier, T.; Aldalbahi, A.; Almarhoon, Z.; Chen, S.; Jiang, D.-e.; Zheng, N.; Zhang, P., Golden Single-Atomic-Site Platinum Electrocatalysts. *Nat. Mater.* **2018,** *17* (11), 1033-1039.

98. Ha, S.; Larsen, R.; Zhu, Y.; Masel, R. I., Direct Formic Acid Fuel Cells with 600 mA cm^{-2} at 0.4 V and 22 °C. *Fuel Cells* **2004,** *4* (4), 337-343.

99. Boot-Handford, M. E.; Abanades, J. C.; Anthony, E. J.; Blunt, M. J.; Brandani, S.; Mac Dowell, N.; Fernández, J. R.; Ferrari, M.-C.; Gross, R.; Hallett, J. P., Carbon Capture and Storage Update. *Energy Environ. Sci.* **2014,** *7* (1), 130-189.

100. Sordakis, K.; Tang, C.; Vogt, L. K.; Junge, H.; Dyson, P. J.; Beller, M.; Laurenczy, G., Homogeneous Catalysis for Sustainable Hydrogen Storage in Formic Acid and Alcohols. *Chem. Rev.* **2018,** *118* (2), 372-433.

101. Ra, E. C.; Kim, K. Y.; Kim, E. H.; Lee, H.; An, K.; Lee, J. S., Recycling Carbon Dioxide through Catalytic Hydrogenation: Recent Key Developments and Perspectives. *ACS Catal.* **2020,** *10* (19), 11318-11345.

102. Inoue, Y.; Sasaki, Y.; Hashimoto, H., Synthesis of Formates from Alcohols, Carbon Dioxide, and Hydrogen Catalysed by a Combination of Group VIII Transition-Metal Complexes and Tertiary Amines. *Chem. Commun.* **1975,** (17), 718-719.

103. Inoue, Y.; Izumida, H.; Sasaki, Y.; Hashimoto, H., Catalytic Fixation of Carbon Dioxide to Formic Acid by Transition-Metal Complexes Under Mild Conditions. *Chem. Lett.* **1976,** *5* (8), 863-864.

104. Jessop, P. G.; Hsiao, Y.; Ikariya, T.; Noyori, R., Homogeneous Catalysis in Supercritical Fluids: Hydrogenation of Supercritical Carbon Dioxide to Formic Acid, Alkyl Formates, and Formamides. *J. Am. Chem. Soc.* **1996,** *118* (2), 344-355.

105. Tanaka, R.; Yamashita, M.; Nozaki, K., Catalytic Hydrogenation of Carbon Dioxide Using Ir(III)−Pincer Complexes. *J. Am. Chem. Soc.* **2009,** *131* (40), 14168-14169.

106. Himeda, Y.; Onozawa-Komatsuzaki, N.; Sugihara, H.; Kasuga, K., Recyclable Catalyst for Conversion of Carbon Dioxide into Formate Attributable to an Oxyanion on the Catalyst Ligand. *J. Am. Chem. Soc.* **2005,** *127* (38), 13118-13119.

107. Farlow, M. W.; Adkins, H., The Hydrogenation of Carbon Dioxide and a Correction of the Reported Synthesis of Urethans. *J. Am. Chem. Soc.* **1935,** *57* (11), 2222-2223.

108. Preti, D.; Resta, C.; Squarcialupi, S.; Fachinetti, G., Carbon Dioxide Hydrogenation to Formic Acid by Using a Heterogeneous Gold Catalyst. *Angew. Chem. Int. Ed.* **2011,** *123* (52), 12759-12762.

109. Filonenko, G. A.; Vrijburg, W. L.; Hensen, E. J. M.; Pidko, E. A., On the Activity of Supported Au Catalysts in the Liquid Phase Hydrogenation of CO_2 to Formates. *J. Catal.* **2016,** *343*, 97-105.

110. Park, H.; Lee, J. H.; Kim, E. H.; Kim, K. Y.; Choi, Y. H.; Youn, D. H.; Lee, J. S., A Highly Active and Stable Palladium Catalyst on a g-C_3N_4 Support for Direct Formic Acid Synthesis Under Neutral Conditions. *Chem. Commun.* **2016,** *52* (99), 14302-14305.

111. Nguyen, L. T. M.; Park, H.; Banu, M.; Kim, J. Y.; Youn, D. H.; Magesh, G.; Kim, W. Y.; Lee, J. S., Catalytic CO_2 Hydrogenation to Formic Acid Over Carbon Nanotube-Graphene Supported PdNi Alloy Catalysts. *RSC Adv.* **2015,** *5* (128), 105560-105566.

112. Liu, Q.; Yang, X.; Li, L.; Miao, S.; Li, Y.; Li, Y.; Wang, X.; Huang, Y.; Zhang, T., Direct Catalytic Hydrogenation of CO_2 to Formate Over a Schiff-Base-Mediated Gold Nanocatalyst. *Nat. Commun.* **2017,** *8* (1), 1407.

113. Beck, J. S.; Vartuli, J. C.; Roth, W. J.; Leonowicz, M. E.; Kresge, C.; Schmitt, K.; Chu, C.; Olson, D. H.; Sheppard, E.; McCullen, S., A New Family of Mesoporous Molecular Sieves Prepared with Liquid Crystal Templates. *J. Am. Chem. Soc.* **1992,** *114* (27), 10834-10843.

114. Zhao, D.; Huo, Q.; Feng, J.; Chmelka, B. F.; Stucky, G. D., Nonionic Triblock and Star Diblock Copolymer and Oligomeric Surfactant Syntheses of Highly Ordered, Hydrothermally Stable, Mesoporous Silica Structures. *J. Am. Chem. Soc.* **1998,** *120* (24), 6024-6036.

115. Tanev, P. T.; Pinnavaia, T. J., A Neutral Templating Route to Mesoporous Molecular Sieves. *Science* **1995,** *267* (5199), 865-867.

116. Björk, E. M., Synthesizing and Characterizing Mesoporous Silica SBA-15: A Hands-On Laboratory Experiment for Undergraduates Using Various Instrumental Techniques. *J. Chem. Educ.* **2017,** *94* (1), 91-94.

117. Marakatti, V. S.; Peter, S. C., Synthetically Tuned Electronic and Geometrical Properties of Intermetallic Compounds as Effective Heterogeneous Catalysts. *Prog. Solid State Chem.* **2018,** *52*, 1-30.

118. Armbrüster, M., Intermetallic Compounds in Catalysis. *Encyclopedia of Catalysis,* Springer*,* **2002**.

119. Dapprich, S.; Frenking, G., Ligand Effects in Transition Metal Dihydrogen Complexes: A Theoretical Study1. *Organomet.* **1996,** *15* (21), 4547-4551.

120. Yang, M.-L.; Zhu, Y.-A.; Zhou, X.-G.; Sui, Z.-J.; Chen, D., First-Principles Calculations of Propane Dehydrogenation over PtSn Catalysts. *ACS Catal.* **2012,** *2* (6), 1247-1258.

121. Nykänen, L.; Honkala, K., Selectivity in Propene Dehydrogenation on Pt and Pt3Sn Surfaces from First Principles. *ACS Catal.* **2013,** *3* (12), 3026-3030.

122. Sharma, V.; Crozier, P. A.; Sharma, R.; Adams, J. B., Direct Observation of Hydrogen Spillover in Ni-loaded Pr-Doped Ceria. *Catal. Today* **2012,** *180* (1), 2-8.

123. Maher, R. C.; Shearing, P. R.; Brightman, E.; Brett, D. J. L.; Brandon, N. P.; Cohen, L. F., Reduction Dynamics of Doped Ceria, Nickel Oxide, and Cermet Composites Probed Using In Situ Raman Spectroscopy. *Adv. Sci.* **2016,** *3* (1), 1500146.

124. Shen, L.; Xu, J.; Zhu, M.; Han, Y.-F., Essential Role of the Support for Nickel-Based CO_2 Methanation Catalysts. *ACS Catal.* **2020,** *10* (24), 14581-14591.

125. Li, M.; Amari, H.; van Veen, A. C., Metal-oxide Interaction Enhanced CO_2 Activation in Methanation Over Ceria Supported Nickel Nanocrystallites. *Appl. Catal. B.* **2018,** *239*, 27-35.

126. Fiordaliso, E. M.; Sharafutdinov, I.; Carvalho, H. W. P.; Grunwaldt, J.-D.; Hansen, T. W.; Chorkendorff, I.; Wagner, J. B.; Damsgaard, C. D., Intermetallic $GaPd_2$ Nanoparticles on SiO_2 for Low-Pressure CO_2 Hydrogenation to Methanol: Catalytic Performance and In Situ Characterization. *ACS Catal.* **2015,** *5* (10), 5827-5836.

127. Schmal, M.; Moya, S., Nanostructured Catalysts. In *Heterogeneous Catalysis and its Industrial Applications*, Springer: 2016; pp 285-327.

128. Bond, G. C.; Keane, M. A.; Kral, H.; Lercher, J. A. J. C. R., Compensation Phenomena in Heterogeneous Catalysis: General Principles and a Possible Explanation. *J. Catal. Rev.* **2000,** *42* (3), 323-383.

129. Siegbahn, K.; Edvarson, K., β-Ray Spectroscopy in the Precision Range of 1 : 105. *Nucl. Phys.* **1956,** *1* (8), 137-159.

130. Konno, H., Chapter 8 - X-ray Photoelectron Spectroscopy. In *Mater. Sci. Eng. Carbon*, Inagaki, M.; Kang, F., Eds. Butterworth-Heinemann: 2016; pp 153-171.

131. Sewell, G. S.; van Steen, E.; O'Connor, C. T., Use of TPR/TPO for Characterization of Supported Cobalt Catalysts. *Catal. Lett.* **1996,** *37* (3), 255-260.

132. Van Leeuwen, P.; Van Koten, G., Homogeneous Catalysis with Transition Metal Complexes. *J. Chem. Inf.* **1994,** *25* (13).

133. Chiarello, G. L.; Nachtegaal, M.; Marchionni, V.; Quaroni, L.; Ferri, D., Adding Diffuse Reflectance Infrared Fourier Transform Spectroscopy Capability to Extended X-ray-absorption Fine Structure in a New Cell to Study Solid Catalysts in Combination with a Modulation Approach. *Rev. Sci. Instrum.* **2014,** *85* (7), 074102.

134. Pompeo, F.; Nichio, N. N.; Souza, M. M. V. M.; Cesar, D. V.; Ferretti, O. A.; Schmal, M., Study of Ni and Pt Catalysts Supported on α-Al_2O_3 and ZrO_2 Applied in Methane Reforming with CO_2. *Appl. Catal. A* **2007,** *316* (2), 175-183.

135. Demoulin, O.; Navez, M.; Ruiz, P., Investigation of the Behaviour of a Pd/γ-Al_2O_3 Catalyst During Methane Combustion Reaction Using *in-situ* DRIFT Spectroscopy. *Appl. Catal. A* **2005,** *295* (1), 59-70.

Chapter 2

Support Textural Properties Induced Active Catalyst Dispersion Enhances Methane and Formic Acid Production from Carbon Dioxide

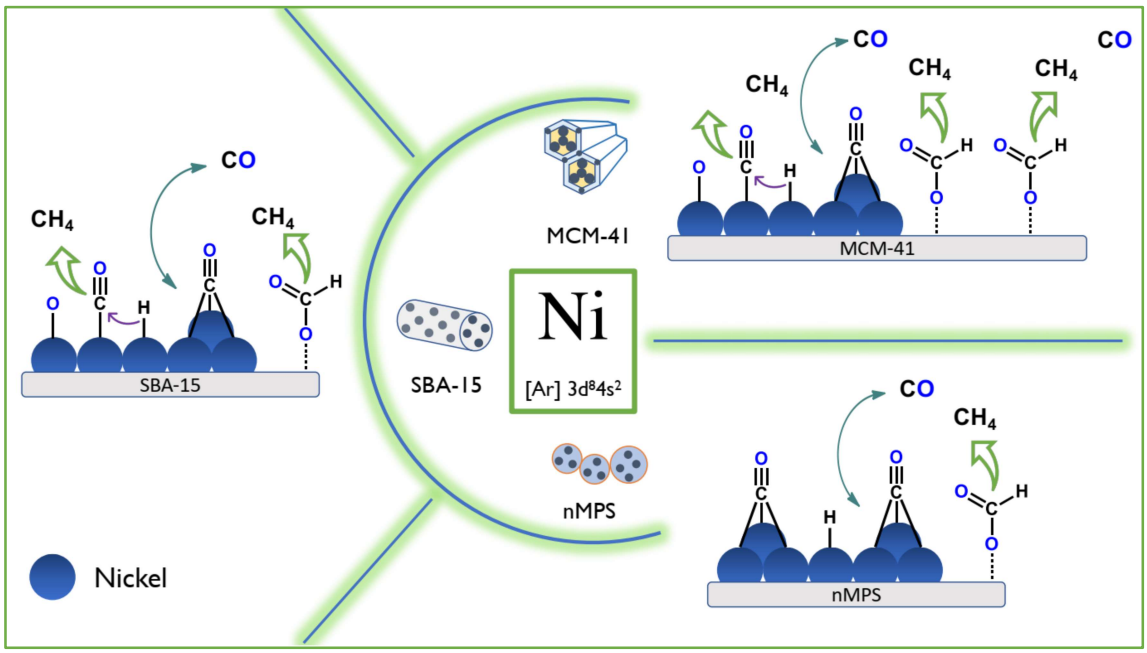

Arjun Cherevotan, Bitan Ray, Sathyapal R. Churipard, Komalpreet Kaur, Ujjal K. Gautam, Chathakudath P. Vinod, and Sebastian C. Peter

(*Manuscript under revision*)

Summary

In heterogeneous catalysis, there have been continuous efforts to understand the CO_2 activity dependence on the interaction between loaded metal nanoparticles and the support with higher emphasis on particle size, morphology, nature of nanoparticles and properties of support materials. Here in this chapter, for the first time, we have investigated the effect of the physicochemical textural properties of inert support on the activity of metal nanoparticles by impregnating Ni on ordered mesoporous silica with different porous nature (SBA-15 & MCM-41) and non-mesoporous silica (nMPS). These Ni/silica catalysts tested for CO_2 hydrogenation yielded the best CO_2 conversion and product selectivity for Ni/SBA-15 followed by Ni/MCM-41 and the least for Ni/nMPS. The difference in the nature of the catalyst, degree of nanoparticle distribution and nanoparticle encapsulation by silica were mapped by N_2 adsorption-desorption and X-ray photoelectron spectroscopy (XPS) experiments. The elucidation of the difference in the CO_2 conversion pathway was sketched by *operando* Diffuse Reflectance Infrared Fourier Transform Spectroscopy (DRIFTS) under simulated reaction conditions. The operando studies revealed that Ni/SBA-15 favors dissociative hydrogenation of CO_2 to methane via Ni-CO intermediate, however, Ni/MCM-41 favors both faster dissociative and slower associative formate pathways while on nMPS Ni sites gets deactivated by bridged Ni-CO formation. This difference in the mechanistic pathway was completely accredited to the physicochemical textural properties of the silica support. Our systematic studies can provide a better understanding in the fundamentals of metal-inert support symbiotic interactions to improve the activity of CO_2 reduction and tuning the selectivity to different CO_2 hydrogenated products and finally contribute towards CO_2 valorization by recycling to reduce global warming.

The work based on this chapter is under revision.

Table of Contents

2.1. Introduction

Last two decades witnessed large number of reports on the hydrogenation of CO_2 with renewable hydrogen to C_1 fuels (CO, CH_4, CH_3OH, HCO_2H and CH_3OCH_3)[1-4] and low molecular weight hydrocarbons. Among them, methane has large utilization in the energy market, particularly in Liquified Natural Gas (LNG)[5] and fuel cell.[6] On the other hand, hydrogen production via water electrolysis is a matured technology to store chemical energy but suffers from large and costly infrastructure requirements for its storage and distribution. Eight electron hydrogenated CO_2 (methane) is highly liquifiable and stored easily compared to hydrogen gas, thus can be considered for large-scale application in various energy sectors. In addition, thermodynamically CO_2 methanation (CO_2M) is an exothermic process with negative Gibb's free energy change requiring only lower reaction temperature.[7] At the same time, CO_2M requires an optimum reaction temperature to overcome the kinetic limitations.[8] Metals like Ni,[9, 10] Pd,[11] Rh, and Ru supported on metal-based oxide materials[12-15] are widely studied catalysts for CO_2M. Among them, Ni being the low-cost metal can be considered as the potential catalyst for various commercial applications.

Rational design of heterogeneous catalysts for CO_2M at mild operating temperatures is a challenging task. During the last couple of decades, the performance of thermocatalytic CO_2M has been thoroughly investigated by understanding the nature of active sites, mechanistic pathways and reaction kinetics.[16-20] Apart from these, the catalyst design strategies, the effect of catalyst loading, the effect of the supports and the role of promoters also documented in depth.[21-29] The metal oxide support typically used in CO_2M can enhance the dispersion of active components of the catalyst and tune the surface structure of the catalyst, which in turn modify the intermediate adsorption characteristics and finally the reaction pathways. Thus, comprehensive knowledge of the support material (physical and chemical) can assist in the effective design of efficient Ni supported on metal oxide methanation catalysts.

In this chapter, we investigated the effect of the textural property of catalyst support on CO_2M activity. Ni metal impregnated on three types of silica materials (SBA-15, MCM-41 and non-mesoporous silica) with different physicochemical textural properties have been used for this study. Silica-based supports were selected for this since they offer no metal support interaction (MSI) and is also non-reducible support incapable of directly activating the reactant CO_2. All the three supported Ni were screened for CO_2M in a vapor phase downflow reactor at a temperature of 593 K which exhibited a marked difference in both CO_2 conversion and methane selectivity depending upon the textural property of silica support. The difference in

the active metal dispersion, thermocatalytic activity, product selectivity, intermediate formation, and reaction pathway of all the three catalysts were studied in detail for the first time with the support of various experiments, including adsorption-desorption measurements, X-ray Photoelectron Spectroscopy (XPS) and *in-situ* Diffuse Reflectance Infrared Fourier Transform Spectroscopy (DRIFTS).

2.2. Experimental Details

2.2.1. Chemicals and reagents

Tetraethyl orthosilicate (TEOS) (>99% GC, Sigma Aldrich), Pluronic P123 or PEG-PPG-PEG (Poly(ethylene glycol)-block-poly(propylene glycol)-block-poly(ethylene glycol)) (Mn~5800, Sigma Aldrich), cetyltrimethylammonium bromide, CTAB (99%, Aldrich), HNO_3 (69% v/v analytical grade, Merck Chemicals), aqueous ammonia solution (25%, SDFCL), H_2SO_4 (98% analytical grade, Merck Chemicals), ethanol (99.9%, CSC), nickel nitrate hexahydrate (98%, SDFCL) and silica (Thomas Baker).

2.2.2. Synthesis

2.2.2.1. SBA-15

Synthesize of Santa Barbara Amorphous (SBA-15) was adopted from the already reported method.[30, 31] In a typical synthesis, 4 grams of Pluronic P123 was dissolved in 105 mL of deionized water and 10.8 mL of 98% H_2SO_4 and stirred for 3 hours at 40 °C. In this step, the surfactant P123 forms spherical micelles which acts as structure-directing agents (soft templates). Then, to this soft template solution 9.063 mL of silica precursor, TEOS was added and stirred for 3.5 hours with a higher rate of stirring to avoid coagulation. During this step, the spherical micelles elongate to give a cylindrical hexagonal array of micelles. The uniform solution after stirring in the round bottom flask was fitted with a condenser and kept for hydrothermal treatment at 100 °C for 30 hours without stirring. During the hydrothermal treatment, the micelles expand to mesoporous range. After the treatment, the solution was filtered and washed with deionized water to remove the maximum surfactant. The obtained white powder was then dried at 100 °C overnight and lastly, it was calcined for 6 hours at 550 °C to remove the organic template.

2.2.2.2. MCM-41

Three grams of CTAB was added to 570 ml of distilled water with stirring at ambient conditions.[32] To this solution, 200 ml of ethanol and 60 ml of ammonia solution were added

and a pH of 11–12 (alkaline) was maintained. Then 12 ml of silica precursor, TEOS was added dropwise to the solution. Further, the mixture was stirred for another 3 hours, then it was filtered and washed thoroughly with deionized water. The product was dried overnight at 100 °C and calcined again at 550 °C for 6h to remove the CTAB from the silica network.

2.2.2.3. Ni Impregnation on Silica support

Incipient wetness impregnation was used to disperse Ni nanoparticles (NPs) into the pores of the support materials. Four molar HNO_3 solution was used as the medium for metal impregnating metals into the pores. A definite volume of HNO_3 solution which is exactly equal to the pore volume of the corresponding porous material is taken and in that the desired amount of Ni (II) nitrate hexahydrate salt was dissolved. The support material was soaked in this solution for 1 hour to propel this solution into the porous channels by capillary action. The excess solution was dried at 60 °C in fume hood and further in vacuum oven at 100 °C overnight. This metal nitrate-support precursor was reduced at 800 °C under continuous H_2 flow. The desired amount of Ni was made by changing the amount of Ni precursor dissolved in the support soaking solute on.

2.2.3. Characterization

2.2.3.1. Powder X-ray Diffraction (PXRD)

The Powder X-ray diffraction (XRD) data were collected at room temperature on a PANalytical X-ray diffractometer with Cu Kα radiation (λ =1.5406 nm) at 45 kV and 40 mA in the 2θ range of 10° to 90° with a step size of 0.02° and a scan rate of 0.5 s/step. The features of the PXRD patterns were compared with the simulated pattern from Pearson Database.

2.2.3.2. N_2 adsorption-desorption measurement

The adsorption isotherms were studied by using N_2 as the probe molecule at liquid nitrogen temperature on BelCat instrument. Prior to the measurements, the powders were degassed at 150 °C for 6 hours to remove any adsorbed gases and moisture. The specific surface area was confirmed by Brunaur-Emmett-Teller (BET) method and pore size distribution by classical BJH (Barrett, Joyner and Halenda) method.

2.2.3.3. Transmission Electron Microscope (TEM)

Transmission electron microscope (TEM) and high-resolution TEM (HRTEM) images were recorded using JEOL JEM-F200. The samples were prepared by drop-casting in ethanol.

2.2.3.4. Temperature Programmed Reduction (TPR)

The reduction properties of Ni-supported silica catalysts were studied by TPR analysis using the Altamira AMI-300 Lite instrument. The TCD response is calibrated after every temperature-programmed reduction (TPR) analysis to calculate the amount of H_2 consumed for the reduction of samples. For every analysis, around 50 mg of sample was taken and reduced in a stream of 10% H_2 in Argon with a ramp rate of 10 °C min^{-1} up to 900 °C followed by a 30 min hold at 900 °C. The reduction % was calculated based on the H_2 consumed, assuming that NiO was reduced during the TPR measurement.

2.2.3.5. X-ray Photoelectron Spectroscopy (XPS)

XPS measurements were carried out using Thermo K-alpha+ spectrometer using micro focused and monochromated Al Kα radiation with energy 1486.6 eV. The pass energy for the spectral acquisition was kept at 50 eV for individual core-levels. The electron flood gun was utilized for providing charge compensation during data acquisition. Further, the individual core-level spectra were checked for charging using C1s at 284.6 eV as standard and corrected if needed. The peak fitting of the individual core-levels was done using CASA XPS software with a Shirley type background.

2.2.3.6. Inductively Coupled Plasma – Optical Emission Spectroscopy (ICP-OES)

ICP-OES was performed using a Perkin Elmer Optima 7000 DV instrument. The samples were first digested in concentrated aqua regia prepared in lab. Then samples were treated with 2-3 drops of HF to remove silica of SBA-15 and finally diluted with distilled water. In a typical experiment, 5 mg of the sample was dissolved in 3-5 ml aqua regia and heated at 333 K for digestion. The digested sample was then treated with 3-5 drops of HF and diluted to 10 ml volume with deionized water, from this 1 ml was again taken and diluted to 10 ml. The solid particles were separated by thorough centrifugation before measurements.

2.2.4. CO_2 reduction in continuous flow process

CO_2 reduction in continuous flow process was carried over in a down-flow vapour phase reactor heated with ATS split furnace and a manual back pressure regulator (BPR) to build the pressure during flow. First 5 g of as-synthesized catalyst was mixed with 30% alumina-based binder (pseudoboehmite) and dilute HNO_3 solution. The mixture was shaped as dough and extruded with the help of a mechanical extruder. The extrudate catalyst was dried overnight prior to activation. The obtained catalyst was loaded in the middle of the reactor with

the help of non-reactive alumina beads and quartz wool to allow the free flow and minimize the back pressure generation. A thermocouple connected to a PID temperature controller was placed to monitor the temperature of the catalyst bed. The temperature of catalyst activation is decided after analyzing the H_2-TPR profile of the respective catalyst. As shown in the **Figure 2.1**, all the Ni-Supported silica materials showed a major reduction peak around 295-315 °C. This characteristic peak is attributed to the reduction of NiO into metallic Ni. All the materials showed more than 90% reducibility suggesting complete reduction of NiO in the materials below 320 °C. The percentage reduction and H_2 uptake are given in **Table 2.1** assuming that NiO is the reducible compound. Thus the catalyst extrudates were activated at 400 °C with H_2 and N_2 for 6 hours to avoid the surface oxidized Ni. After the activation step, the reactor was cooled down to room temperature with the flow of activation gases, then the reaction started by switching to CO_2-H_2 at a flow rate of 10:40 NLPH and 1 NLPH N_2 as the internal standard for GC analysis to yield WHSV of 4.9 h^{-1}. All the catalytic runs were performed at 593 K for 24 hours with two different pressure conditions of 1 and 5 bar maintained by manual BPR. The outlet of the reactor is connected to Gas Chromatograph. All products were analyzed via gas chromatography (GC) equipped with a thermal conductivity detector (TCD) for CO_2 and N_2, a flame ionization detector (FID) for hydrocarbons.

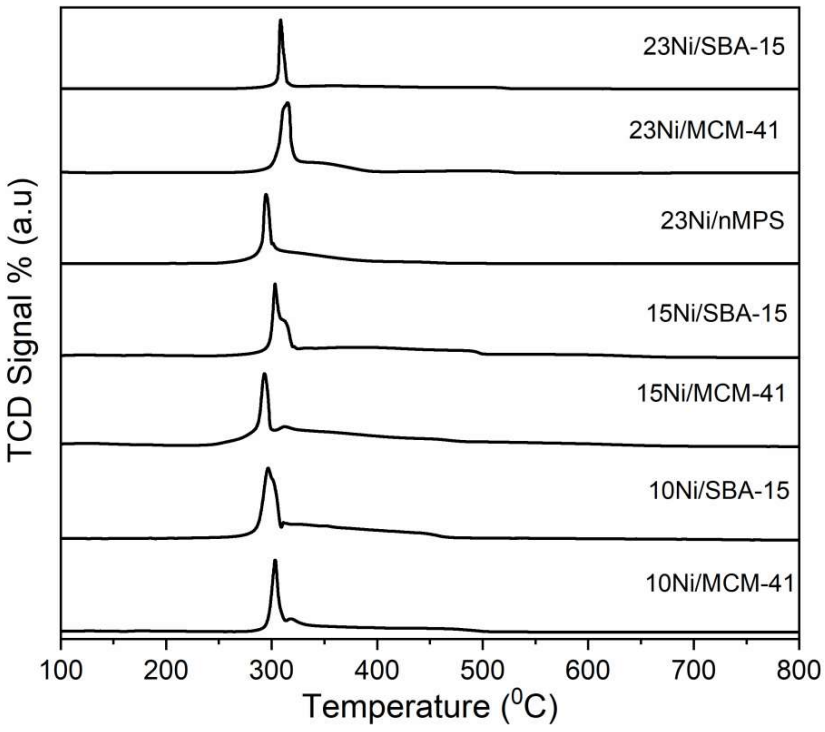

Figure 2.1. TPR profiles of different Ni loading (23, 15 and 10% supported on SBA-15, MCM-41 and nMPS catalysts.

A 5 g of catalyst was loaded in the form of 2-3 mm long wire type extrudates and kept between glass wool to make the catalyst bed. Once the pressure was achieved, the temperature was programmed via ramping of 5 °C/min to desired reaction temperature (320 °C). When the temperature and flow are stabilized, the readings are considered, and the reading just before product formation is taken as t_0. The selectivity and conversion for the rest of the readings are calculated on the compositions based on t_0. After the completion of the reaction, the valve connected to gas-liquid separator is opened to obtain any liquid product and to depressurize the reactor. Again, the activation process was repeated for the next set of experiments.

Table 2.1. Summary of H_2-TPR analysis.

Catalysts	% H_2 uptake (µmol/g)	% Reduction
23Ni/SBA-15	1805	92.1
23Ni/MCM-41	1892	96.6
23Ni/nMPS	1898	96.9
15Ni/SBA-15	1365	106
15Ni/MCM-41	1261	98.1
10Ni/SBA-15	865	101.4
10Ni/MCM-41	790	92.8

2.2.5. CO_2 reduction in batch process

CO_2 reduction in batch process was performed in high pressure and high-temperature reactor vessel from Parr. Schematic illustration of different steps involved in catalyst testing in the batch process is shown in **Figure 2.2**. To make the best comparison in reactivity, these Ni impregnated non-molecular catalysts were directly loaded into 5 mL solution of 0.5 M $NaHCO_3$ and pressurized at different pressure at a ratio of 1:1 CO_2 to H_2. Ten milligrams of catalyst were weighed and transferred into 10 ml quartz vials, 5 ml of 0.5 M $KHCO_3$ solution was added to it. A small magnetic bead (rice magnetic bead) was put into vials, rubber septa and syringe needles were used to prevent the spilling of solvent and to allow the feed gas to pass through the reaction media. The vials were sonicated for a few minutes to obtain a well distribution of catalyst throughout the solvent. The vials were put into the parr vessel. Quartz wools are placed to support the vials, the head assembly was put together with the help of a split ring and wrench. The inside of the vessel was flushed thrice with the reactant gas till 10 bar, after that it was pressurized to our desired pressure. After that the vessel was put into preheated oil bath with a magnetic stirrer.

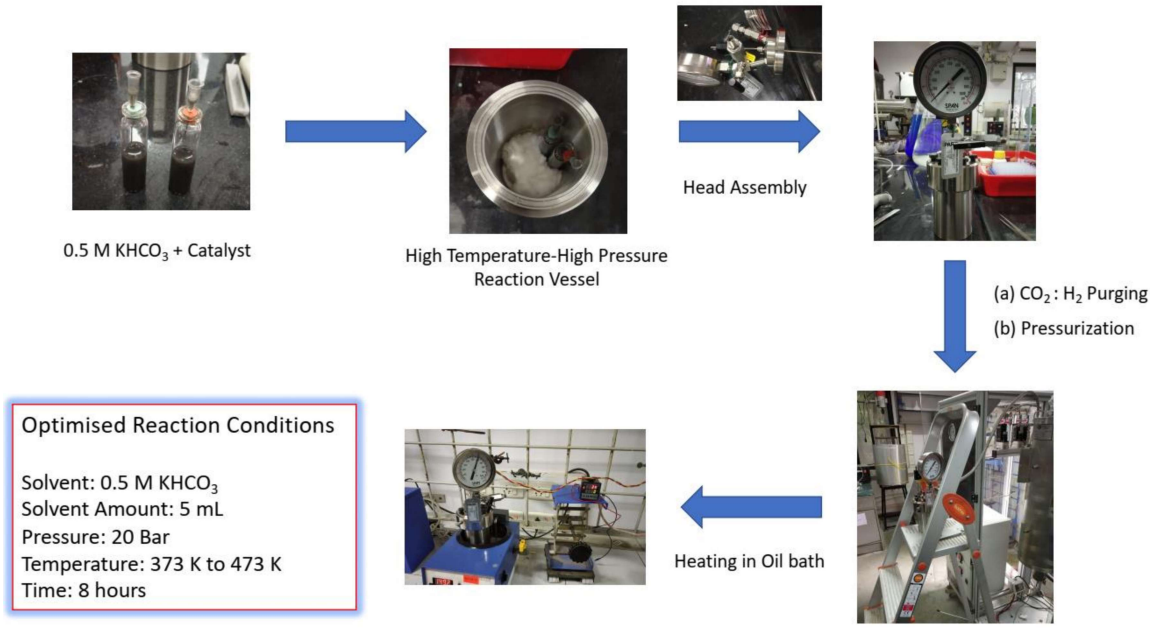

Figure 2.2. Schematic illustration of different steps involved in catalyst testing in batch process.

An external temperature controller was used to monitor the inside temperature throughout the course of the experiment. Upon completion of the reaction, the vessel was removed from the oil bath and cleaned using hexane. The vials are removed from the vessel and centrifuged to obtain the product mixture. The product mixture was transferred into HPLC vials for product quantification and catalysts were retained for post catalytic studies.

2.2.6. Operando DRIFTS analysis: Intermediates and Reaction pathway

The operando Diffused Reflectance Infrared Spectroscopy (DRIFTS) experiment was carried out using a Bruker 70v vertex FTIR spectrometer equipped with a Harrick DRIFTS cell (**Figure 2.3**). The spectra were recorded at 4 cm^{-1} resolution, and each spectrum was averaged 32 times. Each sample was pre-treated at 473 K using 99.999% at a gas flow rate of 1 NLPH H_2 for 1 h to remove adsorbed water and other gas molecules along with activation. The spectrum of the annealed sample at 303 K was used as the background reference for the following reaction. To probe the reaction, 20%CO_2/80%H_2 gas mixture at 1 bar and a total flow rate of 1.25 NLPH was first introduced to the DRIFTS cell, and then the temperature was ramped from 303 to 593 K (ca. 15 K min^{-1}) to determine the relationship between temperature and the reaction intermediate. Then the reaction was maintained at 593 K for 1h to determine the surface intermediates.

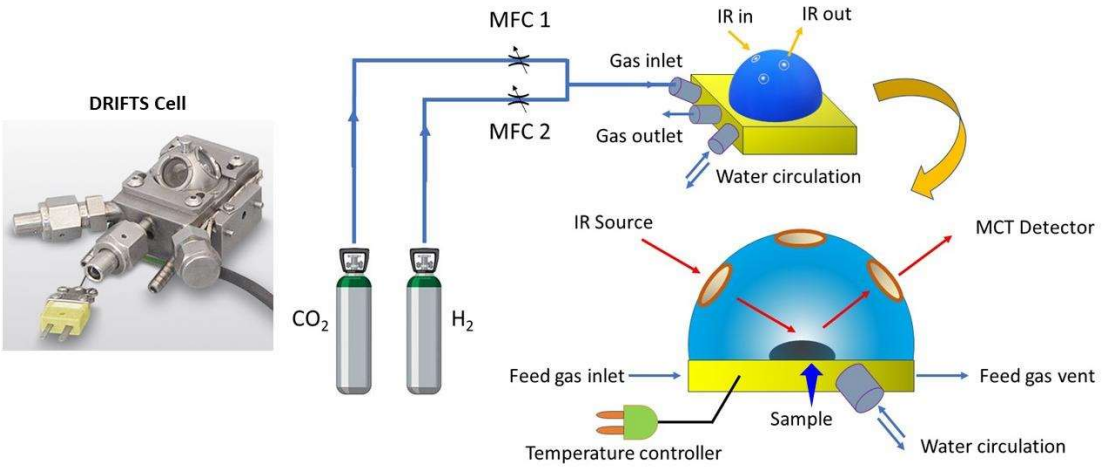

Figure 2.3. Schematic Illustration of DRIFTS set up for CO_2 methanation.

2.2.7. Calculations

2.2.7.1. Weight Hour Space Velocity (WHSV)

WHSV is defined as the mass of reactant per unit time passed per mass of catalyst charged in a reactor. Here we used flow rate of 50 NLPH ($1CO_2$:$4H_2$).

50 NLPH:

CO_2 flow = 10 NLPH (19.8 grams per hour)

H_2 flow = 40 NLPH (3.56 grams per hour)

N_2 flow (internal standard for GC analysis) = 1 NLPH (1.25 grams per hour)

Mass of catalyst charged = 5 g

$$\text{WHSV} = (19.8 + 3.56 + 1.25)/5 = 4.922\ h^{-1} = \sim 4.9\ h^{-1}$$

2.2.7.2. Response factor of GC (RF)

The response factor for a component '*i*' of a detector is the ratio of peak area of component '*i*' to calibration concentration (**Eqn. 2.1**). The unknown concentration of component '*i*' during online gas analysis is determined by multiplying the response factor of the component with the peak area of the component obtained during online analysis. Note that calibration compositions of samples are expressed in percentage.

$$RF_i = \text{Peak Area of } i \div \text{Standard Composition of } i\ (\%) \quad (2.1)$$

$$\text{Unknown Composition of } i \text{ in product gas } (\%) = \text{RF Peak} \times \text{Area of } i \text{ in product} \quad (2.2)$$

The GC RF for TCD are given below:

RF of CO_2 = 0.001617

RF of N_2 = 0.001848

RF of CO = 0.00216

RF of CH_4 = 0.00221

2.2.7.3. Conversion and product selectivity[33]

$$CO_2 \text{ conversion } (\%) = \left(CO_2\ (\text{in}) - CO_2\ (\text{out}) \times \frac{N_2(\text{in})}{N_2(\text{out})}\right) \div CO_2\ (\text{in}) \qquad (2.3)$$

$$\text{Selectivity of } i = (100\text{n} \times \frac{\text{Composition of } i}{N_2(\text{out})}) \div (\frac{CO_2\ (\text{in})}{N_2(\text{in})} - \frac{CO_2\ (\text{out})}{N_2(\text{out})}) \qquad (2.4)$$

CO_2 (in) = Composition of CO_2 in feed gas

CO_2 (out) = Composition of CO_2 in product

N_2 (in) = Composition of N_2 in feed gas

N_2 (out) = Composition of N_2 in product

2.3. Results & Discussion

2.3.1. Synthesis and Catalyst Characterization

SBA-15 and MCM-41 were prepared by a soft template method using Pluronic P123 and CTAB as the organic soft templates, respectively.[30-32] Commercially available non-mesoporous silica (nMPS) was purchased from Thomas Baker for comparison. It is well known that both MCM-41 and SBA-15 have periodically arranged long cylindrical mesopores with different pore sizes and wall thicknesses.[34] Incipient wetness impregnation (IWI) was used to disperse Ni nanoparticles (NPs) into the pores of the support materials.[35, 36] The schematic of materials synthesis is shown in **Figures 2.4**. The materials were characterized by X-ray diffraction (XRD), XPS and adsorption-desorption isotherm.

2.3.1.1. Powder X-ray Diffraction (PXRD) and Low Angle PXRD

Nickel loaded on all three supports showed similar features in PXRD and these were compared with simulated Ni patterns from Pearson database **(Figure 2.5a)**. The 2θ values of 44.28°, 51.6° and 75.98° were identified as (111), (200) and (220) facets of Ni $Fm\bar{3}m$ confirming the formation of Ni on SBA-15, MCM-41 and nMPS. The low angle XRD confirms the mesoporous structural features of SBA-15 and MCM-41 (**Figure 2.5b**).

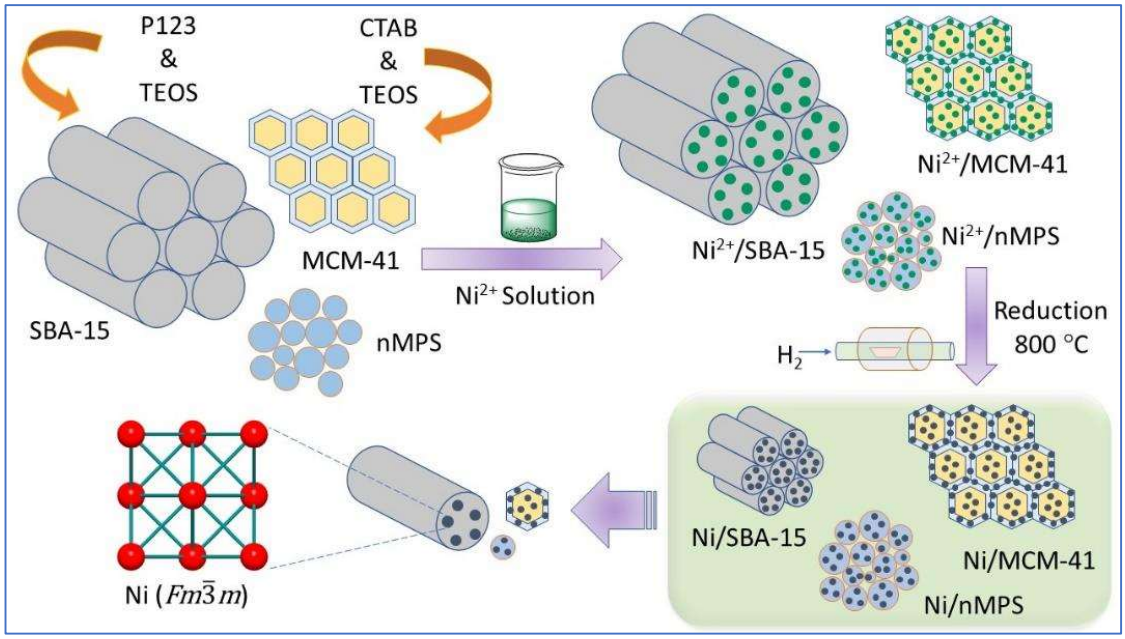

Figure 2.4. Schematic illustration of Ni impregnation on different silica supports.

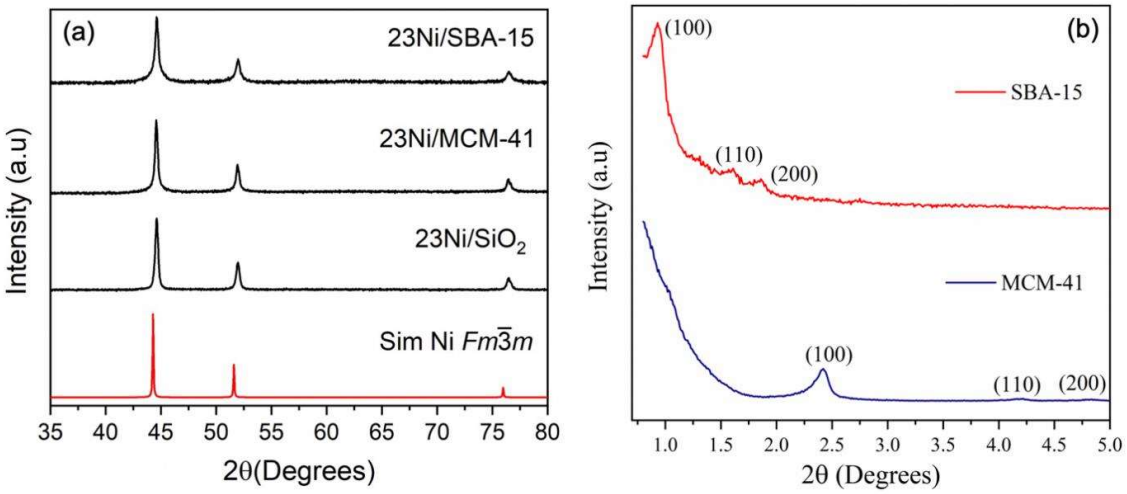

Figure 2.5. (a) Powder XRD of 23 wt.% Ni loaded on SBA-15, MCM-41 and SiO_2 (nMPS), (b) Low angle powder XRD of MCM-41 and SBA-15.

2.3.1.2. Surface Area and Textural Properties

In case of IWI method, the textural properties of support can dictate the size and distribution of the nanoparticle formed since the metal precursor solutions are drawn inside the pores by the capillary action of the support during synthesis. The surface area of MCM-41 is more than double of SBA-15 owing to the 2.8 nm pores of MCM-41 vs 7.3 nm for SBA-15 **(Table 2.2** and **Figure 2.6-7)**. The post impregnation of Ni on MCM-41 destroyed the pore

distribution completely **(Table 2.2 & Figure 2.6c-d)** but that of SBA-15 remains intact with slight decrease in the pore size. This implies that the nanoparticles distributed uniformly inside channels of SBA-15 without any pore blockage and also left room for reactant diffusion, but in case of MCM-41 pores (2.8 nm), they were blocked due to higher metal loading (>20%). MCM-41 is characterized by a hexagonal pore structure with a lower pore size and thinner walls compared to SBA-15. The prepared MCM-41 and SBA-15 were characterized by adsorption-desorption isotherm by using nitrogen as probe molecule at liquid N_2 temperature. The powders were degassed at 150 °C for 6 hours to remove the adsorbed moistures and atmospheric gases. The nitrogen adsorption-desorption isotherms and the corresponding pore size distribution quantified from the desorption isotherm of nitrogen by the BJH method for MCM-41 and SBA-15 products are presented in **Figure 2.6** and **2.7**.

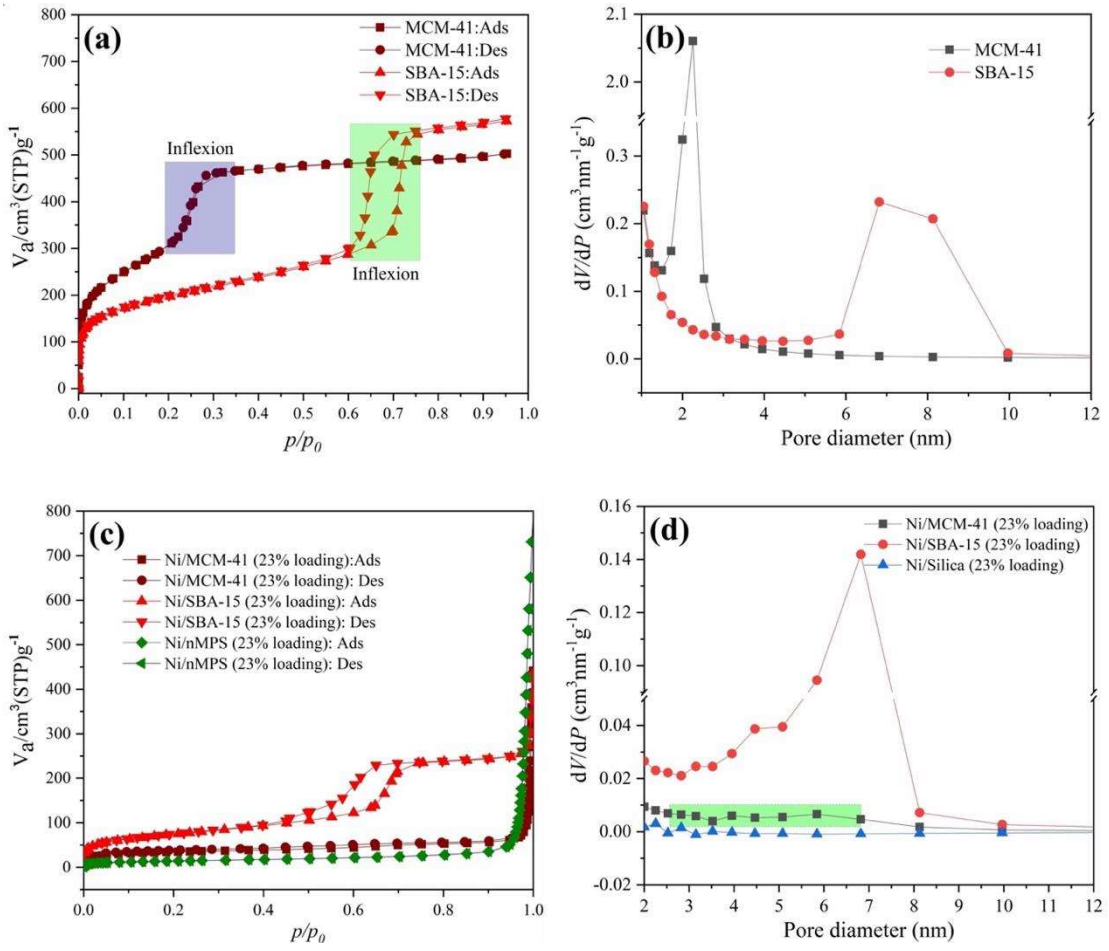

Figure 2.6. (a) Nitrogen adsorption-desorption isotherm of MCM-41 and SBA-15, (b) pore size distribution of MCM-41 and SBA-15, (c) nitrogen adsorption-desorption isotherm of 23 wt % Ni loaded MCM-41, SBA-15, and non-mesoporous silica and (d) pore size distribution of 23 wt.% Ni loaded MCM-41, SBA-15 and non-mesoporous silica.

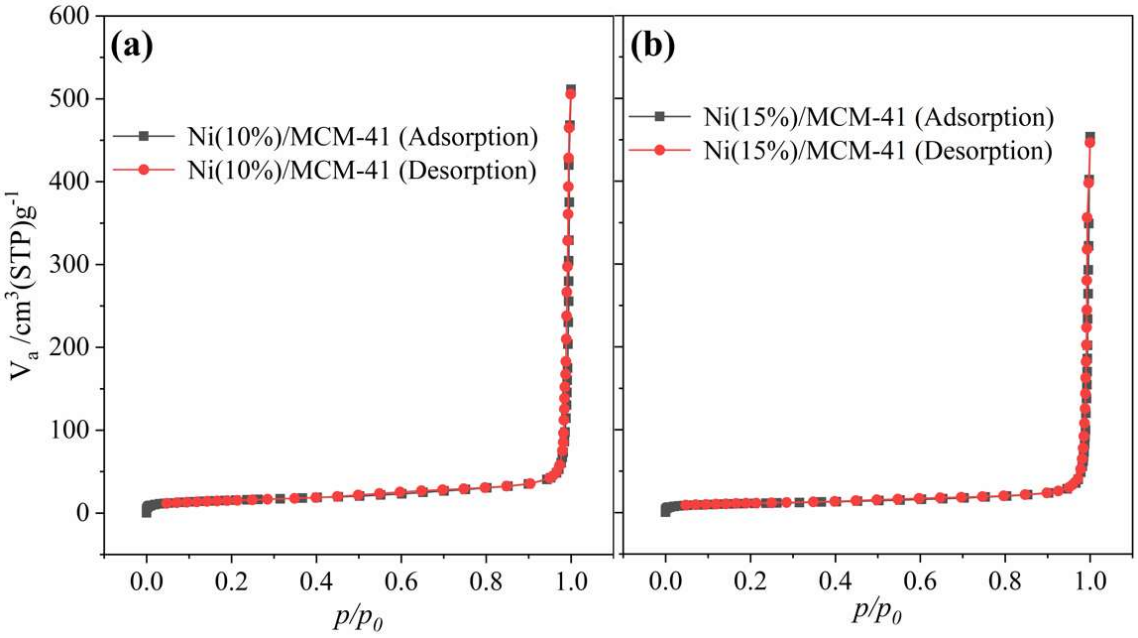

Figure 2.7. (a) Nitrogen Adsorption-Desorption isotherm of 10Ni/MCM-41 and (b) Nitrogen Adsorption-Desorption isotherm of 15Ni/MCM-41.

The adsorption-desorption isotherm for MCM-41 shows Brunauer type IV isotherm with three well distinct regions: (a) monolayer to multilayer adsorption, (b) capillary condensation and (c) multilayer adsorption **(Figure 2.6a)**. These three regions are identified as the characteristic of type IV isotherm. The MCM-41 exhibited a pronounced steep or sharp rise (inflexion) at relative pressures between 0.2 to 0.35, indicating capillary condensation of N_2 inside the mesopores. This also implies the presence of structural ordering inside the mesopores.[37] The isotherm also exhibits a H1 hysteresis loop and the presence of minimum amount of micropores since the inflexion point onsets at a much lower relative pressure.

The SBA-15 adsorption-desorption isotherm again exhibits a type IV adsorption isotherm like MCM-41 but reveals a relatively more pronounced regions of the monolayer to multilayer adsorption, capillary condensation, multilayer adsorption and hysteresis **(Figure 2.6a)**. The hysteresis loop exhibited by SBA-15 falls under H1, which is indicative of ordered 1D cylindrical channels.[31, 38] Further the isotherm confirms the presence of micropores since the regions of monolayer adsorption of isotherm ranges from 0 to 0.6.

The microporosity is a feature that originated in SBA-15 using triblock copolymer as the surfactant and this meso-micro interconnections may lead to better diffusion of both reactant and product gases inside the pores. The presence of micropores overestimates the surface area of SBA-15 because microporous regions are inaccessible for catalysis due to pore

blockages by the loaded metal nanoparticles (NPs). The pore size distribution of both MCM-41 and SBA-15 is depicted in **Figure 2.6b** and this confirms that both synthesized porous materials have mesopores.

Table 2.2. Textural properties of silica and impregnated catalyst.

Sample	Surface Area/m^2g^{-1}	Pore Volume/cm^3g^{-1}	Avg. Pore Diameter/nm
MCM-41	1409	0.85	2.8
SBA-15	675	0.97	7.3
23Ni/nMPS	49	0.8	72.6
23Ni/MCM-41	154	0.21	16.5
23Ni/SBA-15	261	0.44	6.7
15Ni/MCM-41	138	0.25	14.9
10Ni/MCM-41	144	0.29	15.7

According to BJH analysis the average pore diameter of MCM-41 and SBA-15 are 2.8 nm and 7.3 nm respectively, or SBA-15 has larger pores compared to MCM-41 **(Table 2.2)**. Further the mesoporosity of both SBA-15 and MCM-41 were quantified by low angle XRD as shown in **Figure 2.5b**, both SBA-15 and MCM-41 exhibit a high intensity (100) reflection at 2θ values of 0.938° and 2.42°, respectively. The other reflections ((110) and (200)) are seen at higher 2θ values, the shift of each lower angle reflections to higher θ values for MCM-41 compared to SBA-15 further proves that MCM-41 pore size are smaller than other porous material. The surface area of MCM-41 is two times more than that of SBA-15 due to the smaller pores and one would expect MCM-41 as a better support than SBA-15 owing to large surface area. The wall thickness of MCM-41 and SBA-15 was determined by average pore diameter and low angle XRD by using **Equation (2.5)**,[32] **(2.6)** and **(2.7)**.

The wall thickness was determined to be 3.55 nm for SBA-15, which is more than two times that of MCM-41 (1.5 nm) imparting extra thermal stability and rigidity to the former.

$$\text{Wt} = \text{a} - \text{Pore Diameter} \tag{2.5}$$

$$d(100) = n\lambda/2\sin\theta \tag{2.6}$$

$$a = 2d(100)/\sqrt{3} \tag{2.7}$$

The adsorption-desorption isotherm of Ni impregnated (23 wt. %) supports is depicted in **Figure 2.6c**, it clearly reveals that the SBA-15 maintained the type IV adsorption isotherm with type I hysteresis, but the inflection (sharp rise) portion shifted to lower relative pressure region with a lowering in both surface area (675 to 261 m^2/g) and pore size distribution as

shown in **Figure 2.6d** and **Table 2.2**. In the case of MCM-41, the adsorption-desorption isotherm lost its type IV characteristics and hysteresis after Ni loading implying that the pores are either blocked or occupied by the Ni-NPs, making it a non-porous surface like nMPS. Unexpectedly, there is an increase in the pore size distribution of MCM-41 after 23% Ni loading **(Table 2.2)**. This is due to blockage of all major mesopores ranging between 2 to 3 nm and the remaining very few pores show up as an average pore distribution. In short, this unexpected pore distribution is due to the complete blockage of MCM-41 characteristic pores (2-3 nm). This phenomenon can also be observed in nMPS where the average of few larger pores is shown up as the average pore diameter.

2.3.1.3. Microscopic Analysis (TEM)

Microscopic analysis of Ni-loaded supports showed distinct features in each support. In Ni loaded on SBA-15 (Ni/SBA-15), it appears that spherical Ni nanoparticles are well dispersed inside the hexagonal mesoporous channels with minimum aggregation or channel blockage (**Figure 2.8a)**. The particle size distribution was obtained by counting 50 particles fitted with a Gaussian function and revealing a particle size of 7.2 nm as average. This implies that the majority of the metal nanoparticles are well impregnated within the SBA-15 pores. In case of Ni loaded on MCM-41 (Ni/MCM-41), the mesoporous channels were not visible, and the average particle size was about 8.4 nm inferring that during the IWI of Ni over MCM-41 at the higher temperature, MCM-walls collapsed upon weakening and resulted in the aggregation of Ni nanoparticles **(Figure 2.8b)**.

On nMPS support, relatively larger nanoparticles of Ni are formed (**Figure 2.8c**), indicating that the capillary action of mesoporous material is crucial during IWI process to disperse the nanoparticles. Larger mesopores with good pore interconnectivity can efficiently disperse higher metal loading without particle aggregation and better NPs encapsulation. On the other hand, a smaller mesopore may lead to poor NP distribution without encapsulation of NPs. HRTEM analysis of Ni NPs on SBA-15, MCM-41 and nMPS showed similar lattice fringe of 0.211 nm, 0.213 nm and 0.213 nm, respectively, corresponding to Ni(111) crystal plane **(Figure 2.8a, 2.8b** and **2.8c)**. This implies that the Ni NP facet offered by all the three silica supports are the same, and one would expect all three catalysts to offer similar catalytic activity of Ni loaded on silica. To understand the effect of loading percentage on MCM-41, 2, 5, 10 and 15 wt.% of Ni was loaded on MCM-41 and analyzed by TEM. It was observed that above 2 wt.% Ni loading, porous nature is disturbed and the particle aggregations start collapsing the pore wall **(Figure 2.9)**.

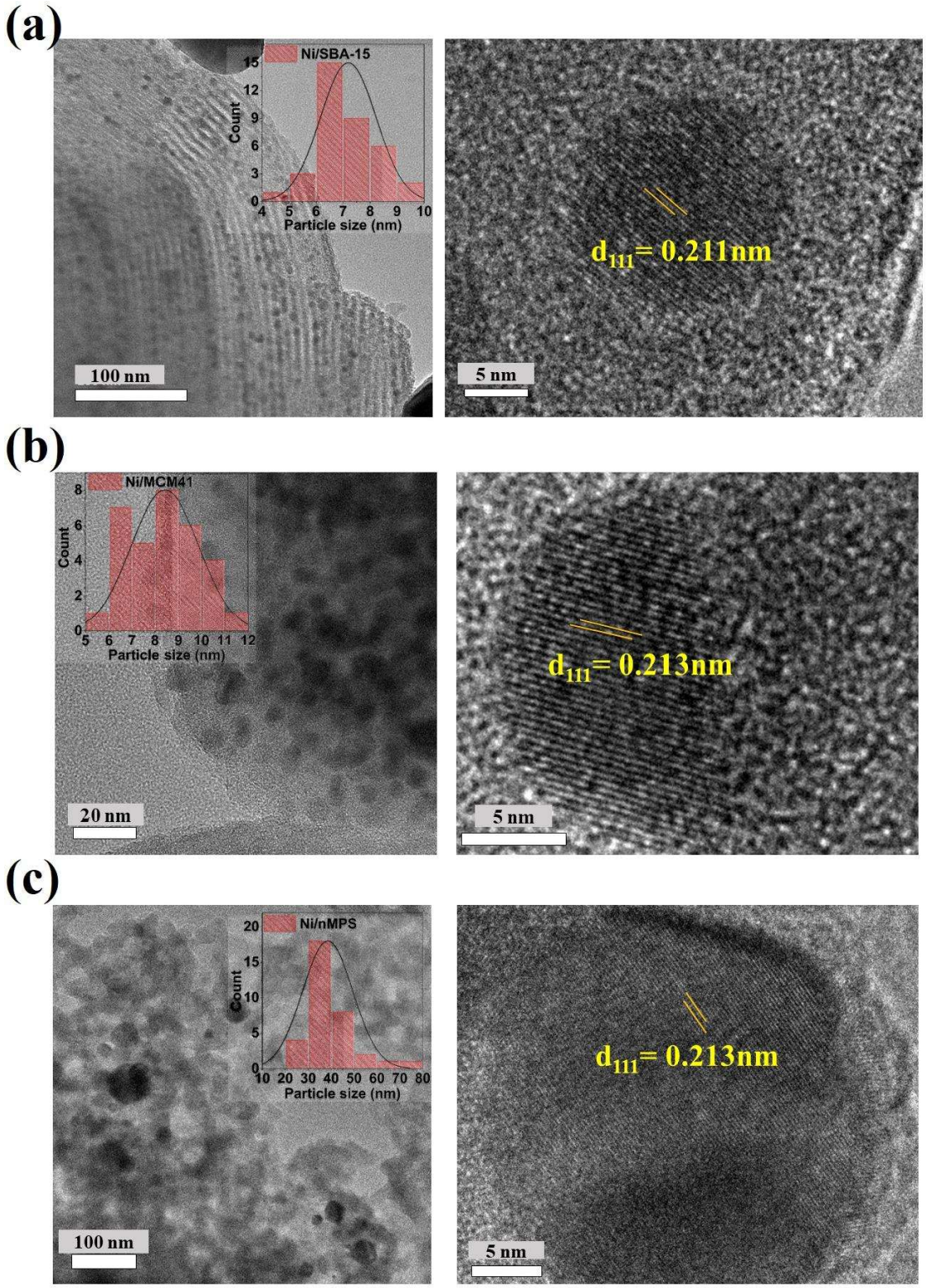

Figure 2.8. TEM images, particle size distribution curve and HRTEM of (a) Ni/SBA-15, (b) Ni/MCM-41 and (c) Ni/nMPS.

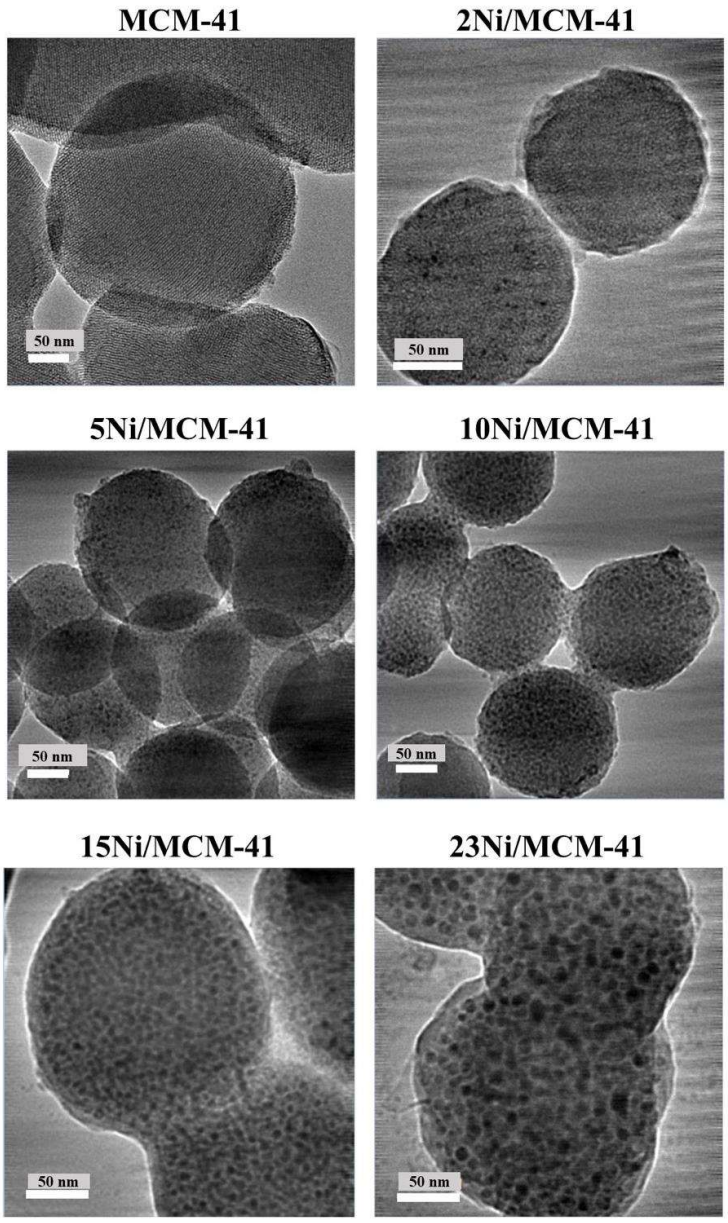

Figure 2.9. TEM image of Ni loaded on MCM-41 with different weight percentage loading.

Further, the characteristic type IV adsorption isotherm is lost for MCM-41 with 10, 15 and 23 wt.% Ni loading proving the collapse of pore wall and the generation of disorderness **(Figure 2.6)**. In case of nMPS, the lack of ordered pores and lower surface area caused larger sized nanoparticles to settle on their surfaces.

2.3.1.4. Amount of Ni loading and Relative Encapsulation over the Support

The relative encapsulation of Ni NPs on SBA-15, MCM-41 and nMPS were analyzed by studying the surface chemical composition of Ni on these support with the help of XPS. In Ni core level XPS, the peaks corresponding to Ni^0 $2p_{3/2}$ was observed at 852.8 eV, 852.6 eV

and 851.8 eV for Ni/SBA-15, Ni/MCM-41 and Ni/nMPS, respectively, which is in excellent agreement with the literature reports[39] with slight higher energy shift for SBA-15 and MCM-41 while lower energy shift for nMPS loaded Ni. Similar trend was observed for Ni^{2+} $2p_{3/2}$ also; 856.1 eV, 855.4 eV and 855.2 eV for SBA-15, MCM-41 and nMPS, respectively (**Figure 2.10** and **Table 2.3)**. The relative ratio of Ni^{0} $2p_{3/2}$ to Ni^{2+} $2p_{3/2}$ was calculated from XPS hinted that Ni in the reduced state was observed as the highest on SBA-15 followed by MCM-41 and least on nMPS (**Figure 2.10d** and **2.10e)**. This can be directly correlated with the relative encapsulation of active Ni metal nanoparticles inside SBA-15 is high compared to MCM-41 because of the structure collapse and almost negligible metallic Ni was supported on nMPS because of its non-porous nature. Apart from the individual species quantifications, the overall Ni species were also estimated using ICP-OES. The calculated data are at par with the loading percentage considered for the catalyst preparation, showing the complete incorporation of Ni within the support material (**Table 2.4**).

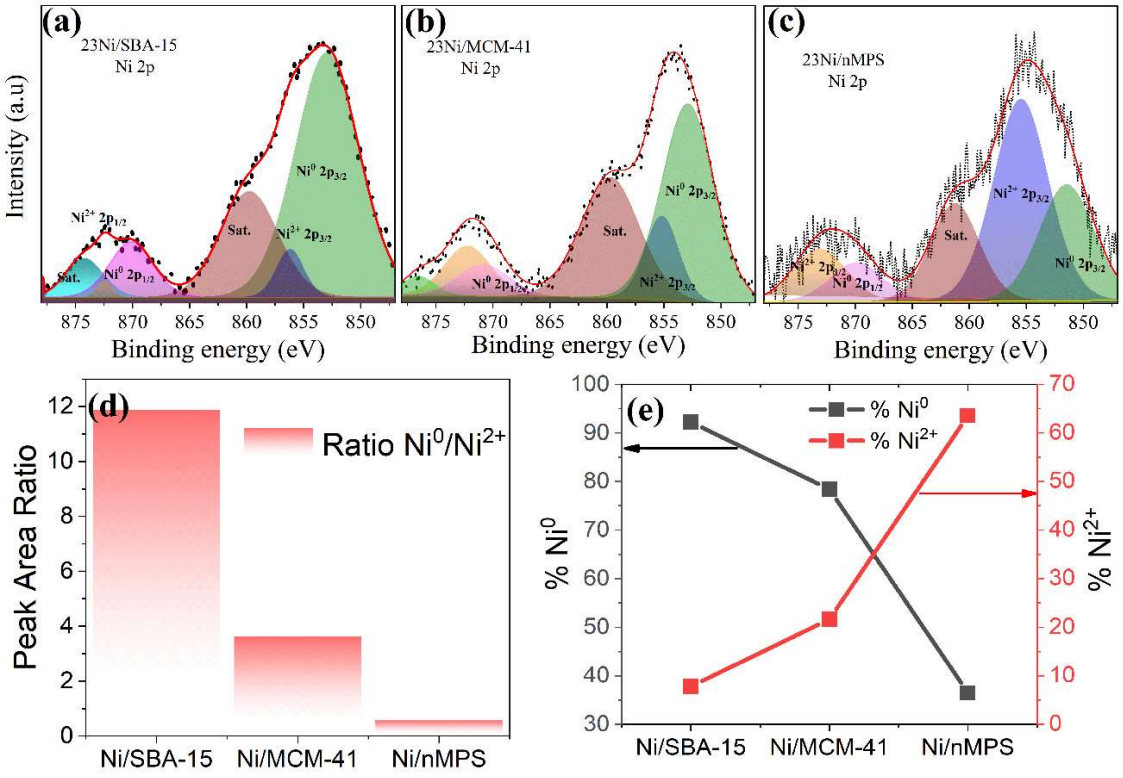

Figure 2.10. (a) Ni 2p XPS spectrum of 23Ni/SBA-15, (b) Ni 2p XPS spectrum of 23Ni/MCM-41and (c) Ni 2p XPS spectrum of 23Ni/nMPS, (d) Peak area ratio of Ni^{0} $2p_{3/2}$ to Ni^{2+} $2p_{3/2}$ plot of Ni/SBA-15, Ni/MCM-41 & Ni/nMPS and (e) percentage of Ni^{0} & Ni^{2+} of Ni/SBA-5, Ni/MCM-41 and Ni/nMPS.

Table 2.3. Summary of peak position and peak area of Ni^0 $2p_{3/2}$ and Ni^{2+} $2p_{3/2}$.

Ni/SBA-15	Position (eV)	Peak Area (a.u.)	% of Ni^0
Ni^0 $2p_{3/2}$	852.8	65683	92.22
Ni^{2+} $2p_{3/2}$	856.1	5541	
Ni/MCM-41	**Position (eV)**	**Peak Area (a.u.)**	78.38
Ni^0 $2p_{3/2}$	852.6	28644	
Ni^{2+} $2p_{3/2}$	855.4	7901	
Ni/nMPS	**Position (eV)**	**Peak Area (a.u.)**	36.44
Ni^0 $2p_{3/2}$	851.8	6047	
Ni^{2+} $2p_{3/2}$	855.2	10547	

Table 2.4. ICP-OES data of different Ni-silica.

Catalyst	Wt % of Ni Expected	Calculated by ICP-OES
23Ni/SBA-15	23	22.78
23Ni/MCM-41	23	22.8
23Ni/nMPS	23	22.46
15Ni/SBA-15	15	14.7
15Ni/MCM-41	15	14.2
15Ni/nMPS	15	14.4
10Ni/SBA-15	10	9.5
10Ni/MCM-41	10	9.6
10Ni/nMPS	10	9.9

2.3.2. CO_2 Reduction

CO_2 reduction test has been performed via the thermocatalytic pathway in a fixed bed vapor phase flow reactor by optimizing the reduction conditions from the temperature programmed reduction experiment (**Figure 2.1**). The catalytic performance of three catalysts at optimized conditions (593 K, 24 hrs, 4.9 h^{-1} WHSV (weight hour space velocity)) are shown in **Figures 2.11a**, **2.11b** and **2.12** at 1 and 5 bar pressures, respectively. CO_2 hydrogenation activity was found to be in the order of Ni/SBA-15 > Ni/MCM-41 > Ni/nMPS with 23% Ni loading. The methane activity and selectivity were observed best at 5 bar, and the order of activity was found to be Ni/SBA-15 (117 $\mu mol/g_{Ni}.s$) > Ni/MCM-41 (96 $\mu mol/g_{Ni}.s$) and negligible for Ni/nMPS (major product was CO). A methane activity comparison of Ni/silica-based catalyst reported recently is listed in **Table 2.5**.

Table 2.5. Comparison of different Ni/silica catalyst for CO_2 to methane conversion.
*** (This work)**

Catalyst	Reaction Condition	Conversion (%)	Selectivity (%)
Ni/SiO_2[40]	350 ºC, 1atm, CO_2:H_2 = 1:4	50	65
Ni(5.9 wt%)/SBA-16[41]	500 ºC, 1 atm, CO_2:H_2 = 1:1	21	>95
Ni(2 wt%)/SiO_2[42]	350 ºC, 1atm, CO_2:H_2 = 1:4	>40	>90
Ni(5 wt%)/MCM-41[43]	300 ºC, 1atm, CO_2:H_2 = 1:4	56.5	98.3
Ni(5 wt%)/MSN[43]	300 ºC, 1atm, CO_2:H_2 = 1:4	64.1	99.9
Ni(30 wt%)/Al_2O_3- SiO_2[44]	350 ºC, 1atm, CO_2:H_2 = 1:4	82.38	98.19
Ni(10 wt%)/MSN[45]	350 ºC, 1atm, CO_2:H_2 = 1:4	85	100
Ni-CeO_2(20 wt%)/MCM-41[46]	380 ºC, 1atm, CO_2:H_2 = 1:4	85.6	99.8
Ni(23 wt%)/SBA-15*	320 ºC, 1atm, CO_2:H_2 = 1:4	83	99.9
Ni(23 wt%)/MCM-41*	320 ºC, 5atm, CO_2:H_2 = 1:4	79	88

The CO_2 reduction activity was performed in a batch process as well (**Figure 2.12**), which favoured the conversion of CO_2 to formic acid instead of methane. The best-optimized reaction conditions were obtained by screening these catalysts at different conditions of pressure, temperature, and reaction time (**Figure 2.11c).** The CO_2 reduction activity trend towards formic acid was exactly similar to that of methanation activity with Ni/SBA-15 as the best catalyst. However, the formic acid production on the Ni/silica catalyst reported in our studies gives very less activity compared to Ru based or Pd based catalyst reported in literature. A brief comparison of the same is given in **Table 2.6**.

Table 2.6. Comparison of different Ni/silica catalyst for CO_2 to formic acid conversion.
*** (This work)**

Catalyst	Reaction Condition		Pressure (CO_2/H_2) in MPa	Temp (℃)	TON
	Solvent	Additives			
Ru/SiO_2 [47]	Water	Ionic liquid	9/9	60	206
Ru/TiO_2 [48]	Water	Ionic liquid	2/2	80	234
Au/Al_2O_3 [49]	DMF	NEt_3	2/2	70	1088
Au/SiO_2-schiff [50]	H_2O/CH_3OH	NEt_3	3/5	90	14470
Ru/LDH [51]	Water	NaOH	1/1	100	698
Pd/C_3N_4 [52]	Water	-	2.5/2.5	40	5.4
Ni/SBA-15*	Water	$KHCO_3$	2/2	200	21
Ni/MCM-41*	Water	$KHCO_3$	2/2	200	18
Ni/nMPS*	Water	$KHCO_3$	2/2	200	0.8

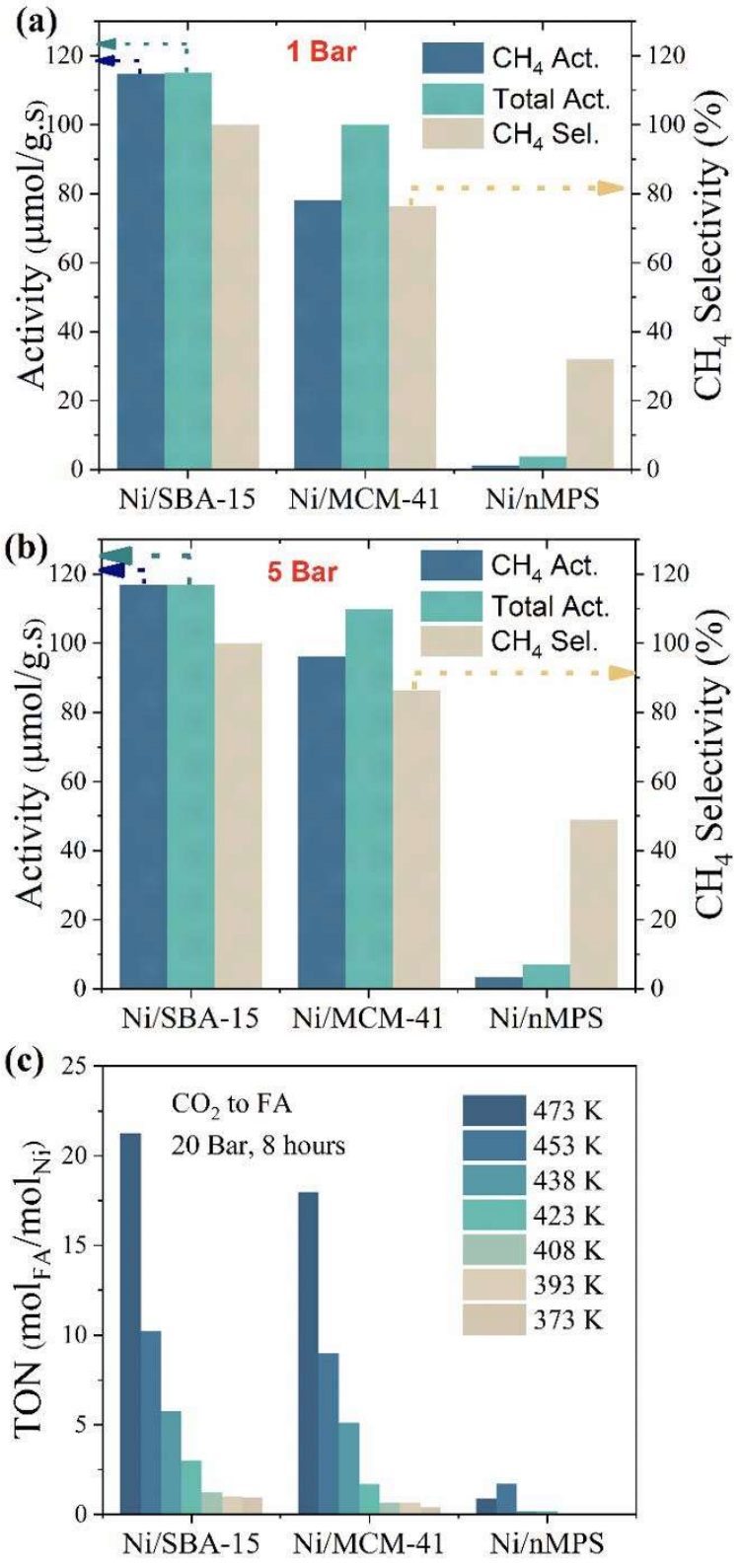

Figure 2.11. Methanation activity and selectivity for 23Ni/SBA-15, 23Ni/MCM-41 and 23Ni/nMPS at (a) 1 bar and (b) 5 bar. (c) Turn over number plot for CO_2 to formic acid over Ni/SBA-15, Ni/MCM-41 and Ni/nMPS at 20 bar and various temperature condition.

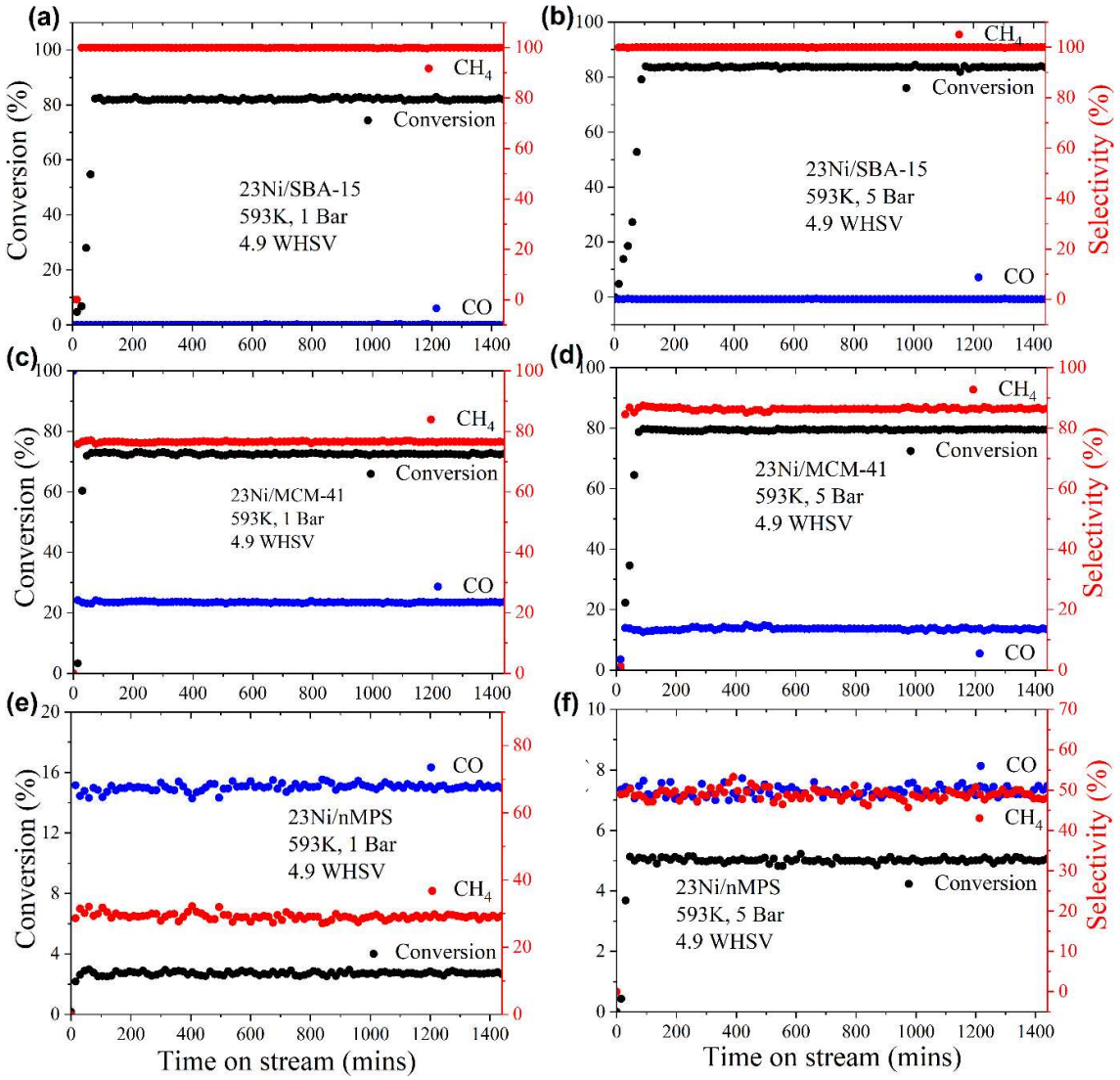

Figure 2.12. CO_2 conversion and methane selectivity of (a) 23Ni/SBA-15 at 593 K, 1bar, 4.9 h^{-1}, (b) 23Ni/SBA-15 at 593 K, 5bar, 4.9 h^{-1} (c) 23Ni/MCM-41 at 593 K, 1bar, 4.9 h^{-1} (d) 23Ni/MCM-41 at 593 K, 5bar, 4.9 h^{-1} (e) 23Ni/nMPS at 593 K, 1bar, 4.9 h^{-1} (f) 23Ni/nMPS at 593 K, 5bar, 4.9 h^{-1}.

2.3.3. CO_2 Reduction Mechanistic Study via *In-situ* DRIFTS

An *in-situ* DRIFTS study with mixed CO_2 and H_2 was performed on all the catalysts to elucidate the transformation of surface-adsorbed CO_2 and is depicted in **Figures 2.13** and **Figure 2.14.** Adsorption of CO_2 at room temperature reveals peaks centered at 2340 cm^{-1} with a small shoulder band at 2300 cm^{-1} assigned to linearly adsorbed CO_2[53] and the peak observed at 1357 cm^{-1} can be assigned to the adsorption of CO_2 as hydrogenated carbonate while the peaks corresponding to free carbonates are observed at 1270 cm^{-1} and 1260 cm^{-1} for all three

catalytic surfaces even at low temperature.[54] The peaks corresponding to carbonates (1395 cm^{-1} and 1456 cm^{-1}) are found to be low intense for Ni/SBA-15 and peaks corresponding to formates are absent, indicating that carbonates easily get hydrogenated, and formates formed in negligible quantity. For Ni/SBA-15 there is the emergence of a new peak at 3016 cm^{-1} can be assigned to sp^3 C-H_{str} of methane,[55] which started to emerge at 548 K and improves its intensity subsequently and maximize at 593 K, proving that methane formation increases upon reaction temperature (**Figure 2.13a)**.

The other peaks identified for Ni/SBA-15 at 2028 cm^{-1} and 1930 cm^{-1} can be assigned to linear Ni-CO and Ni_3-CO bridged CO_{str}, respectively **(Figure 2.13b** and **2.13c)**.[56-58] At lower temperature CO_2 gets transformed into carbonate and hydrogenated carbonate by the surface hydroxyl groups of SBA-15, but at higher temperature, the Ni NPs decomposes CO_2 into CO and O which gets hydrogenated to methane via the CO pathway utilizing spilled H atoms (H_{ads}). In case of Ni/MCM-41 (**Figure 2.13d-f)**, the peaks corresponding to linear and bridged CO are of very weak intensity, while there is an intense feature at 1576 cm^{-1} and a less intense peaks emerging at 2179 cm^{-1} and 2115 cm^{-1} can be assigned to formate and free CO stretching, respectively. DRIFTs data indicates the mechanism of CO_2M is different at the surface of Ni/MCM-41 surface as it follows the formate pathway (major) along with CO pathway (minor) as it can be observed that small quantity of CO may be re-adsorbed and hydrogenated to methane on Ni.

The activation of CO_2 by dangling -OH to yield formate on MCM-41 and subsequent hydrogenation is identified as a slower and less active pathway, although this is identified as a major route rather than direct CO_2 decomposition to CO and O.[59] It is reported that hydrogenation via CO pathway is faster compared to formate pathway with higher CH_4 selectivity.[59-61] However, the absence of free CO_{str} in Ni/SBA-15 supports CO pathway is more favorable for CO_2M.

Ni/nMPS exhibits relatively high intense free CO and free carbonate stretching on their surface. Most importantly, the Ni-CO linear stretching is absent and there is high intensity of 1950 cm^{-1} peak corresponding to Ni_3-CO bridged CO_{str} **(Figure 2.13g-2.13i)**. According to a recent report, the larger Ni NPs form highly stable bridged Ni-CO bonds, which deactivates the metal surface by poisoning and lowering CO_2M activity.[64] Additionally, the poisoning by CO also diminishes the ability of Ni to adsorb H_2 molecules. A minor peak with negligible intensity observed at 3016 cm^{-1} for Ni/nMPS sample further confirming the poisoning effect. To understand the effect of weight percentage of metal loading on the intermediates formed,

the lower loading of Ni on both MCM-41 and SBA-15 were further characterized by DRIFTS (**Figure 2.14)**. In case of Ni/SBA-15, 15% Ni loading yielded relatively lower intense peaks (with respect to 23% loading) corresponding to linear and bridged Ni-CO with no formate intermediates confirm CO pathway, but the presence of only peak corresponding to bridged Ni-CO for 10% Ni loading implying deactivation of catalyst. On the other hand, 10% and 15% Ni loading on MCM-41 produce formate peak as the major one with mild bridged Ni-CO peak at 1950 cm^{-1} confirms the pathway remains the same, but CO_2M activity reduced.

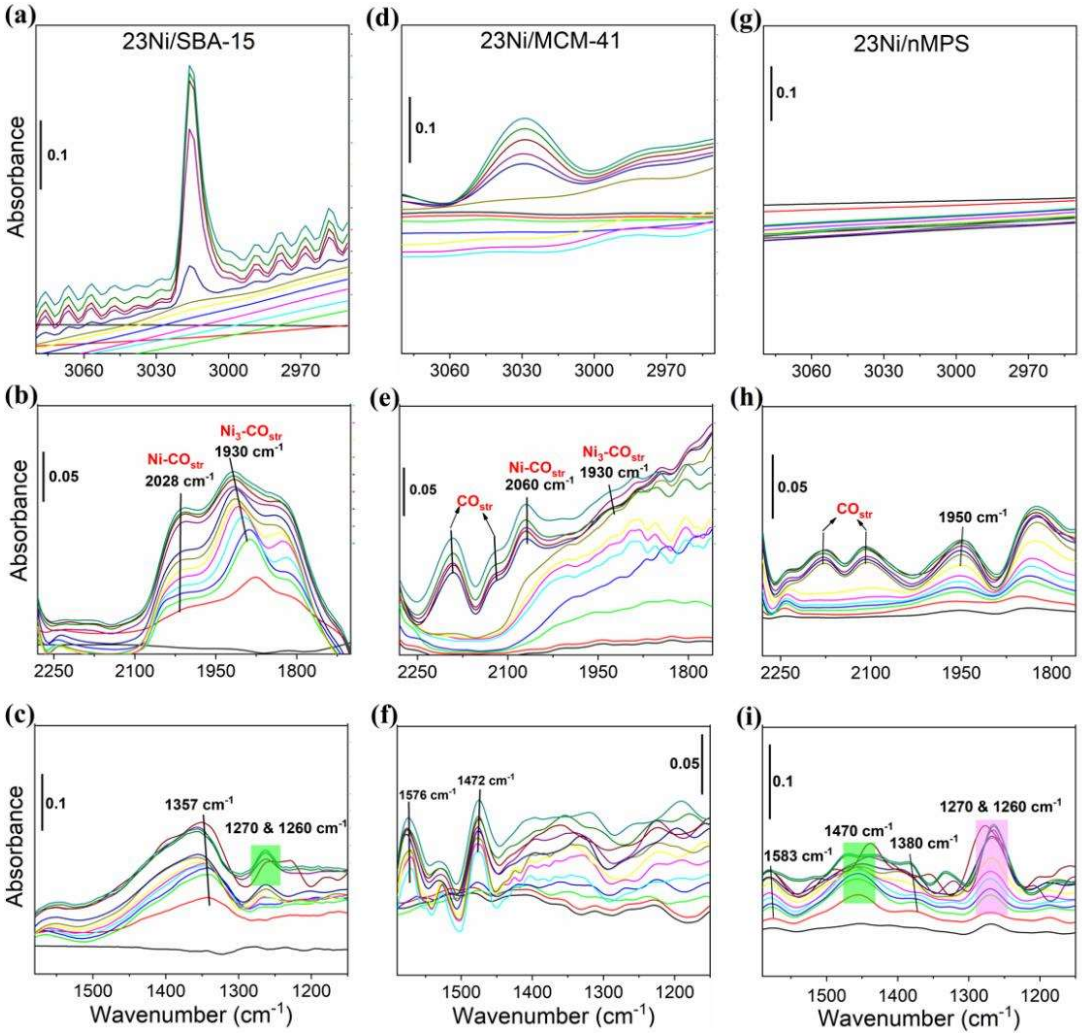

Figure 2.13. Successive DRIFTS spectra of (a) C-H stretching region over 23Ni/SBA-15, (b) CO stretching region over 23Ni/SBA-15, (c) formate and carbonate stretching regions over 23Ni/SBA-15, (d) C-H stretching region over 23Ni/MCM-41, (e) CO stretching regions over 23Ni/MCM-41, (f) formate and carbonate stretching regions over 23Ni/SBA-15, (g) C-H stretching region over 23Ni/nMPS, (h) CO stretching regions over 23Ni/nMPS and (i) formate and carbonate stretching regions over 23Ni/nMPS.

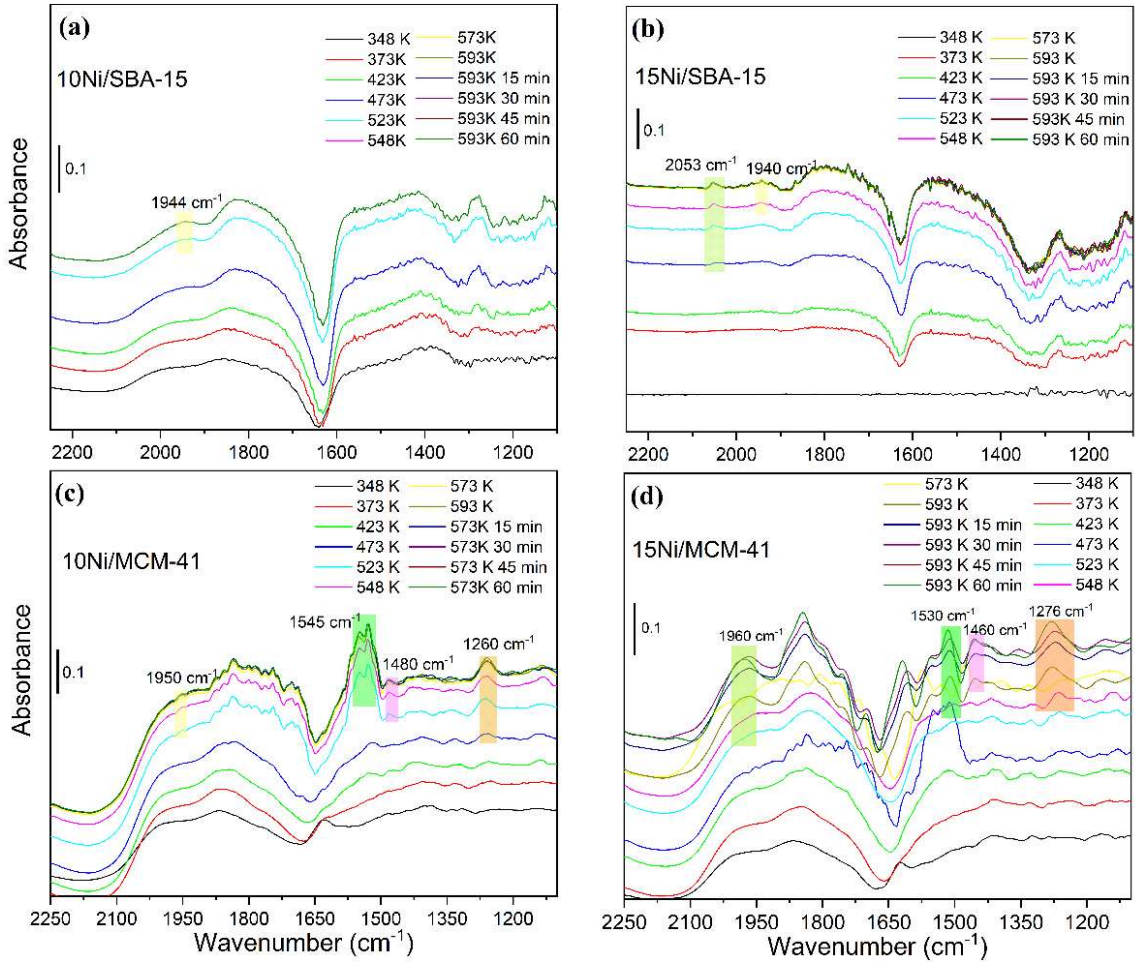

Figure 2.14. Successive DRIFTS spectra of carbonyl stretching regions over (a) 10Ni/SBA-15, (b) 15Ni/SBA-15, (c) 10Ni/MCM-41 and (d) 15Ni/MCM-41.

2.4. Conclusion

In conclusion, textural properties of a selected class of support materials (silica) have been exploited to tune the active catalyst dispersion to enhance the CO_2 reduction activity. The catalytic screening results (CO_2 to methane and CO_2 to formic acid) and the mechanistic reaction pathway mapped by DRIFTS reveal that 23% Ni loading on SBA-15 exhibits the best interaction between support and active metal center. This distinct reactivity and CO_2 hydrogenation mechanistic properties of Ni/MCM-41, Ni/SBA-15 and Ni/nMPS were identified to originate from the physicochemical textural property of their respective supports, which in turn decides the size, morphology, nanoparticle dispersion, aggregation and sintering during the reaction conditions. The understanding of structural sensitivity of loaded nanoparticles on the physicochemical textural property of support can be used as a better tool for the rational design of loaded metal support catalyst systems for a wide variety of catalysis.

2.5. References

1. Kattel, S.; Ramírez, P. J.; Chen, J. G.; Rodriguez, J. A.; Liu, P., Active Sites for CO_2 Hydrogenation to Methanol on Cu/ZnO Catalysts. *Science* **2017,** *355* (6331), 1296-1299.
2. Cherevotan, A.; Raj, J.; Dheer, L.; Roy, S.; Sarkar, S.; Das, R.; Vinod, C. P.; Xu, S.; Wells, P.; Waghmare, U. V.; Peter, S. C., Operando Generated Ordered Heterogeneous Catalyst for the Selective Conversion of CO_2 to Methanol. *ACS Energy Lett.* **2021,** *6* (2), 509-516.
3. Peter, S. C., Reduction of CO_2 to Chemicals and Fuels: A Solution to Global Warming and Energy Crisis. *ACS Energy Lett.* **2018,** *3* (7), 1557-1561.
4. Goud, D.; Gupta, R.; Maligal-Ganesh, R.; Peter, S. C., Review of Catalyst Design and Mechanistic Studies for the Production of Olefins from Anthropogenic CO_2. *ACS Catal.* **2020,** *10* (23), 14258-14282.
5. Aziz, M.; Jalil, A.; Triwahyono, S.; Mukti, R.; Taufiq-Yap, Y.; Sazegar, M., Highly active Ni-Promoted Mesostructured Silica Nanoparticles for CO_2 Methanation. *Appl. Catal. B* **2014,** *147*, 359-368.
6. Galletti, C.; Specchia, S.; Saracco, G.; Specchia, V., CO-Selective Methanation Over Ru–γAl_2O_3 Catalysts in H_2-Rich Gas for PEM FC Applications. *Chem. Eng. Sci.* **2010,** *65* (1), 590-596.
7. Ghaib, K.; Nitz, K.; Ben-Fares, F.-Z., Chemical Methanation of CO_2: A Review. *ChemBioEng Rev.* **2016,** *3* (6), 266-275.
8. Thampi, K. R.; Kiwi, J.; Grätzel, M., Methanation and Photo-Methanation of Carbon Dioxide at Room Temperature and Atmospheric Pressure. *Nature* **1987,** *327* (6122), 506-508.
9. Lim, J. Y.; McGregor, J.; Sederman, A. J.; Dennis, J. S., The Role of the Boudouard and Water–Gas Shift Reactions in the Methanation of CO or CO_2 Over Ni/γ-Al_2O_3 Catalyst. *Chem. Eng. Sci.* **2016,** *152*, 754-766.
10. Rahmani, S.; Rezaei, M.; Meshkani, F., Preparation of Promoted Nickel Catalysts Supported on Mesoporous Nanocrystalline Gamma Alumina for Carbon Dioxide Methanation Reaction. *J. Ind. Eng. Chem.* **2014,** *20* (6), 4176-4182.
11. Park, J.-N.; McFarland, E. W., A Highly Dispersed Pd–Mg/SiO_2 Catalyst Active for Methanation of CO_2. *J. Catal.* **2009,** *266* (1), 92-97.

12. Akamaru, S.; Shimazaki, T.; Kubo, M.; Abe, T., Density Functional Theory Analysis of Methanation Reaction of CO_2 on Ru Nanoparticle Supported on TiO_2 (101). *Appl. Catal. A* **2014,** *470*, 405-411.
13. Tada, S.; Shimizu, T.; Kameyama, H.; Haneda, T.; Kikuchi, R., Ni/CeO_2 Catalysts with High CO_2 Methanation Activity and High CH_4 Selectivity at Low Temperatures. *Int. J. Hydrogen Energy* **2012,** *37* (7), 5527-5531.
14. Aldana, P. A. U.; Ocampo, F.; Kobl, K.; Louis, B.; Thibault-Starzyk, F.; Daturi, M.; Bazin, P.; Thomas, S.; Roger, A. C., Catalytic CO_2 Valorization into CH_4 on Ni-based Ceria-Zirconia. Reaction Mechanism by Operando IR Spectroscopy. *Catal. Today* **2013,** *215*, 201-207.
15. Cárdenas-Arenas, A.; Quindimil, A.; Davó-Quiñonero, A.; Bailón-García, E.; Lozano-Castelló, D.; De-La-Torre, U.; Pereda-Ayo, B.; González-Marcos, J. A.; González-Velasco, J. R.; Bueno-López, A., Design of active sites in Ni/CeO_2 catalysts for the methanation of CO_2: tailoring the Ni-CeO_2 contact. *Appl. Mater. Today* **2020,** *19*, 100591.
16. Shen, L.; Xu, J.; Zhu, M.; Han, Y.-F., Essential Role of the Support for Nickel-Based CO_2 Methanation Catalysts. *ACS Catal.* **2020,** *10* (24), 14581-14591.
17. Mutz, B.; Sprenger, P.; Wang, W.; Wang, D.; Kleist, W.; Grunwaldt, J.-D., Operando Raman Spectroscopy on CO_2 Methanation Over Alumina-Supported Ni, Ni_3Fe and $NiRh_{0.1}$ Catalysts: Role of Carbon Formation as Possible Deactivation Pathway. *Appl. Catal. A* **2018,** *556*, 160-171.
18. Shahul Hamid, M. Y.; Triwahyono, S.; Jalil, A. A.; Che Jusoh, N. W.; Izan, S. M.; Tuan Abdullah, T. A., Tailoring the Properties of Metal Oxide Loaded/KCC-1 Toward a Different Mechanism of CO_2 Methanation by In-situ IR and ESR. *Inorg. Chem.* **2018,** *57* (10), 5859-5869.
19. Miguel, C. V.; Mendes, A.; Madeira, L. M., Intrinsic Kinetics of CO_2 Methanation Over an Industrial Nickel-Based Catalyst. *J. CO_2 Util.* **2018,** *25*, 128-136.
20. Pan, Q.; Peng, J.; Wang, S.; Wang, S.; Technology, In-situ FTIR Spectroscopic Study of the CO_2 Methanation Mechanism on Ni/$Ce_{0.5}Zr_{0.5}O_2$. *Catal. Sci. Technol.* **2014,** *4* (2), 502-509.
21. Zhang, Z.; Tian, Y.; Zhang, L.; Hu, S.; Xiang, J.; Wang, Y.; Xu, L.; Liu, Q.; Zhang, S.; Hu, X., Impacts of Nickel Loading on Properties, Catalytic Behaviors of Ni/γ–Al_2O_3 Catalysts and the Reaction Intermediates Formed in Methanation of CO_2. *Int. J. Hydrogen Energy* **2019,** *44* (18), 9291-9306.

22. Liu, Q.; Bian, B.; Fan, J.; Yang, J., Cobalt Doped Ni Based Ordered Mesoporous Catalysts for CO_2 Methanation with Enhanced Catalytic Performance. *Int. J. Hydrogen Energy* **2018,** *43* (10), 4893-4901.

23. Sharma, S.; Hu, Z.; Zhang, P.; McFarland, E. W.; Metiu, H., CO_2 Methanation on Ru-doped Ceria. *J. Catal.* **2011,** *278* (2), 297-309.

24. Liang, C.; Ye, Z.; Dong, D.; Zhang, S.; Liu, Q.; Chen, G.; Li, C.; Wang, Y.; Hu, X., Methanation of CO_2: Impacts of Modifying Nickel Catalysts with Variable-Valence Additives on Reaction Mechanism. *Fuel* **2019,** *254*, 115654.

25. Song, F.; Zhong, Q.; Yu, Y.; Shi, M.; Wu, Y.; Hu, J.; Song, Y., Obtaining Well-Dispersed Ni/Al_2O_3 Catalyst for CO_2 Methanation with a Microwave-Assisted Method. *Int. J. Hydrogen Energy* **2017,** *42* (7), 4174-4183.

26. Zhao, K.; Wang, W.; Li, Z., Highly Efficient Ni/ZrO_2 Catalysts Prepared Via Combustion Method for CO_2 Methanation. *J. CO_2 Util.* **2016,** *16*, 236-244.

27. Lechkar, A.; Barroso Bogeat, A.; Blanco, G.; Pintado, J. M.; Soussi el Begrani, M., Methanation of Carbon Dioxide Over Ceria-Praseodymia Promoted Ni-Alumina Catalysts. Influence of Metal Loading, Promoter Composition and Alumina Modifier. *Fuel* **2018,** *234*, 1401-1413.

28. Zhao, A.; Ying, W.; Zhang, H.; Ma, H.; Fang, D., $Ni–Al_2O_3$ Catalysts Prepared by Solution Combustion Method for Syngas Methanation. *Catal. Commun.* **2012,** *17*, 34-38.

29. Ahmad, W.; Younis, M. N.; Shawabkeh, R.; Ahmed, S., Synthesis of Lanthanide Series (La, Ce, Pr, Eu & Gd) Promoted $Ni/\gamma\text{-}Al_2O_3$ Catalysts for Methanation of CO_2 at Low Temperature Under Atmospheric Pressure. *Catal. Commun.* **2017,** *100*, 121-126.

30. Björk, E. M., Synthesizing and Characterizing Mesoporous Silica SBA-15: A Hands-on Laboratory Experiment for Undergraduates Using Various Instrumental Techniques. *J. Chem. Educ.* **2017,** *94* (1), 91-94.

31. Zhao, D.; Feng, J.; Huo, Q.; Melosh, N.; Fredrickson, G. H.; Chmelka, B. F.; Stucky, G. D., Triblock Copolymer Syntheses of Mesoporous Silica with Periodic 50 to 300 Angstrom Pores. *Science* **1998,** *279* (5350), 548-552.

32. Melendez-Ortiz, H. I.; Garcia-Cerda, L. A.; Olivares-Maldonado, Y.; Castruita, G.; Mercado-Silva, J. A.; Perera-Mercado, Y. A., Preparation of Spherical MCM-41 Molecular Sieve at Room Temperature: Influence of the Synthesis Conditions in the Structural Properties. *Ceram. Int.* **2012,** *38* (8), 6353-6358.

33. Bavykina, A.; Yarulina, I.; Al Abdulghani, A. J.; Gevers, L.; Hedhili, M. N.; Miao, X.; Galilea, A. R.; Pustovarenko, A.; Dikhtiarenko, A.; Cadiau, A.; Aguilar-Tapia, A.; Hazemann, J.-L.; Kozlov, S. M.; Oud-Chikh, S.; Cavallo, L.; Gascon, J., Turning a Methanation Co Catalyst into an In–Co Methanol Producer. *ACS Catal.* **2019,** *9* (8), 6910-6918.

34. Kittaka, S.; Morimura, M.; Ishimaru, S.; Morino, A.; Ueda, K., Effect of Confinement on the Fluid Properties of Ammonia in Mesopores of MCM-41 and SBA-15. *Langmuir* **2009,** *25* (3), 1718-1724.

35. Bourikas, K.; Kordulis, C.; Lycourghiotis, A., The Role of the Liquid-Solid Interface in the Preparation of Supported Catalysts. *Catal. Rev.* **2006,** *48* (4), 363-444.

36. Studt, F.; Sharafutdinov, I.; Abild-Pedersen, F.; Elkjær, C. F.; Hummelshøj, J. S.; Dahl, S.; Chorkendorff, I.; Nørskov, J. K., Discovery of a Ni-Ga Catalyst for Carbon dioxide Reduction to Methanol. *Nat. Chem.* **2014,** *6* (4), 320-324.

37. Hukkamäki, J.; Suvanto, S.; Suvanto, M.; Pakkanen, T. T., Influence of the Pore Structure of MCM-41 and SBA-15 Silica Fibers on Atomic Layer Chemical Vapor Deposition of Cobalt Carbonyl. *Langmuir* **2004,** *20* (23), 10288-10295.

38. Zhao, D.; Sun, J.; Li, Q.; Stucky, G. D., Morphological Control of Highly Ordered Mesoporous Silica SBA-15. *Chem. Mater.* **2000,** *12* (2), 275-279.

39. Marakatti, V. S.; Arora, N.; Rai, S.; Sarma, S. C.; Peter, S. C., Understanding the Role of Atomic Ordering in the Crystal Structures of NixSny toward Efficient Vapor Phase Furfural Hydrogenation. *ACS Sustain. Chem. Eng.* **2018,** *6* (6), 7325-7338.

40. Vrijburg, W. L.; van Helden, J. W.; van Hoof, A. J.; Friedrich, H.; Groeneveld, E.; Pidko, E. A.; Hensen, E. J.; Technology, Tunable Colloidal Ni Nanoparticles Confined and Redistributed in Mesoporous Silica for CO_2 Methanation. *Catal. Sci. Technol.* **2019,** *9* (10), 2578-2591.

41. Chen, C.-S.; Budi, C. S.; Wu, H.-C.; Saikia, D.; Kao, H.-M., Size-Tunable Ni Nanoparticles Supported on Surface-Modified, Cage-Type Mesoporous Silica as Highly Active Catalysts for CO_2 Hydrogenation. *ACS Catal.* **2017,** *7* (12), 8367-8381.

42. Wang, K.; Men, Y.; Liu, S.; Wang, J.; Li, Y.; Tang, Y.; Li, Z.; An, W.; Pan, X.; Li, L., Decoupling the Size and Support/Metal Loadings Effect of Ni/SiO_2 Catalysts for CO_2 Methanation. *Fuel* **2021,** *304*, 121388.

43. Aziz, M. A. A.; Jalil, A. A.; Triwahyono, S.; Mukti, R. R.; Taufiq-Yap, Y. H.; Sazegar, M. R., Highly Active Ni-Promoted Mesostructured Silica Nanoparticles for CO_2 Methanation. *Appl. Catal. B.* **2014,** *147*, 359-368.

44. Moghaddam, S. V.; Rezaei, M.; Meshkani, F.; Daroughegi, R., Synthesis of Nanocrystalline Mesoporous Ni/$Al_2O_3SiO_2$ Catalysts for CO_2 Methanation Reaction. *Int. J. Hydrogen Energy* **2018,** *43* (41), 19038-19046.
45. Aziz, M. A. A.; Jalil, A. A.; Triwahyono, S.; Saad, M. W. A., CO2 Methanation Over Ni-Promoted Mesostructured Silica Nanoparticles: Influence of Ni Loading and Water Vapor on Activity and Response Surface Methodology Studies. *Chem. Eng. J.* **2015,** *260*, 757-764.
46. Wang, X.; Zhu, L.; Liu, Y.; Wang, S., CO_2 Methanation on the Catalyst of Ni/MCM-41 Promoted with CeO2. *Sci. Total Environ.* **2018,** *625*, 686-695.
47. Zhang, Z.; Xie, Y.; Li, W.; Hu, S.; Song, J.; Jiang, T.; Han, B., Hydrogenation of Carbon Dioxide is Promoted by a Task-Specific Ionic Liquid. *Angew. Chem. Int. Ed.* **2008,** *120* (6), 1143-1145.
48. Upadhyay, P. R.; Srivastava, V., Selective Hydrogenation of CO_2 Gas to Formic Acid Over Nanostructured Ru-TiO_2 Catalysts. *RSC Adv.* **2016,** *6* (48), 42297-42306.
49. Filonenko, G. A.; Vrijburg, W. L.; Hensen, E. J. M.; Pidko, E. A., On the Activity of Supported Au Catalysts in the Liquid Phase Hydrogenation of CO_2 to Formates. *J. Catal.* **2016,** *343*, 97-105.
50. Liu, Q.; Yang, X.; Li, L.; Miao, S.; Li, Y.; Li, Y.; Wang, X.; Huang, Y.; Zhang, T., Direct Catalytic Hydrogenation of CO_2 to Formate Over a Schiff-Base-Mediated Gold Nanocatalyst. *Nat. Commun.* **2017,** *8* (1), 1407.
51. Mori, K.; Taga, T.; Yamashita, H., Isolated Single-Atomic Ru Catalyst Bound on a Layered Double Hydroxide for Hydrogenation of CO_2 to Formic Acid. *ACS Catal.* **2017,** *7* (5), 3147-3151.
52. Park, H.; Lee, J. H.; Kim, E. H.; Kim, K. Y.; Choi, Y. H.; Youn, D. H.; Lee, J. S., A Highly Active and Stable Palladium Catalyst on a gC_3N_4 Support for Direct Formic Acid Synthesis Under Neutral Conditions. *Chem. Commun.* **2016,** *52* (99), 14302-14305.
53. Hakim, A.; Marliza, T. S.; Abu Tahari, N. M.; Wan Isahak, R. W. N.; Yusop, R. M.; Mohamed Hisham, W. M.; Yarmo, A. M., Studies on CO_2 Adsorption and Desorption Properties from Various Types of Iron Oxides (FeO, Fe_2O_3, and Fe_3O_4). *Ind. Eng. Chem. Res.* **2016,** *55* (29), 7888-7897.
54. Li, H.; Jiao, X.; Li, L.; Zhao, N.; Xiao, F.; Wei, W.; Sun, Y.; Zhang, B. J. C. S.; Technology, Synthesis of Glycerol Carbonate by Direct Carbonylation of Glycerol

with CO_2 Over Solid Catalysts Derived from Zn/Al/La and Zn/Al/La/M (M= Li, Mg and Zr) Hydrotalcites. *Catal. Sci. Technol.* **2015,** *5* (2), 989-1005.

55. Schädle, T.; Pejcic, B.; Mizaikoff, B. J. A. M., Monitoring Dissolved Carbon Dioxide and Methane in Brine Environments at High Pressure Using IR-ATR Spectroscopy. *Anal. Methods* **2016,** *8* (4), 756-762.

56. Campuzano, J. C.; Greenler, R. G., The Adsorption Sites of CO on Ni(111) as Determined by Infrared Reflection-Absorption Spectroscopy. *Surf. Sci.* **1979,** *83* (1), 301-312.

57. Layman, K. A.; Bussell, M. E., Infrared Spectroscopic Investigation of CO Adsorption on Silica-Supported Nickel Phosphide Catalysts. *J. Phys. Chem. B* **2004,** *108* (30), 10930-10941.

58. Courtois, M.; Teichner, S. J., Infrared Studies of CO, O_2, and CO_2 Gases and their Interaction Products, Chemically Adsorbed on Nickel Oxide. *J. Catal.* **1962,** *1* (2), 121-135.

59. Wang, Y.; Winter, L. R.; Chen, J. G.; Yan, B., CO_2 Hydrogenation Over Heterogeneous Catalysts at Atmospheric Pressure: From Electronic Properties to Product Selectivity. *Green Chem.* **2021,** *23* (1), 249-267.

60. Feng, K.; Tian, J.; Guo, M.; Wang, Y.; Wang, S.; Wu, Z.; Zhang, J.; He, L.; Yan, B., Experimentally Unveiling the Origin of Tunable Selectivity for CO_2 Hydrogenation Over Ni-Based Catalysts. *Appl. Catal. B* **2021,** *292*, 120191.

61. Zhao, B.; Yan, B.; Jiang, Z.; Yao, S.; Liu, Z.; Wu, Q.; Ran, R.; Senanayake, S. D.; Weng, D.; Chen, J., High Selectivity of CO_2 Hydrogenation to CO by Controlling the Valence State of Nickel Using Perovskite. *Chem. Commun.* **2018,** *54* (53), 7354-7357.

Chapter 3

Operando Generated Ordered Heterogeneous Catalyst for the Selective Conversion of CO_2 to Methanol

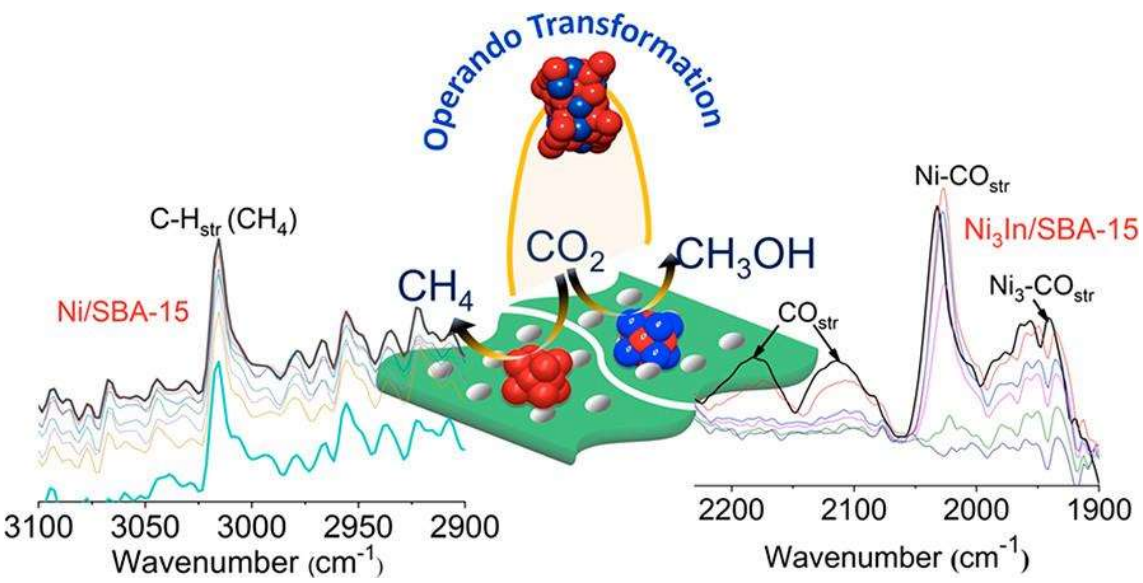

Arjun Cherevotan, Jithu Raj, Lakshay Dheer, Soumyabrata Roy, Shreya Sarkar, Risov Das, Chathakudath P. Vinod, Shaojun Xu, Peter Wells, Umesh V. Waghmare, Sebastian C. Peter.

ACS Energy Lett., **2021**, *6* (2), 509-516.

Summary

In this chapter, the catalytic nature of a well-known methanation catalyst nickel (Ni) has been tuned with the introduction of inactive indium (In) to discover a new efficient catalyst selective towards methanol. We report an operando generated stable Ni-In kinetic phase that selectively converts of CO_2 to energy dense methanol at lower pressure compared to the state-of-the-art materials. To this end, we demonstrate that the thermodynamically stable Ni_7In_3 phase transforms to well-ordered Ni_3In under operando conditions, which enhance the conversion of CO_2 to methanol (CTM). The remarkable change in the mechanistic pathways towards methanol production has been mapped by operando Diffuse Reflectance Infrared Fourier Transform Spectroscopy (DRIFTS) analysis, corroborated by first principles calculations. The ordered arrangement and pronounced electronegativity difference between Ni and In are attributed to the complete shift in mechanism towards methanol from methane in the case of metallic Ni. The approach and findings of this work provide a unique advancement step in the path towards next-generation catalyst discovery for going beyond the state-of-the-art in CO_2 reduction technologies.

The work based on this chapter has been published in ACS Energy Letters.

Operando Generated Ordered Heterogeneous Catalyst for the Selective Conversion of CO_2 to Methanol. **Arjun Cherevotan**, Jithu Raj, Lakshay Dheer, Soumyabrata Roy, Shreya Sarkar, Risov Das, Chathakudath P. Vinod, Shaojun Xu, Peter Wells, Umesh V. Waghmare, Sebastian C. Peter. *ACS Energy Lett.*, **2021**, *6* (2), 509-516.

Table of Contents

3.1. Introduction

Methanol (MeOH), among other catalytic products, has been projected as a future transportation fuel due to its high octane number.[1] It can be directly used as additive to gasoline in internal combustion engines or its derivatives such as dimethyl ether (DME) or oxymethylene ethers.[2-4] Also, it is an important starting material for the production of several multi-carbon compounds including alcohols, ethers, esters, olefins and alkanes.[5, 6] The catalytic conversion of CO_2 to methanol (CTM) via thermochemical route of hydrogenation has been investigated since early 1990s.[7] $CuO/ZnO/Al_2O_3$ (CZA) is the state-of-the-art catalyst being used for CTM in high pressure-temperature regimes.[8] Since then, many advances in catalyst design have been made to facilitate the hydrogenation of CTM.[9-13] Investigations into improved efficiency via the design of catalysts in the nanosized regime and support-based effects, have resulted in greater mechanistic insight into the process.[14-16]

A relatively new area in CTM catalyst engineering has seen the advent of transition-metal based bimetallic or intermetallic catalysts (IMCs). Even in the state-of-the-art CZA system, interfacial Cu-Zn alloy is strongly speculated to be the efficient catalytic site for CTM under the reaction conditions.[17-19] Given the role bimetallic alloys have played in various catalytic processes, such as Cu-Zn in CTM, more recent studies have explored the possibilities of their ordered intermetallinc (IM) variants.[20-22] They differ from their bimetallic counterparts or even alloys having unique long-range crystalline order and exhibit drastic changes from their parent elements in terms of both electronic and geometric properties.[23-25] This inimitable feature significantly improves the CTM activity of ordered IMCs over bimetallic or alloys that can potentially surpass the CZA benchmarks.[26, 27] One of the major advantages of transforming metals or bimetallic systems to IMCs is the generation of the ordered arrangement of the atoms, which indirectly isolates the active metallic site within the chemical atmosphere made up of non-active elements.[28, 29] In addition to the ordered arrangement and site isolation, the performance of the catalysts can be improved further with appropriate selection of support materials.[30, 31] The carbon neutrality and the key techno-economic bottleneck of the CTM process is associated with the minimization of hydrogen consumption and energy requirements of high pressure conditions. Both the issues have been addressed here by significantly enhancing the methanol selectivity at relatively lower pressures.

In this work, we have discovered a novel non-noble metal-based IMC comprising Ni and In atoms, Ni_3In, through in-situ stabilization of kinetic Ni-In phase. This nanoscale ordered catalyst dispersed on high surface mesoporous silica SBA-15 exhibit high methanol yields in

CTM. SBA-15 surface stabilizes the carbonyl intermediates together with enabling ideal intermetallic distribution.[32] Nickel is a well-known and highly selective CO_2 methanation catalyst at ambient pressures,[33] and also different ratios of Ni to In in a phyllosilicate based composite catalyst is reported to enhance CO_2 to methanol conversion at lower pressure.[34] Here we aimed to understand and sketch the catalytic evolution upon the introduction of inert In into the active Ni structure. The dramatic mechanistic divergence towards MeOH upon formation of this IMC was mapped by operando DRIFTS studies, which is well corroborated with DFT calculations. Both studies illustrate how changes in the Ni-Ni coordination with more electropositive In, alter the product selectivity from 100% methane on Ni catalyst to more than 80% methanol over intermetallic Ni_3In. The electronegativity difference between Ni and In atoms, confirmed by X-ray absorption spectroscopy (XAS) and X-ray photoelectron spectroscopy (XPS) studies, and the ordered atomic arrangements of the constituents yield the high production of methanol from CO_2 under lower pressures.

3.2. Experimental Section

3.2.1. Chemicals and Reagents

Tetraethyl orthosilicate (TEOS) (>99% GC, Sigma Aldrich), Pluronic P123 (M_n~5800, Sigma Aldrich), HNO_3 (69% analytical grade, Merck Chemicals), H_2SO_4 (98% analytical grade, Merck Chemicals), nickel nitrate hexahydrate (98%, SDFCL) and indium nitrate hydrate (99.99%, Sigma Aldrich).

3.2.2. Synthesis

3.2.2.1. Synthesis of SBA-15

The support material Santa Barbara Amorphous (SBA-15)[35] was synthesized by modifying an already reported method.[36] Four grams of Pluronic P123 was dissolved in 105 mL of deionized water and 10.8 mL of 98% H_2SO_4 to act as a soft template. Then 9.063 mL of TEOS was added to the solution with high rate of stirring for 3.5 hours at 313 K, followed by hydrothermal treatment at 373 K for 30 hours. The obtained white powder was filtered, washed with deionized water and dried at 373 K overnight. Lastly it was calcined for 6 hours at 823 K.

3.2.2.2. Ni-In/SBA-15

A typical method of incipient wetness impregnation was followed with slight modification to distribute Ni-In system on SBA-15.[27, 37] Ni(II) and In(III) nitrates were dissolved in 4 M HNO_3 solution. The nitrate salts were weighed to get 23% of metal loading

with different ratio of Ni:In – 3:1 (Ni-In/SBA-15-a), 2:1 (Ni-In/SBA-15-b), 1:1 (Ni-In/SBA-15-c) and 7:3 (Ni-In/SBA-15-d). SBA-15 was soaked in the solution for an hour, which propels the solution impregnation into the channels by capillary action. The excess solution was dried at 333 K in fume hood and further in vacuum oven at 393 K overnight. The precursor was reduced at 1083 K under H_2 flow. The controlled catalyst (without In) Ni/SBA-15 was synthesized by following same steps. The NiO-In_2O_3/SBA-15 was synthesized by oxidizing Ni-In/SBA-15-d at 773 K for 5 hours under air.

3.2.3. Material Characterization

3.2.3.1. Powder X-ray Diffraction (PXRD)

The phase formation on SBA-15 was confirmed by X-ray diffraction (XRD) collected on PANalytical X-ray diffractometer with Cu Kα radiation at 45 kV and 40 mA. The features of the PXRD patterns were compared with simulated pattern from Pearson Database.

3.2.3.2. N_2 Adsorption-Desorption Measurement

The adsorption isotherms were studied by using N_2 at 77 K on BelCat instrument. Prior to the measurements the powders were treated for degassing at 423 K for 6 hours. The specific surface area was confirmed by Brunaur-Emmett-Teller (BET) method and pore size distribution by classical BJH (Barrett, Joyner and Halenda) method.

3.2.3.3. Transmission Electron Microscopy (TEM)

TEM images and selected area electron diffraction patterns were collected using a JEOL JEM-2010 TEM instrument and color mapping was done in TECHNAI. The samples for these measurements were prepared by sonicating the nanocrystalline powders in ethanol and drop-casting a small volume onto a carbon-coated copper grid.

3.2.3.4. X-ray Photoelectron Spectroscopy (XPS)

XPS measurements were carried out using Thermo K-alpha+ spectrometer using micro focused and monochromated Al Kα radiation with energy 1486.6 eV. The pass energy for spectral acquisition was kept at 50 eV for individual core-levels. The electron flood gun was utilized for providing charge compensation during data acquisition. Further, the individual core-level spectra were checked for charging using C1s at 284.6 eV as standard and corrected if needed. The peak fitting of the individual core-levels was done using CasaXPS software with a Shirley type background.

3.2.3.5. X-ray Absorption Spectroscopy (XAS)

Ni XAFS measurements of Ni-edge of Ni/SBA-15, Ni_7In_3/SBA-15 and Ni_3In/SBA-15 were carried out in fluorescence mode at PETRA III, P65 beamline of DESY, Germany. Pellets for the measurements were made by homogenously mixing the sample with an inert cellulose matrix to have an X-ray absorption edge jump close to one. Standard data analysis procedure was used to extract the extended X-ray absorption fine structure (EXAFS) signal from the measured absorption spectra. Background subtraction, normalization, and alignment of the EXAFS data were performed by ATHENA software.

3.2.4. Catalyst Extrusion

Wire type extrudates were used for the tubular reactor. A paste was made from catalyst powder by grinding 5 g of it with 1.5 g of pseudoboehmite (AlO(OH)) and 10 mL of 0.5 M HNO_3. This was then passed through a manually operated wire profiled die to get a wire of 0.5 mm diameter and 1 mm length. The extrudates were dried in atmospheric conditions and then calcined overnight at 373 K to make it strong. The extrudates were crushed and characterized by XRD.

3.2.5. Catalyst Screening Test

The efficiency of the catalysts towards CO_2 reduction was screened by a fixed bed vapor phase down flow reactor having a bed volume of 9.2 cm^3. Two flow rates were used, that is, 40 NLPH ($1CO_2$:$3H_2$) and 50 NLPH ($1CO_2$:$4H_2$). The reactions were performed at different temperatures (523 K and 573 K) and different pressures (ambient to 50 bar). The catalyst after loading was activated by passing 5:10 mixture of H_2 and N_2 at 673 K. The gases were analyzed in real time by Agilent GC 7890B, with TCD and FID as the detector. The liquid products were condensed by chiller and analysis by FID after 15 hours of reaction. N_2 and isopropyl alcohol (IPA) were used as the internal standards for gas and liquid analysis, respectively.

3.2.6. Operando DRIFTS

The operando DRIFTS experimental were carried out using an Agilent Carey 680 FTIR Spectrometer equipped with a Harrick DRIFTS cell. The spectra were recorded at 4 cm^{-1} resolution and each spectrum was averaged 64 times. Each sample was pre-treated at 473 K using 99.999% argon at a gas flow rate of 50 mL min^{-1} for 1h to remove adsorbed water and other gas molecules. Then the temperature of the sample was increased to 723 K and gas switched to 20%H_2/Ar at 50 mL min^{-1} for 2h reduction. After that, the temperature of the sample was annealed to 303 K under Ar flow. The spectrum of the annealed sample at 303 K

was used as the background reference for the following reaction. To probe the reaction, 25%CO_2/75%H_2 gas mixture at 1 bar and a total flow rate of 50 mL min^{-1} was first introduce to the DRIFTS cell, and then temperature was ramped from 303 to 573 K (ca. 15 K min^{-1}) to determine the relationship between temperature and the reaction intermedia. Then the reaction was maintained at 573 K for 1h to determine the surface intermedia revolution.

3.2.7. Computational Details

Our first-principles calculations are based on density functional theory (DFT) as implemented in the Quantum ESPRESSO code[38] employing plane-wave basis and ultra-soft pseudopotentials[39] to represent the interaction between ionic cores and valence electrons. We adopt the exchange-correlation energy functional of Perdew-Burke-Ernzerhof (PBE)[40] obtained within a generalized gradient approximation (GGA).

We smear the discontinuity in occupation numbers of electronic states with Fermi–Dirac distribution having a smearing width (k_BT) of 0.04 eV. An energy cut-off of 50 Ry is used to truncate the plane-wave basis used in representation of Kohn-Sham wave functions, and of 400 Ry to represent the charge density. Optimized structures were determined through minimization of energy until the Hellmann-Feynman force on each atom is smaller than 0.03 eV/Å in magnitude. We use a supercell (2×2) to model the (111) surface of Ni_3In ($Ni_{48}In_{16}$) introducing a vacuum layer of 15 Å thickness parallel to the slab separating its adjacent periodic images.

To this end, we modelled 2×2 in-plane supercell of its (111) surface ($Ni_{48}In_{16}$). Each supercell contains a slab of 4 atomic planes of which, the bottom 2 atomic planes were kept fixed and the top 2 were allowed to relax. We sampled Brillouin-zone integrations on uniform grid of 6×6×1 k-points in the Brillouin zone of (111) surface of Ni_3In. The projected density of states of each structure was obtained from calculations on a denser, 15×15×1, k-point mesh. Calculated lattice constants of bulk Ni_3In (a_{Ni_3In} = 3.74 Å) are within the typical GGA errors with respect to their observed values (a_{Ni_3In} = 3.73 Å).

3.2.8. Calculations

3.2.8.1. Weight Hour Space Velocity (WHSV)

WHSV is defined as the mass of reactant per unit time passed per mass of catalyst charged in a reactor. Here we used two flow rates 40 NLPH ($1CO_2$:$3H_2$) and 50 NLPH ($1CO_2$:$4H_2$).

40 NLPH:

CO_2 flow = 10 NLPH (19.8 grams per hour)

H_2 flow = 30 NLPH (2.67 grams per hour)

N_2 flow (internal standard for GC analysis) = 0.8 NLPH (1 grams per hour)

Mass of catalyst charged = 5 g

$$WHSV = (19.8 + 2.67 + 1)/5 \quad = 4.69\ h^{-1} = \sim 4.7\ h^{-1}$$

50 NLPH:

CO_2 flow = 10 NLPH (19.8 grams per hour)

H_2 flow = 40 NLPH (3.56 grams per hour)

N_2 flow (internal standard for GC analysis) = 1 NLPH (1.25 grams per hour)

Mass of catalyst charged = 5 g

$$WHSV = (19.8 + 3.56 + 1.25)/5 = 4.922\ h^{-1} = \sim 4.9\ h^{-1}$$

3.2.8.2. Response factor of GC (RF)

Response factor for a component '*i*' of a detector is the ratio of peak area of component '*i*' to calibration concentration (**Eqn. 3.1**). The unknown concentration of component '*i*' during online gas analysis is determined multiplying response factor of component with peak area of the component obtained during online analysis. Note that calibration compositions of samples are expressed in percentage.

$$RF_i = \text{Peak Area of } i \div \text{Standard Composition of } i\ (\%) \qquad (3.1)$$

$$\text{Unknown Composition of } i \text{ in product gas } (\%) = RF \text{ Peak} \times \text{Area of } i \text{ in product} \qquad (3.2)$$

The GC RF for TCD are given below:

RF of CO_2 = 0.001617

RF of N_2 = 0.001848

RF of CO = 0.00216

RF of CH_4 = 0.00221

3.2.8.3. Conversion and product selectivity[41]

$$CO_2 \text{ conversion } (\%) = \left(CO_2\ (\text{in}) - CO_2\ (\text{out}) \times \frac{N_2(\text{in})}{N_2(\text{out})}\right) \div CO_2\ (\text{in}) \qquad (3.3)$$

$$\text{Selectivity of } i = (100\text{n} \times \frac{\text{Composition of } i}{N_2(\text{out})}) \div (\frac{CO_2\ (\text{in})}{N_2(\text{in})} - \frac{CO_2\ (\text{out})}{N_2(\text{out})}) \qquad (3.4)$$

$$\text{MeOH Selectivity } (\%) = 100 - (\text{CO Selectivity} + CH_4 \text{ Selectivity}) \qquad (3.5)$$

CO_2 (in) = Composition of CO_2 in feed gas

CO_2 (out) = Composition of CO_2 in product

N_2 (in) = Composition of N_2 in feed gas

N_2 (out) = Composition of N_2 in product

3.2.8.4. Liquid analysis

The liquid products reaction is collected by condensation after 15 hours of reaction. The condensed liquid is analyzed for methanol by auto-liquid sampler of GC with FID as a detector. The liquid analysis is done by mixing 1.5 mL of liquid product with 100 µl of isopropyl alcohol (IPA). A calibration plot of different MeOH volume % vs peak area ratio of MeOH to IPA is plotted (**Figure 3.1**) by making different standards of MeOH-water mixture. The MeOH volume % of unknown sample is determined from peak area ratio of MeOH/IPA peak area by GC.

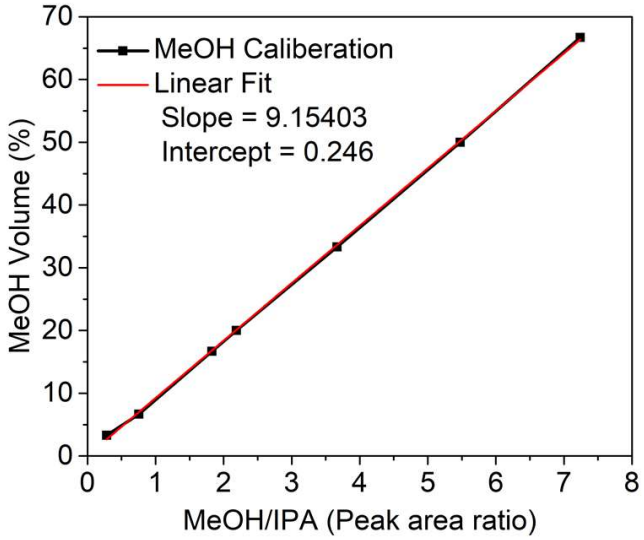

Figure 3.1. Methanol Calibration Curve.

$$\text{MeOH selectivity by gas analysis} = [100 - (S_{CO} + S_{CH_4}]\ \% \quad (3.6)$$

Ni_7In_3/SBA-15-573K-50B-4.7 h^{-1}

Conversion = 17 %

CO selectivity = ~12.75 %

CH_4 selectivity = 0.4 %

From **eqn. 3.6**, MeOH selectivity = 100 – (12.75 + 0.4) = 86.85 %

Out of 100 moles of product 86.85 moles are MeOH, 12.75 are CO and negligible 0.4 % are CH_4.

$$CO_2 + 3H_2 \rightarrow CH_3OH + H_2O \quad (3.7)$$

$$CO_2 + H_2 \rightarrow CO + H_2O \quad (3.8)$$

$$CO_2 + 4H_2 \rightarrow CH_4 + 2H_2O \quad (3.9)$$

$$\text{MeOH mol \% in liquid product} = 86.85 \times \frac{100}{86.85 + 86.85 + 12.75 + 0.8}$$

Each mole of methanol and carbon monoxide gives one mole of water while each mole of methane gives 2 moles of water.

Thus, in liquid product MeOH mol % = 46.4 %

MeOH weight % in liquid $= (100 \times 46.4 \times 32) \div \big((46.4 \times 32) + (53.6 \times 18)\big)$

MeOH weight % in liquid = 60.6 %

From density of methanol (0.791 gmL^{-1}) and water (1 gmL^{-1}),

MeOH vol. % in liquid. = 66.04% (expected volume % of Methanol in liquid by gas analysis)

The average peak area ratio is 6.24

MeOH vol. % in liquid $= (6.24 \times 9.154) + 0.246$

MeOH vol. % in liquid = 57.37% (The value is lesser than expected by gas analysis, this may be due to evaporation losses of MeOH during liquid condensation)

Similarly, liquid analysis is presented in table below

Table 3.1. Liquid Calibration Curve for Methanol

Peak Area		Peak Area Ratio
MeOH	**IPA**	**MeOH/IPA**
2995	464	6.45
2890	462	6.25
2895	464	6.24

3.3. Results and Discussions

3.3.1. Catalyst preparation and material characterization

Ni metal and Ni-In IMCs supported on mesoporous SBA-15 were prepared by the facile incipient wetness impregnation and subsequent thermal reduction. Since, several IMCs reported within the Ni-In family, the initial target was to map all these phases. Four compounds NiIn/SBA-15, Ni_2In/SBA-15, Ni_3In/SBA-15 and Ni_7In_3/SBA-15 were targeted by stoichiometric modification of the precursor combination. Ni and In nitrate solutions (precursors) were impregnated thoroughly into SBA-15 pores, and co-reduced under hydrogen flow at higher temperature to form the supported IMC phases as shown in **Figure 3.2**. The powder X-ray diffraction (XRD) pattern of Ni/SBA-15 (**Figure 3.2a)** exhibits characteristic peaks of Ni metal observed at 2θ = 44.5°, 51.9° and 76.4° confirming the formation of metallic Ni nanoclusters (cubic, $Fm\bar{3}m$ space group) on SBA-15. Interestingly, identical features were observed in the XRD patterns of all the aforementioned combinations of Ni-In (NiIn, Ni_2In, Ni_3In and Ni_7In_3) phases on SBA-15 regardless of the ratio of metal precursor solution (**Figure 3.2a**), which confirm the formation of triclinic Ni_7In_3 IMC phase having space group $P\bar{1}$**.** Among the four phases, Ni_7In_3/SBA-15 was found to form in the pure targeted phase up to the XRD detection limits (**Figure 3.2b**). On the other hand, peaks at 41.6° and 48.5° corresponding to Ni_3In IMC (S.G: $Pm\bar{3}m$*)* occurred as a minor impurity alongside the major Ni_7In_3 phase obtained in Ni_3In/SBA-15 **(Figure 3.2)** synthesis. The other targeted phases Ni_3In/SBA-15 and Ni_2In/SBA-15 lead to the formation of Ni ($Fm\bar{3}m$) as a minor phase along with Ni_7In_3 as the major phase. These controlled synthesis studies, repeated over several batches, revealed that all high temperature reaction routes in the Ni-In system lead majorly to the thermodynamically stable Ni_7In_3 phase irrespective of the compositions targeted **(Figure 3.2c)**. In the next step, SBA-15 was selected as the support to impregnate Ni_7In_3 nanoparticles within the ordered mesoporous channel.

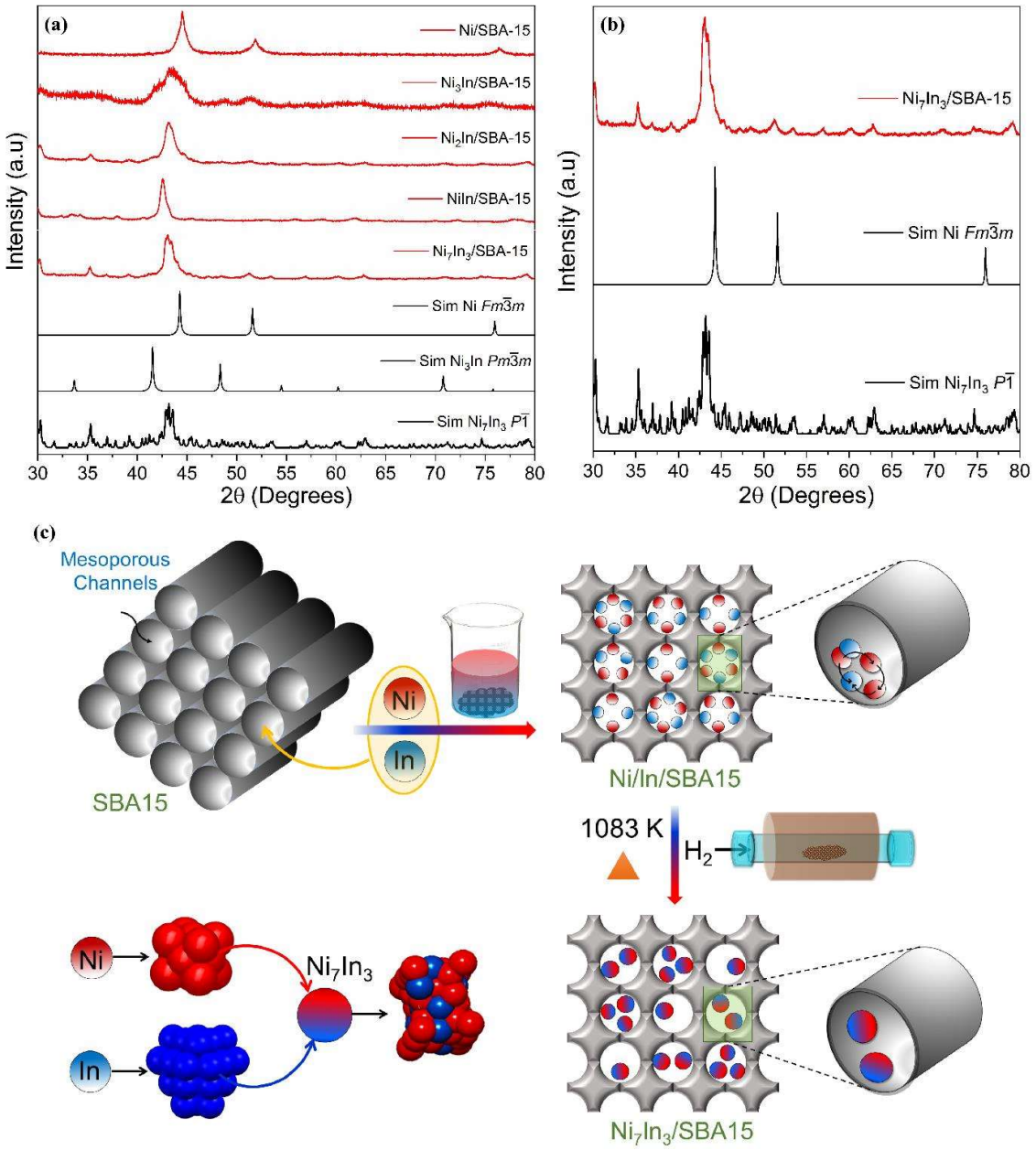

Figure 3.2. (a) Powder XRD comparison between Ni/SBA-15, Ni_3In/SBA-15, Ni_2In/SBA-15, NiIn/SBA-15 and Ni_7In_3/SBA-15 with simulated Ni $Fm\bar{3}m$, simulated Ni_3In $Pm\bar{3}m$ and simulated Ni_7In_3 $P\bar{1}$ (b) Powder XRD comparison between Ni_7In_3/SBA-15 and simulated Ni $Fm\bar{3}m$ and simulated Ni_7In_3 $P\bar{1}$. (c) Schematic for Ni_7In_3 intermetallic nanoparticle formation inside the SBA-15 pores by incipient wetness impregnation.

Impregnation of the IMC nanoclusters in the mesoporous SBA-15 presents two advantages: (a) it helps in the formation of ordered IMs in the nanoscale within its channels and (b) it favors uniform distribution of the IM nanoparticles. These parameters are very crucial

in improving the active surface area in addition to the inherent chemical nature of the catalyst, which dictates the overall CTM activity of the material. The TEM and SEM micrographs of SBA-15 visualize the separated hexagonal channels of the mesoporous support (**Figure 3.3a and Figure 3.3d**).

The TEM images for both Ni/SBA-15 and Ni_7In_3/SBA-15 were indistinguishable due to extensive distribution of metal/IM nanoparticles (NPs) over the channels of SBA-15 (**Figure 3.3b**). STEM color mapping on the NPs of Ni_7In_3/SBA-15 shows the uniform elemental distribution of Ni and In all over the spherical nanoparticles confirming the formation of the IMC (**Figure 3.3c**), which is well complemented by the SEM images (**Figure 3.3e**). The average particle size in the case of Ni_7In_3 was found to be 7.7 nm **(Figure 3.3c)**. The N_2 adsorption-desorption experiment exhibits type IV isotherm (Brunauer definition) with hysteresis loop (**Figure 3.3g**), typical of hexagonal and cylindrical mesoporous materials.[42] There is a fast increase in adsorption volume between 0.6-0.8 p/p_0 which is indicative of capillary condensation attributed to the pre-formation of N_2 on the pore walls due to multilayer adsorption.[43]

Ni/SBA-15 and Ni_7In_3/SBA-15 samples, exhibited a left-shift of the sharp rise in the adsorption isotherms and drastically diminished surface areas [from 675 m^2/g (SBA-15) to 290 m^2/g (Ni/SBA-15) and 265 m^2/g (Ni_7In_3/SBA-15)]. This lowering of surface area concludes that impregnated Ni and Ni_7In_3 clusters decreases the N_2 probing surface inside the mesopores.[44] Additionally, the decrease in pore size upon the impregnation further confirms the formation Ni metal and Ni_7In_3 IMC as nanoparticles within the channels of mesoporous SBA-15 **(Figure 3.3h)**.

3.3.2. Thermocatalytic CO_2 hydrogenation performance

The catalytic performance of Ni/SBA-15 and Ni_7In_3/SBA-15 towards CO_2 reduction was evaluated in the continuous flow fixed bed reactor. Consistent to the earlier works,[32, 45] Ni/SBA-15 converts CO_2 to methane with almost 100% selectivity (**Figure 3.4**). Under various pressure regimes, CO_2:H_2 ratios and varying WHSV, Ni/SBA-15 favored the conversion of CO_2 into methane (**Figure 3.4a, 3.4b** and **3.4c**). Furthermore, at a given pressure better conversion was obtained for 1:4 ratio of CO_2 to H_2 (4.9 h^{-1} WHSV) without significantly affecting the methane selectivity. Bare SBA-15 (without metal loading) under similar conditions did not favor the CO_2 conversion (**Table 3.2**), which indicates that the support alone is inactive.

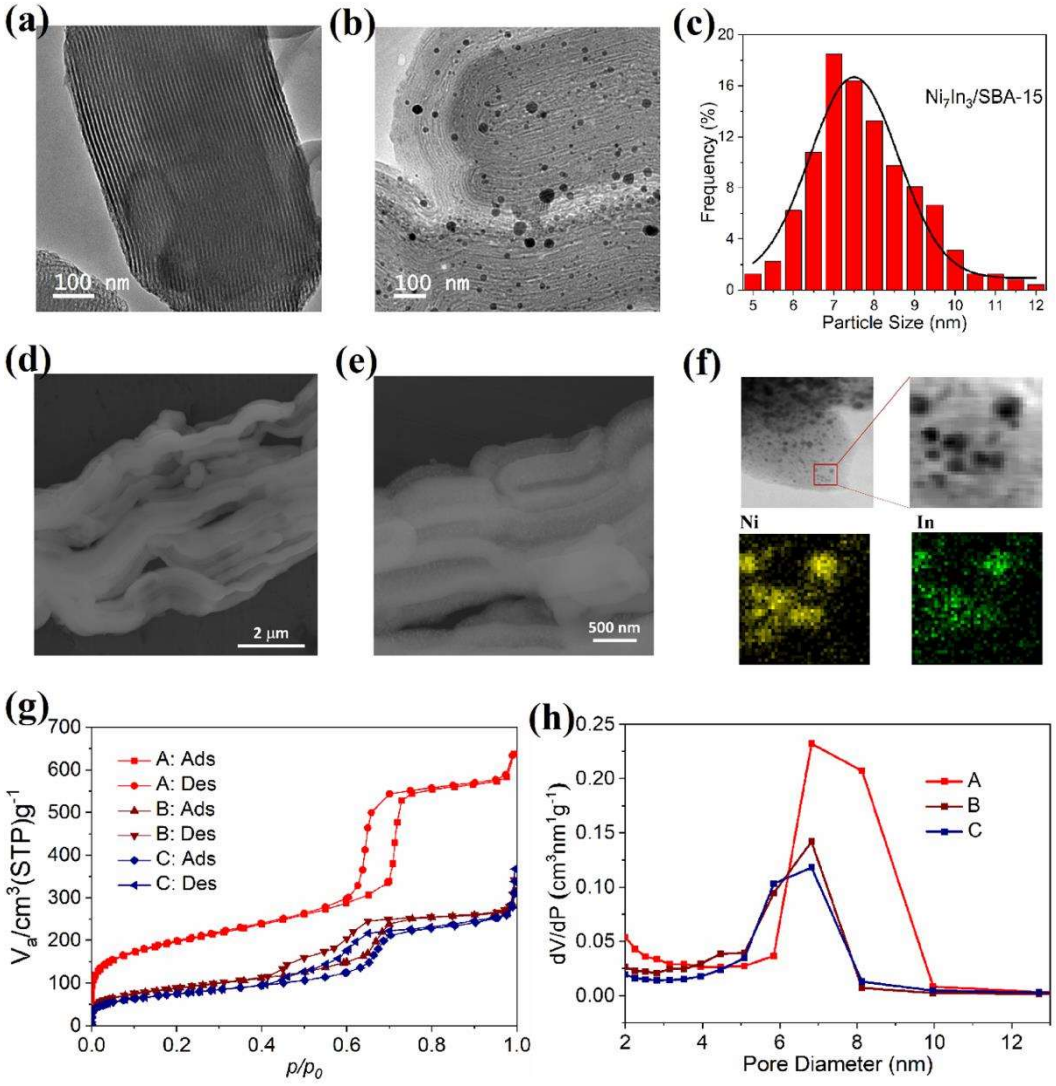

Figure 3.3. TEM image of (a) SBA-15, (b) Ni_7In_3/SBA-15, (c) particle size distribution of Ni_7In_3 on SBA-15; SEM image of (d) SBA-15 and (e) Ni_7In_3/SBA-15. (f) STEM and elemental color mapping of Ni_7In_3 nanoparticles, (g) N_2 adsorption-desorption isotherm of A: SBA-15, B: Ni/SBA-15 and C: Ni_7In_3/SBA-15 at 77 K, and (h) corresponding pore size distribution by BJH method.

The experiments at higher pressures for Ni/SBA-15 exhibit a notable 12% decline in the conversion, but the selectivity towards methane remain unchanged at ~99.5%. This confirms that the selectivity of Ni catalyst towards methane is an inherent catalytic property of Ni and is independent of operating pressure and WHSVs. Methanation on Ni catalysts commences with the dissociative adsorption of CO_2 on Ni to give CO and O, which gets spilled over, interacts with the surface oxides of silica support and gets trapped in the O-vacancy of the silica adjacent to Ni.[46]

Table 3.2. Catalytic performances of different catalyst with respect to the reaction condition

Catalyst	Reaction Condition	Conversion (%)	Selectivity towards MeOH (%)	Selectivity Towards CO (%)	Selectivity Towards CH_4 (%)
SBA-15	573K-20B-4.7/h	<0.001	-	100	-
	573K-20B-4.7/h	<0.001	-	100	-
Ni/SBA-15	573K-40B-4.7/h	60	-	<0.05	>99.5
	573K-40B-4.9/h	80	-	<0.05	>99.5
	573K-20B-4.7/h	50	-	<0.05	>99.5
	573K-20B-4.9/h	68	-	<0.05	>99.5
Ni_3In/SBA-15	573K-50B-4.7/h	17.5	87-88	12-13	<1
	573K-40B-4.7/h	17	79	20	0.5
	573K-40B-4.9/h	14.8	63	36	0.55
	523K-40B-4.7/h	4.75	73	27	-
	523K-40B-4.9/h	6	83	17.8	-
	573K-20B-4.7/h	16-16.5	75	23.8	0.04
	573K-20B-4.9/h	13	67	32	0.08
	523K-20B-4.7/h	4.5	83	17	-
	523K-20B-4.9/h	4	85	14	-
	573K-5B-4.7/h	<1	-	100	-
	573K-10B-4.7/h	1-2	1	99 -100	-
	573K-15B-4.7/h	15.8	75	13-14	2
NiO-In_2O_3/SBA-15	573K-50B-4.7/h	9	75	24	<1
	573K-40B-4.7/h	11	77	22	< 1
	573K-20B-4.7/h	10.5	85	14.5	0.5

Further, CO and O interacts to form linear and bridged carbonyls. These carbonyls are hydrogenated to form formates and then to methane by the spilled over hydrogen produced over Ni. A recent report concludes that CO can form on Ni by two types of Reverse Water Gas Shift (RWGS) pathways (one involving formate and another involving CO_2^- ion), which in either case gets further hydrogenated by spilled H atom from Ni.[47] Thus, regardless of the pathways, the key feature of Ni is its ability to spill H and reduce CO_2 and the adsorbed intermediates to form methane. The Ni atoms function as the site for both hydrogen splitting and catalyzing the kinetically uphill 8-electron reduction process. Based on the optimized

reactions conditions for Ni/SBA-15, the catalytic activity of Ni_7In_3/SBA-15 towards CO_2 reduction has been tested (**Figure 3.5a-d)**.

At 573 K temperature, 50 bar pressure and 4.7 h^{-1} WHSV, Ni_7In_3/SBA-15 converted ~17% of CO_2, but interestingly negligible amount of methane (~1%) could be detected in the product mixture. GC analysis of the product mixture confirmed ~86% selectivity towards MeOH and the rest (13%) was identified as CO (**Figure 3.6a)**. The dramatic turnaround of the product selectivity from 100% methane on Ni to 86% methanol (~1% methane) over IM Ni_7In_3 can be attributed to the stark structural changes upon alloying Ni with In, which triggers a different mechanistic pathway in the overall CO_2 reduction process.

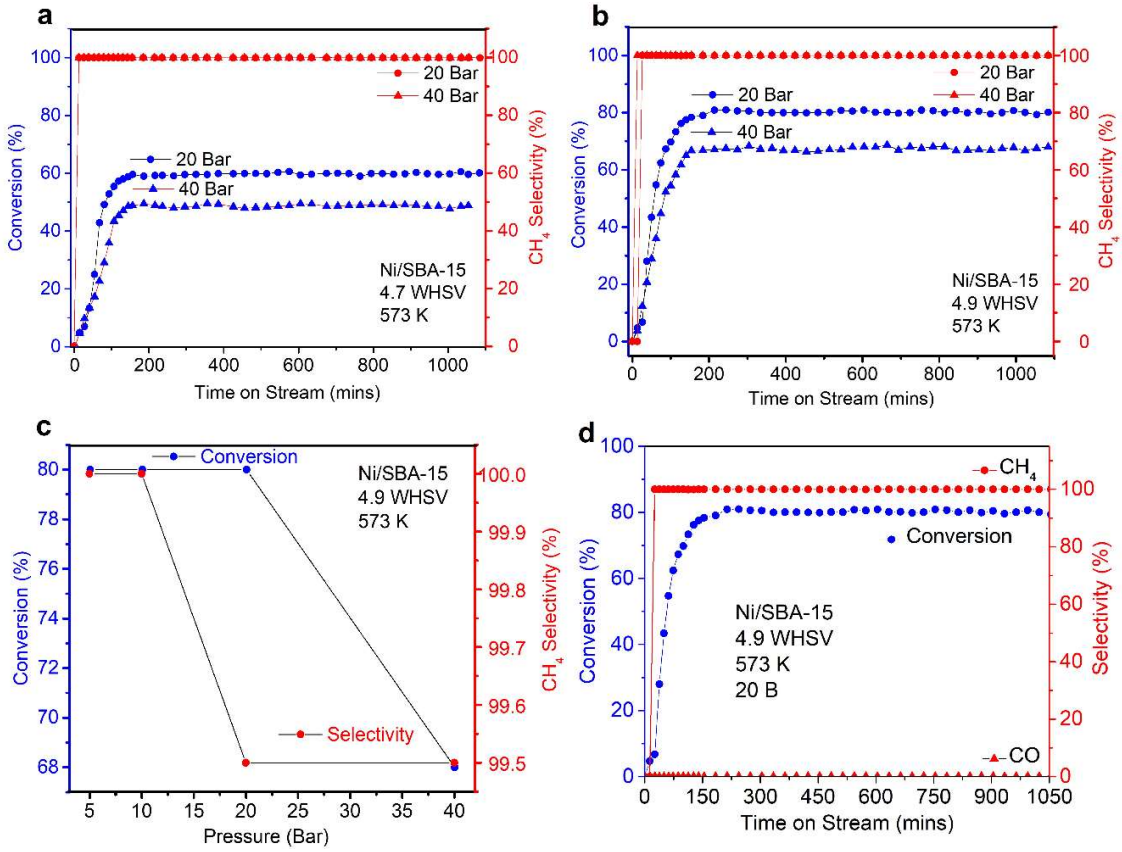

Figure 3.4. Catalytic performance of Ni/SBA-15, (a) CO_2 conversion and methane selectivity at reaction condition of 20 bar and 40 bar pressure with WHSV 4.7 h^{-1} (CO_2/H_2=1:3) and at 573 K temperature, (b) CO_2 conversion and methane selectivity at reaction condition of 20 bar and 40 bar with 4.9 h^{-1} (CO_2/H_2 = 1:4) and 573 K, (c) CO_2 conversion and methane selectivity at different pressures (5-40 bar) with 4.9 h^{-1} and 573 K, (d) CO_2 conversion and selectivity for 15 hours of time on stream at reaction condition of 4.9 h^{-1}, 20 bar and 573K.

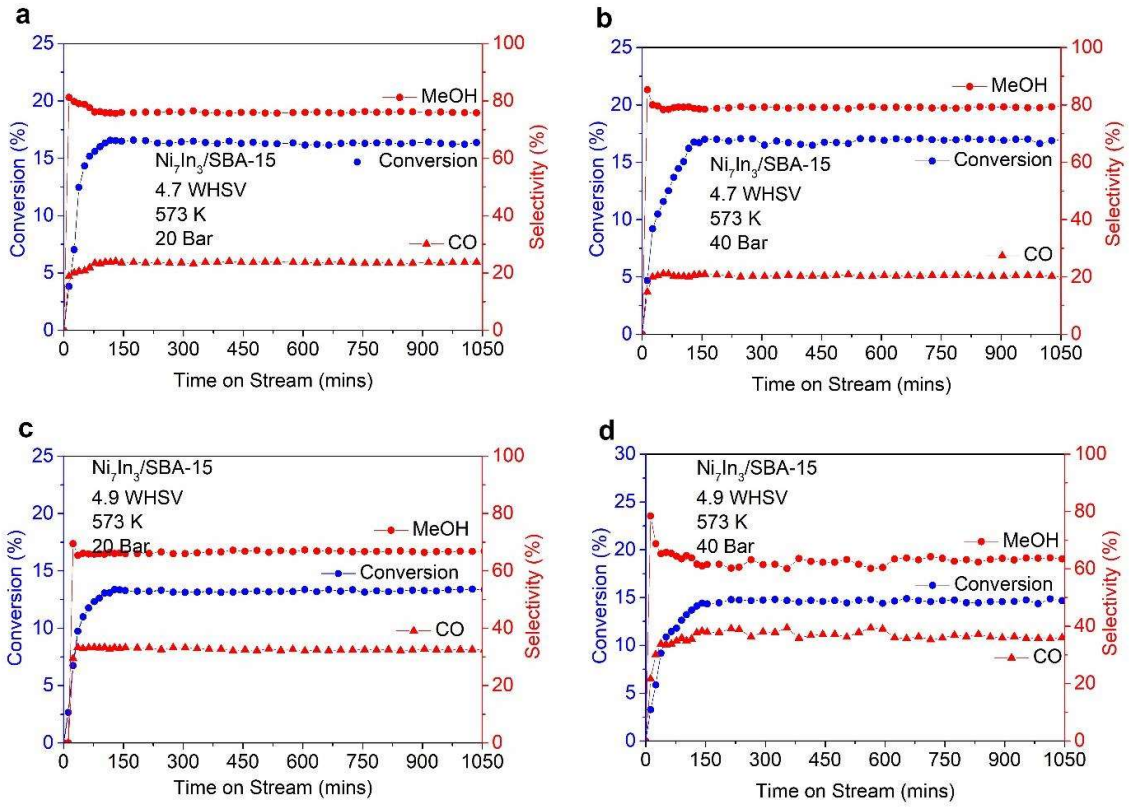

Figure 3.5. Catalytic test on Ni_7In_3/SBA-15 at 573 K, (a) CO_2 conversion and selectivity for 15 hours of time on stream at reaction condition of 4.7 h^{-1} (1:3) and 20 bar, (b) CO_2 conversion and selectivity for 15 hours of time on stream at reaction condition of 4.7 h^{-1} (1:3) and 40 bar, (c) CO_2 conversion and selectivity for 15 hours of time on stream at reaction condition of 4.9 h^{-1} (1:4), and 20 bar, (d) CO_2 conversion and selectivity for 15 hours of time on stream at reaction condition of 4.9 h^{-1} (1:4) and 40 bar.

In addition to conversion and selectivity, the other important direction in CTM research aims to reduce the operating pressure to make the overall process economically viable. Towards this, Ni_7In_3/SBA-15 was further tested for CO_2 reduction at different pressure range, starting from ambient to 50 bar, at a constant temperature of 573 K and 4.7 h^{-1} WHSV (**Figure 3.6b**). As shown, the conversion increases from 0% at ambient pressure to more than 16% at 20 bar. A further increase in pressure from 20 to 50 bar yields less than 2% increment in the CO_2 conversion. A similar trend was obtained for the methanol selectivity, which increases from 0% at ambient pressure to 75% methanol at 20 bar. A relatively small increment (13%) in the methanol selectivity was achieved between 20 and 50 bar (**Table 3.2 and 3.3**). CO was obtained as the major product at low pressure, but methane was never found to be more than 1% at any of the operating conditions.

Table 3.3. Methanol selectivity by liquid analysis.

Catalyst	Reaction condition	MeOH vol.% by gas analysis	Ratio of MeOH/IPA	MeOH vol. % by liquid analysis
Ni_7In_3/SBA-15	573K-50B-4.7/h	66.04	6.24	57.47
	573K-40B-4.7/h	63.96	5.76	53.03
	573K-20B-4.7/h	63.18	5.98	54.98
	573K-40B-4.9/h	58.58	5.55	51.05
	573K-20B-4.9/h	55.04	5.16	47.46
	523K-40B-4.7/h	61.76	4.66	42.81
	523K-20B-4.7/h	65.10	6.03	55.45
	523K-40B-4.9/h	65.1	6.02	55.36
	523K-20B-4.9/h	65.1	5.19	47.77
NiO-In_2O_3/SBA-15	573K-50B-4.7/h	62.65	5.77	53.11
	573K-40B-4.7/h	63.15	6.33	58.17
	573K-20B-4.7/h	65.53	6.21	57.1

A sharp change in both conversion and selectivity was occurred between 10 and 20 bar pressure range can be correlated to a sudden change in the chemical nature of Ni_7In_3/SBA-15 during the catalysis test. PXRD studies on the spent Ni_7In_3/SBA-15 catalysts tested at each pressure, were deployed to understand this chemical change and to assess the stability of the catalysts, (**Figure 3.6c**). The studies revealed an interesting phase transformation of the IMC phase from the most unsymmetrical triclinic Ni_7In_3 (S.G: $P\bar{1}$) to most symmetrical cubic Ni_3In (S.G: $Pm\bar{3}m$) (**Figure 3.6c**). The Ni_3In phase progressively evolved from Ni_7In_3 with an increase of pressure of the reaction from ambient pressure to 20 bar at 573 K (**Figure 3.6c**).

Above 20 bar, the phase transformation of Ni_7In_3 to Ni_3In was observed along with a negligible amount of metallic Ni formation. The phase transformation is perfectly aligned with the enhancement in CO_2 conversion and methanol selectivity, which ascertains that the operando generated cubic Ni_3In is the real active phase for CTM.

From a fundamental crystallographic perspective, the structural transition of Ni_7In_3 to Ni_3In is complex, although earlier reports have proposed Ni deficient Ni_7In_3 as the superstructure of Ni_3In based on the neutron diffraction and XRD studies.[48] We speculate that Ni_7In_3 transformed into a perfectly ordered and kinetically stable Ni_3In structure under the high temperature and pressure conditions.

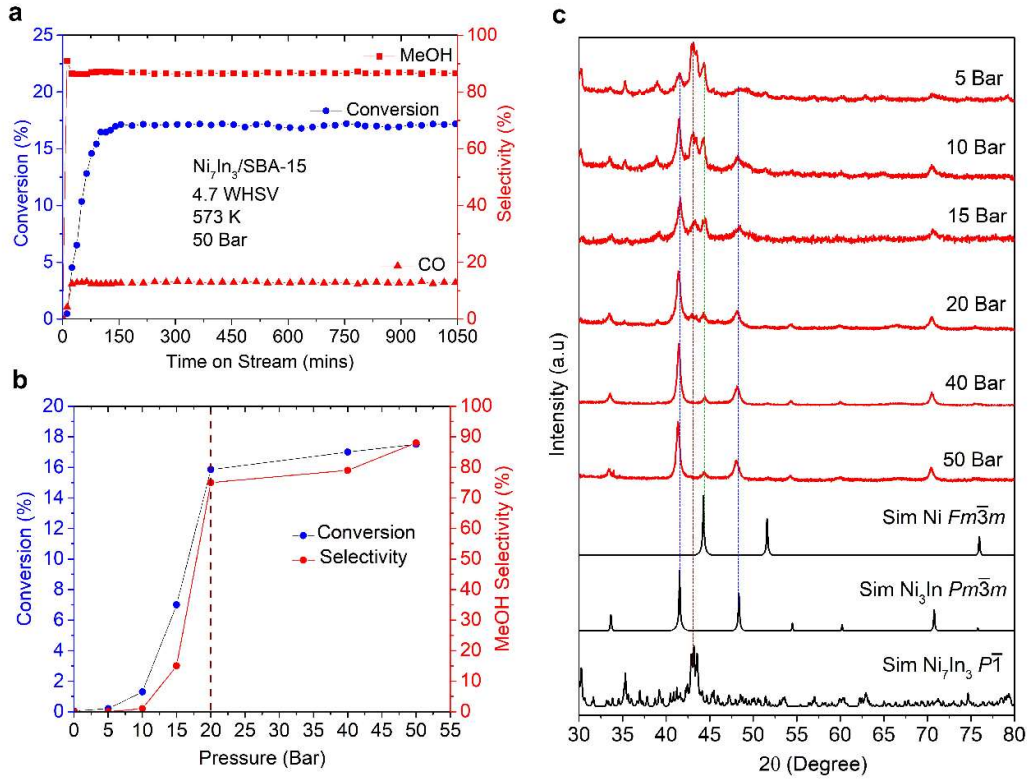

Figure 3.6. Catalytic performance of Ni_7In_3/SBA-15, (a) CO_2 conversion and selectivity for 15 hours of time on stream at reaction condition of 4.7 h^{-1} (1:3), 50 bar and 573 K, (b) CO_2 conversion and methanol selectivity at different pressures (5-50 bar) with 4.7 h^{-1} and 573 K, (c) XRD pattern of spent catalyst after reaction at 5 bar, 10 bar, 15 bar, 20 bar, 40 bar and 50 bar compared with simulated patterns of Ni (S.G:$Fm\bar{3}m$), Ni_3In (S.G:$Pm\bar{3}m$) and Ni_7In_3 (S.G:$P\bar{1}$).

This arises a couple of critical questions about the mechanistic pathway of metastable Ni_3In formation: (a) Is it a direct transformation from Ni_7In_3 to Ni_3In or (b) the pathway entails the decomposition of Ni_7In_3 to the constituent Ni and In metals followed by their diffusion into the ordered Ni_3In phase under the reaction conditions. To confirm this, an alternate synthetic route has been explored. The as synthesized Ni_7In_3/SBA-15 was oxidized by calcining in open atmosphere at 773 K for 5 hours, which resulted in the formation mixed oxide NiO-In_2O_3/SBA-15 (**Figure 3.7a**). CO_2 hydrogenation on NiO-In_2O_3/SBA-15 has been performed at 20 B and 50 B (4.7 h^{-1} and 573 K) by avoiding the catalyst activation process to eliminate the formation of IMC. Although the conversion of CO_2 reduces by 7% compared to Ni_7In_3/SBA-15, the methanol selectivity was found to be similar to the reactions run over without oxidizing the catalyst (**Figure 3.7b, 3.7c, Table 3.2 and 3.3**). 15 and NiO-In_2O_3/SBA-15 with the simulated patterns of NiO (S.G: $Fm\bar{3}m$), In_2O_3 (S.G: $Ia\bar{3}$), Ni (S.G: $Fm\bar{3}m$) and Ni_3In (S.G: $Pm\bar{3}m$).

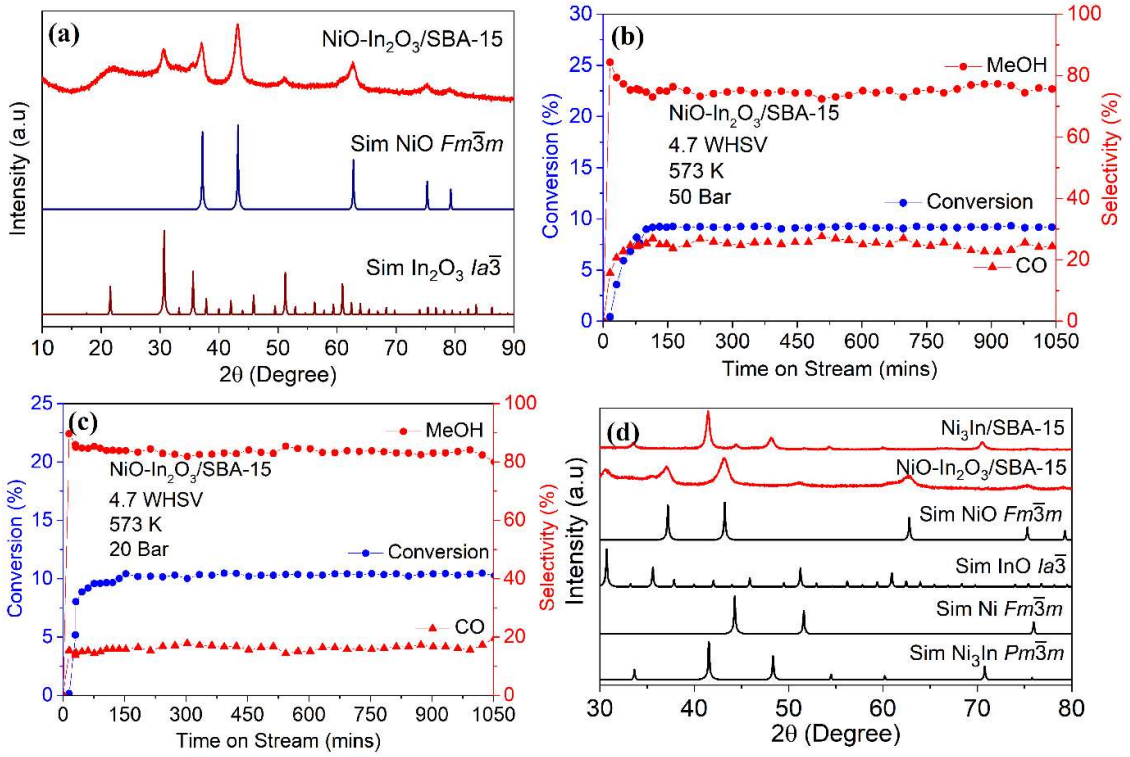

Figure 3.7. Catalytic performance of NiO-In_2O_3/SBA-15 at 573 K, (a) powder XRD pattern of NiO-In_2O_3/SBA-15, simulated NiO ($Fm\bar{3}m$) and simulated In_2O_3 ($Ia\bar{3}$), (b) CO_2 conversion and selectivity for 15 hours of time on stream at reaction condition of 4.7 h^{-1} (1:3) and 50 bar, (c) CO_2 conversion and selectivity for 15 hours of time on stream at reaction condition of 4.7 h^{-1} (1:3) and 20 bar, and (d) comparison of the powder XRD patterns of experimental Ni_3In/SBA-15.

The O-vacancies of In_2O_3 has been shown to favour CTM conversion,[49-51] and also recent reports discuss the enhancement of In_2O_3 O-vacancies by metals (Ni)[52] and bimetallic systems (In-Pd and In-Ni)[53] dispersed on them improving their CTM activity. Thus, one can possibly attribute the activity of the catalyst due to the presence of In_2O_3. But interestingly, the PXRD of the NiO-In_2O_3/SBA-15 spent catalyst also confirmed the formation of Ni_3In (S.G: $Pm\bar{3}m$) with minor peaks of elemental Ni (S.G: $Fm\bar{3}m$) (**Figure 3.7d**). This confirms that the CTM activity derives from the Ni_3In phase and not due to the enhancement of O-vacancies on In_2O_3 by Ni metal. We conclude that NiO-In_2O_3 heterostructure reduces to the corresponding Ni and In metals, under the stream of hydrogen at high temperature and pressure followed by their diffusion to form the Ni_3In phase. The mechanistic pathways for the transformation of the phases can be schematically represented as shown in **Figure 3.8**.

Furthermore, the spent catalyst after maximum applied pressure (50 bar) reaction (now onwards denoted as Ni_3In) when re-tested at various pressures (0-20 bar), exhibited CO_2 conversion and MeOH selectivity similar to that of the first cycle (**Figure 3.9**). This proves that the metastable (or kinetic) phase of Ni_3In formed in the operando condition is catalytically stable with good CO_2 conversion and excellent MeOH selectivity at lower pressures. The lowering of pressure in industrial catalysis can save fuel in the form of electricity, which is one of the major costs in a large-scale chemical process.

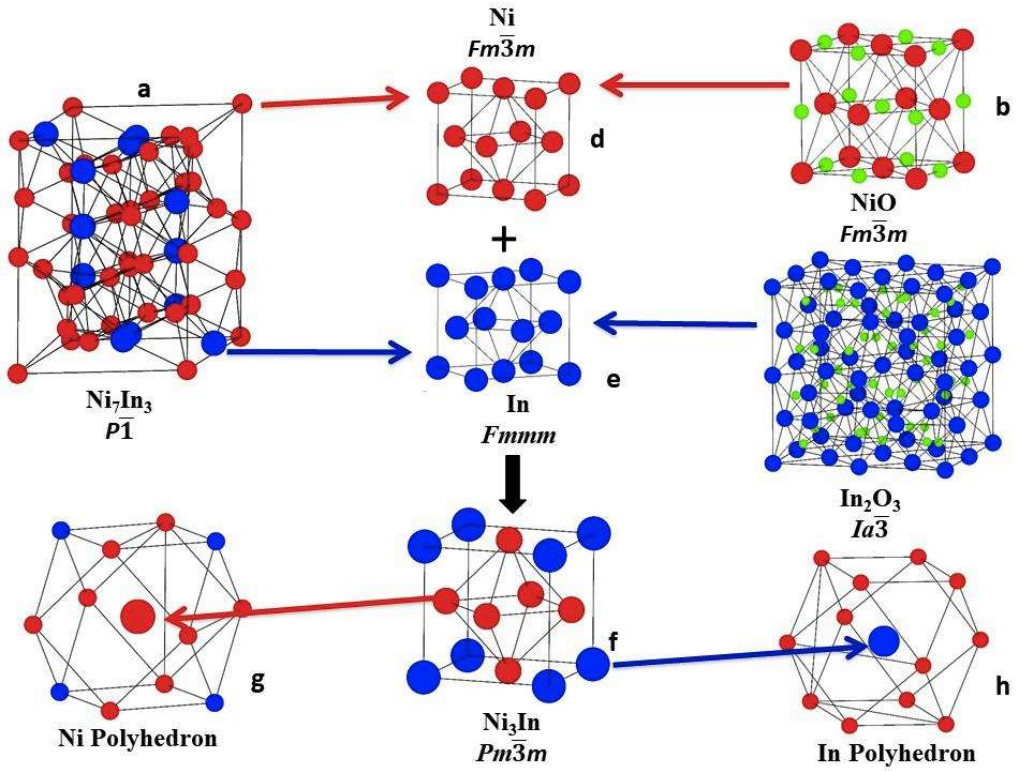

Figure 3.8. Operando structural phases transformation of different starting materials Ni7In3/SBA-15 (a) and NiO-In_2O_3/SBA-15 (b and c) to Ni_3In/SBA-15 (f) through the intermediates Ni (d) and In (e) metals under 573 K and above 20 bar pressure. The coordination environment of Ni (g) and In (f) in Ni_3In structure.

3.3.3. X-ray photoelectron spectroscopy and XAS

For better understanding of surface oxidation state, electronic interactions and bonding nature, XPS was performed on as synthesized Ni_7In_3/SBA-15 and operando generated Ni_3In/SBA-15 catalysts. The Ni^0 $2p_{3/2}$ peak identified at 851.6 and 852.1 eV for Ni_7In_3/SBA-15 and Ni_3In/SBA-15, respectively, (**Figure 3.10a** and **3.10b)** are in close agreement with the literature accepted value of 852.6 eV for metallic Ni.[54]

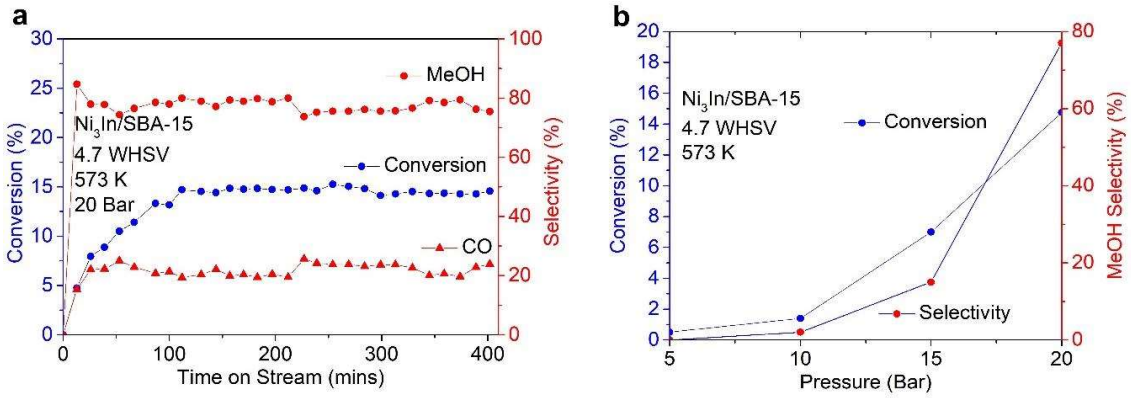

Figure 3.9. Catalytic performance of Ni_3In/SBA-15, (a) CO_2 conversion and selectivity for 6 hours of time on stream at reaction condition of 4.7 h^{-1} (1:3) and 20 bar, (b) CO_2 conversion and methanol selectivity at different pressures (5-20 bar) with 4.7 h^{-1} and 573 K.

The slight shift towards lower binding energy can be attributed to the difference in bonding due to the formation of IMC. This also signifies partial electron transfer from In to Ni which confirms the formation of relatively electron rich Ni sites upon IM formation.[54] Additionally, the broad peaks at 855.7 eV 861.3 eV and 873.56 eV identified as Ni^{+2} $2p_{3/2}$, Ni^{2+} $2p_{3/2}$ (satellite) and Ni^{+2} $2p_{1/2}$, respectively, can be assigned to Ni-O due to surface oxidation. The peak area ratio of Ni^{+2} $2p_{3/2}$ to Ni^{0} $2p_{3/2}$ of as synthesized Ni_7In_3/SBA-15 is two times higher than that of Ni_3In/SBA-15 (**Table 3.4**). The as synthesized catalyst having more surface oxidation gets reduced during catalyst activation and then by hydrogen stream in operando condition. This is well supported by the O 1s XPS spectra of Ni_7In_3/SBA-15 and Ni_3In/SBA-15 (**Figure 3.10c** and **3.10d**). The peaks at 531.34 eV and 528.6 eV correspond to surface hydroxyl and lattice O^{2-} of NiO respectively.[55] The peak at 528.6 eV gets reduced significantly in Ni_3In/SBA-15 as compared to Ni_7In_3/SBA-15 indicating the reduction in surface NiO in operando condition.

Table 3.4. Summary of Ni 2p XPS spectrum of Ni_7In_3/SBA-15 and Ni_3In/SBA-15

Chemical State	Ni_7In_3/SBA-15		Ni_3In/SBA-15	
	Binding Energy (eV)	Peak Area	Binding Energy (eV)	Peak area
Ni^{2+} $2p_{3/2}$	855.69	23566	856.462	10000
Ni^{2+} $2p_{1/2}$	873.055	6554	874.379	5932.2
Ni^{0} $2p_{3/2}$	851.627	5764.3	852.11	4734.8
Ni^{0} $2p_{1/2}$	869.318	2566.8	870.493	3483.2

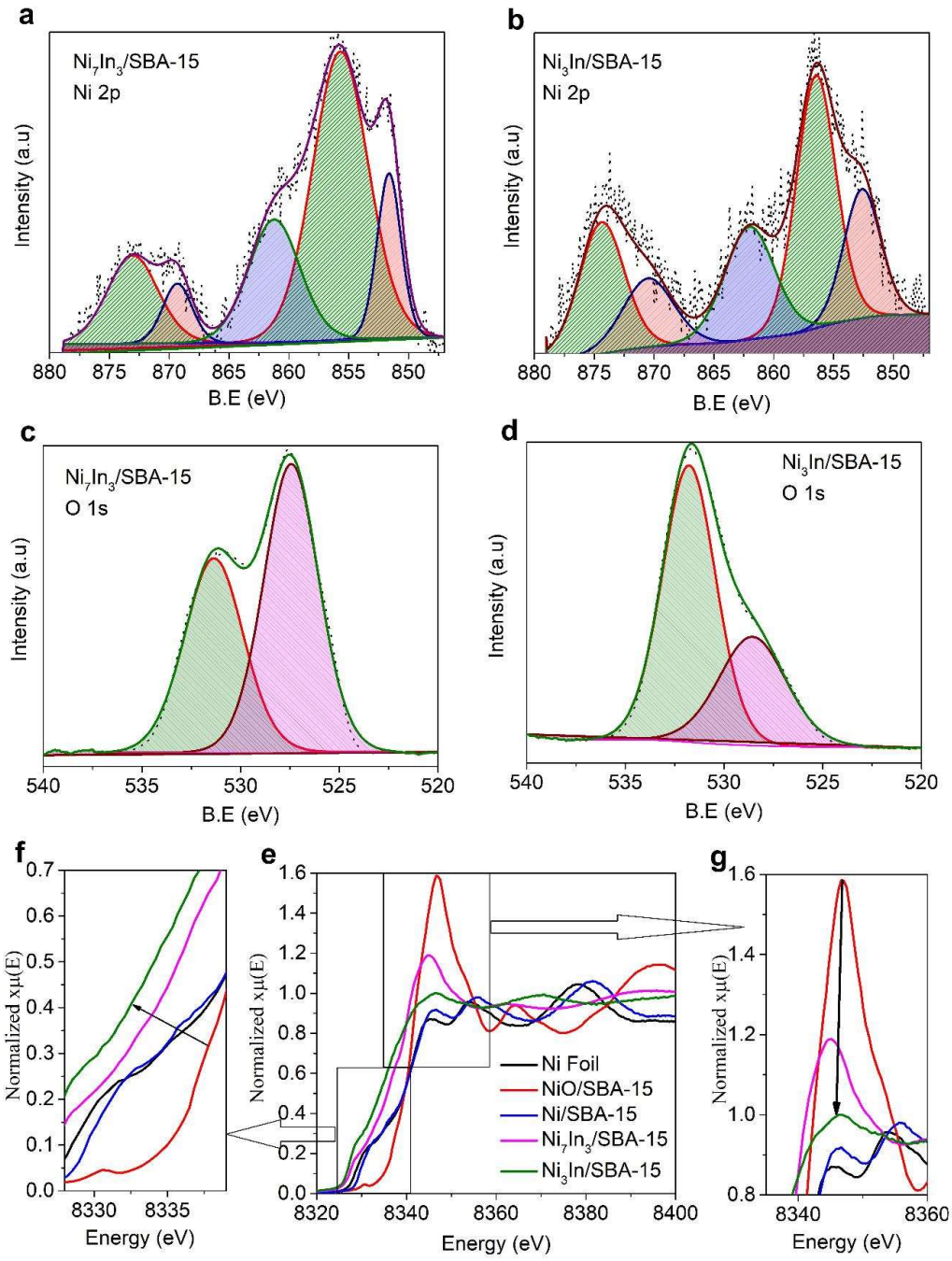

Figure 3.10. (a) Ni $2p_{3/2}$ XPS spectrum Ni_7In_3/SBA-15, (b) Ni $2p_{3/2}$ XPS spectrum of Ni_3In/SBA-15, (c) O 1s XPS spectrum of Ni_7In_3/SBA-15, (d) O 1s XPS spectrum of Ni_3In/SBA-15, (e) XAS spectra of Ni K-edge of Ni/SBA-15, Ni_7In_3/SBA-15 and Ni_3In/SBA-15, (f) enlarged absorption edge region of Ni K-edge of XANES spectra and (g) enlarged view of the white line intensity region in XANES spectra.

Further to elucidate the change in the intrinsic catalytic property of Ni upon the formation of Ni_7In_3 followed by the transformation to highly active CTM catalyst Ni_3In,

Ni/SBA-15, Ni_7In_3/SBA-15, Ni_3In/SBA-15 and NiO/SBA-15 were analyzed by XANES. The normalized Ni K edge spectra of the aforementioned species are shown in **Figure 3.10e.** The Ni K absorption edge of Ni_7In_3/SBA-15 and Ni_3In/SBA-15 lowered by 2 eV and 3.5 eV, respectively, compared to Ni/SBA-15 (**Figure 3.10f**) proving the charge transfer from In to Ni upon IM formation which is more prominent in Ni_3In. The white line intensity, which is a characteristic indicator of charge transfer[11] also drops upon the transformation of Ni_7In_3 to Ni_3In (**Figure 3.10g**).

3.3.4. Operando DRIFTS measurements and difference in reactivity of intermediates

Previous reports reveals that CO_2 methanation over Ni can proceed via the CO or formate ($HCOO^-$) pathway followed by subsequent reduction by spilled over H_2.[32, 45, 47, 56, 57] Contrarily, in case of CTM, instead of direct hydrogenation to methane, the adsorbed formates follows multiple intermediate steps to methanol. The reaction starts with hydrogenation of formates to acetal (H_2COO*), then further to methoxy (H_3CO*) and eventually desorption of methanol happens. To understand the mechanism in depth, experimental and theoretical studies were employed to understand the difference in the CO_2 reduction mechanistic pathways between Ni/SBA-15 and Ni_3In/SBA-15. Operando Diffuse Reflectance Infrared Fourier Transform Spectroscopy (DRIFTS) has been used to map the intermediates formed during the CO_2 reduction process. The operando DRIFTS on all the catalysts were conducted at ambient pressure in a stream of 1:3 CO_2 to H_2 ratio.

Three key intermediates identified when Ni_3In/SBA-15 was used as the CTM catalyst: free CO_{str} (2178 and 2111 cm^{-1}), Ni-CO_{str} (linear) at 2028 cm^{-1}, Ni_3-CO_{str} (bridged) at 1930 cm^{-1} and conjugated C-O/C=O_{str} of formate at 1588 cm^{-1} (**Figure 3.11**).[58, 59] All the above mentioned peaks started appearing around 9 mins (~450 K) of temperature ramp (15 k min^{-1} from 303 K), which corresponds to the starting temperature for CO_2 hydrogenation. The peaks intensify and saturates within an hour of reaction at 573 K (**Figure 3.11a** and **3.11b**). In contrast, over Ni/SBA-15, bands corresponding to formate, bridge Ni-CO and linear Ni-CO originates at the onset temperature. On further increase of temperature, the linear Ni-CO_{str} (2030 cm^{-1}) band subsidizes to noise (after 12 mins of ramp along with a slight intensification of bands at 2178 and 2111 cm^{-1} (free CO) (**Figure 3.11d**). Furthermore, during one hour on stream there is no enhancement of the peak intensity at 2030 cm^{-1}, instead other peaks gets intensified and saturated. A new band corresponding to C-H_{str} of methane, starts to appear at 3015 cm^{-1} after 15 minutes of ramp and gets intensified further upon time on stream (**Figure 3.11e** and **3.11f**).[47]

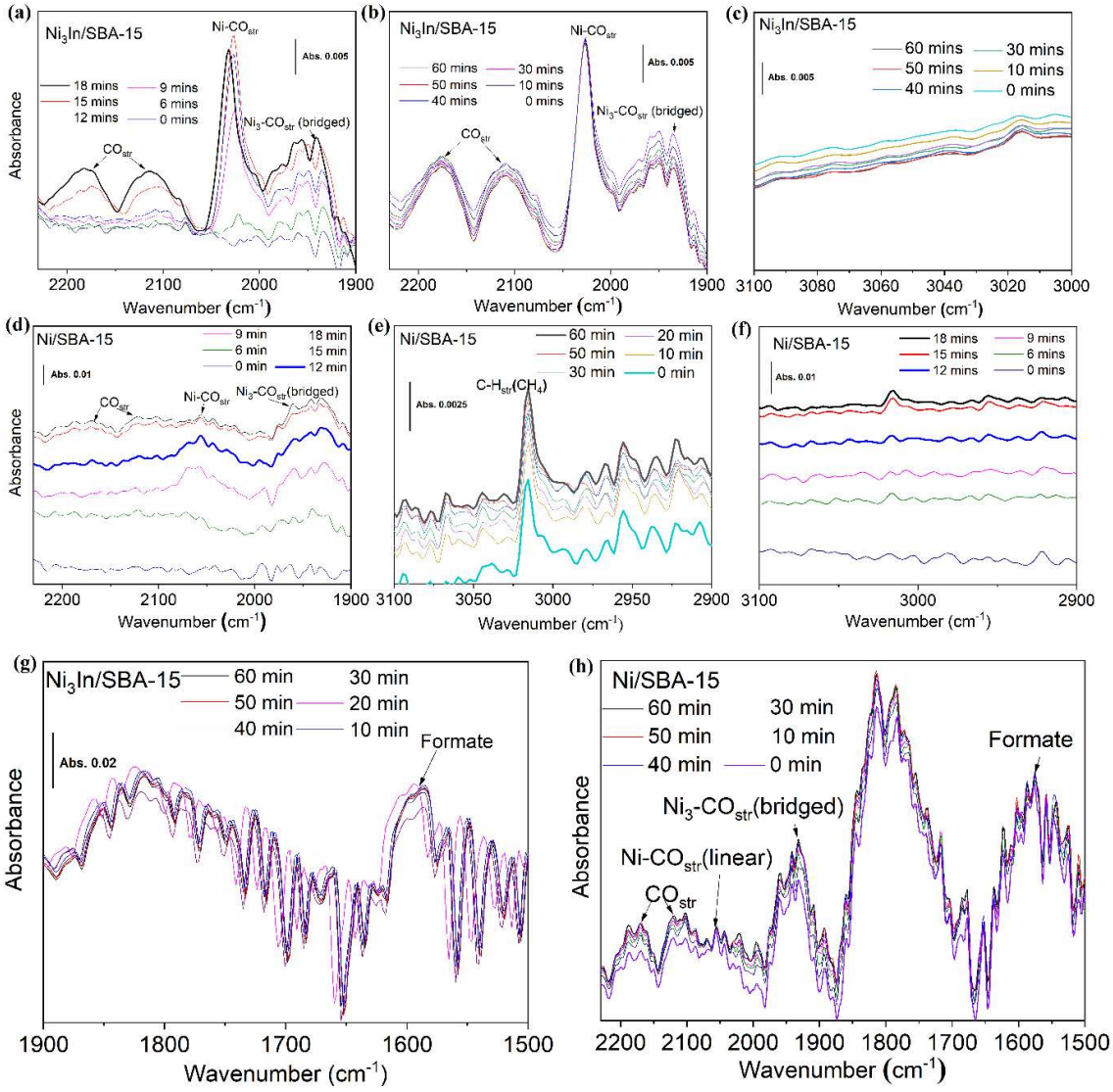

Figure 3.11. Operando DRIFTS measurements; (a) Successive spectra of CO stretching regions over Ni_3In/SBA-15 plotted with time of temperature ramp from 303 K to 573 K, (b) successive spectra of CO stretching regions over Ni_3In/SBA-15 for an hour on stream, (c) successive DRIFTS spectra of CH_{str} stretching regions over Ni_3In/SBA-15 for an hour on stream, (d) successive spectra of CO stretching regions over Ni/SBA-15 plotted with time of temperature ramp from 303 K to 573 K, (e) successive spectra of CH stretching regions over Ni/SBA-15 for an hour on stream, (f) successive spectra of CH stretching regions over Ni/SBA-15 plotted with time of temperature ramp from 303K to 573 K, (g) successive DRIFTS spectra of formate and CO stretching regions over Ni_3In/SBA-15 plotted against time over Ni_3In/SBA-15, and (h) successive DRIFTS spectra of formate and CO stretching regions over Ni/SBA-15 for an hour on stream.

The appearance of bands corresponding to C-H_{str}, free CO_{str} and subsidized Ni-CO_{str} bands confirms that linear Ni bound CO gets reduced to methane at temperature above 500 K or the Ni-CO bond gets dissociated to free CO_{str}. The absence of C-H_{str} characteristic peak proves that Ni_3In/SBA-15 doesn't favor methane formation **(Figure 3.11c)**. As compared to the pure metal, the reduction ability of Ni has been reduced by the formation of IMC. This was evident as the linear Ni bound CO were not further reduced by Ni_3In, eventually no methane formation as well. The decrease of Ni reducibility in Ni_3In may be due to modification of hydrogen spilling power of Ni, which got optimized to perform $6e^-$ reduction upon the IMC formation.

3.3.5. First Principle Calculations

To shed further light on the mechanism of CTM conversion on Ni_3In, we performed first-principles calculations. Eight CO_2 hydrogenation pathways (HCOO, CO hydrogenation, *trans*-COOH and *cis*-COOH) were analysed by determining their reaction energies to pinpoint the most feasible pathway for CTM conversion on Ni_3In. We use a supercell (2×2) to model the (111) surface of Ni_3In ($Ni_{48}In_{16}$) introducing a vacuum layer of 15 Å thickness parallel to the slab separating its adjacent periodic images. To this end, we modelled 2×2 in-plane supercell of its (111) surface ($Ni_{48}In_{16}$). Each supercell contains a slab of 4 atomic planes of which, the bottom 2 atomic planes were kept fixed and the top 2 were allowed to relax. We sampled Brillouin-zone integrations on uniform grid of 6×6×1 k-points in the Brillouin zone of (111) surface of Ni_3In. The projected density of states of each structure was obtained from calculations on a denser, 15x15x1, k-point mesh. Calculated lattice constants of bulk Ni_3In ($a_{Ni_3In} = 3.74$ Å) are within the typical GGA errors with respect to their observed values ($a_{Ni_3In} = 3.73$ Å). Relative energies of the intermediate steps were plotted taking pristine Ni_3In (111) surface + CO_2 + $3H_2$ as the reference. We simulated adsorption of various intermediates occurring during the CO_2 reduction reaction (CO_2RR) and calculated their adsorption energies (see **Figure 3.12 and eqn. 3.10**)

$$\Delta E_{ads} = E_{adsorbate+Ni_3In} - \left(E_{Ni_3In} + E_{adsorbate}\right) \quad (3.10)$$

where, $E_{adsorbate+Ni_3In}$, E_{Ni_3In} and $E_{adsorbate}$ are the energies of adsorbate locally stabilized on Ni_3In (111) surface, bare Ni_3In (111) surface and the adsorbate molecule, respectively. The transition states (TSs) were obtained using the nudged elastic band (NEB)[60] method. Five images were used in all the NEB calculations in this paper. All transition states

were fully relaxed until the Hellmann–Feynman forces acting on the atoms were within 0.05 eV Å.

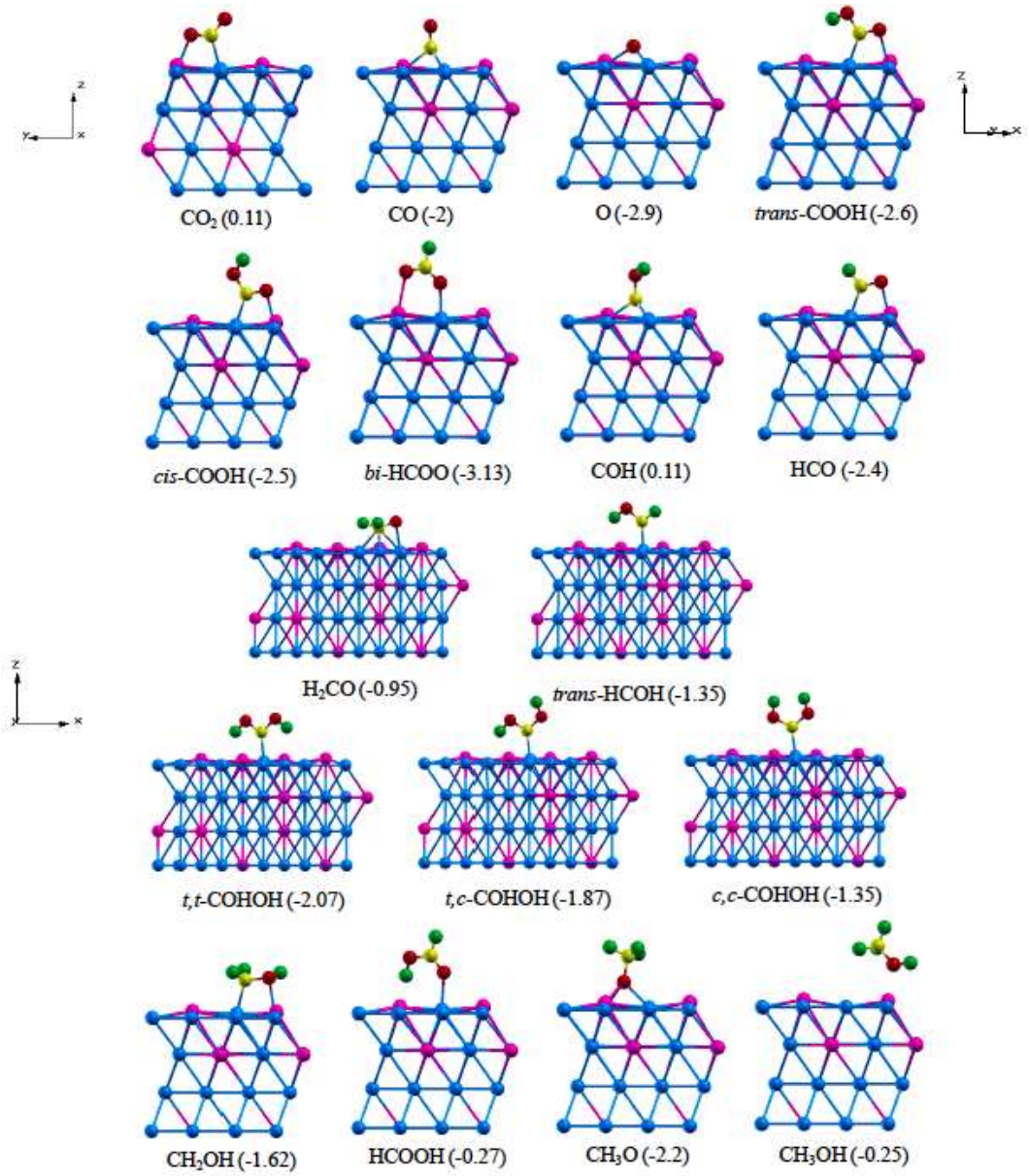

Figure 3.12. Optimized structures and binding energies of various intermediates occurring via various CO_2 hydrogen pathways on Ni_3In (111) surface. Magenta, blue, red, green and yellow spheres correspond to In, Ni, O, H and C atoms respectively. Binding energies are in eV.

All intermediates occurring on various CO_2 reduction pathways, with the exceptions of CH_3O and *bi*-HCOO, stabilize in configurations of adsorption at the surface Ni sites indicating Ni atoms to be the active centers of (111) surface of Ni_3In. Energy landscape plots show that the initial and final steps, i.e., adsorption of CO_2 and desorption of CH_3OH, are both

non-spontaneous and exhibit an energy cost of ~0.11 eV and ~0.25 eV respectively (**Figure 3.13**). Thermodynamically most feasible CO_2 reduction pathway has the lowest energy barrier associated with the potential determining step (PDS). In the context of a thermocatalytic reaction, PDS gives a measure of thermodynamic energy barrier. As is evident in **Figure 3.13**, the CO hydrogenation pathway is energetically most expensive and formation of *CO molecule from adsorbed $*CO_2$ species is the PDS (ΔE = 0.9 eV). For *trans*-COOH pathway, hydrogenation of *COH to form **trans*-HCOH is the PDS with an energy barrier of 0.82 eV. Both, *cis*-COOH and formate pathways exhibit similar energy barriers of 0.25 eV wherein, the final step, i.e., desorption of CH_3OH is the potential determining step.

To conclusively determine the most feasible pathway, we estimated the energy of second elementary step in *cis*-COOH and formate pathways, i.e.,

$$*CO_2 + 3H_2 \rightarrow *bi\text{-}HCOO + H + 2H_2 \quad (3.11)$$

$$*CO_2 + 3H_2 \rightarrow *trans\text{-}COOH + H + 2H_2 \quad (3.12)$$

Formation of *bi*-HCOO from CO_2 adsorbed on (111) surface of Ni_3In is quite spontaneous (ΔE = −0.53 eV) **(eqn. 3.11)** and more exothermic than that of its competing intermediate, *trans*-COOH, occurring in the *cis*-COOH pathway (ΔE = −0.32 eV). Also, both intermediates show a bi-dentate attachment to the (111) surface however, the chemical bonds formed by the adsorbates with Ni_3In are distinct **(eqn. 3.12)**: Ni-O and In-O in case of *bi*-HCOO; Ni-C and Ni-O bonds in the case of *trans*-COOH. The fact that indium doesn't bind with *trans*-COOH, suggests that Ni_3In will prefer *bi*-HCOO.

To shed light on the nature of bonding between intermediates and the catalyst, we examine the projected density of states (PDOS) of the first intermediates occurring along the formate and *cis*-COOH pathways of CO_2 reduction on the (111) surface of Ni_3In: *bi*-HCOO*Ni_3In and *trans*-COOH*Ni_3In, respectively. The PDOS of *bi*-HCOO*Ni_3In and *trans*-COOH*Ni_3In reveal the highest occupied molecular orbitals (HOMO) of the adsorbates lie close to the bottom of the 3d-bands of Ni. HOMO of **bi*-HCOO exhibits a sharp peak close to −3.5 eV, (similar to HOMO of $*CO_2$) accompanied by another smaller peak at a slightly higher energy. The degeneracy in the HOMO peaks is because of charge transfer from the surface to the adsorbate (see **Figure 3.14**), which is also evident from the Löwdin charges that show a reduction the occupancy of Ni-3d and In-5s orbitals and an increased occupancy of O-2p orbitals of both the O-atoms of HCOO (**Table 3.5**).

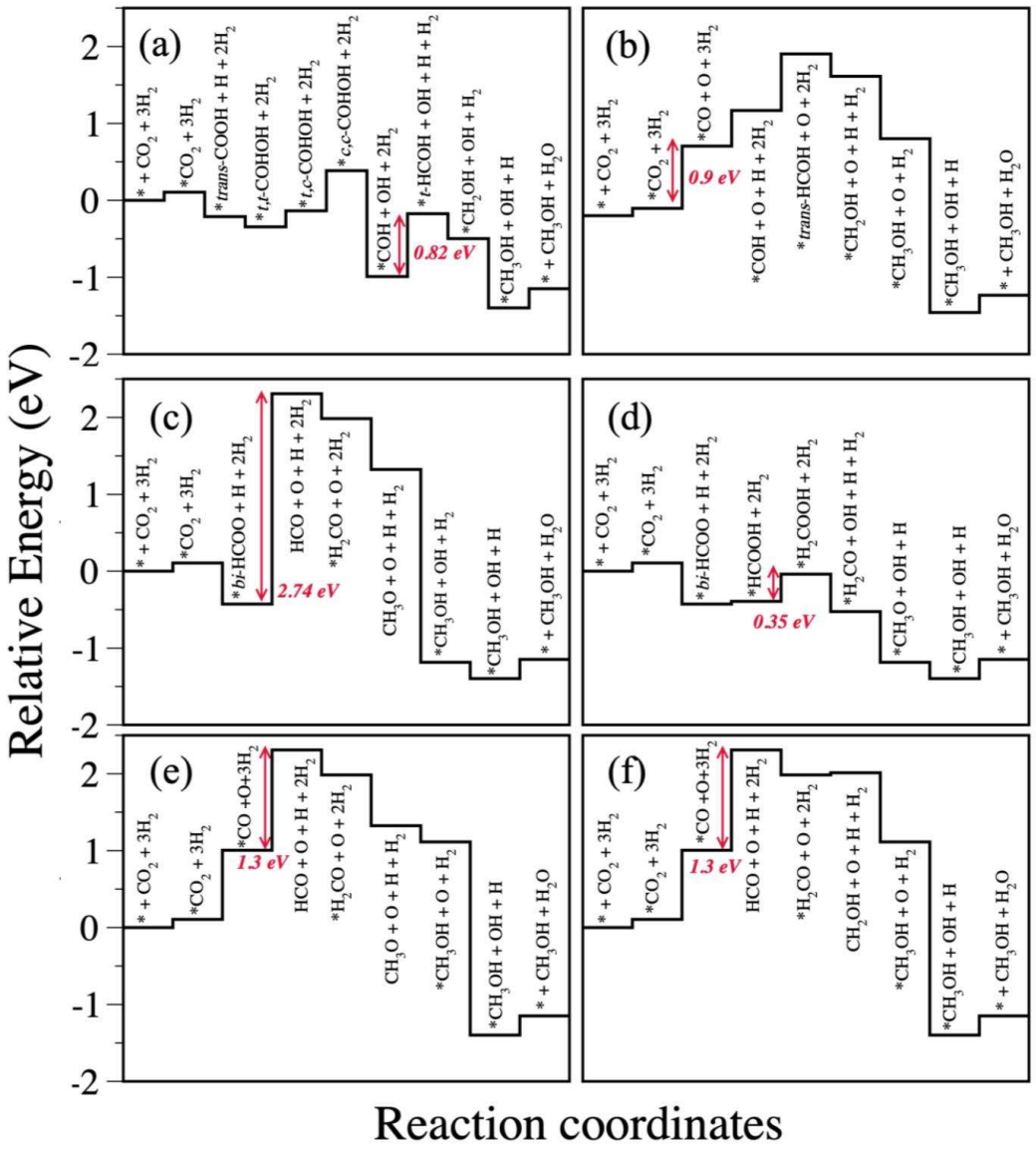

Figure 13. Relative energy diagrams of CO_2 to methanol conversion on Ni_3In occurring via (a) *trans*-COOH, (b) CO-hydrogenation, (c) HCOO (2), (d) HCOO (3), (e) CO-hydrogenation (2) and (f) CO-hydrogenation (3) pathway. Red double headed arrows represent the energetically most expensive elementary step along each pathway. All values are in eV.

Also, HOMO of *bi*-HCOO splits and broadens because of its covalent interaction with the In-5p and Ni-4p orbitals of the catalyst, which are in resonance. HOMO of **trans*-COOH lies deeper in energy and resonates with Ni-3d, Ni-4p and In-5p orbitals of the surface. Löwdin charge analysis shows a charge transfer from the Ni_3In surface to the adsorbate. We find a decrease in the number of electrons in Ni-3d states due to transfer to C-2s and C-2p orbitals (**Table 3.5**). To comment on the kinetics of the CTM conversion on the present catalyst, we determined the activation energy barriers for each elementary steps along the *cis*-COOH and

bi-HCOO pathways using nudged elastic band (NEB) method. These pathways are very similar and differ only in the initial intermediates. From this analysis, we find the following step to be the rate-determining step with activation energy barrier of 1.2 eV (**Figure 3.15**).

$$*HCO + OH + 2H_2 \rightarrow *H_2CO + OH + H + H_2 \quad (3.13)$$

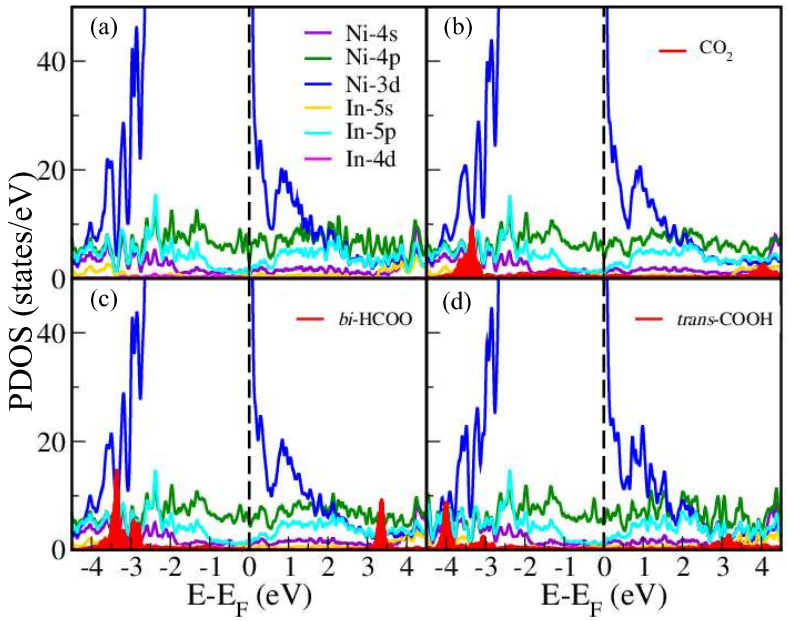

Figure 3.14. PDOS of (a) pristine Ni_3In (111) surface and (b) CO_2, (c) *bi*-HCOO and (d) *trans*-COOH adsorbed on Ni_3In (111) surface. Dashed black line represents the Fermi energy.

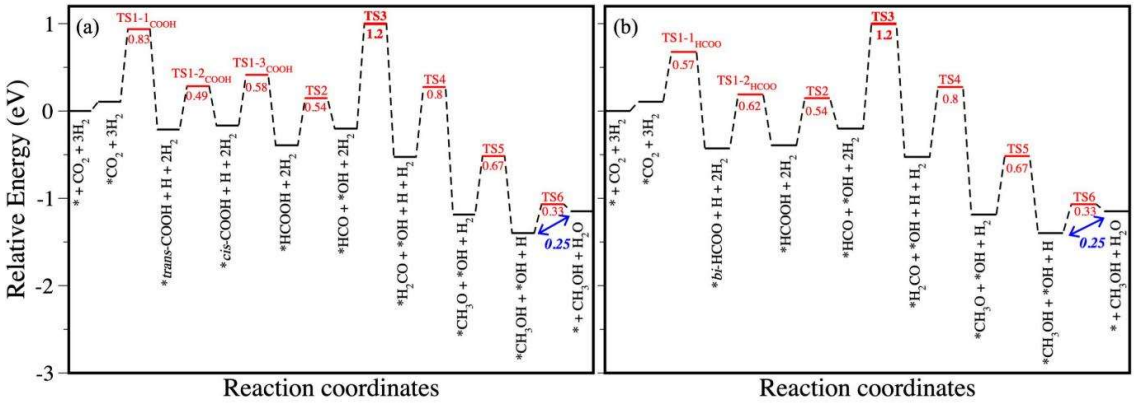

Figure 3.15. Relative activation energy diagrams of CO_2 to methanol conversion on Ni_3In occurring via **(a)** *cis*-COOH, and **(b)** *bi*-HCOO pathway. Black and red bars denote the intermediates and transition states along the CO_2 hydrogenation pathways. TS3 (transition state 3) is the kinetic bottleneck along both pathways, while the desorption of CH_3OH is the thermodynamically most energy demanding step (denoted by blue double headed arrows). All values are in eV.

Table 3.5. Calculated Löwdin charges of Ni, In, C and O atoms for (a) pristine (111) surface of Ni_3In, (b) isolated CO_2 molecule, and (c) CO_2, (d) *bi*-HCOO and (e) *trans*-COOH adsorbed on the (111) surface of Ni_3In, respectively.

Sample	Atom	Number of Valence electrons			Total number of valence electrons	Valence configuration in pseudopotential
		s	p	d		
(a) Ni_3In	Ni	0.42	0.99	8.8	10.21	$4s^2\,3d^8$ (10)
	In	0.8	1.46	9.94	12.2	$5s^2\,4d^{10}\,5p^1$ (13)
(b) CO_2 isolated	C	0.74	2.46	0	3.2	$2s^2\,2p^2$ (4)
	O	1.66	4.61	0	6.27	$2s^2\,2p^4$ (6)
(c) Ni_3In (CO_2 adsorbed)	Ni_C	0.42	**1.09**	**8.76**	10.27	$4s^2\,3d^8$ (10)
	Ni_O	0.4	1.03	**8.72**	10.15	$4s^2\,3d^8$ (10)
	C	**0.88**	2.61	0	3.49	$2s^2\,2p^2$ (4)
	O	1.63	4.64	0	6.27	$2s^2\,2p^4$ (6)
	In	0.79	1.44	9.94	12.17	$5s^2\,4d^{10}\,5p^1$ (13)
(d) Ni_3In (*bi*-HCOO adsorbed)	Ni_{O1}	0.4	1.06	**8.72**	10.18	$4s^2\,3d^8$ (10)
	In_{O2}	**0.73**	1.43	9.95	12.11	$5s^2\,4d^{10}\,5p^1$ (13)
	O1	1.66	**4.73**	0	6.39	$2s^2\,2p^4$ (6)
	O2	1.61	**4.71**	0	6.32	$2s^2\,2p^4$ (6)
(e) Ni_3In (*trans*-COOH adsorbed)	Ni_C	0.4	**1.19**	**8.72**	10.34	$4s^2\,3d^8$ (10)
	Ni_O	0.39	1.02	**8.74**	10.15	$4s^2\,3d^8$ (10)
	C	**0.97**	**2.6**	0	3.57	$2s^2\,2p^2$ (4)
	O	1.63	4.63	0	6.26	$2s^2\,2p^4$ (6)
	In	0.79	1.44	9.95	12.17	$5s^2\,4d^{10}\,5p^1$ (13)

However, the formation of the first intermediate i.e., trans-COOH and *bi*-HCOO along the carboxylic acid and formate pathways respectively, have different activation energy barriers associated with them. Formation of *bi*-HCOO from adsorbed CO_2 has an activation energy of 0.57 eV while the *trans*-COOH intermediate requires crossing of energy barrier of 0.83 eV to form. Hence, the activation energy barrier and the thermodynamic reaction energies of the second elementary step in carboxylic acid and formate pathways conclusively show the latter to be more feasible. Therefore, CTM conversion on Ni_3In is most feasible via the formate pathway because of its low energy barrier and thermodynamically spontaneous hydrogenation of CO_2 to yield *bi*-HCOO. These results are concurrent with the in-situ DRIFT studies and

firmly confirm the formate pathway for selective methanol production over the operando generated Ni_3In phase. Based on both experimental and theoretical studies the mechanism on Ni and Ni_3In can be schematically represented in **Figure 3.16**.

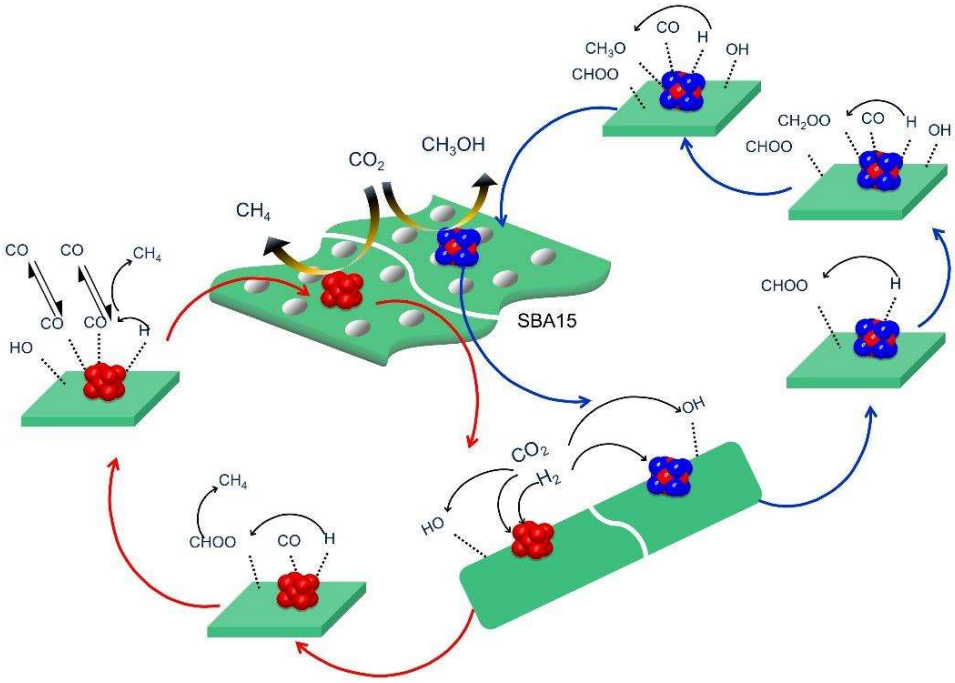

Figure 3.16. Schematic mechanism for the CO_2 to methane formation over Ni/SBA-15 and CO_2 to methanol formation over Ni_3In/SBA-15 catalysts.

3.4. Conclusion

In conclusion, we demonstrate the concept of operando catalyst generation by identifying the metastable kinetic Ni_3In phase as a new efficient and stable catalyst for CTM conversion. The in-situ transformation of the thermodynamically stable Ni_7In_3 phase highlights the importance of identifying and exploring the true active phases of catalysts when subjected to drastic thermochemical conditions. The catalytic selectivity of cheap Ni catalyst was completely modulated towards the formate mediated methanol pathway by ordered alloying with In, as evinced by in-situ DRIFTS and computational studies. This mechanistic tunability can be attributed to the ordered arrangement of Ni and In atoms and strong difference in their electronegativity, leading to interatomic charge transfer. More importantly, the catalyst's conversion efficiency can be optimized at much lower pressures, which have huge energy saving implications for the overall process. This works attempts at advancing the state-of-the-art in CTM catalysis and demonstrate a new avenue for targeting metastable active phases as efficient catalysts for CO_2 reduction.

3.5. References

1. Goeppert, A.; Czaun, M.; Jones, J.-P.; Prakash, G. S.; Olah, G. A., Recycling of Carbon dioxide to Methanol and Derived Products–Closing the Loop. *J. Chem. Soc. Rev.* **2014,** *43* (23), 7995-8048.
2. Artz, J.; Müller, T. E.; Thenert, K.; Kleinekorte, J.; Meys, R.; Sternberg, A.; Bardow, A.; Leitner, W., Sustainable Conversion of Carbon Dioxide: An Integrated Review of Catalysis and Life Cycle Assessment. *Chem. Rev.* **2018,** *118* (2), 434-504.
3. Zhong, J.; Yang, X.; Wu, Z.; Liang, B.; Huang, Y.; Zhang, T., State of the art and Perspectives in Heterogeneous Catalysis of CO_2 Hydrogenation to Methanol. *Chem. Soc. Rev.* **2020,** *49* (5), 1385-1413.
4. González-Garay, A.; Frei, M. S.; Al-Qahtani, A.; Mondelli, C.; Guillén-Gosálbez, G.; Pérez-Ramírez, J., Plant-to-Planet Analysis of CO_2-based Methanol Processes. *Energy Environ. Sci.* **2019,** *12* (12), 3425-3436.
5. Kondratenko, E. V.; Mul, G.; Baltrusaitis, J.; Larrazábal, G. O.; Pérez-Ramírez, J., Status and Perspectives of CO_2 Conversion into Fuels and Chemicals by Catalytic, Photocatalytic and Electrocatalytic Processes. *Energy Environ. Sci.* **2013,** *6* (11), 3112-3135.
6. Centi, G.; Quadrelli, E. A.; Perathoner, S., Catalysis for CO_2 Conversion: A key Technology for Rapid Introduction of Renewable Energy in the Value Chain of Chemical Industries. *J. Energy Environ. Sci.* **2013,** *6* (6), 1711-1731.
7. Fujimoto, K.; Yu, Y., Spillover Effect on the Stabilization of Cu-Zn Catalyst for CO_2 Hydrogenation to Methanol. In *Stud. Surf. Sci. Catal.*, lnui, T.; Fujimoto, K.; Uchijima, T.; Masai, M., Eds. Elsevier: 1993; Vol. 77, pp 393-396.
8. Lunkenbein, T.; Girgsdies, F.; Kandemir, T.; Thomas, N.; Behrens, M.; Schlögl, R.; Frei, E., Bridging the Time Gap: A Copper/Zinc Oxide/Aluminum Oxide Catalyst for Methanol Synthesis Studied under Industrially Relevant Conditions and Time Scales. *Angew. Chem. Int. Ed.* **2016,** *55* (41), 12708-12712.
9. Behrens, M.; Studt, F.; Kasatkin, I.; Kühl, S.; Hävecker, M.; Abild-Pedersen, F.; Zander, S.; Girgsdies, F.; Kurr, P.; Kniep, B.-L., The Active Site of Methanol Synthesis Over $Cu/ZnO/Al_2O_3$ industrial catalysts. *Science* **2012,** *336* (6083), 893-897.
10. Zhang, X.; Han, S.; Zhu, B.; Zhang, G.; Li, X.; Gao, Y.; Wu, Z.; Yang, B.; Liu, Y.; Baaziz, W.; Ersen, O.; Gu, M.; Miller, J. T.; Liu, W., Reversible loss of Core–shell Structure for Ni–Au Bimetallic Nanoparticles during CO_2 Hydrogenation. *Nat. Catal.* **2020,** *3* (4), 411-417.
11. Tsoukalou, A.; Abdala, P. M.; Stoian, D.; Huang, X.; Willinger, M.-G.; Fedorov, A.; Müller, C. R., Structural Evolution and Dynamics of an In_2O_3 Catalyst for CO_2 Hydrogenation

to Methanol: An Operando XAS-XRD and In Situ TEM Study. *J. Am. Chem. Soc.* **2019,** *141* (34), 13497-13505.

12. van den Berg, R.; Prieto, G.; Korpershoek, G.; van der Wal, L. I.; van Bunningen, A. J.; Lægsgaard-Jørgensen, S.; de Jongh, P. E.; de Jong, K. P., Structure Sensitivity of Cu and CuZn Catalysts relevant to Industrial Methanol Synthesis. *Nat. Commun.* **2016,** *7* (1), 13057.
13. Kuld, S.; Conradsen, C.; Moses, P. G.; Chorkendorff, I.; Sehested, J., Quantification of Zinc Atoms in a Surface Alloy on Copper in an Industrial-type Methanol Synthesis Catalyst. *Angew. Chem. Int. Ed.* **2014,** *126* (23), 6051-6055.
14. Liu, C.; Yang, B.; Tyo, E.; Seifert, S.; DeBartolo, J.; von Issendorff, B.; Zapol, P.; Vajda, S.; Curtiss, L. A., Carbon Dioxide Conversion to Methanol over Size-Selected Cu_4 Clusters at Low Pressures. *J. Am. Chem. Soc.* **2015,** *137* (27), 8676-8679.
15. Qian, C.; Sun, W.; Hung, D. L. H.; Qiu, C.; Makaremi, M.; Hari Kumar, S. G.; Wan, L.; Ghoussoub, M.; Wood, T. E.; Xia, M.; Tountas, A. A.; Li, Y. F.; Wang, L.; Dong, Y.; Gourevich, I.; Singh, C. V.; Ozin, G. A., Catalytic CO_2 Reduction by Palladium-decorated Silicon–Hydride Nanosheets. *Nat. Catal.* **2019,** *2* (1), 46-54.
16. Parastaev, A.; Muravev, V.; Huertas Osta, E.; van Hoof, A. J. F.; Kimpel, T. F.; Kosinov, N.; Hensen, E. J. M., Boosting CO_2 Hydrogenation via Size-dependent Metal–Support Interactions in Cobalt/Ceria-based Catalysts. *Nat. Catal.* **2020,** *3* (6), 526-533.
17. Martin, O.; Martín, A. J.; Mondelli, C.; Mitchell, S.; Segawa, T. F.; Hauert, R.; Drouilly, C.; Curulla-Ferré, D.; Pérez-Ramírez, J., Indium Oxide as a Superior Catalyst for Methanol Synthesis by CO_2 Hydrogenation. *Angew. Chem. Int. Ed.* **2016,** *55* (21), 6261-6265.
18. Prieto, G.; Zečević, J.; Friedrich, H.; De Jong, K. P.; De Jongh, P. E., Towards Stable Catalysts by Controlling Collective Properties of Supported Metal Nanoparticles. *Nat. Mater.* **2013,** *12* (1), 34-39.
19. Kattel, S.; Ramírez, P. J.; Chen, J. G.; Rodriguez, J. A.; Liu, P., Active Sites for CO_2 Hydrogenation to Methanol on Cu/ZnO Catalysts. *Science* **2017,** *355* (6331), 1296-1299.
20. García-Trenco, A.; White, E. R.; Regoutz, A.; Payne, D. J.; Shaffer, M. S. P.; Williams, C. K., Pd_2Ga-Based Colloids as Highly Active Catalysts for the Hydrogenation of CO_2 to Methanol. *ACS Catal.* **2017,** *7* (2), 1186-1196.
21. García-Trenco, A.; Regoutz, A.; White, E. R.; Payne, D. J.; Shaffer, M. S. P.; Williams, C. K., PdIn Intermetallic Nanoparticles for the Hydrogenation of CO_2 to Methanol. *Appl. Catal. B* **2018,** *220*, 9-18.
22. Shi, Z.; Tan, Q.; Tian, C.; Pan, Y.; Sun, X.; Zhang, J.; Wu, D., CO_2 Hydrogenation to Methanol over Cu-In Intermetallic Catalysts: Effect of Reduction Temperature. *J. Catal.* **2019,** *379*, 78-89.

23. Marakatti, V. S.; Peter, S. C., Synthetically Tuned Electronic and Geometrical Properties of Intermetallic Compounds as Effective Heterogeneous Catalysts. *Prog. Solid State Chem.* **2018,** *52*, 1-30.
24. Gamler, J. T. L.; Ashberry, H. M.; Skrabalak, S. E.; Koczkur, K. M., Random Alloyed versus Intermetallic Nanoparticles: A Comparison of Electrocatalytic Performance. *Adv. Mater.* **2018,** *30* (40), 1801563.
25. Iihama, S.; Furukawa, S.; Komatsu, T., Efficient Catalytic System for Chemoselective Hydrogenation of Halonitrobenzene to Haloaniline Using PtZn Intermetallic Compound. *ACS Catal.* **2016,** *6* (2), 742-746.
26. Fiordaliso, E. M.; Sharafutdinov, I.; Carvalho, H. W. P.; Grunwaldt, J.-D.; Hansen, T. W.; Chorkendorff, I.; Wagner, J. B.; Damsgaard, C. D., Intermetallic $GaPd_2$ Nanoparticles on SiO_2 for Low-Pressure CO_2 Hydrogenation to Methanol: Catalytic Performance and In Situ Characterization. *ACS Catal.* **2015,** *5* (10), 5827-5836.
27. Studt, F.; Sharafutdinov, I.; Abild-Pedersen, F.; Elkjær, C. F.; Hummelshøj, J. S.; Dahl, S.; Chorkendorff, I.; Nørskov, J. K., Discovery of a Ni-Ga Catalyst for Carbon Dioxide Reduction to Methanol. *Nat. Chem.* **2014,** *6* (4), 320-324.
28. Osswald, J.; Giedigkeit, R.; Jentoft, R. E.; Armbrüster, M.; Girgsdies, F.; Kovnir, K.; Ressler, T.; Grin, Y.; Schlögl, R., Palladium–Gallium Intermetallic Compounds for the Selective Hydrogenation of Acetylene: Part I: Preparation and structural Investigation under Reaction Conditions. *J. Catal.* **2008,** *258* (1), 210-218.
29. Osswald, J.; Kovnir, K.; Armbrüster, M.; Giedigkeit, R.; Jentoft, R. E.; Wild, U.; Grin, Y.; Schlögl, R., Palladium–Gallium Intermetallic Compounds for the Selective Hydrogenation of Acetylene: Part II: Surface Characterization and Catalytic Performance. *J. Catal.* **2008,** *258* (1), 219-227.
30. Jiao, F.; Frei, H., Nanostructured Cobalt Oxide Clusters in Mesoporous Silica as Efficient Oxygen-evolving Catalysts. *Angew. Chem. Int. Ed.* **2009,** *121* (10), 1873-1876.
31. Xu, C.; Chen, G.; Zhao, Y.; Liu, P.; Duan, X.; Gu, L.; Fu, G.; Yuan, Y.; Zheng, N., Interfacing with Silica boosts the Catalysis of Copper. *Nat. Commun.* **2018,** *9* (1), 3367.
32. Aziz, M. A. A.; Jalil, A. A.; Triwahyono, S.; Mukti, R. R.; Taufiq-Yap, Y. H.; Sazegar, M. R., Highly Active Ni-promoted Mesostructured Silica Nanoparticles for CO_2 Methanation. *Appl. Catal. B* **2014,** *147*, 359-368.
33. Wu, H.; Chang, Y.; Wu, J.; Lin, J.; Lin, I.; Chen, C., Methanation of CO_2 and Reverse Water Gas Shift Reactions on Ni/SiO_2 Catalysts: the Influence of Particle Size on Selectivity and Reaction Pathway. *Catal. Sci. Technol.* **2015,** *5* (8), 4154-4163.
34. Richard, A. R.; Fan, M., Low-Pressure Hydrogenation of CO_2 to CH_3OH Using Ni-In-Al/SiO_2 Catalyst Synthesized via a Phyllosilicate Precursor. *ACS Catal.* **2017,** *7* (9), 5679-5692.

35. Zhao, D.; Huo, Q.; Feng, J.; Chmelka, B. F.; Stucky, G. D., Nonionic Triblock and Star Diblock Copolymer and Oligomeric Surfactant Syntheses of Highly Ordered, Hydrothermally Stable, Mesoporous Silica Structures. *J. Am. Chem. Soc.* **1998,** *120* (24), 6024-6036.

36. Björk, E. M., Synthesizing and Characterizing Mesoporous Silica SBA-15: A Hands-On Laboratory Experiment for Undergraduates Using Various Instrumental Techniques. *J. Chem. Educ.* **2017,** *94* (1), 91-94.

37. Bourikas, K.; Kordulis, C.; Lycourghiotis, A., The Role of the Liquid-Solid Interface in the Preparation of Supported Catalysts. *Catal. Rev.* **2006,** *48* (4), 363-444.

38. Giannozzi, P.; Baroni, S.; Bonini, N.; Calandra, M.; Car, R.; Cavazzoni, C.; Ceresoli, D.; Chiarotti, G. L.; Cococcioni, M.; Dabo, I.; Dal Corso, A.; de Gironcoli, S.; Fabris, S.; Fratesi, G.; Gebauer, R.; Gerstmann, U.; Gougoussis, C.; Kokalj, A.; Lazzeri, M.; Martin-Samos, L.; Marzari, N.; Mauri, F.; Mazzarello, R.; Paolini, S.; Pasquarello, A.; Paulatto, L.; Sbraccia, C.; Scandolo, S.; Sclauzero, G.; Seitsonen, A. P.; Smogunov, A.; Umari, P.; Wentzcovitch, R. M., QUANTUM ESPRESSO: A Modular and Open-source Software Project for Quantum Simulations of Materials. *J. Phys.: Condens. Matter* **2009,** *21* (39), 395502.

39. Vanderbilt, D., Soft Self-consistent Pseudopotentials in a Generalized Eigenvalue Formalism. *Phys. Rev. B* **1990,** *41* (11), 7892.

40. Perdew, J. P.; Burke, K.; Ernzerhof, M., Generalized Gradient Approximation made Simple. *Phys. Rev. Lett.* **1996,** *77* (18), 3865.

41. Bavykina, A.; Yarulina, I.; Al Abdulghani, A. J.; Gevers, L.; Hedhili, M. N.; Miao, X.; Galilea, A. R.; Pustovarenko, A.; Dikhtiarenko, A.; Cadiau, A.; Aguilar-Tapia, A.; Hazemann, J.-L.; Kozlov, S. M.; Oud-Chikh, S.; Cavallo, L.; Gascon, J., Turning a Methanation Co Catalyst into an In–Co Methanol Producer. *ACS Catal.* **2019,** *9* (8), 6910-6918.

42. Grosman, A.; Ortega, C., Capillary Condensation in Porous Materials. Hysteresis and Interaction Mechanism without Pore Blocking/Percolation Process. *Langmuir* **2008,** *24* (8), 3977-3986.

43. Storck, S.; Bretinger, H.; Maier, W. F., Characterization of Micro- and Mesoporous Solids by Physisorption Methods and Pore-size Analysis. *Appl. Catal. A* **1998,** *174* (1), 137-146.

44. Marakatti, V. S.; Peter, S. C., Nickel–Antimony Nanoparticles confined in SBA-15 as Highly Efficient Catalysts for the Hydrogenation of Nitroarenes. *New J. Chem.* **2016,** *40* (6), 5448-5457.

45. Aziz, M. A. A.; Jalil, A. A.; Triwahyono, S.; Sidik, S. M., Methanation of Carbon dioxide on Metal-promoted Mesostructured Silica Nanoparticles. *Appl. Catal. A* **2014,** *486*, 115-122.

46. Ren, J.; Guo, H.; Yang, J.; Qin, Z.; Lin, J.; Li, Z., Insights into the Mechanisms of CO_2 Methanation on Ni (111) Surfaces by Density Functional Theory. *Appl. Surf. Sci.* **2015,** *351*, 504-516.
47. Vogt, C.; Groeneveld, E.; Kamsma, G.; Nachtegaal, M.; Lu, L.; Kiely, C. J.; Berben, P. H.; Meirer, F.; Weckhuysen, B. M., Unravelling Structure Sensitivity in CO_2 Hydrogenation over Nickel. *Nat. Catal.* **2018,** *1* (2), 127-134.
48. Norén, L.; Larsson, A. K.; Withers, R. L.; Rundlöf, H., A Neutron and X-ray Powder Diffraction Study of $B8_2$ related Superstructure Phases in the Ni–In System. *J. Alloys Compd.* **2006,** *424* (1), 247-254.
49. Roy, S.; Cherevotan, A.; Peter, S. C., Thermochemical CO2 Hydrogenation to Single Carbon Products: Scientific and Technological Challenges. *ACS Energy Lett.* **2018,** *3* (8), 1938-1966.
50. Ye, J.; Liu, C.; Mei, D.; Ge, Q., Active Oxygen Vacancy Site for Methanol Synthesis from CO2 Hydrogenation on In_2O_3 (110): A DFT Study. *ACS Catal.* **2013,** *3* (6), 1296-1306.
51. Martin, O.; Martín, A. J.; Mondelli, C.; Mitchell, S.; Segawa, T. F.; Hauert, R.; Drouilly, C.; Curulla-Ferré, D.; Pérez-Ramírez, J., Indium Oxide as a Superior Catalyst for Methanol Synthesis by CO_2 Hydrogenation. *Angew. Chem. Int. Ed.* **2016,** *55* (21), 6261-6265.
52. Jia, X.; Sun, K.; Wang, J.; Shen, C.; Liu, C.-j., Selective Hydrogenation of CO_2 to Methanol over Ni/In_2O_3 Catalyst. *J. Energy Chem.* **2020,** *50*, 409-415.
53. Snider, J. L.; Streibel, V.; Hubert, M. A.; Choksi, T. S.; Valle, E.; Upham, D. C.; Schumann, J.; Duyar, M. S.; Gallo, A.; Abild-Pedersen, F.; Jaramillo, T. F., Revealing the Synergy between Oxide and Alloy Phases on the Performance of Bimetallic In–Pd Catalysts for CO2 Hydrogenation to Methanol. *ACS Catal.* **2019,** *9* (4), 3399-3412.
54. Marakatti, V. S.; Arora, N.; Rai, S.; Sarma, S. C.; Peter, S. C., Understanding the Role of Atomic Ordering in the Crystal Structures of NixSny toward Efficient Vapor Phase Furfural Hydrogenation. *ACS Sustainable Chem. Eng.* **2018,** *6* (6), 7325-7338.
55. Yan, X.; Tian, L.; Chen, X., Crystalline/Amorphous Ni/NiO Core/Shell Nanosheets as Highly Active Electrocatalysts for Hydrogen Evolution Reaction. *J. Power Sources* **2015,** *300*, 336-343.
56. Aldana, P. A. U.; Ocampo, F.; Kobl, K.; Louis, B.; Thibault-Starzyk, F.; Daturi, M.; Bazin, P.; Thomas, S.; Roger, A. C., Catalytic CO_2 Valorization into CH_4 on Ni-based Ceria-Zirconia. Reaction Mechanism by Operando IR Spectroscopy. *Catal. Today* **2013,** *215*, 201-207.
57. Wang, X.; Shi, H.; Kwak, J. H.; Szanyi, J., Mechanism of CO_2 Hydrogenation on Pd/Al_2O_3 Catalysts: Kinetics and Transient DRIFTS-MS Studies. *ACS Catal.* **2015,** *5* (11), 6337-6349.
58. Courtois, M.; Teichner, S. J., Infrared Studies of CO, O_2, and CO_2 Gases and their Interaction Products, Chemically Adsorbed on Nickel Oxide. *J. Catal.* **1962,** *1* (2), 121-135.

59. Campuzano, J. C.; Greenler, R. G., The Adsorption Sites of CO on Ni (111) as Determined by Infrared Reflection-Absorption Spectroscopy. *Surf. Sci.* **1979,** *83* (1), 301-312.

60. Henkelman, G.; Uberuaga, B. P.; Jónsson, H., A Climbing Image Nudged Elastic Band Method for Finding Saddle Points and Minimum Energy Paths. *J. Chem. Phys.* **2000,** *113* (22), 9901-9904.

Chapter 4

Metal Substitution Induced Surface Oxygen Vacancy and Operando Generated Medium Entropy Intermetallic Compound Enhances the Conversion of Carbon Dioxide to Methanol

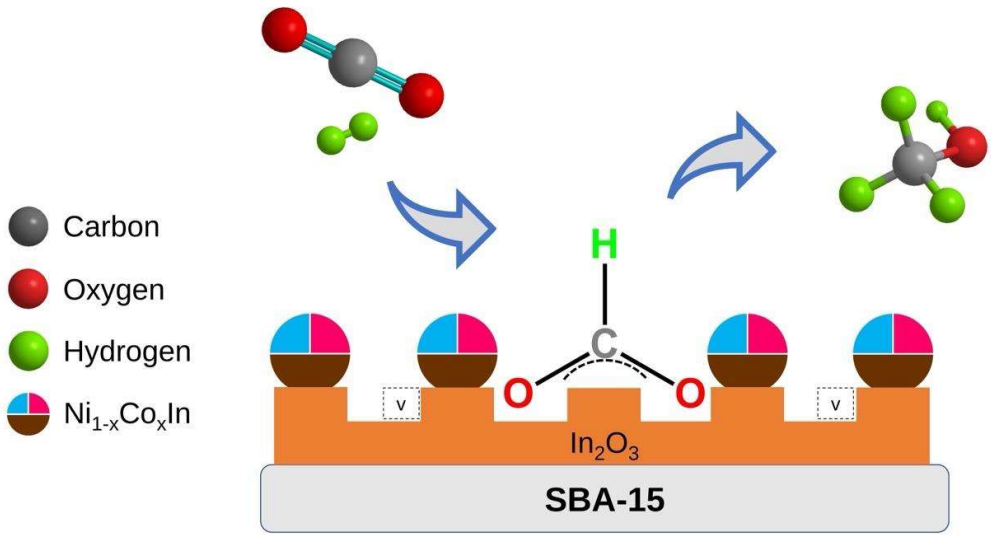

Arjun Cherevotan, Anish Yadav, Ashutosh Kumar Singh, Debabrata Bagchi, Sathyapal R. Churipard, Bitan Ray, Komalpreet Kaur, Ujjal K. Gautam, Chathakudath P. Vinod, and Sebastian C. Peter

(*Manuscript under review*)

Summary

The selective conversion of carbon dioxide (CO_2) to methanol (MeOH) has seen a recent advent of In_2O_3 as a promising catalyst owing to its surface oxygen vacancy (Ov) assisted MeOH production. Recently, dispersing Pd, Pt, Ir, Au, Ni, Cu and Co has been proven to improve the MeOH yield further due to the synergy between the transition metals and support. In this chapter, we introduced a novel strategy by combining the above two concepts that leads to the generation of an ordered compound with enhanced entropy and enhanced CO_2 to methanol conversion. The catalyst generated, In_2(NiCo)/SBA-15, favors MeOH yield of 10.9 μmol/g_{cat}.h, which is the highest ever reported on In_2O_3 silica composite. X-ray photoelectron spectroscopic results suggest that the Ov gets enhanced in $In_2(Ni_xCo_y)$/SBA-15 in comparison to single metal promoter catalysts In_2(Ni)/SBA-15 and In_2(Co)/SBA-15. The combination of two metals favors the operando generation of medium entropy intermetallic of $Ni_{1-x}Co_xIn$ and oxygen vacant In_2O_{3-x}. The transmission electron microscopic studies visualized synergy between $Ni_{1-x}Co_xIn$ and In_2O_{3-x}, which enhances the CO_2 to methanol activity. The nature of CO_2 and H_2 interaction with catalyst and intermediates were investigated with the help of CO_2 temperature programmed desorption (TPD), H_2 temperature programmed reduction (TPR) and *in-situ* diffuse reflectance infrared fourier transform spectroscopy (DRIFTS) studies.

The work based on this chapter is under review.

Table of Contents

4.1. Introduction

The last decade has seen the advent of transition metal-based bimetallics[1] and intermetallics (IMs)[2] used for selective CO_2 hydrogenation to MeOH. Intermetallics based on Ni, Cu, Pd, Ga and In are reported to surpass the MeOH selectivity compared to the state-of-the-art CZA catalyst.[2-5] Parallel to this, oxygen-deficient (Ov) In_2O_3 has started gaining lot of attention towards high MeOH selectivity from CO_2 reduction.[6-8] Detailed investigations by Density Functional Theory (DFT) suggested that the in-situ creation and annihilation of Ov over In_2O_3 surface activates the thermodynamically stable CO_2 molecules.[9, 10] However, this selective hydrogenation of CO_2 to MeOH suffers from low conversion percentage since the number of CO_2 molecules getting activated directly depends on the amount of Ov on In_2O_3. Hence, there have been constant attempts to improve the Ov and hence conversion by using mixed oxides In_2O_3/ZrO_2[11-16] and metal impregnation.[17-19] This led to an enhanced CO_2 activation and hydrogenation with >20 % conversion and >70 % MeOH selectivity. The relationship between impregnated metal and In_2O_3 is complex and elusive, it can create surface Ov on In_2O_3[19, 20] or in some other instance causes changes in electronic properties of supported metal (In) and impregnated metal, this may be by alloying between In and impregnated transition metal to yield IMs along with the presence of In_2O_3.[20, 21] All these interactions improve the synergy between loaded metal and In_2O_3 leading to improved methanol activity. In 2019, Snider et. al. synthesized varying Pd:In ratios and Ni:In on SiO_2 support with the highest activity and selectivity (61%) for methanol was obtained for Pd-In.[22] The DFT analysis and experiments suggested a synergy between bimetallic In-Pd phase and In_2O_3 phase. Coinage metals offer good hydrogen dissociation; however, they are quite expensive. Hence, replacing Pd with other transition metals (TM) to realize similar hydrogen spill over activity is a recent trend. For instance, multiple reports showing Ni,[23, 24] Ir[25, 26] and Cu[5, 27] with In_2O_3 have come in the recent past. In 2019, Bavykina et. al. tuned methanation cobalt catalyst into favouring MeOH formation.[28] The enhancement was contributed to the charge transfer taking place between Co and In_2O_3 films that eventually leads to an increase in Ov at the surface. Recently, Frei et. al made Ni-promoted In_2O_3 catalyst for selective CO_2 hydrogenation to MeOH.[21] Introduction of silica mesoporous support materials (SBA-15)[24] enhances the catalyst active metal dispersion, controls metal nanoparticle size and offers a low-cost alternative in comparison to ZrO_2 and CeO_2 as support materials.

In this current chapter, our quest is to enhance the Ov by using combination of two methanation catalysts, Ni and Co, capable of in-situ reduction of In_2O_3 surface in the reducing

environment. The reduced metals facilitate strong diffusion and leads into the operando generation of ordered intermetallics. The close resemblance of chemical nature of Ni and Co introduces local entropy in the ordered structure, which improved the CO_2 to MeOH performance.

4.2. Experimental Section

4.2.1. Chemicals and Reagents

Tetraethyl orthosilicate (TEOS) (>99% GC, Sigma Aldrich), Pluronic P123 (M_n~5800, Sigma Aldrich), HNO_3 (69% analytical grade, Merck Chemicals), H_2SO_4 (98% analytical grade, Merck Chemicals), nickel nitrate hexahydrate (98%, SDFCL) and indium nitrate hydrate (99.99%, Sigma Aldrich).

4.2.2. Synthesis

4.2.2.1. Synthesis of SBA-15

The support material Santa Barbara Amorphous (SBA-15) was synthesized by using similar procedure in Chapter 2 and Chapter 3.

4.2.2.2. Synthesis of $In_2(Ni_xCo_y)$/SBA-15

A typical method of incipient wetness impregnation was followed with slight modification to distribute $In_2(Ni_xCo_y)$ system on SBA-15. Ni(II), Co(II) and In(III) nitrates were dissolved in 4 M HNO_3 solution. The nitrate salts were weighed to get 23% of metal loading with different ratio of Ni:Co – 3:1 ($(Ni_3Co)In_2$/SBA-15-a), 2:1 ($(Ni_2Co)In_2$/SBA-15-b), 1:1 ($(NiCo)In_2$/SBA-15-c), 1:2 ($(NiCo_2)In_2$/SBA 15-d) and 1:3 ($(NiCo_3)In_2$/SBA 15-e). Metal nitrates were soaked with SBA-15 in the solution for an hour, which propels the solution impregnation into the channels by capillary action. The excess solution was dried at 333 K on a hotplate and further in vacuum oven at 393 K overnight. The precursor was calcined at 623 K under air in muffle furnace for 5 hrs **(Figure 4.1)**. The controlled catalyst (without Ni or Co) In_2Ni/SBA-15 or In_2Co/SBA-15 was synthesized by following the same steps.

4.2.3. Material Characterization

4.2.3.1. ICP-OES

ICP-OES was performed using a Perkin Elmer Optima 7000 DV instrument. The samples were first digested in concentrated aqua regia prepared in lab. Then samples were treated with 2-3 drops of HF to remove silica of SBA-15 and finally diluted with distilled water.

In a typical experiment 5 mg of the sample was dissolved in 3-5 ml aqua regia and heated at 333 K for digestion. The digested sample was then treated with 3-5 drops of HF and diluted to 10 ml volume with deionized water, from this 1 ml was again taken and diluted to 10 ml. The solid particles were separated by thorough centrifugation before measurements

4.2.3.2. Powder X-ray Diffraction (PXRD)

The phase formation on SBA-15 was confirmed by X-ray diffraction (XRD) collected on PANalytical X-ray diffractometer with Cu K_α radiation at 45 kV and 40 mA. The features of the PXRD patterns were compared with simulated pattern from Pearson Database.

4.2.3.3. N_2 Adsorption-Desorption Measurement

The adsorption isotherms were studied by using N_2 at 77 K on BelCat instrument. Prior to the measurements the powders were treated for degassing at 423 K for 6 hours. The specific surface area was confirmed by Brunaur-Emmett-Teller (BET) method and pore size distribution by classical BJH (Barrett, Joyner and Halenda) method.

4.2.3.4. CO_2 temperature programmed desorption (TPD)

The CO_2 TPD analysis was performed using Altamira AMI-300 Lite instrument. In a typical procedure approximately 70-80 mg of sample was taken in the TPD cell. Prior to the CO_2-TPD analysis the material was reduced at 200 °C with 10% H_2 in argon with a flow rate of 25 ml/min and a ramp rate of 10 °C/min. After the pre-treatment, it was cooled down to 50 °C and the sample was treated with a flow of 50 ml/min gas mixture containing 5 ml CO_2 and 45 ml helium for 60 minutes to saturate the material with CO_2.

After the CO_2 treatment, the material was post flushed with helium gas to remove the physisorbed CO_2. The CO_2 TPD analysis was started from 50 °C up to 800 °C with a ramp rate of 10 °C with a flow rate of 25 ml/min of helium as a carrier gas. The amount of CO_2 desorbed was detected by the TCD detector. After every analysis the TCD response is calibrated to quantify the amount of CO_2 desorbed from the material during the TDP analysis.

4.2.3.5. Transmission Electron Microscopy (TEM)

TEM images and selected area electron diffraction patterns were collected using a JEOL JEM-2010 TEM instrument and color mapping was done in TECHNAI. The samples for these measurements were prepared by sonicating the nanocrystalline powders in ethanol and drop-casting a small volume onto a carbon-coated copper grid.

4.2.3.6. X-ray Photoelectron Spectroscopy (XPS)

XPS measurements were carried out using Thermo K-alpha+ spectrometer using micro focused and monochromated Al Kα radiation with energy 1486.6 eV. The pass energy for spectral acquisition was kept at 50 eV for individual core-levels. The electron flood gun was utilized for providing charge compensation during data acquisition. Further, the individual core-level spectra were checked for charging using C1s at 284.6 eV as standard and corrected if needed. The peak fitting of the individual core-levels was done using CasaXPS software with a Shirley type background.

4.2.3.7. X-ray Absorption Spectroscopy (XAS)

Co, Ni and In K-edge XAS measurements of the catalyst on SBA-15 were carried out in transmittance and fluorescence mode at PETRA III, P64 beamline of DESY, Germany. Pellets for the measurements were made by homogeneously mixing the sample with an inert cellulose matrix to have an X-ray absorption edge jump close to 1. The XAS data processing were done using the ATHENA[29] software. The multiple data were collected and averaged out before proceeding to the background correction. The averaged data were smoothed out using the standard kernel size of 11. The weak spline was used for background correction in the pre-edge region. All the data were normalized for standard data analysis procedure was used to extract the extended X-ray absorption fine structure (EXAFS) signal from the measured absorption spectra. Theoretical EXAFS models were constructed and fitted to the experimental data in ARTEMIS.[29] To obtain the value of amp factor and enot for respective elemental k-edge, all the oxide were fit using the crystallographic information file (CIF). The obtained amp factor and enot were used for EXAFS data fitting of the compounds. The EXAFS fitting of spent catalyst for In_2(NiCo) on SBA-15 was done by taking the CIF files of Co_3O_4/NiO/In_2O_3 along with $Ni_{0.5}Co_{0.5}In$. The EXAFS data were Fourier transformed in the range of 3−11 $Å^{-1}$. Data were fitted in R-space between 1 and 5.1 Å for all the samples. The fitting parameters consist of bond length change between atoms (ΔR), change in energy scale between data and theory (ΔE_0), and mean-square displacement of the bond length (σ^2). The coordination numbers (CNs) were taken from the respective crystal structures and varied until a low R-factor was achieved.

4.2.4. Catalyst Extrusion

Wire type extrudates were used for the tubular reactor. A paste was made from catalyst powder by grinding 5 g of it with 1.5 g of pseudoboehmite (AlO(OH)) and 10 mL of 0.5 M

HNO_3. This was then passed through a manually operated wire profiled die to get a wire of 0.5 mm diameter and 1 mm length. The extrudates were dried in atmospheric conditions and then calcined overnight at 373 K to make it strong. The extrudates were crushed and characterized by XRD.

4.2.5. Catalyst Screening Test

The efficiency of the catalysts towards CO_2 reduction was screened by a fixed bed vapor phase down flow reactor having a bed volume of 9.2 cm^3. Optimized flow rate of 4.9 WHSV h^{-1} ($1CO_2$:$4H_2$) were used. The reactions were performed at 523 K, 548 K and 573 K at 45 bar pressures. The catalyst after loading was reduced by passing 5:10 mixture of H_2 and N_2 at 673 K and 5 bar pressure for 6 hours. The gases were analyzed in real time by Agilent GC 7890B, with TCD and FID as the detector. The liquid products were condensed by chiller after 15 hours of reaction. N_2 and was used as the internal standards for gas analysis.

4.2.6. Operando DRIFTS

The operando DRIFTS experimental were carried out using an Agilent Carey 680 FTIR Spectrometer equipped with a Harrick DRIFTS cell. The spectra were recorded at 4 cm^{-1} resolution and each spectrum was averaged 64 times. Each sample was pre-treated at 473 K using 99.999% argon at a gas flow rate of 50 mL min^{-1} for 1h to remove adsorbed water and other gas molecules. Then the temperature of the sample was increased to 723 K and gas switched to 20%H_2/Ar at 50 mL min^{-1} for 2h reduction. After that, the temperature of the sample was annealed to 303 K under Ar flow. The spectrum of the annealed sample at 303 K was used as the background reference for the following reaction. To probe the reaction, 25%CO_2/75%H_2 gas mixture at 1 bar and a total flow rate of 50 mL min^{-1} was first introduce to the DRIFTS cell, and then temperature was ramped from 303 to 573 K (ca. 15 K min^{-1}) to determine the relationship between temperature and the reaction intermedia. Then the reaction was maintained at 573 K for 1h to determine the surface intermedia revolution.

4.2.7. Calculations

4.2.7.1. Weight Hour Space Velocity (WHSV)

WHSV is defined as the mass of reactant per unit time passed per mass of catalyst charged in a reactor. Here we used the flow rate of 50 NLPH ($1CO_2$:$4H_2$).

50 NLPH:

CO_2 flow = 10 NLPH (19.8 grams per hour)

H_2 flow = 40 NLPH (3.56 grams per hour)

N_2 flow (internal standard for GC analysis) = 1 NLPH (1.25 grams per hour)

Mass of catalyst charged = 5 g

$$\text{WHSV} = (19.8 + 3.56 + 1.25)/5 = 4.922\ h^{-1} = \sim 4.9\ h^{-1}$$

4.2.7.2. Response factor of GC (RF)

Response factor for a component '*i*' of a detector is the ratio of peak area of component '*i*' to calibration concentration (**eqn. 4.1**). The unknown concentration of component '*i*' during online gas analysis is determined multiplying response factor of component with peak area of the component obtained during online analysis. Note that calibration compositions of samples are expressed in percentage.

$$RF_i = \text{Peak Area of } i \div \text{Standard Composition of } i\ (\%) \quad (4.1)$$

$$\text{Unknown Composition of } i \text{ in product gas } (\%) = \text{RF Peak} \times \text{Area of } i \text{ in product} \quad (4.2)$$

The GC RF for TCD are given below:

RF of CO_2 = 0.001617; RF of N_2 = 0.001848; RF of CO = 0.00216; RF of CH_4 = 0.00221

4.2.7.3. Conversion and product selectivity[28]

$$CO_2 \text{ conversion } (\%) = \left(CO_2\ (\text{in}) - CO_2\ (\text{out}) \times \frac{N_2(\text{in})}{N_2(\text{out})}\right) \div CO_2\ (\text{in}) \quad (4.3)$$

$$\text{Selectivity of } i = (100\text{n} \times \frac{\text{Composition of } i}{N_2(\text{out})}) \div (\frac{CO_2\ (\text{in})}{N_2(\text{in})} - \frac{CO_2\ (\text{out})}{N_2(\text{out})}) \quad (4.4)$$

CO_2 (in) = Composition of CO_2 in feed gas

CO_2 (out) = Composition of CO_2 in product

N_2 (in) = Composition of N_2 in feed gas

N_2 (out) = Composition of N_2 in product

4.3. Results and Discussions

4.3.1. Catalyst preparation and material characterization

A series of $In_2O_3/(Ni_xCo_y)$/SBA-15 catalysts were synthesized using previously mentioned incipient wetness impregnation (IWI) method. Twenty weight percentage of metals (In, Ni and Co) were loaded inside porous silica (SBA-15) with 2/3rd weight of In and rest were

Ni and Co with different ratio (x:y = 3:1, 2:1, 1:1 and 1:3) to yield 4 different catalysts ($In_2(Ni_xCo_y)$/SBA-15), starting from $In_2(Ni_3Co)$/SBA-15 to $In_2(NiCo_3)$/SBA-15 **(Figure 4.1)**. All the calcined catalysts analyzed by powder XRD revealed mixed oxide phases of cubic In_2O_3 (S.G: $I\bar{3}a$), Co_3O_4 (S.G: $F4\bar{3}m$) and NiO (S.G: $Fm\bar{3}m$) as shown in **Figure 4.2a**. Further the ICP analysis confirmed the ratio of the metals present in each catalyst **(Table 4.1)**. The N_2 adsorption-desorption curve of impregnated catalyst confirmed the retention of pore ordering despite of 20 wt% of metal loading and the decrease in both surface area and pore size of SBA-15 upon impregnation confirmed uniform distribution of oxides of In, Co and Ni with minimum pore blockage **(Table 4.2** and **Figure 4.2b-c)**.

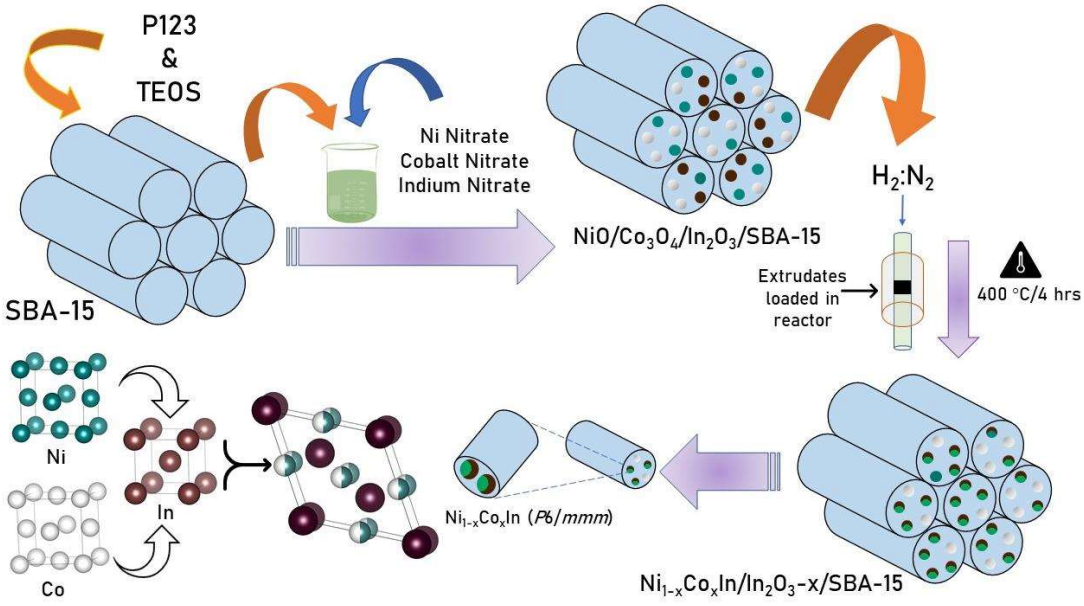

Figure 4.1. Schematic illustration of various steps involved in Ni, Co and In co-impregnation over SBA-15 and operando formation of intermetallic $Ni_{1-x}Co_xIn$/SBA-15 catalyst.

Table 4.1. ICP-OES data of different $In_2(Ni_xCo_y)$/SBA-15 catalysts.

Catalyst	Metal Conc. from ICP-OES (ppm)			Stoichiometric Ratio (Ni/Co)	
	Ni	Co	In	Expected	Observed by ICP-OES
$20In_2(Ni_3Co)$/SBA-15	2.912	0.92	8.9	3	3.17
$20In_2(Ni_2Co)$/SBA-15	2.245	1.18	7.72	2	1.91
$20In_2(NiCo)$/SBA-15	2.242	2.253	9.59	1	1.004
$20In_2(NiCo_2)$/SBA-15	1.468	2.951	9.545	0.5	0.499
$20In_2(NiCo_3)$/SBA-15	1.40	3.771	11.67	0.333	0.3719
$20In_2(Ni)$/SBA-15	4.355	-	10.37	-	-
$20In_2(Co)$/SBA-15	-	4.460	10.79	-	-

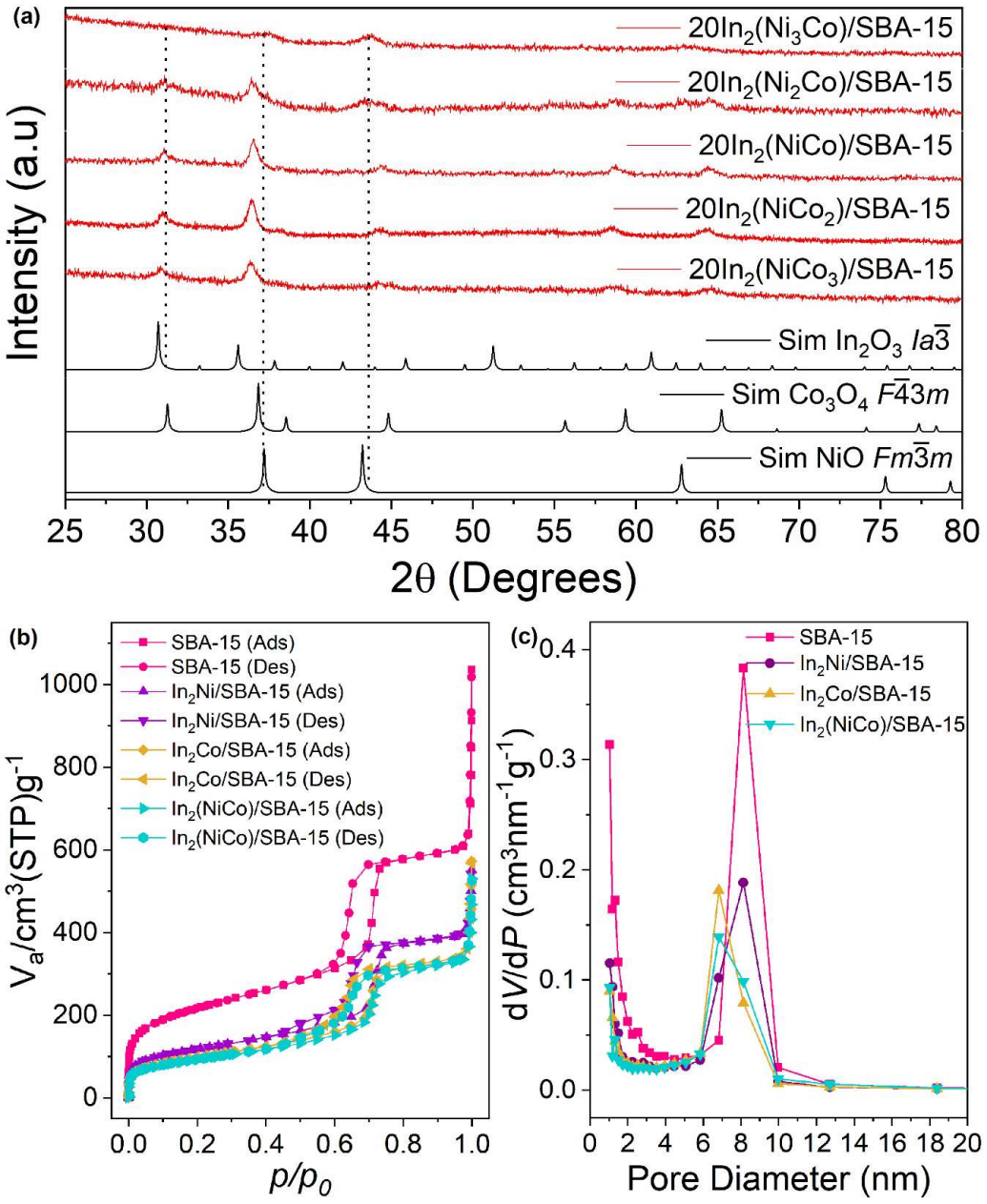

Figure 4.2. (a) X-ray diffraction pattern of calcined $In_2(Ni_xCo_y)$/SBA-15, (b) nitrogen adsorption-desorption isotherm of In_2(Ni)/SBA-15, In_2(Co)/SBA-15 and In_2(NiCo)/SBA-15 and (c) pore size distribution of In_2(Ni)/SBA-15, In_2(Co)/SBA-15 and In_2(NiCo)/SBA-15.

Table 4.2. Textural properties of SBA-15 and impregnated catalyst.

Sample	BET Surface Area (m^2/g)	Pore Size Distribution (nm)
SBA-15	808.69	7.7
23% In_2Ni/SBA-15	410.5	7.3
23% In_2Co/SBA-15	342.73	6.6
23% In_2(NiCo)/SBA-15	330.84	7

All the catalysts were loaded in the extrudate form without pre-reduction for the catalytic screening. Before screening, extrudates were activated by flowing H_2:N_2 at 673 K. At optimized screening condition, methanol activity ($MeOH_{act}$) was found to be better than individual In_2Ni/SBA-15 and In_2Co/SBA-15, and best reported In_2Pd/SiO_2.[22] This was attributed to synergistic effects between Ni, Co and In_2O_3 on SBA-15. Hence, to deconvolute these synergistic effects various techniques including X-Ray Diffraction (XRD), H_2-temperature programmed reduction (TPR), CO_2-TPD, X-ray photoelectron spectroscopy (XPS) and transmission electron microscopy (TEM) have been utilized systematically.

4.3.2. Thermocatalytic CO_2 hydrogenation performance

The CO_2 hydrogenation to MeOH performance of the catalysts were accessed at 1:4 CO_2 to H_2 flow to yield 4.9 WHSV (5 g catalyst). Extra hydrogen (1:4 flow instead of 1:3) was used to improve the Ov under operando conditions. Similarly, all screenings were done at 45 bar pressures owing to the fact that higher pressure is required for number of moles decreasing gas to liquid process driven by Le-Chateleir's principle.[12] At 4.9 WHSV and 45 bar, all the catalysts were screened with three different temperature 523 K, 548 K and 573 K. The major products in all the cases constituted of MeOH and CO with very trace amount of CH_4. At 523 K, all the catalyst including In_2(Ni)/SBA-15 and In_2(Co)/SBA-15 exhibited highest selectivity towards MeOH compared to 548 K and 573 K **(Figure 4.3a)**. But at 573 K, the overall CO_2 hydrogenation improved with major selectivity towards RWGS reaction. Both mass normalised MeOH activity and space time yield was better for all the catalysts at 548 K except $In_2(NiCo_3)$/SBA-15.

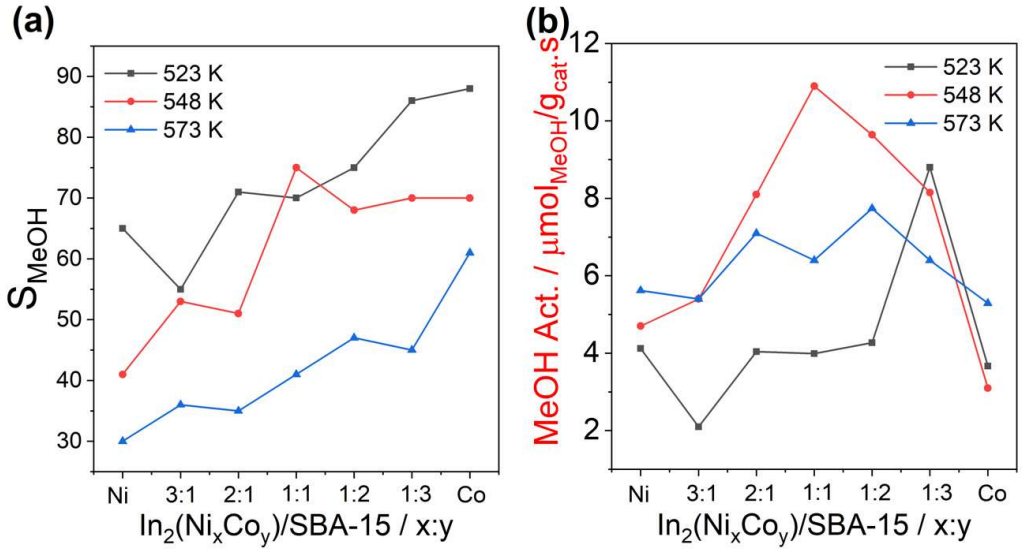

Figure 4.3. (a) $MeOH_{sel}$ of $In_2(Ni_xCo_y)$/SBA-15 catalyst at 523 K, 548 K and 573 K.

The best $MeOH_{act}$ and STY of 10.9 µmol/g_{cat}.h and 1.25 g_{MeOH}/g_{cat}.h respectively is exhibited by $In_2(NiCo)/SBA-15$ at 548 K, 45 bar with 4.9 WHSV **(Figure 4.3b** and **Figure 4.4a)**. This activity is better than all the transition metal (TM) modified In_2O_3/Silica catalysts reported till date **(Figure 4.4b, 4.4c** and **Table 4.3)**.[7]

Table 4.3. Summary of catalytic performance of indium oxide-based catalysts. *** (This work)**

Catalyst	Pressure (MPa)	Temperature (°C)	H_2/CO_2 ratio	MeOH selectivity (%)	STY (g_{MeOH}/g_{cat}.h)
In_2O_3	5	200	4	100	0.011[19]
In_2O_3	5	300	4	70	0.35[19]
Pd/In_2O_3	5	300	4	72	0.885[19]
Pd/In_2O_3-CP	5	280	4	75	0.610[30]
Pt/In_2O_3	5	300	4	53	0.542[31]
Au/In_2O_3	5	300	4	68	0.47[18]
Ni/In_2O_3	5	300	4	54	0.55[17]
In_2O_3/ZrO_2	5	300	4	99.5	0.295[12]
Pd/In_2O_3/SBA-15	5	260	4	84	0.352[24]
In:Pd/SiO_2 85	4	300	4	61	0.587[22]
$In_2(NiCo)/SBA-15$	**4.5**	**275**	**4**	**75**	**1.25***
$In_2(Ni)/SBA-15$	4.5	275	4	41	0.538*
$In_2(Co)/SBA-15$	4.5	275	4	70	0.35*
$In_2(Ni_3Co)/SBA-15$	4.5	275	4	53	0.63*
$In_2(Ni_2Co)/SBA-15$	4.5	275	4	51	0.93*
$In_2(NiCo_2)/SBA-15$	4.5	275	4	68	1.11*
$In_2(NiCo_3)/SBA-15$	4.5	275	4	65	0.948*
$In_2(NiCo)/SBA-15$	**4.5**	**250**	**4**	**55**	**0.459***
$In_2(Ni)/SBA-15$	4.5	250	4	65	0.474*
$In_2(Co)/SBA-15$	4.5	250	4	88	0.424*
$In_2(Ni_3Co)/SBA-15$	4.5	250	4	55	0.241*
$In_2(Ni_2Co)/SBA-15$	4.5	250	4	71	0.466*
$In_2(NiCo_2)/SBA-15$	4.5	250	4	75	0.492*
$In_2(NiCo_3)/SBA-15$	4.5	250	**4**	86	1.01*
$In_2(NiCo)/SBA-15$	**4.5**	**300**	**4**	**41**	**0.742***
$In_2(Ni)/SBA-15$	4.5	300	4	30	0.648*
$In_2(Co)/SBA-15$	4.5	300	4	61	0.609*
$In_2(Ni_3Co)/SBA-15$	4.5	300	4	36	0.630*
$In_2(Ni_2Co)/SBA-15$	4.5	300	4	35	0.817*
$In_2(NiCo_2)/SBA-15$	4.5	300	4	47	0.891*
$In_2(NiCo_3)/SBA-15$	4.5	300	4	45	0.742*

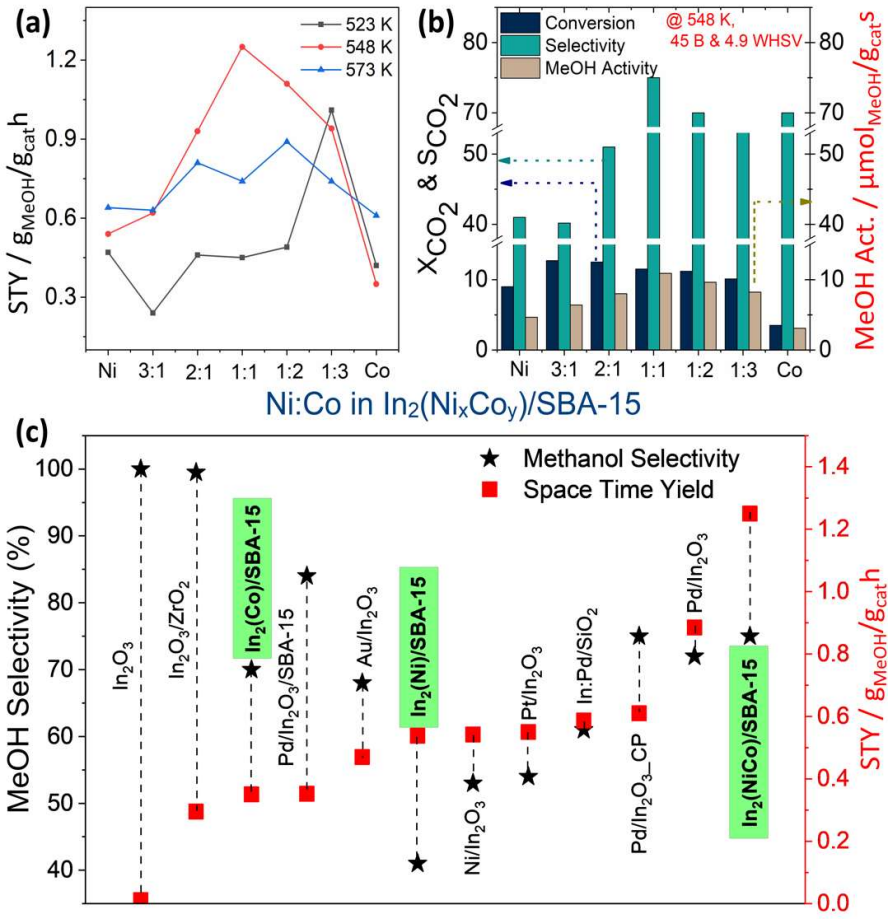

Figure 4.4. (a) MeOH space time yield of $In_2(Ni_xCo_y)$/SBA-15 catalyst at 523 K, 548 K and 573 K and (b) conversion, selectivity and $MeOH_{act}$ of $In_2(Ni_xCo_y)$/SBA-15 at optimized screening condition of 548 K, 45 bar and 4.9 WHSV. (c) A comparison of $MeOH_{sel}$ and $MeOH_{STY}$ of different transition metal impregnated In_2O_3 catalyst from literature and this work (highlighted in green).

From the catalytic screening results, it is evident that the $MeOH_{act}$ of In_2O_3/SBA-15 has been improved upon the impregnation of two methanation catalysts Ni and Co. Previous theoretical studies by DFT have revealed that the activation of CO_2 molecules completely depends on the amount of Ov created at In_2O_3 surface upon the substitution of TM.[9, 10]

4.3.3. X-ray photoelectron spectroscopy

All the reports till date deconvoluted the O 1s spectra into 529.4 eV, 530.7 eV and 531.7 eV as lattice O of In_2O_3, O atom next to defect site and hydroxyl O respectively to quantify the Ov created over In_2O_{3-x} catalyst surface.[30, 32, 33] In case of the SBA-15 impregnated In_2O_3 catalyst, analyzing the O 1s spectra to quantify Ov may lead to erroneous results due to

the intervention of the surface hydroxyl group of silica with that of In_2O_3. Thus, to understand and quantify the changes in Ov, we resorted to the deconvolution of the In 3d XPS spectra of the spent catalysts used at 548 K. The In $3d_{5/2}$ peaks fitted at 443.5 eV and lesser are identified as In^{0-2+} oxidation state while the peaks fitted between 444.8 to 444.1 eV are identified as In^{3+} peaks as shown in **Figure 4.5.**[34, 35] We assumed the peak area ratio of In^{0-2+} to In^{3+} as the measure to quantify the Ov on the surface.

The In $3d_{5/2}$ peak of oxidized (fresh sample) In_2(NiCo)/SBA-15 were fitted only with a single peak centered at 444.47 eV corresponding to In^{3+} **(Figure 4.5d)**, this further supports our assumption. The area ratio of In^{0-2+} to In^{3+} improved drastically with the presence of both Ni and Co in combination when compared to spent In_2(Ni)/SBA-15 and spent In_2(Co)/SBA-15 as shown in **Figure 4.5** and **Table 4.4**. The peak area ratio of In^{0-2+}/In^{3+} were directly compared with the $MeOH_{act.}$ of different Ni to Co ratio **(Figure 4.5i)**, the highest peak area ratio of In^{0-2+}/In^{3+} was observed in In_2(NiCo)/SBA-15 (1.47) and it occurs to be the catalyst with the highest mass normalized MeOH activity of 10.9 μmol/g_{cat}.h. From the plot of area ratio of In^{0-2+}/In^{3+} with $MeOH_{act}$, it is evident that with the Ov is dictating the hydrogenation activity towards MeOH of the catalysts. The In $3d_{5/2}$ peaks fitted at 443.5 eV and lesser are identified as In^{0-2+} oxidation state while the peaks fitted between 444.8 to 444.1 eV are identified as In^{3+} peaks as shown in **Figure 4.5.**[34, 35] We assumed the peak area ratio of In^{0-2+} to In^{3+} as the measure to quantify the Ov on the surface. The In $3d_{5/2}$ peak of oxidized (fresh sample) In_2(NiCo)/SBA-15 were fitted only with a single peak centered at 444.47 eV corresponding to In^{3+} **(Figure 4.5d)**, this further supports our assumption. The area ratio of In^{0-2+} to In^{3+} improved drastically with the presence of both Ni and Co in combination when compared to spent In_2(Ni)/SBA-15 and spent In_2(Co)/SBA-15 as shown in **Figure 4.5** and **Table 4.4**. The peak area ratio of In^{0-2+}/In^{3+} were directly compared with the $MeOH_{act.}$ of different Ni to Co ratio **(Figure 4.5i)**, the highest peak area ratio of In^{0-2+}/In^{3+} was observed in In_2(NiCo)/SBA-15 (1.47) and it occurs to be the catalyst with the highest mass normalized MeOH activity of 10.9 μmol/g_{cat}.h. From the plot of area ratio of In^{0-2+}/In^{3+} with $MeOH_{act}$, it is evident that with the Ov is dictating the hydrogenation activity towards MeOH of the catalysts.

4.3.4. CO_2 TPD Experiment

The CO_2-TPD experiment is an ideal tool for understanding the nature of the interaction between CO_2 and catalysts surface. The CO_2-TPD profiles of In_2O_3/SBA-15 surfaces can be broadly divulged into a lower temperature part (<220 ºC) corresponding to

physisorbed CO_2 and two higher temperature part (250 to 490 ºC) corresponding to chemically adsorbed CO_2 due to hydrogen induced Ov (β: around 300 ºC) and thermally induced Ov (γ: around 460 ºC) formation.[12, 19] The intensity of normalized TPD profile of In_2O_3/SBA-15 and metal impregnated (Ni-Co or Ni and Co separately) In_2O_3/SBA-15 directly compares the amount of Ov created by the metal impregnation. The co-presence of Ni and Co over In_2O_3/SBA-15 surface highly improves the intensity of CO_2-TPD profile as evident from the **Figure 4.6**. This enhancement was negligible for the samples with only Ni or only Co impregnation. Further, the presence of Ni and Co in equal proportion by moles over In_2O_3/SBA-15 caused a merging of β and γ regions corresponding to Ov induced by hydrogen and thermally induced Ov, respectively. This concludes that a unique synergy between In, Co and Ni improves the surface Ov and modifies the nature of CO_2-catalyst interaction.

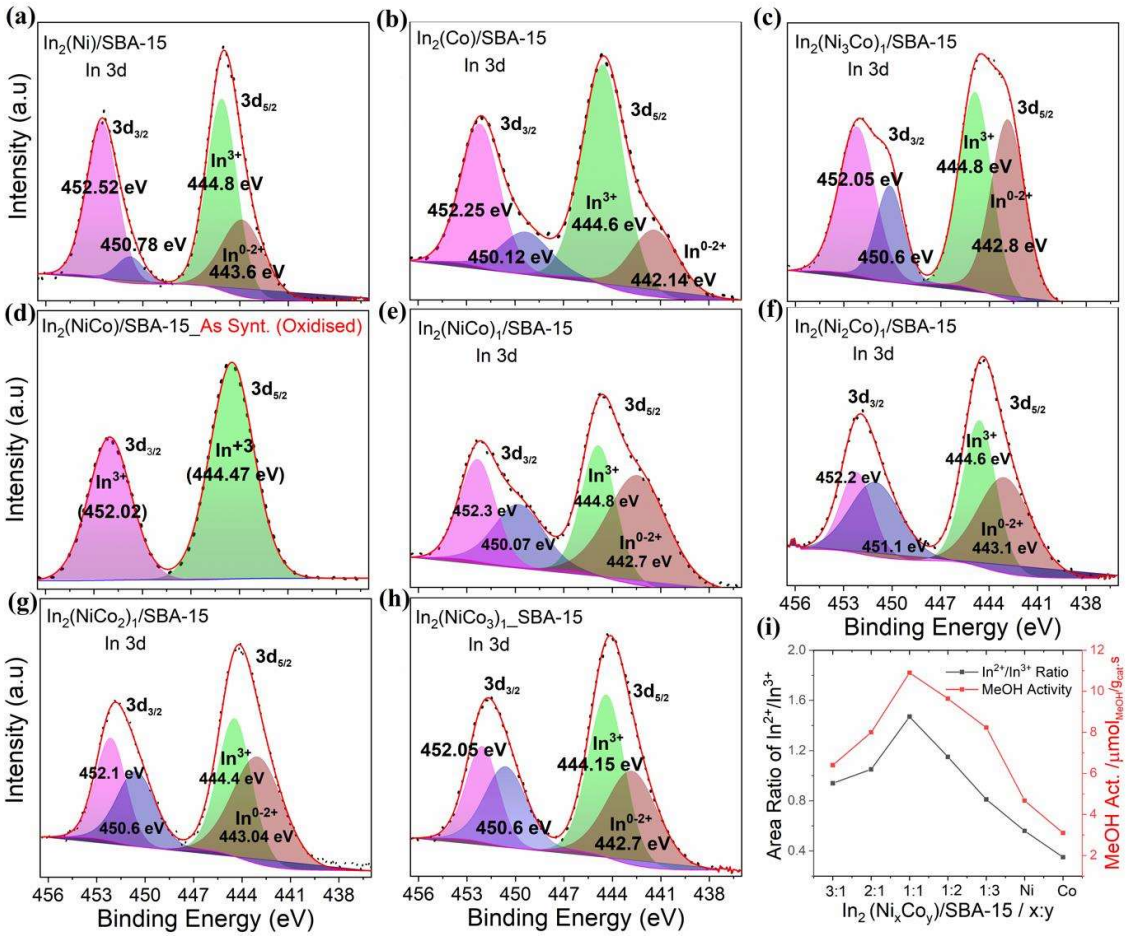

Figure 4.5. Indium 3d XPS spectra of (a) In_2(Ni)/SBA-15, (b) In_2(Co)/SBA-15, (c) $In_2(Ni_3Co)$, (d) fresh (oxidized) In_2(NiCo)/SBA-15 & (e) In_2(NiCo)/SBA-15, (f) $In_2(Ni_2Co)$/SBA-15, (g) $In_2(NiCo_2)$/SBA-15, (h) $In_2(NiCo_3)$/SBA-15 (i) Plot of peak area ratio of In^{0-2+}/In^{3+} vs $MeOH_{act}$ of $In_2(Ni_xCo_y)$/SBA-15.

Table 4.4. XPS data for spent $In_2(Ni_xCo_y)$/SBA-15 catalysts.

Spent Catalyst	Peak Area (a.u)		Peak Area Ratio
	In^{0-2+} $3d_{5/2}$	In^{3+} $3d_{5/2}$	
$In_2(Ni)$_SBA-15	10874	19400	0.56
$In_2(Co)$_SBA-15	17432	49300	0.35
$In_2(Ni_3Co)_1$_SBA-15	19869	21131	0.94
$In_2(Ni_2Co)_1$_SBA-15	18306	17365	1.05
$In_2(NiCo)_1$_SBA-15	**23667**	**16044**	**1.47**
$In_2(NiCo_2)_1$_SBA-15	16849	14555	1.15
$In_2(NiCo_3)_1$_SBA-15	16878	20856	0.81

4.3.5. Characterization of Spent Catalyst

To further understand the superior activity of In_2(NiCo)/SBA-15, the spent catalyst was observed by TEM. The impregnated metal nanoparticles of spent In_2(NiCo)/SBA-15 were uniformly dispersed inside the channels of SBA-15 (**Figure 4.7a**). Further, STEM energy dispersive X-ray spectroscopy elemental mapping (EDS) showed the uniform distribution of Ni, Co and In metal inside the SBA-15 channels (**Figure 4.7b** and **4.7c**).

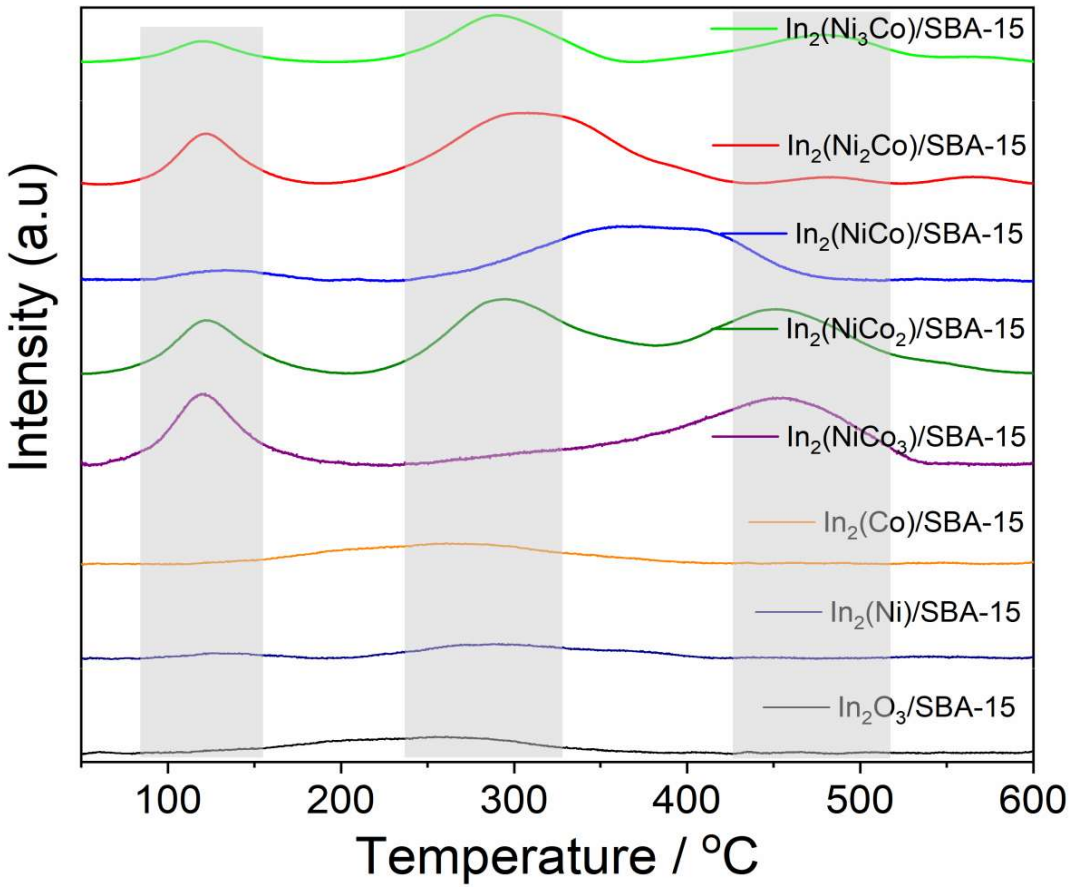

Figure 4.6. The CO_2 -TPD profiles of freshly prepared In_2O_3/SBA-15 based catalysts.

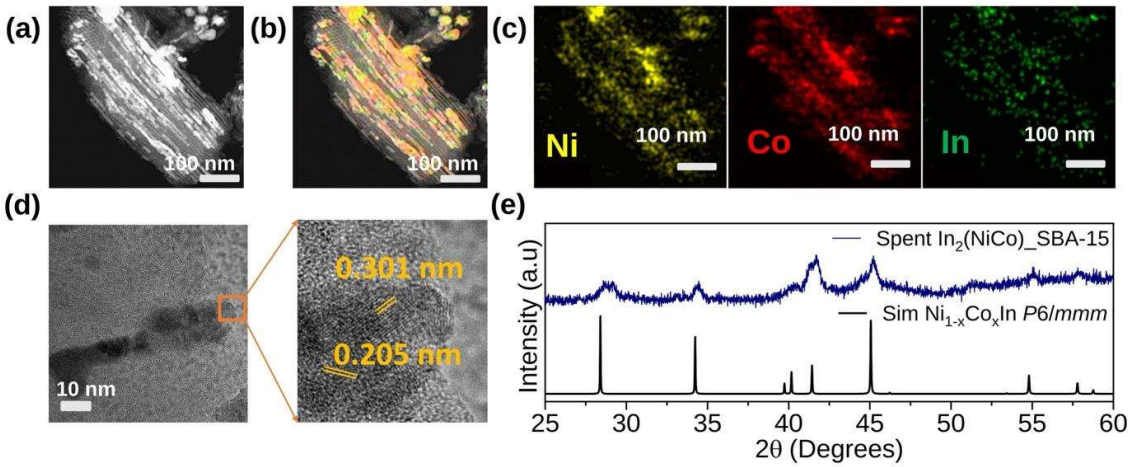

Figure 4.7. (a) TEM image of spent In_2(NiCo)/SBA-15. (b) Elemental mapping of In_2(NiCo)/SBA-15: Ni(yellow), Co (red) and In (green). (c) TEM image of In_2(NiCo)/SBA-15 and HRTEM image of In_2(NiCo)/SBA-15. (d) XRD pattern of In_2(NiCo)/SBA-15 compared with simulated pattern of NiIn *P6/mmm* and NiO $Fm\bar{3}m$.

The high-resolution TEM identified In_2O_3 and $Ni_{1-x}Co_xIn$ nanoparticles formed in operando CO_2 hydrogenation conditions **(Figure 4.7d),** which are distinguishable by difference in distance of lattice fringes. The lattice distance of 0.301 and 0.205 nm were identified as In_2O_3 (222) and intemetallic $Ni_{1-x}Co_xIn$ *P6/mmm* (201) respectively.[36] Further, to confirm different phases formed in-situ during the catalytic reaction, the powder XRD of spent In_2(NiCo)/SBA-15 was analyzed. The powder XRD confirms an in-situ generation of $Ni_{1-x}Co_xIn$ intermetallic (S.G: *P6/mmm)* along with minor peaks of $Ni_{2-x}Co_xIn_3$ (S.G: $P\bar{3}m1$) as shown in **Figure 4.7e**.[36]

4.3.6. Operando DRIFTS measurements and difference in reactivity of intermediates

Fresh catalysts were analysed by in-situ DRIFTS to identify the intermediates formed during the CO_2 hydrogenation. The peaks identified at 1590 to 1500 cm^{-1} and 1350 cm^{-1} correspond to formate (both bi and mono-dentate) and polydentate carbonates, respectively **(Figure 4.8)**.[37] CO_2 molecules get adsorbed as carbonates and then formate, which are the key intermediates of CO_2 to MeOH formed at the surface of indium oxide. The successive hydrogenation of formate ends up in MeOH on the In_2O_3 surface evident by the appearance of $*OCH_3$ peaks (1200-1000 cm^{-1}) at later stage of the experiment. The peak intensity of the formate peak observed in the case of In_2(NiCo)/SBA-15 substantially higher than that of In_2(Ni)/SBA-15, In_2(Co)/SBA-15 and In_2O_3/SBA-15 **(Figure 4.8a)** clearly manifest the fact that the unique synergy between In_2O_{3-x} and NiIn phases and Co improves the CO_2 adsorption as formate, which is in good agreement with CO_2-TPD experiments.

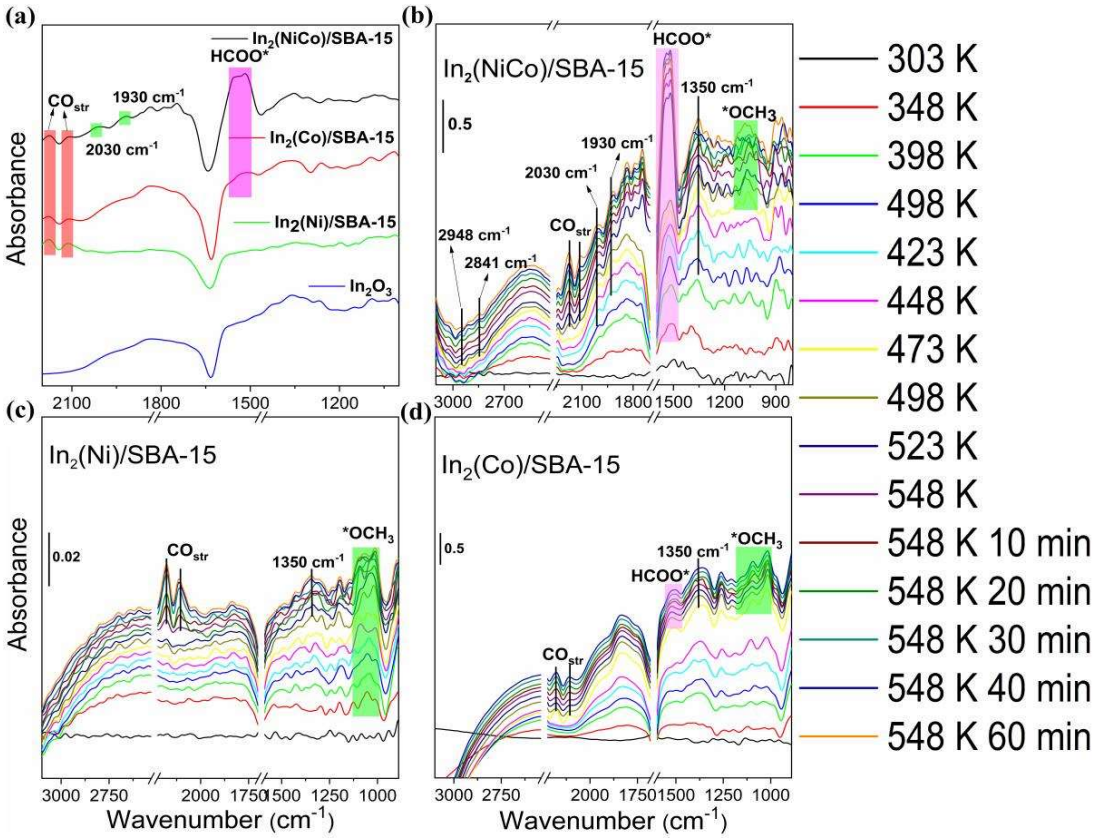

Figure 4.8. (a) Absorbance normalized comparison of operando DRIFTS of In_2(NiCo)/SBA-15, In_2(Co)/SBA-15, In_2(Ni)/SBA-15 and In_2O_3/SBA-15. Operando DRIFTS measurements of CO_2 hydrogenation to MeOH at 1:4 CO_2 to hydrogen flow over (b) as synthesized In_2(NiCo)/SBA-15, (c) In_2(Ni)/SBA-15 and (d) In_2(Co).

4.3.7. X-Ray Absorption Spectroscopy (XAS)

The X-Ray absorption spectroscopy (XAS) is an important tool to understand the oxidation state and local coordination behavior of materials. The Fast Fourier Transformed (FFT) of X-ray absorption near edge are represented as EXAFS. A comparison EXAFS data for respective k-edge standard along with as synthesized and spent catalyst in the range of 0-6 Å are presented in the **Figure 4.9a, 4.9b,** and **4.9c** for Co, Ni and In, respectively. The EXAFS data of standard oxides are in close match with the spent catalyst confirming the presence of oxides in the native state in the as synthesized catalyst. A substantial amount of change can be seen in the spent catalyst indicating some change has occurred to the oxides during reaction. The EXAFS data of spent catalyst does not fit well with respective oxides. As the powder XRD of spent catalyst indicates the operando generated Ni-Co-In intermetallic phase, data fits well with the combination of respective oxides and In_2(NiCo) phase. The fitting model confirms the presence of oxides in the spent catalyst as indicated qualitatively in **Figure 4.9d, 4.9e,** and **4.9f**.

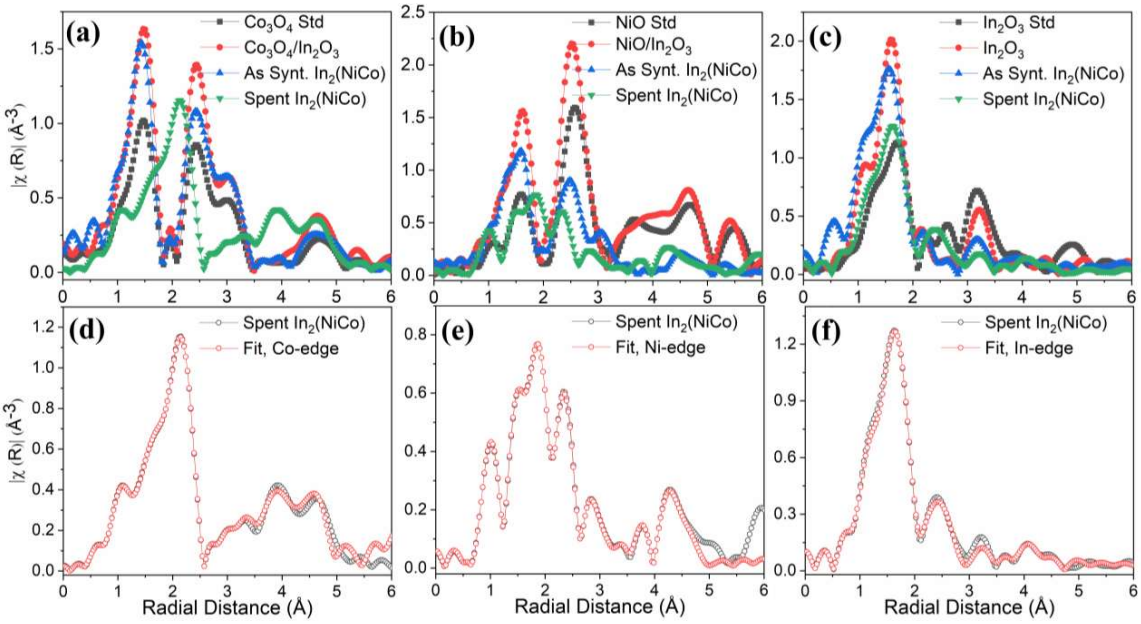

Figure 4.9. *Ex-situ* R-space data for standard, as synthesized and spent catalyst for In_2(NiCo). In the top panel, there is comparison of standard as synthesized and spent catalyst with Co, Ni and In k-edge EXAFAS data in a), b) and c). The bottom panel shows the EXFAS data fitting in the range of 1- 5.1 Å in the k range of 3-11 $Å^{-1}$. The EXAFS data were fitted using the corresponding oxide and NiIn crystal structure. The F_{eff} calculations were modified and 50% of Ni were substituted with Co atomic position to incorporate the Co atoms at Ni.

The increase in bond length of Co-O and Co-Co for the Co_3O_4 in the spent catalyst as compared to the standard Co_3O_4, confirms the Co_3O_4 has deteriorated during the course of the reaction. The Co-Co, Co-Ni and Co-In bond distance are in close agreement with covalent bond distance further confirming the operando generation of intermetallic phase between Ni-Co-In **(Table 4.5).** A very similar story also applies for the In k-edge data, but there is substantial change in the Ni k-edge.

The Ni-O and Ni-Ni bond distance decreases as compared to the NiO oxide standard data, indicating NiO is more stable than the Co_3O_4 and In_2O_3, which is further confirmed by powder XRD of spent catalyst. There is a right- shift in the powder XRD as compared to NiO peaks around 2θ value of 44° **(Figure 4.7d)**, which can be attributed to smaller lattice size of NiO as the Ni-Ni and Ni-O bond length decreases in the spent catalyst. So, the combination of powder XRD and EXAFS data fitting confirms the operando generation of an intermetallic phase along with trace amount of Co_3O_4 and In_2O_3 are present in the spent catalyst on the other side NiO stable.

Table 4.5. Bond distance determined by fitting EXAFS data for standard oxides and spent catalysts.

K-edge	Compound	Bond	Bond distance (Å)	Spent	Bond	Bond distance (Å)
Co	Co_3O_4	Co-O	1.917	Co_3O_4-$In_2(NiCo)$	Co-O (Co_3O_4)	2.122
		Co-Co	2.844		Co-Co (Co_3O_4)	3.224
		Co-O (2^{nd} CS)	4.324		Co-O (2^{nd} CE)	4.757
					Co-Ni ($In_2(NiCo)$)	2.284
					Co-Co ($In_2(NiCo)$)	2.640
					Co-In ($In_2(NiCo)$)	2.885
Ni	NiO	Ni-O	2.075	NiO-$In_2(NiCo)$	Ni-O (NiO)	2.088
		Ni-Ni	2.963		Ni-Ni (NiO)	2.674
		Ni-O (2^{nd} CS)	4.831		Ni-O (2^{nd} CE)	4.520
					Ni-Co ($In_2(NiCo)$)	2.483
					Ni-Ni ($In_2(NiCo)$)	2.674
					Ni-In ($In_2(NiCo)$)	2.925
In	In_2O_3	In-O	2.021	In_2O_3 - $In_2(NiCo)$	In-O (In_2O_3)	2.018
		In-In	3.346		In-In (In_2O_3)	3.510
		In-O (2^{nd} CS)	4.842		In-O (2^{nd} CE)	4.658
					In-Co ($In_2(NiCo)$)	2.662
					In-Ni ($In_2(NiCo)$)	3.172
					In-In ($In_2(NiCo)$)	3.510

The XANES data analysis reveals the oxidation state and rough structure of the measured edge in the sample. The normalized XANES spectra were plotted in **Figure 4.10**. There is higher energy shift for the Co absorption edge for the as synthesized sample compared to standard $Co(acac)_3$ and Co_3O_4, confirming the Co is in slightly higher oxidation state than +3. There is further right shift observed in the spent catalyst and corroborated with white line intensity. A compete change in the EXAFS region can be seen which is evident in EXAFS R-space data. A very similar observation in the case of Ni k-edge as well. However, In k-edge deviates from the Ni and Co. The In_2O_3, as synthesized and spent catalyst absorption edge is close together, however their white line intensity differs a lot. The white line intensity for spent catalyst decreases as compared to as synthesized catalyst, confirming oxidation state of In decreases leading to the Ov in the system, supplemented by XPS fitting.

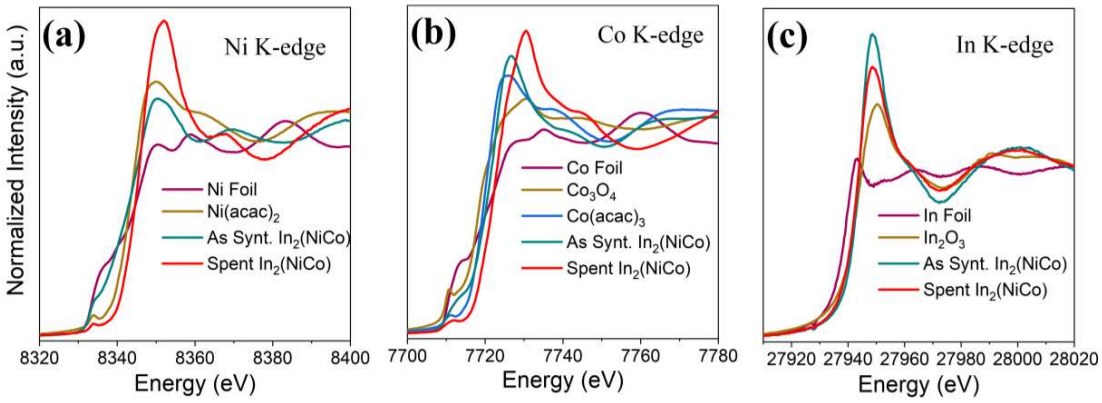

Figure 4.10. XAS spectra of (a) Ni k-edge, (b) Co k-edge and (c) In k-edge of foil, standard, pre and spent catalyst.

4.4. Conclusion

In conclusion, we have enhanced the oxygen vacancy of In_2O_3 in Ni/In_2O_3 by impregnating another non-coinage transition metal cobalt. The best $MeOH_{act}$ of 10.9 µmol/g_{cat}.h was obtained for $In_2(NiCo)/SBA\text{-}15$ at 548 K and 45 bar which is the highest reported till now for In_2O_3 based catalyst. The XPS analysis revealed the relative improvement in Ov of In_2O_3 by the co-presence of Co and Ni. The CO_2-TPD and DRIFTS experiments complement the XPS data. The catalytically active centre is proposed to be $Ni_{1-x}Co_xIn$ intermetallic phases (SG: *P6/mmm*) coexisting with NiO and surface oxygen deficient In_2O_3 over SBA-15. The promotional effect of Co can be extended to precious metal impregnated indium oxide and reported mixed oxides based on indium to improve the $MeOH_{act}$ opening new area of catalytic studies.

4.5. References

1. Bai, S.; Shao, Q.; Wang, P.; Dai, Q.; Wang, X.; Huang, X., Highly Active and Selective Hydrogenation of CO_2 to Ethanol by Ordered Pd–Cu Nanoparticles. *J. Am. Chem. Soc.* **2017,** *139* (20), 6827-6830.
2. Studt, F.; Sharafutdinov, I.; Abild-Pedersen, F.; Elkjær, C. F.; Hummelshøj, J. S.; Dahl, S.; Chorkendorff, I.; Nørskov, J. K., Discovery of a Ni-Ga Catalyst for Carbon dioxide Reduction to Methanol. *Nat. Chem.* **2014,** *6* (4), 320-324.
3. Fiordaliso, E. M.; Sharafutdinov, I.; Carvalho, H. W. P.; Grunwaldt, J.-D.; Hansen, T. W.; Chorkendorff, I.; Wagner, J. B.; Damsgaard, C. D., Intermetallic $GaPd_2$ Nanoparticles on SiO_2 for Low-Pressure CO_2 Hydrogenation to Methanol: Catalytic Performance and In Situ Characterization. *ACS Catal.* **2015,** *5* (10), 5827-5836.
4. Cherevotan, A.; Raj, J.; Dheer, L.; Roy, S.; Sarkar, S.; Das, R.; Vinod, C. P.; Xu, S.; Wells, P.; Waghmare, U. V.; Peter, S. C., Operando Generated Ordered Heterogeneous Catalyst for the Selective Conversion of CO_2 to Methanol. *ACS Energy Lett.* **2021,** *6* (2), 509-516.
5. Shi, Z.; Tan, Q.; Tian, C.; Pan, Y.; Sun, X.; Zhang, J.; Wu, D., CO_2 Hydrogenation to Methanol over Cu-In Intermetallic Catalysts: Effect of Reduction Temperature. *J. Catal.* **2019,** *379*, 78-89.
6. Tsoukalou, A.; Abdala, P. M.; Stoian, D.; Huang, X.; Willinger, M.-G.; Fedorov, A.; Müller, C. R., Structural Evolution and Dynamics of an In_2O_3 Catalyst for CO_2 Hydrogenation to Methanol: An Operando XAS-XRD and In Situ TEM Study. *J. Am. Chem. Soc.* **2019,** *141* (34), 13497-13505.
7. Wang, J.; Zhang, G.; Zhu, J.; Zhang, X.; Ding, F.; Zhang, A.; Guo, X.; Song, C., CO_2 Hydrogenation to Methanol over In_2O_3-Based Catalysts: From Mechanism to Catalyst Development. *ACS Catal.* **2021,** *11* (3), 1406-1423.
8. Araújo, T. P.; Shah, A.; Mondelli, C.; Stewart, J. A.; Curulla Ferré, D.; Pérez-Ramírez, J., Impact of Hybrid CO_2-CO Feeds on Methanol Synthesis over In_2O_3-Based Catalysts. *Appl. Catal. B* **2021,** *285*, 119878.
9. Ye, J.; Liu, C.; Mei, D.; Ge, Q., Active Oxygen Vacancy Site for Methanol Synthesis from CO_2 Hydrogenation on In_2O_3(110): A DFT Study. *ACS Catal.* **2013,** *3* (6), 1296-1306.
10. Ye, J.; Liu, C.; Ge, Q., DFT Study of CO_2 Adsorption and Hydrogenation on the In_2O_3 Surface. *J. Phys. Chem. C* **2012,** *116* (14), 7817-7825.

11. Zhang, M.; Dou, M.; Yu, Y., Theoretical Study of the Promotional Effect of ZrO_2 on In_2O_3 Catalyzed Methanol Synthesis from CO_2 Hydrogenation. *Appl. Surf. Sci.* **2018,** *433*, 780-789.
12. Martin, O.; Martín, A. J.; Mondelli, C.; Mitchell, S.; Segawa, T. F.; Hauert, R.; Drouilly, C.; Curulla-Ferré, D.; Pérez-Ramírez, J., Indium Oxide as a Superior Catalyst for Methanol Synthesis by CO2 Hydrogenation. *Angew. Chem. Int. Ed.* **2016,** *55* (21), 6261-6265.
13. Frei, M. S.; Mondelli, C.; Cesarini, A.; Krumeich, F.; Hauert, R.; Stewart, J. A.; Curulla Ferré, D.; Pérez-Ramírez, J., Role of Zirconia in Indium Oxide-Catalyzed CO_2 Hydrogenation to Methanol. *ACS Catal.* **2020,** *10* (2), 1133-1145.
14. Chen, T.-y.; Cao, C.; Chen, T.-b.; Ding, X.; Huang, H.; Shen, L.; Cao, X.; Zhu, M.; Xu, J.; Gao, J.; Han, Y.-F., Unraveling Highly Tunable Selectivity in CO_2 Hydrogenation over Bimetallic In-Zr Oxide Catalysts. *ACS Catal.* **2019,** *9* (9), 8785-8797.
15. Jiang, X.; Nie, X.; Gong, Y.; Moran, C. M.; Wang, J.; Zhu, J.; Chang, H.; Guo, X.; Walton, K. S.; Song, C., A Combined Experimental and DFT Study of H_2O Effect on In_2O_3/ZrO_2 Catalyst for CO_2 Hydrogenation to Methanol. *J. Catal.* **2020,** *383*, 283-296.
16. Numpilai, T.; Kidkhunthod, P.; Cheng, C. K.; Wattanakit, C.; Chareonpanich, M.; Limtrakul, J.; Witoon, T., CO_2 Hydrogenation to Methanol at High Reaction Temperatures over In_2O_3/ZrO_2 Catalysts: Influence of Calcination Temperatures of ZrO_2 Support. *Catal. Today* **2021,** *375*, 298-306.
17. Han, Z.; Tang, C.; Wang, J.; Li, L.; Li, C., Atomically Dispersed Ptn+ Species as Highly Active Sites in Pt/In_2O_3 Catalysts for Methanol Synthesis from CO_2 Hydrogenation. *J. Catal.* **2021,** *394*, 236-244.
18. Rui, N.; Zhang, F.; Sun, K.; Liu, Z.; Xu, W.; Stavitski, E.; Senanayake, S. D.; Rodriguez, J. A.; Liu, C.-J., Hydrogenation of CO_2 to Methanol on a $Au^{\delta+}$–In_2O_{3-x} Catalyst. *ACS Catal.* **2020,** *10* (19), 11307-11317.
19. Rui, N.; Wang, Z.; Sun, K.; Ye, J.; Ge, Q.; Liu, C.-j., CO_2 Hydrogenation to Methanol Over Pd/In_2O_3: Effects of Pd and Oxygen Vacancy. *Appl. Catal. B* **2017,** *218*, 488-497.
20. Ye, J.; Liu, C.-j.; Mei, D.; Ge, Q., Methanol Synthesis from CO_2 Hydrogenation over a Pd_4/In_2O_3 Model Catalyst: A Combined DFT and Kinetic Study. *J. Catal.* **2014,** *317*, 44-53.

21. Frei, M. S.; Mondelli, C.; García-Muelas, R.; Morales-Vidal, J.; Philipp, M.; Safonova, O. V.; López, N.; Stewart, J. A.; Ferré, D. C.; Pérez-Ramírez, J., Nanostructure of Nickel-Promoted Indium Oxide Catalysts Drives Selectivity in CO_2 Hydrogenation. *Nat. Comm.* **2021,** *12* (1), 1960.

22. Snider, J. L.; Streibel, V.; Hubert, M. A.; Choksi, T. S.; Valle, E.; Upham, D. C.; Schumann, J.; Duyar, M. S.; Gallo, A.; Abild-Pedersen, F.; Jaramillo, T. F., Revealing the Synergy between Oxide and Alloy Phases on the Performance of Bimetallic In–Pd Catalysts for CO_2 Hydrogenation to Methanol. *ACS Catal.* **2019,** *9* (4), 3399-3412.

23. Jia, X.; Sun, K.; Wang, J.; Shen, C.; Liu, C.-j., Selective Hydrogenation of CO_2 to Methanol over Ni/In_2O_3 catalyst. *J. Energy Chem.* **2020,** *50*, 409-415.

24. Jiang, H.; Lin, J.; Wu, X.; Wang, W.; Chen, Y.; Zhang, M., Efficient Hydrogenation of CO_2 to Methanol over Pd/In_2O_3/SBA-15 Catalysts. *J. CO_2 Util.* **2020,** *36*, 33-39.

25. Shen, C.; Sun, K.; Zhang, Z.; Rui, N.; Jia, X.; Mei, D.; Liu, C.-j., Highly Active Ir/In_2O_3 Catalysts for Selective Hydrogenation of CO_2 to Methanol: Experimental and Theoretical Studies. *ACS Catal.* **2021,** *11* (7), 4036-4046.

26. Ye, X.; Yang, C.; Pan, X.; Ma, J.; Zhang, Y.; Ren, Y.; Liu, X.; Li, L.; Huang, Y., Highly Selective Hydrogenation of CO_2 to Ethanol via Designed Bifunctional Ir_1–In_2O_3 Single-Atom Catalyst. *J. Am. Chem. Soc.* **2020,** *142* (45), 19001-19005.

27. Sharma, S. K.; Paul, B.; Pal, R. S.; Bhanja, P.; Banerjee, A.; Samanta, C.; Bal, R., Influence of Indium as a Promoter on the Stability and Selectivity of the Nanocrystalline Cu/CeO_2 Catalyst for CO_2 Hydrogenation to Methanol. *ACS Appl. Mater. Interfaces* **2021,** *13* (24), 28201-28213.

28. Bavykina, A.; Yarulina, I.; Al Abdulghani, A. J.; Gevers, L.; Hedhili, M. N.; Miao, X.; Galilea, A. R.; Pustovarenko, A.; Dikhtiarenko, A.; Cadiau, A.; Aguilar-Tapia, A.; Hazemann, J.-L.; Kozlov, S. M.; Oud-Chikh, S.; Cavallo, L.; Gascon, J., Turning a Methanation Co Catalyst into an In–Co Methanol Producer. *ACS Catal.* **2019,** *9* (8), 6910-6918.

29. Ravel, B.; Newville, M., ATHENA, ARTEMIS, HEPHAESTUS: Data Analysis for X-ray Absorption Spectroscopy Using IFEFFIT. *J. Synchrotron Radiat.* **2005,** *12* (4), 537-541.

30. Frei, M. S.; Mondelli, C.; García-Muelas, R.; Kley, K. S.; Puértolas, B.; López, N.; Safonova, O. V.; Stewart, J. A.; Curulla Ferré, D.; Pérez-Ramírez, J., Atomic-Scale

Engineering of Indium Oxide Promotion by Palladium for Methanol Production via CO_2 Hydrogenation. *Nat. Comm.* **2019,** *10* (1), 3377.

31. Sun, K.; Rui, N.; Zhang, Z.; Sun, Z.; Ge, Q.; Liu, C.-J., A highly Active Pt/In_2O_3 Catalyst for CO_2 Hydrogenation to Methanol with Enhanced Stability. *Green Chem.* **2020,** *22* (15), 5059-5066.
32. Gao, P.; Li, S.; Bu, X.; Dang, S.; Liu, Z.; Wang, H.; Zhong, L.; Qiu, M.; Yang, C.; Cai, J.; Wei, W.; Sun, Y., Direct Conversion of CO_2 into Liquid Fuels with High Selectivity over a Bifunctional Catalyst. *Nat. Chem.* **2017,** *9* (10), 1019-1024.
33. Gao, P.; Dang, S.; Li, S.; Bu, X.; Liu, Z.; Qiu, M.; Yang, C.; Wang, H.; Zhong, L.; Han, Y.; Liu, Q.; Wei, W.; Sun, Y., Direct Production of Lower Olefins from CO_2 Conversion via Bifunctional Catalysis. *ACS Catal.* **2018,** *8* (1), 571-578.
34. Anwar, M.; Ghauri, I. M.; Siddiqi, S. A., An XPS Study of Amorphous Thin Films Mixed Oxides In_2O_3-SnO_2 Sytem Deposited Co-Evaporation. *Int. J. Mod. Phys. B* **2007,** *21* (07), 1027-1042.
35. Gan, J.; Lu, X.; Wu, J.; Xie, S.; Zhai, T.; Yu, M.; Zhang, Z.; Mao, Y.; Wang, S. C. I.; Shen, Y.; Tong, Y., Oxygen Vacancies Promoting Photoelectrochemical Performance of In_2O_3 Nanocubes. *Sci. Rep.* **2013,** *3* (1), 1021.
36. Yang, T.; He, W.; Chen, G.; Zeng, W.; Wang, J.; Zeng, L.; Liang, J., The Phase Relations of the Co-Ni-In Ternary System at 673 K and 873 K and Magnetic Properties of Their Compounds. *Materials* **2020,** *13* (18), 3990.
37. Chou, C.-Y.; Lobo, R. F., Direct Conversion of CO_2 into Methanol Over Promoted Indium Oxide-Based Catalysts. *Appl. Catal. A* **2019,** *583*, 117144.

Chapter 5

Tuning Hybridization and Charge Polarization in Metal Nanoparticles Dispersed over Schiff Base Functionalized SBA-15 Enhances CO_2 Capture and Conversion to Formic Acid

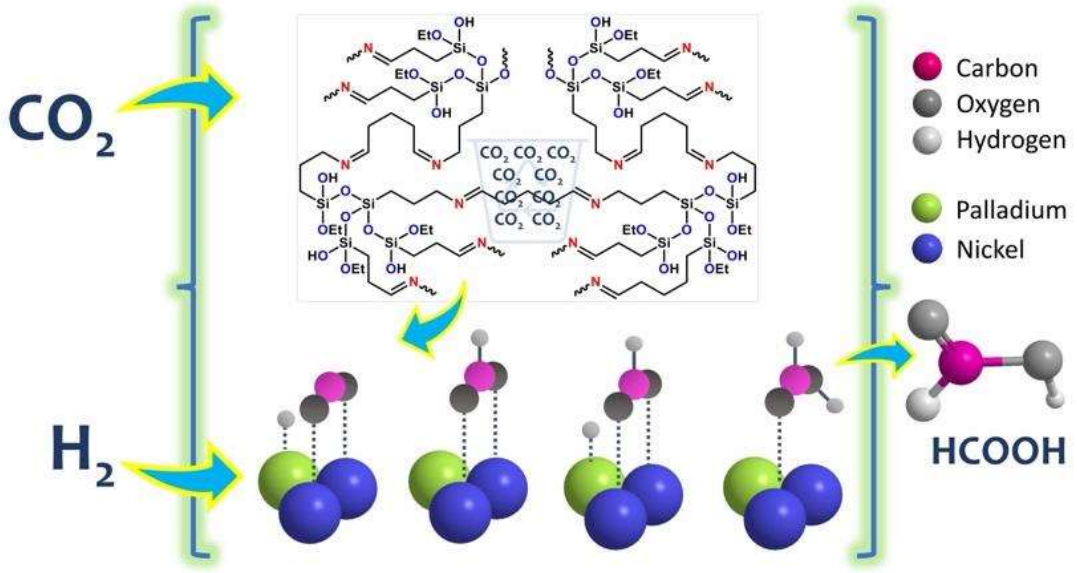

Arjun Cherevotan, Bitan Ray, Anish Yadav, Debabrata Bagchi, Ashutosh Kumar Singh, Sathyapal R. Churipard, Vinay Naral, Komalpreet Kaur, Ujjal K. Gautam, Chathakudath P. Vinod, and Sebastian C. Peter

(*Manuscript under review*)

Summary

Different Schiff base functionalized SBA-15 materials were synthesized through the condensation reactions between 3-aminopropyltriethoxysilane (APTES) and different aldehydes (Glutaraldehyde and Butyraldehyde) over a mesoporous silica, SBA-15 (APTES-GLU/SBA-15 and APTES-BUT/SBA-15). Both static and dynamic experiments have been used for testing the CO_2 capture efficiency of these materials. The hybridization of the N atom in APTES has been tuned from sp^3 to sp^2 upon condensation facilitating the optimum CO_2 capture in the direct synthesis of APTES-GLU/SBA-15. The unfavourable oxides of nitrogen have been removed during the synthesis process to improve the CO_2 capture efficiency. These materials were employed as supports for Pd-Ag and Pd-Ni bi-metallic systems for the selective conversion of the captured CO_2 to formic acid (FA) in 0.5 M $KHCO_3$ solution. Pd-Ni catalyst system exhibited best ever CO_2 to FA activity in the heterogeneous system, which is ~4 times better than the Pd-Ag system in this study. The X-ray absorption studies over the catalyst material confirmed that the relative electron-deficient Ni in Pd-Ni compared to Ag in Pd-Ag favoured higher charge polarization between the metals in Pd-Ni system enhancing the CO_2 to FA conversion.

The work based on this chapter is under review.

Table of Contents

5.1. Introduction

Hydrogenation of CO_2 can result in a plethora of value-added chemicals, including the simplest possible form of carboxylic acid like formic acid (FA).[1, 2] FA is an organic compound with excellent environmental compatibility that has been employed in a range of industries, including pharmaceuticals, agriculture, and textiles.[3-6] In general, industrial FA production relies mostly on methanol carbonylation followed by hydrolysis. Recently, direct CO_2 hydrogenation to FA has gained a lot of attention as a potential pathway for the efficient utilization of anthropogenic CO_2.[7] Carbon dioxide to FA hydrogenation via thermocatalytic routes are efficiently done in batch process which requires a high pressure autoclaved reactor and a catalyst dispersed in solvent bubbled or pressurized with CO_2 and H_2. In last three chapters we discussed about designing heterogenous catalyst for CO_2 reduction to C_1 products by vapour phase continuous flow process. In this chapter we design a efficient catalyst for FA production via CO_2 hydrogenation. The batch processes require a high pressure autoclaved reactor and a catalyst dispersed in solvent bubbled or pressurized with CO_2 and H_2 high pressure MFCs. Further, the batch process necessitates a substantial amount of difference in catalyst design strategy as compared to that of flow process. The activation of CO_2 is equally challenging in both flow and batch process owing to the CO_2 stability and difficulty in gaseous hydrogen and CO_2 dissolution in the reaction medium in case of batch process and lower interaction with solid catalyst bed in case of flow reaction. Here better CO_2 dissolution in solvent medium is ensured by adding basic additives in solvent or introducing electron donating group in the catalyst. For instance, to ensure higher CO_2 conversion, in homogenous catalysis electron donating ligands are present over metal sites. However, the catalytic activity of homogeneous catalysis is highly dependent on the ligand utilised, which may expensive and leachable limiting their utilisation in commercial scale. The disadvantages posed by homogenous catalyst can overcome by heterogenous catalyst since they are easy to recover after a reaction and can be used in a big industrial process as a part of continuous reaction systems. In case of heterogenous catalysis instead of basic electron donating ligands, the base additives in the reaction medium make CO_2 gas dissolve and interact with catalyst. The basic additives also activates CO_2 by formation of bent conformation.[8] CO_2 combines chemically with an aqueous base, such as KOH or NaOH, to produce bicarbonates (HCO_3), which are the true precursors for further hydrogenation to produce formate/formic acid.

In comparison to homogeneous systems, fewer heterogeneous catalysts for FA synthesis via CO_2 hydrogenation have been described to date. The process is often activated by

a noble metal such as Pd,[9, 10] Ru,[11] or Au[12] in the case of heterogeneous catalysts, with Pd demonstrating particularly high performance. Yamashita *et al.* have shown that when the composition of a binary Pd-Ag alloy is improved, it has substantially higher activity than Pd.[13] Heterogenous catalysis of CO_2 to FA suffers from low activity owing to their lower interaction ability with CO_2. The interaction of CO_2 and heterogenous catalysts can be improved by optimizing the support and active metal interaction. For instance, Liu *et al.* developed a Schiff base modified gold catalyst activating CO_2 as carbamates and facilitating subsequent hydrogenation.[12] Here CO_2 gets captured by the dissolved amines in the solution as carbamates which gets transferred to Schiff base of the catalyst and reduced by expensive Au catalyst leading to scaling up issues. A recent report by Yamashita and co-workers inevitably proves that the CO_2 capture efficiency of the catalyst support directly improves the CO_2 conversion to FA.[14] They condensed different aldehydes with 3-aminopropyltriethoxysilane (APTES) to generate nano-porous polymer silica (NPS) composites by 12 hour hydrothermal treatment, which acted as CO_2 capture efficient support to distribute active metals. The longer hydrothermal treatment makes it a less green catalyst.

In this chapter, we rationally designed a few integrated systems for the capture of CO_2. SBA-15 was functionalized by condensing APTES and aldehydes (Butyraldehyde or Glutaraldehyde) by a longer hydrothermal treatment. Direct Schiff base formation and functionalisation over SBA-15 have been succeeded in a single step process. These supports were loaded with various active metals including Pd, Ni, Ag and Co and screened for CO_2 to FA in batch process. The support with highest CO_2 capture capacity measured *via* both dynamic and static capture experiments happens to be the best catalyst for CO_2 to FA conversion. The relationship between the activity and electronic state of Ag and Ni in Pd-Ag and Pd-Ni were studied with the help of XAS, which proposed Ni system induce better charge polarization favoured highest ever activity reported towards CO_2 to FA in a heterogenous catalyst.

5.2. Experimental Section

5.2.1. Chemicals and reagents

Pluronic P123, cetyltrimethylammonium bromide (CTAB), tetraethylorthosilicate (TEOS), ethanol, dry toluene, (3-aminopropyl) triethoxysilane were used as purchased without any further purification except toluene. Molecular sieves were heated at 200 °C and commercially procured toluene was poured to it slowly. Using this process toluene was dried and water-free, and it was stored and kept for further synthetic application.

5.2.2. Material Synthesis

5.2.2.1. Preparation of SBA-15

The support material Santa Barbara Amorphous (SBA-15) was synthesized by following the procedure given in previous chapters.

5.2.2.2. Functionalisation of SBA-15

APTES-Aldehyde + SBA-15 (Direct Method): An amount of 1.5 g of as synthesized SBA-15 was suspended in dry toluene; amine loading was conducted via the addition of 2.4 ml APTES and 9.82 ml of the respective aldehyde in complete inert condition using nitrogen to make sure there is no oxidation of APTES prior to amine grafting. The mixture was stirred at 40 °C overnight in the nitrogen atmosphere. The resulting compound was dried overnight at 60 °C.

Aldehyde-APTES/SBA-15 (Indirect Method): An amount of 1.5 g of as synthesized SBA-15 was suspended in dry toluene; amine loading was conducted via the addition of 2.4 ml APTES in complete inert condition using the nitrogen atmosphere. The mixture was stirred at 40 °C overnight in the nitrogen atmosphere. The resulting compound (APTES/SBA-15) was dried overnight at 60 °C.

An amount of 0.5 g of APTES grafted SBA-15 (APTES/SBA-15) was dispersed in 20 ml deionized water and 6.61 ml of the respective aldehyde was slowly added under constant stirring. Hydrothermal treatment of the mixture was done using a 50 ml autoclave at 150 °C for 12 hours. The resulting compound was filtered and washed using deionized water and further dried overnight at 60 °C.Glutaraldehyde and Butyraldehyde were used in this reaction for the condensation of amines. The synthesized materials were acronym as APTES-BUT-D/Ex and APTES-GLU-D/Ex for Butyraldehyde and Glutaraldehyde based aldehyde respectively, whereas D and Ex reflects the direct method synthesis and Ex stands for the *ex-situ* preparation *via* indirect method of synthesis.

5.2.2.3. Metal nanoparticle incorporation to functionalised support

APTES-Aldehyde-D (0.2 g) was suspended in 50 ml deionized water and stirred for 10 mins. The nitrate salts of Pd and Ni/Ag/Co were weighed to get respective loading concentration and stirred for 30 mins. The metal nitrates were reduced using $NaBH_4$ addition and stirred for another 30 mins. The resulting precipitate was filtered and washed using DI water. A similar method was used for the metal impregnation on APTES-Aldehyde-Ex and other supports.

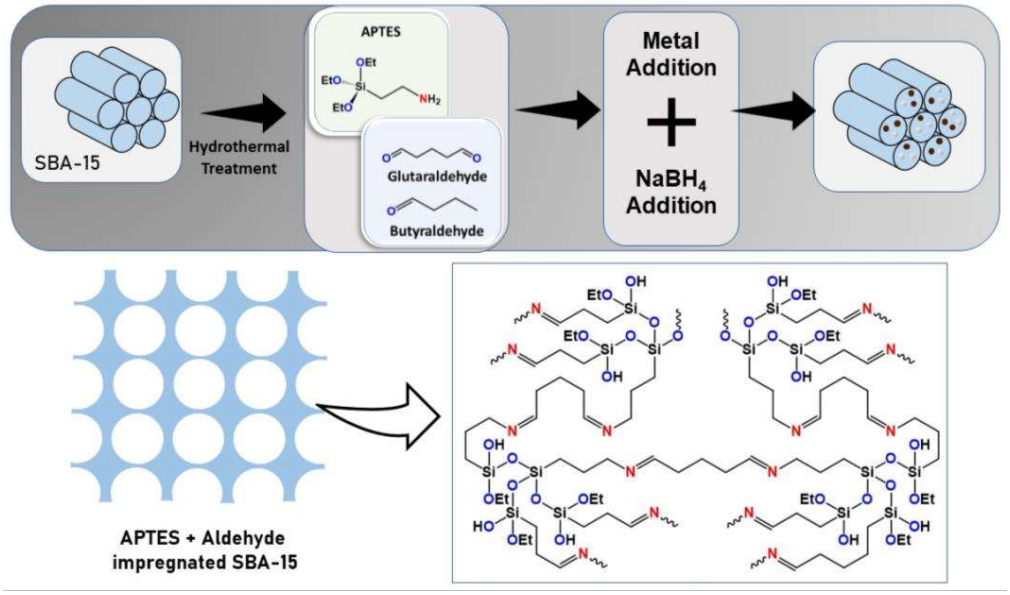

Figure 5.1. Schematic illustration of steps involved during synthesis of Metal(s)/APTES-(GLU/BUT)-(D/Ex).

For better reactivity comparison different ratio of Pd to Ni/Ag combinations were also used. The schematic representation of the procedure is given in **Figure 5.1**. Monometallic Pd, Ni, Ag and Co were also synthesized by same metal incorporation synthetic steps taking respective concentration of their nitrate salt solution.

5.2.3. Material Characterization

5.2.3.1. Inductively Coupled Plasma – Optical Emission Spectroscopy (ICP-OES)

ICP-OES was performed using a Perkin Elmer Optima 7000 DV instrument. The samples were first digested in concentrated aqua regia prepared in the lab. Then samples were treated with 2-3 drops of HF to remove silica of SBA-15 and finally diluted with distilled water. In a typical experiment, 5 mg of the sample was dissolved in 3-5 ml aqua regia and heated at 333 K for digestion. The digested sample was then treated with 3-5 drops of HF and diluted to 10 ml volume with deionized water, from this 1 ml was again taken and diluted to 10 ml. The solid particles were separated by thorough centrifugation before measurements.

5.2.3.2. Fourier Transformed Infrared Spectra (FTIR)

FTIR spectra were recorded with Perkin Elmer L125000P in the mid-IR region ($\tilde{\upsilon}$ = 4000–400 cm^{-1}) using the powdered samples. The functionalised silica as well as the aldehyde condensed samples were analysed and functional groups are confirmed using the standard wavenumber values available in literature.

5.2.3.3. X-ray Photoelectron Spectroscopy (XPS)

XPS measurements were carried out using Thermo K-alpha+ spectrometer using micro focused and monochromated Al Kα radiation with energy 1486.6 eV. The pass energy for spectral acquisition was kept at 50 eV for individual core-levels. The electron flood gun was utilized for providing charge compensation during data acquisition. Further, the individual core-level spectra were checked for charging using C1s at 284.6 eV as standard and corrected if needed. The peak fitting of the individual core-levels was done using CasaXPS software with a Shirley type background.

5.2.3.4. Powder X-ray Diffraction (XRD)

The phase formation on SBA-15 was confirmed by X-ray diffraction (XRD) collected on PANalytical X-ray diffractometer with Cu Kα radiation at 45 kV and 40 mA. The features of the PXRD patterns were compared with simulated pattern from Pearson Database. The catalysts powder XRD were compared with simulated phases of cubic Ag (S.G: $Fm\bar{3}m$), Pd (S.G: $Fm\bar{3}m$) and Ni (S.G: $Fm\bar{3}m$).

5.2.3.5. N_2 adsorption-desorption isotherms

The adsorption isotherms were studied by using N_2 at 77 K on BELSORP max II analyzer. Prior to the measurements, the powders were treated for degassing at 423 K for 6 hours. The specific surface area was confirmed by Brunaur-Emmett-Teller (BET) method and pore size distribution by classical BJH (Barrett, Joyner and Halenda) method. The N_2 adsorption-desorption experiment exhibits type IV isotherm (Brunauer definition) with hysteresis loop, typical of hexagonal and cylindrical mesoporous materials. There is a fast increase in adsorption volume between 0.6-0.8 p/p_0 which is indicative of capillary condensation attributed to the pre-formation of N_2 on the pore walls due to multilayer adsorption. The metal impregnated samples exhibited a left shift of the sharp rise in the adsorption isotherms and drastically diminished surface areas. This lowering of surface area concludes that impregnated clusters decrease the N_2 probing surface inside the mesopores.

5.2.3.6. Transmission Electron Microscope (TEM)

TEM images and selected area electron diffraction patterns were collected using a JEOL JEM-2010 TEM instrument and color mapping was done in TECHNAI. The samples for these measurements were prepared by sonicating the nanocrystalline powders in ethanol and drop-casting a small volume onto a carbon-coated copper grid.

5.2.3.7. X-ray Absorption Spectroscopy (XAS)

Measurements of Pd-*K*, Ni-*K* and Ag-*K* edges at ambient pressure were performed in fluorescence as well as transmission mode using gas ionization chambers to monitor the incident and transmitted X-ray intensities. at PETRA III, P64 beamline of DESY, Germany. Monochromatic X-rays were obtained using a Si (111) double crystal monochromator, which was calibrated by defining the inflection point (first derivative maxima) of Cu foil as 8980.5 eV. The beam was focused by employing a Kirkpatrick-Baez (K-B) mirror optic. Rhodium-coated X-ray mirror was used to suppress higher-order harmonics. A CCD detector was used to record the transmitted signals. Pellets for the ex-situ measurements were made by homogeneously mixing the sample with an inert cellulose matrix to obtain an X-ray absorption edge jump close to one. The XAS data processing were done using the ATHENA[15] software. The multiple data were collected and averaged out before proceeding to the background correction. The averaged data were smoothed out using the standard kernel size of 11. The weak spline was used for background correction in the pre-edge region. All the data were normalized for the Standard data analysis procedure was used to extract the extended X-ray absorption fine structure (EXAFS) signal from the measured absorption spectra.

5.2.4. CO_2 Capture test

5.2.4.1. Dynamic Uptake Experiment

CO_2 capture capacity of a material can be calculated at constant pressure by flowing CO_2 containing simulated gas through the capture material distributed in a bed loaded inside a tubular reactor **(Figure 5.2)**.

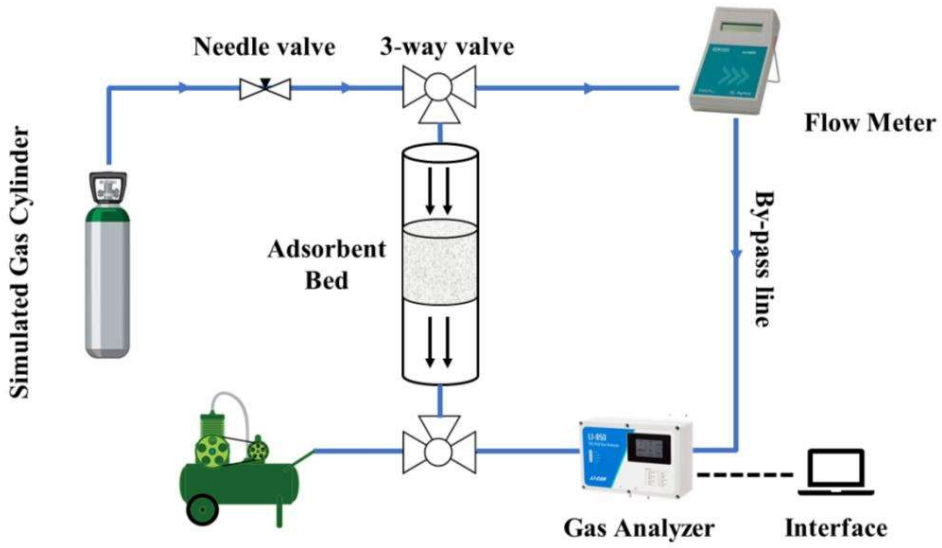

Figure 5.2. Schematic representation of dynamic uptake experiment setup.

Overall adsorption kinetics of the material can only be observed from the dynamic experiment. To perform the dynamic uptake experiment, sample were taken in a quartz tube, and simulated gas cylinder (5000 ppm CO_2 balanced with air) was connected to it and gas is allowed to pass through the adsorbent bed at a particular flow rate. The outlet of the quartz tube is connected to an IR-based gas analyzer LI COR (LI-850) to sense the CO_2 (**Figure 5.2**). The experiment is performed till the saturation of material. In order to calculate the uptake, the relative CO_2 concentration (C_t/C_0) is plotted against the time, where C_t represent the outlet concentration of CO_2 at time t, and C_0 is the CO_2 concentration of simulated gas cylinder. Breakthrough point is defined as the duration till material is sustained to adsorb CO_2 at its full efficiency. After that adsorption capacity is decreased, and slowly the material moves towards the saturation (**Figure 5.3**).

The uptake value till breakthrough point can be calculated straight forward using the conventional equation, (**eqn. 5.1**)

$$q_b = \frac{F \times C_0 \times t_b}{W} \tag{5.1}$$

q_b is the uptake capacity till breakthrough point. F is the flow rate (ml/s), C_0 is the concentration of CO_2 inside simulated gas cylinder, t_b is breakthrough time (s), W is the mass of adsorbent (g). Thus, the q_b can be obtained in terms of ml of CO_2 per g of sorbent, which can also be converted to mg of CO_2 per g of sorbent. (CO_2; 1 mole ≡ 44.01 g ≡ 22400 ml).

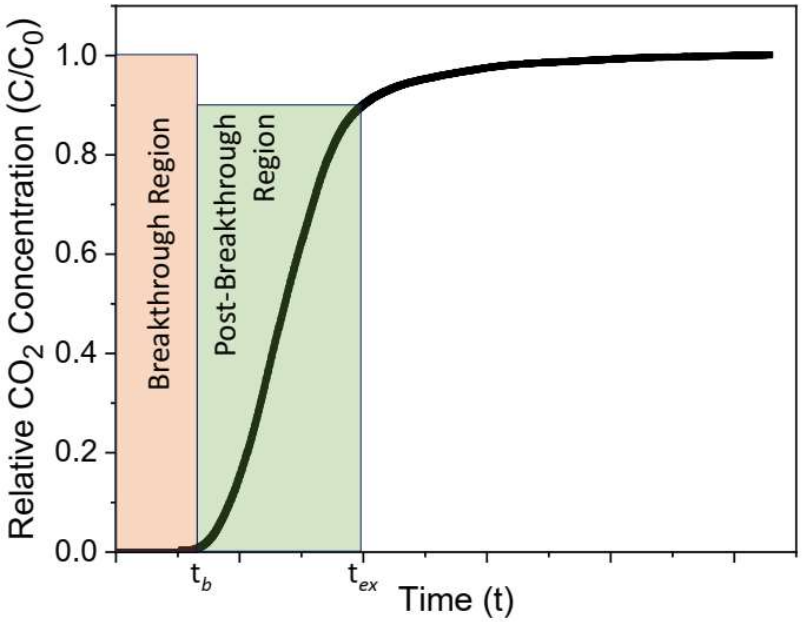

Figure 5.3. CO_2 Uptake Profile: Relative Conc. vs Time.

Even after the breakthrough point, the CO_2 adsorption occur with a lesser efficiency when it is compared to the breakthrough region. In order to calculate the uptake for that particular region, Avirami kinetics model has been used, which considers multiple adsorption pathways. (**eqn. 5.2**)

Considering this model, the uptake is considered from breakthrough point to exhaustion point (C_t/C_0 is 0.9).[16] The value has been taken based on criterion that the adsorption kinetics is very slow after 0.9 value and extrapolated that the uptake is too negligible to consider. Hence in the conventional equation, time can be replaced with stoichiometric time to calculate CO_2 uptake. (**eqn. 5.3**) As the plot is considered for C_t/C_0 vs time, C_t/C_0 is an unitless entity, hence the product is nothing but the time.

$$q_b = \frac{F \times C_0 \times t_b}{W} \tag{5.2}$$

$$t_q = \int_{t_b}^{t_{ex}} \left(1 - \frac{C_t}{C_0}\right).dt \tag{5.3}$$

t_q is the stoichiometric time, t_{ex} is exhaustion time, t_b is the breakthrough time. C_t is concentration of CO_2 at t time. The overall uptake for the adsorbent material can be considered as the sum of q_b and q_a. (**eqns. 5.1** and **5.2**).

5.2.4.2. Static Uptake Experiment

The static uptake experiment was performed via BELSORP max II analyzer using CO_2 gas as the adsorbate. For the desired experiment two different temperatures were taken into consideration; one being 40 °C to mimic the experimental condition as implemented for the batch process CO_2 hydrogenation, and another is 0 °C or 273 K. During the experiment small amount of sample (200 – 500 mg) was weighed and transferred into sample tube and vacuumized thoroughly at 50 °C for 12 hours to ensure maximum degassing without degrading the amine part present in the samples, prior to the experiment. The temperatures 40 °C and 0 °C were maintained using water and methanol respectively, taken into solvent bath.

5.3. Results and Discussion

5.3.1. Catalyst Characterization

Monometallic (Co, Ni, Ag and Pd) and bimetallic (Pd-Ag and Pd-Ni and Pd-Co) nanoparticles (NPs) on different APTES-Aldehyde/SBA-15 supports were synthesized. The

details of the synthesis are already provided in the experimental section and schematic illustration is depicted in **Figure 5.1**. Two different synthesis strategies have been used; (1) Direct method - SBA-15 was dispersed in dry toluene and functionalized and condensed with APTES and aldehyde in a concerted step and (2) Indirect method - APTES was functionalized first on SBA-15 followed by condensation with the aldehyde and hydrothermal treatment at 150 °C for 12 hours. These Schiff bases are named as APTES-(GLU/BUT)-(D/Ex), where GLU or BUT represents the aldehyde (Glutaraldehyde and Butyraldehyde respectively) used in the condensation, D; represents direct one-pot aldehyde addition and Ex; *ex-situ* aldehyde addition with hydrothermal treatment over functionalized SBA-15. The schematic depiction of APTES-aldehyde condensation is shown in **Figure 5.4**. Wet impregnation was used to deposit the metal precursors on these supports, which were then reduced by $NaBH_4$. The ICP-OES analysis of the catalyst presented in **Table 5.1** confirming the loading amount of metals on Schiff base functionalized SBA-15.

The XRD patterns obtained from the supported Pd-Ag and Pd-Ni catalysts are shown in **Figure 5.5**. It was reported that Pd interact with amine or imine N during the reduction procedure on amine-modified mesoporous surfaces to yield very smaller particles of 1.2 nm.[14, 17] However, Ag has weak interaction with N species causing the aggregation of the nanoparticles.

Table 5.1. ICP-OES data of different Pd-Ni, Pd-Ag and Pd-Co system on different Schiff base functionalized SBA-15.

Catalyst	Wt % of Metals	
	Pd	Ni or Co or Ag
Pd-Ni/APTES-GLU-D (200 mmol)	9.40	8.67
Pd-Co/APTES-GLU-D (200 mmol)	9.36	9.74
Pd-Ag/APTES-GLU-D (200 mmol)	9.83	9.4
Pd-Ag/APTES-BUT-D (200 mmol)	9.11	9.5
Pd-Ag/APTES-GLU-Ex (200 mmol)	9.62	9.3
Pd-Ni/APTES-GLU-Ex (200 mmol)	9.58	9.16
Pd-Ag/APTES-BUT-Ex (200 mmol)	9.36	8.94
Pd-Ni/APTES-BUT-Ex (200 mmol)	9.2	9.10
Pd_3Ni/APTES-GLU-D (200 mmol)	14.81	4.93
$PdNi_3$/APTES-GLU-Ex (200 mmol)	4.87	14.94
Pd_3Ag/APTES-GLU-D (200 mmol)	14.95	4.63
$PdAg_3$/APTES-GLU-D (200 mmol)	4.83	14.88
Pd-Ag/APTES-GLU-D (20 mmol)	0.92	0.93
Pd-Ni/APTES-GLU-D (20 mmol)	0.89	0.94

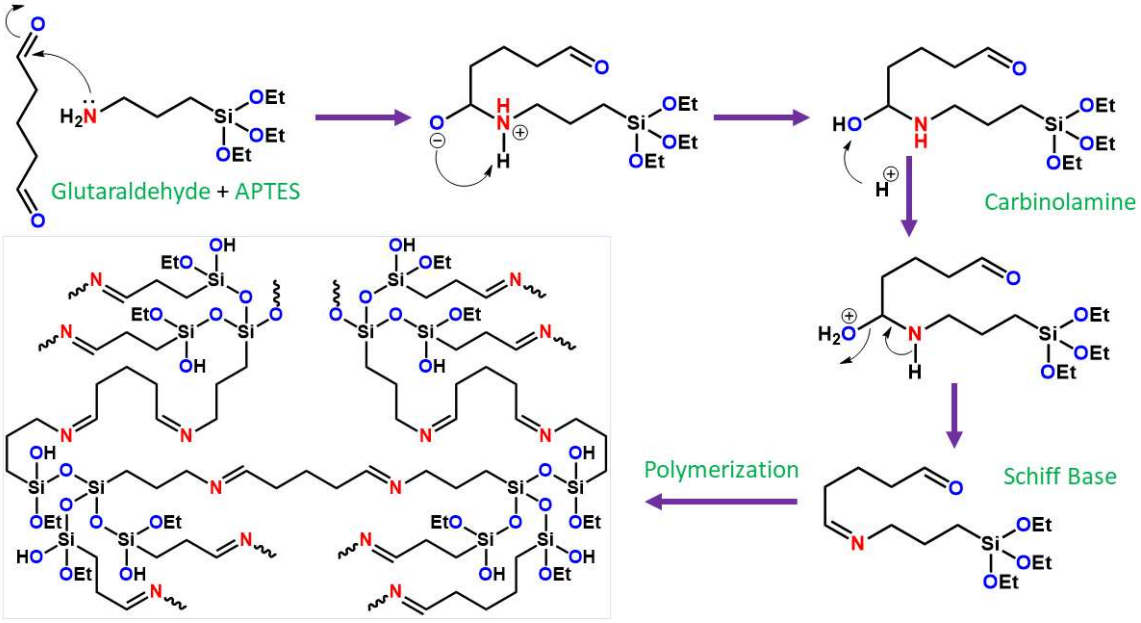

Figure 5.4. Schematic representation of condensation of glutaraldehyde with APTES.

Since there is a notable difference in the formation nanoparticle size between Pd (small) and Ag (large), the XRD pattern of Pd-Ag over APTES-GLU-D will show up only peaks corresponding to metallic Ag.[14] Consequently, Pd alloyed with Ag NPs crystallizing in the Ag structure formed in the case of Pd-Ag system. On the other hand, Pd-Ni on support **(Figure 5.5b)** crystallizes in the face-centered cubic (fcc) Pd confirming the substitution of Ni into the Pd lattice. The new peaks corresponding to N-H_{str}, CH_2 bending and CH_2 stretching are clearly exhibited by APTES functionalized SBA-15 confirming the APTES functionalization inside mesoporous SBA-15 **(Figure 5.6a)**.

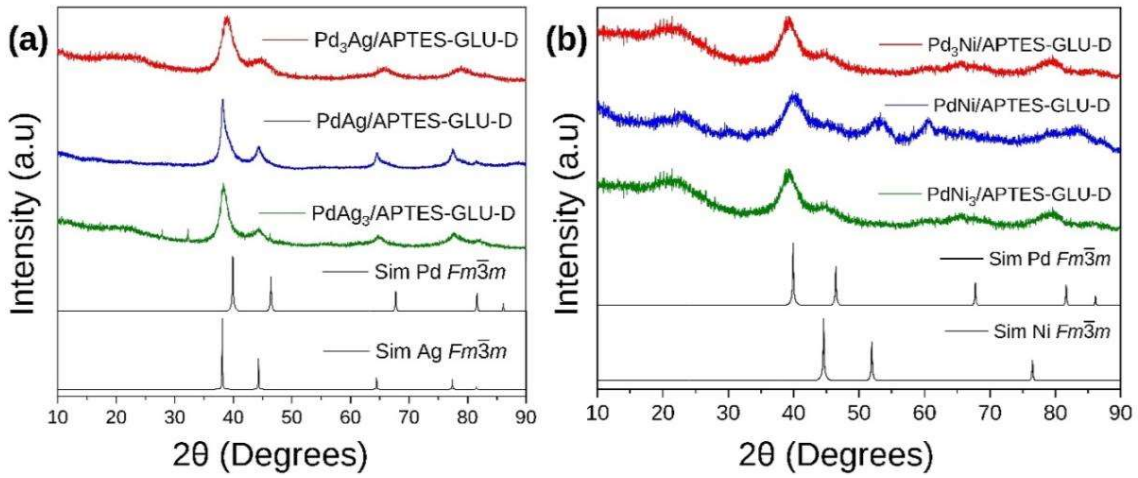

Figure 5.5. (a) XRD patterns of Pd-Ag/APTES-GLU-D and (b) Pd-Ni/APTES-GLU-D compared with corresponding metal nanoparticles.

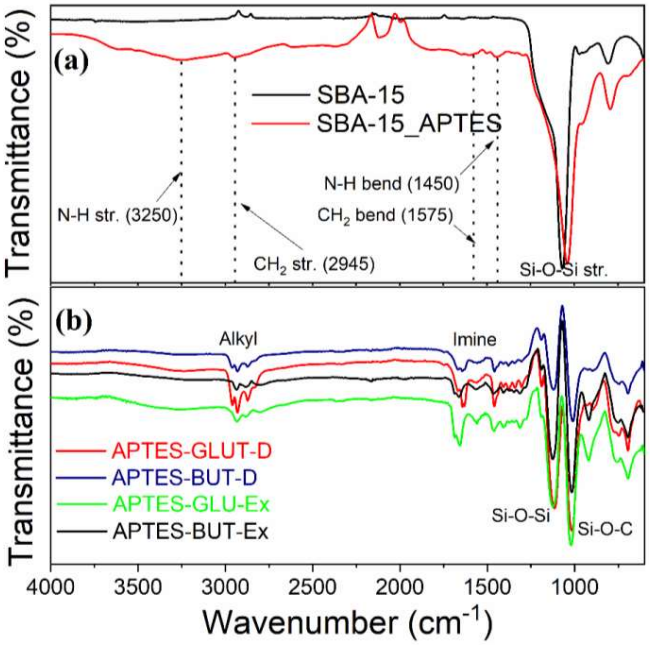

Figure 5.6. FTIR spectra of (a) SBA-15 and APTES functionalized SBA-15 and (b) various SBA-15/APTE-aldehyde support (Schiff base functionalized SBA-15).

Although a substantial difference in the IR spectra between APTES functionalized SBA-15 and the aldehyde condensed samples, all the spectra of condensed samples produced similar peaks, including alkyl (2930 cm^{-1}), imine (1650 cm^{-1}), and Si-O-Si and Si-O-C groups (1000-1150 cm^{-1}) **(Figure 5.6b)**. The appearance of imine peak at 1650 cm^{-1} and disappearance of $N\text{-}H_{str}$ clearly confirm a Schiff base formation by the condensation of carbonyl of glutaraldehyde/butyraldehyde with the amine groups of APTES. The N_2 adsorption-desorption isotherm of SBA-15 and Schiff base functionalized SBA-15 (**Figures S5.7a** and **S5.7b)** confirms the blockage of mesopores by the silica nanoparticles formed from APTES. The pore blockage and loss of meso-porosity are further confirmed by TEM images of SBA-15 before and after Schiff base functionalization. **Figure S5.7c** shows well defined mesoporous channels of SBA-15 while in **Figure S5.7d** and **S5.7e** corresponding to APTES-GLU-D and APTES-GLU-Ex, respectively, are devoid of any channels. Both mesoporosity and high surface area of SBA-15 lost during the functionalization, but the porosity of SBA-15 has led to better distribution of Schiff base throughout the silica matrix.

5.3.2. CO_2 Capture Capacity

To estimate the CO_2 interaction with the support, the as-synthesized materials were tested for their CO_2 uptake via both dynamic and static (at 0 and 40 °C) mode of experiments (**Figures 5.8-5.9** and **Tables 5.2-5.3**).

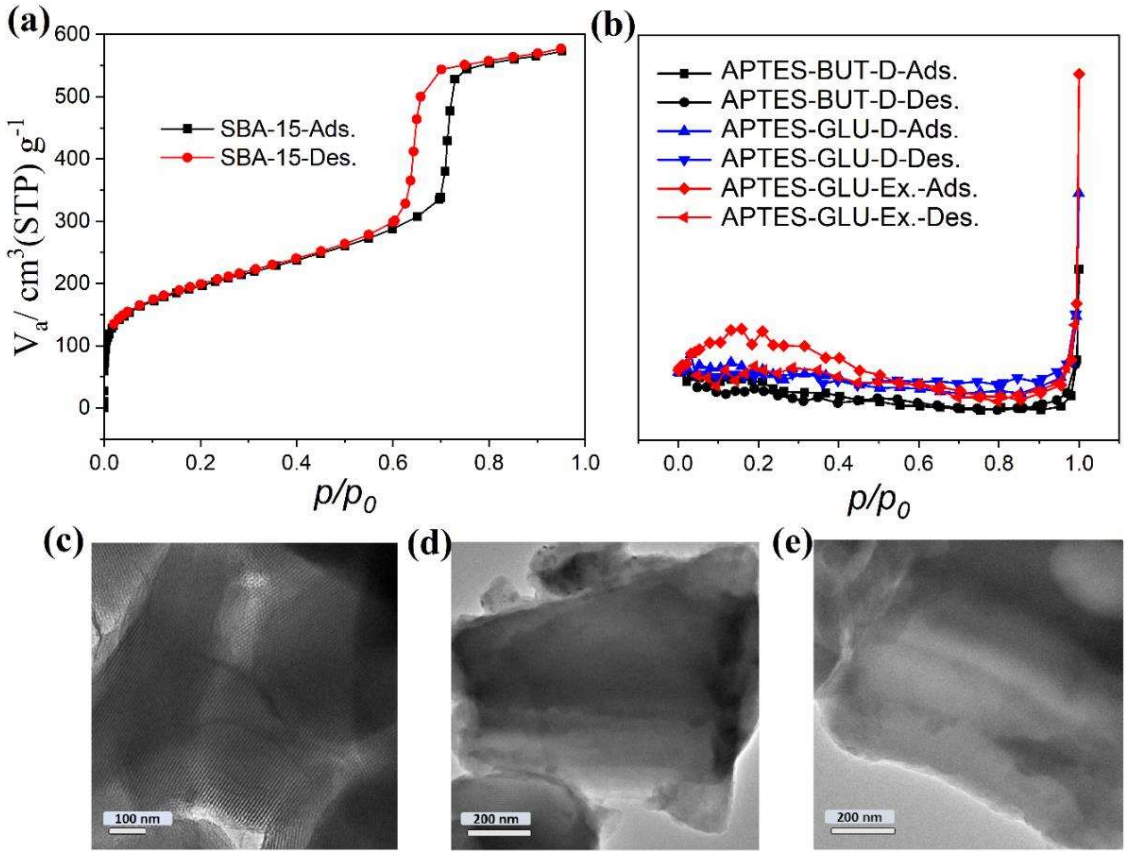

Figure 5.7. N_2 adsorption-desorption spectra of (a) SBA-15, (b) APTES-GLU-D, APTES-BUT-D and APTES-GLU-Ex combined. (c) TEM image of SBA-15, (d) TEM image of APTES-GLU-D and (e) APTES-GLU-Ex.

It is well clear that APTES-GLU-D has the highest CO_2 capture efficiency as reflected in both experiments. Depending on the mode of amine functionalization, the amine-based sorbents can be classified into four class of materials.[18-20] According to the classifications, either the aminosilanes can be tethered to the dangling OH groups of the support materials *via* co-condensation (Class II),[21] or amine monomers are *in-situ* polymerized on porous support material (Class III).[22, 23] However, this work propose the condensation and polymerization between aldehyde and aminosilane to form a nitrogen doped polymer silica network over SBA-15. The data depicted in **Figures 5.8-9** and **Tables 5.2**-5.**3** suggest that one-pot synthesis of APTES-GLU is the best adsorbent material compared to APTES-GLU-Ex and other two supports. On the other hand, APTES-BUT-Ex obtained via two-step synthetic procedure shows a better result compared to APTES-BUT-D. It can be concluded that the synthetic procedures are the quintessential parameter to govern the uptake property of the APTES-Aldehyde materials.

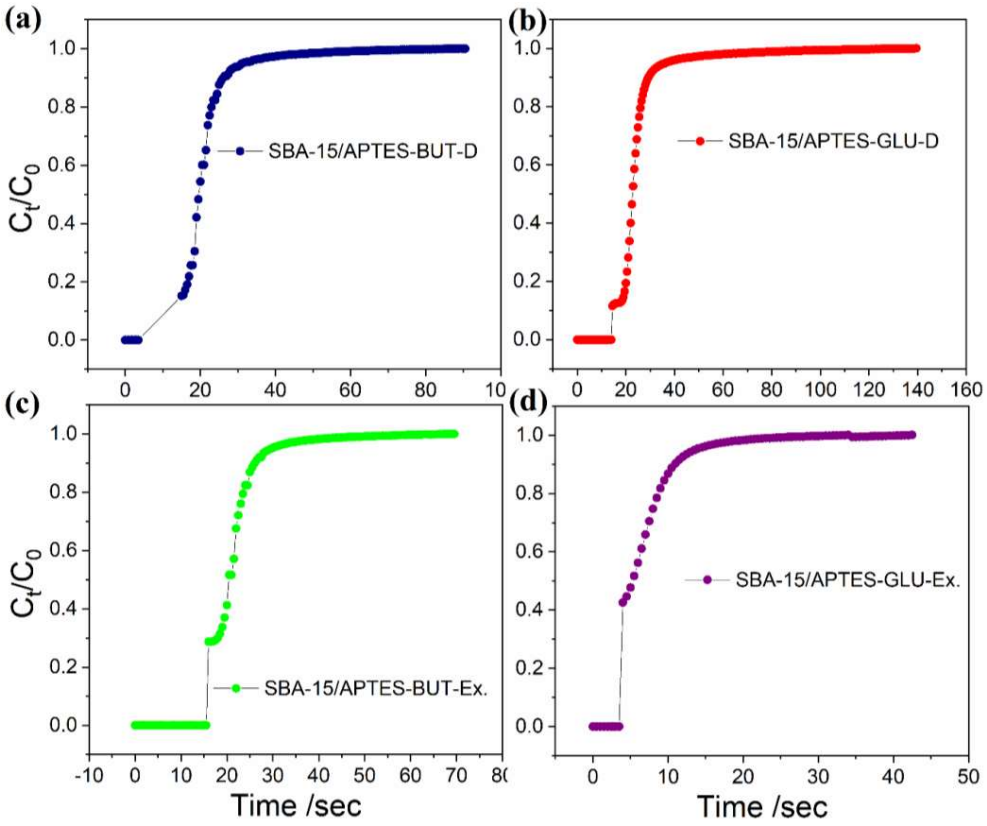

Figure 5.8 CO_2 uptake profile obtained from dynamic uptake experiment; (a) APTES-BUT-D, (b) APTES-GLU-D, (c) BUT-APTES-Ex, (d) GLU-APTES-Ex.

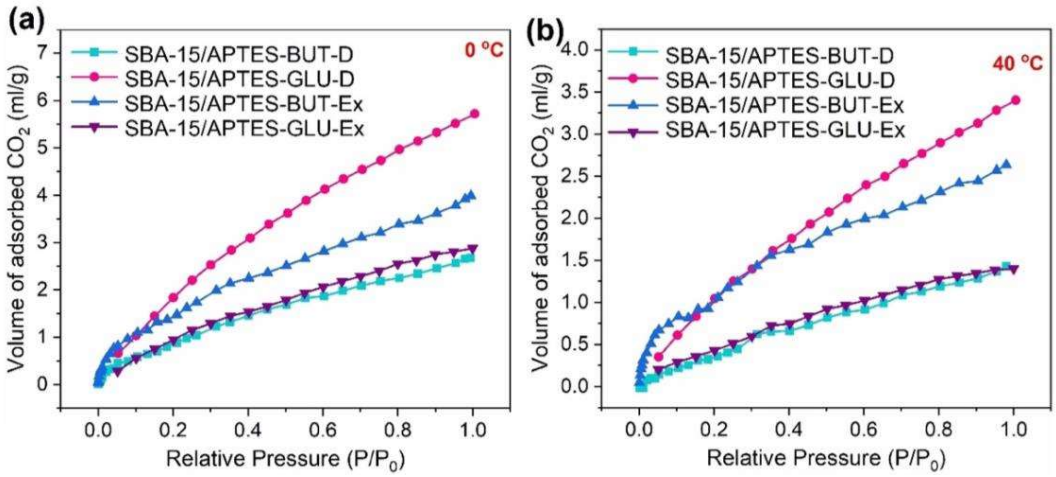

Figure 5.9. CO_2 uptake profile obtained from static uptake experiment (a) at 273 K and (b) at 303 K.

XPS analysis was exploited to understand the driving force behind the high CO_2 uptake by APTES-BUT-D, which shows characteristic C-1s and N-1s core level peaks for all the materials (**Figure 5.10a-h)**.

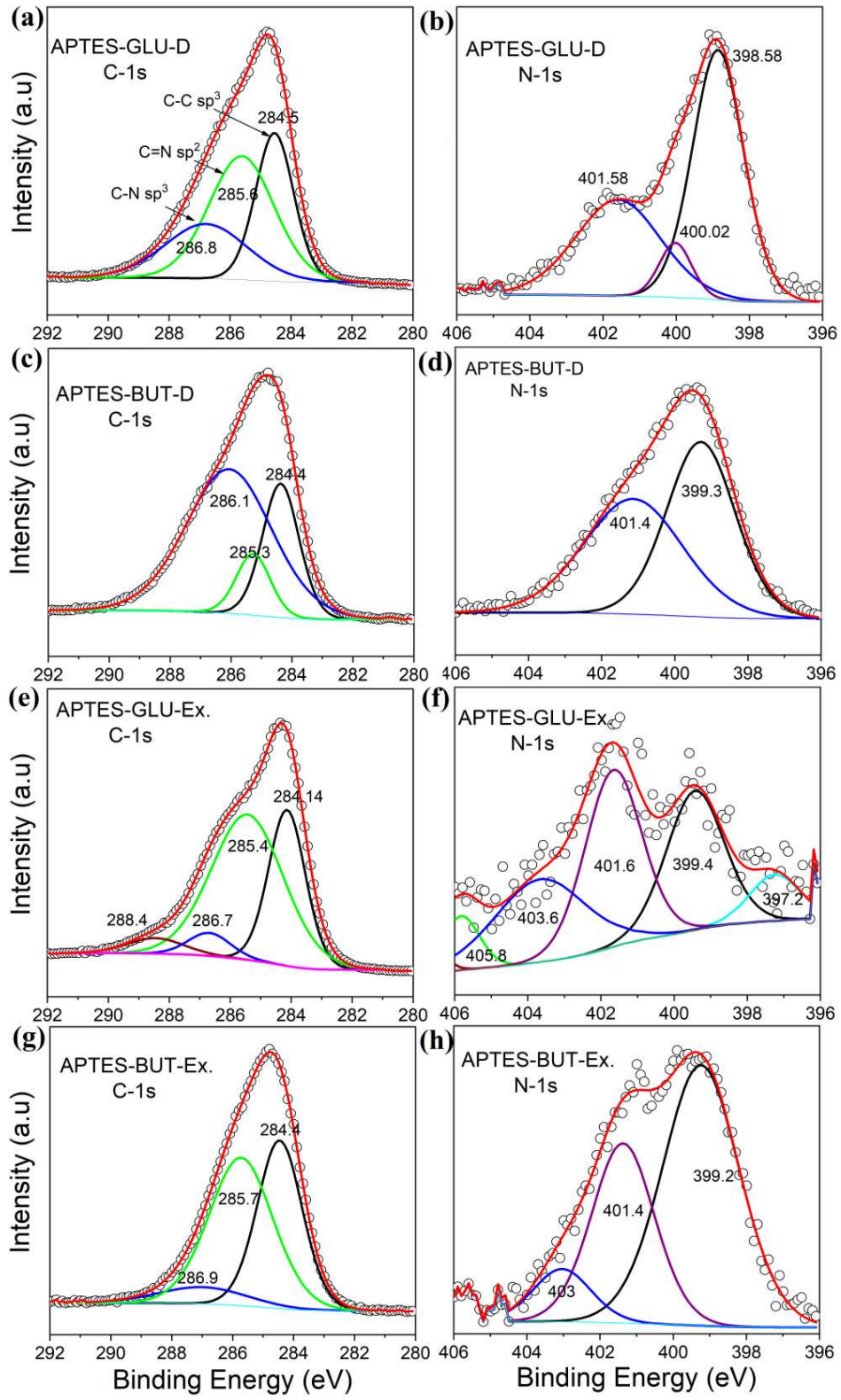

Figure 5.10. XPS spectra of (a) C-1s and (b) N-1s spectra of APTES-GLU-D, XPS spectra of (c) C-1s and (d) N-1s spectra of APTES-BUT-D, (e) C-1s and (f) N-1s spectra of APTES-GLU-Ex, (g) C-1s and (h) N-1s spectra of APTES-BUT-Ex.

Table 5.2. CO_2 uptake results obtained from Dynamic uptake experiment.

Adsorbent Materials	CO_2 Uptake (ml $CO_2/g_{sorbent}$)		Total Uptake	
	Breakthrough	Post-Breakthrough	(ml $CO_2/g_{sorbent}$)	(mg $CO_2/g_{sorbent}$)
APTES-BUT-D	0.69	0.17	0.86	1.69
APTES-GLU-D	1.17	0.59	2.29	4.5
APTES-BUT-Ex	0.39	1.49	1.88	3.69
APTES-GLU-Ex	0.29	0.19	0.48	0.94

Table 5.3. CO_2 uptake comparison in static mode of experiment in different temperatures.

Adsorbent Materials	CO_2 Uptake (ml $CO_2/g_{sorbent}$)	
	40 °C (303 K)	0 °C (273 K)
APTES-BUT-D	1.43	2.68
APTES-GLU-D	3.4	5.72
APTES-BUT-Ex	2.64	1.88
APTES-GLU-Ex	1.4	2.88

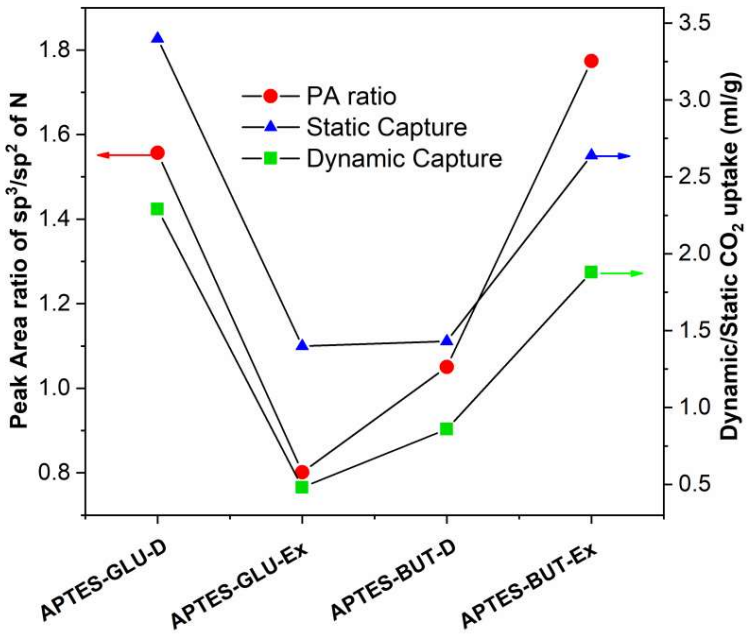

Figure 5.11. Comparison between CO_2 uptake (dynamic and static) with relative peak area ratio of amine-N (sp^3 N) and imine-N (sp^2 N) deconvoluted by XPS fitting of N-1s.

The C-1s peaks were deconvoluted into Gaussian components revealed the peaks corresponding to C-C sp^3, C-N sp^2 (-C=N-) and C-N sp^3 assigned at 284.5 eV, 285.6 eV, 286.5

eV, respectively, with slight left/right shift in all Schiff base functionalized silica samples.[24-26] The peak corresponding to C-N sp^2 confirms the formation of imine linkage or carbonyl-amine condensation to form Schiff base. It should be noted that an additional peak corresponding to sp^2 C-O is seen in APTES-GLU-Ex pointing un-reacted carbonyl group **(Figure 5.10e)**. The N-1s core level peaks corresponding to amine-N (around 399 eV) and imine-N (around 401.5 eV) commonly for all samples again implying a Schiff base formation.[27] The peak area ratio of sp^3 to sp^2 N of each Schiff base condensed supports were determined to understand the relative presence of amine-N and imine-N in each sample and extend of condensation between aldehyde and APTES. The decreasing order of sp^3 to sp^2 peak area ratio is APTES-BUT-Ex > APTES-GLU-D > APTES-BUT-D > APTES-GLU-Ex (**Figure 5.11)**. Both dynamic and static CO_2 capture also follows same trend except a slight lesser capture uptake by APTES-BUT-Ex compared to that of APTES-GLU-D. The CO_2 capture trend is in accordance with the fact that the amine-N with less s-orbital character is more basic than imine-N with higher s-orbital character. However, the slight lesser capture performance of APTES-BUT-Ex compared to that of APTES-GLU-D, despite of higher amine-N presence in the former can be attributed to the oxidation of N due to ex-situ functionalization process in the former confirmed by an high energy peak observed at 403 eV **(Figure 5.10h)**.[28] The presence of oxidized-N species hampers the Lewis basicity of the support and adversely affect the CO_2-Support interaction. The lowest CO_2 capture in case of APTES-GLU-Ex is accredited to maximum condensation of APTES-GLU to form imines (sp^2 N) along with the presence of oxidized N **(Figure 5.10f)**. Based on the XPS analysis, it can be concluded that synthetic conditions have been optimized to tune the hybridization of N in these materials, which facilitates efficient uptake of CO_2.

5.3.3. CO_2 to Formic Acid

The CO_2 reduction performance of the catalyst were studied in a Parr autoclave batch reactor at 30 °C, 40 °C and 50 °C in a H_2/CO_2 mixture (20/20 bar) with 0.5 M $KHCO_3$ as an additive in the liquid phase. The HPLC analysis identified the exclusive formation of formic acid (FA) while no gaseous products other than CO_2 and H_2 are observed in the GC analysis. In the initial step, the best support material APTES-GLU-D was used for the impregnation of metals Pd, Ni, Ag and Co independently. From the comparison at various temperature and pressure conditions, it is evident that Pd impregnated on APTES-GLU-D yielded FA, but negligible amount of FA was observed in the case of Ni, Ag and Co monometallic based systems **(Figure 5.11a** and **Table 5.4)**.

The notable activity of Pd based system compared to others can be attributed due to their hydrogen spill-over ability to the intermediates of CO_2 to FA process.[29, 30] To improve the CO_2 reduction to FA activity further, Pd metal along with other metals as bimetallic (Pd-Co, Pd-Ni and Pd-Ag) have impregnated to APTES-GLU-D and tested their activity using similar conditions. The results are summarized in **Table 5.5**. The best optimized TON was obtained for Pd-Ag impregnated on APTES-GLU-D for 12 hrs operation owing to its best CO_2 capture by APTES-GLU-D support (**Figure 5.12b** and **Table 5.5**). It was concluded that the FA production in 12 hours is almost 2.4 times higher on Pd-Ag compared to Pd-Ni while leaving Pd-Co as the least. The activity has been tested at variable temperature and found that the optimum condition for the best performance is at 40 °C (**Figure 5.12c** and **Table 5.6**). The activity towards CO_2 to FA has been reduced at higher temperature can be correlated to the exothermic nature,[18] while lower temperature (below 40 °C) may be inefficient to activate both CO_2 capture[31, 32] and conversion. In the next step, pressure condition is also optimized by performing the reactions at 30 and 40 bar pressure. As expected, the catalytic activity has been increased upon increasing the pressure **(Figure 5.12d** and **Table 5.7)**. Since our high-pressure reactor has the set maximum 45 bar pressure, the rest of the experiments have been performed at a safer pressure of 40 bar.

Table 5.4. CO_2 reduction test results of monometallic (Pd, Ni, Co, and Ag) (200 μM) on APTES-GLU-D/SBA-15 support at 40 ºC and 40 Bar.

Catalyst	Reaction Condition			TON (mol_{FA}/mol_{Pd})	TOF (h^{-1})
	Temperature (°C)	Pressure / CO_2:H_2 (Bar)	Time (h)		
Pd/APTES-GLU-D	40	20/20	12	51.6	4.3
Ag/APTES-GLU-D	40	20/20	12	0.15	0.012
Ni/APTES-GLU-D	40	20/20	12	0.19	0.016
Co/APTES-GLU-D	40	20/20	12	0.11	0.009

Table 5.5. CO_2 reduction test results of Bi-metallic (Pd-Co, Pd-Ni, and Pd-Ag) (200 μM) on APTES-GLU-D/SBA-15 support at 40 ºC and 40 Bar.

Catalyst	Reaction Condition			TON (mol_{FA}/mol_{Pd})	TOF (h^{-1})
	Temperature (°C)	Pressure / CO_2:H_2 (Bar)	Time (h)		
Pd-Ni/APTES-GLU-D	40	20/20	12	63.2	5.3
Pd-Co/APTES-GLU-D	40	20/20	12	11.1	0.92
Pd-Ag/APTES-GLU-D	40	20/20	12	146	12.2

Table 5.6. CO_2 reduction test results of Pd-Ni/APTES-GLU-D (200 μM) at different temperature and 40 Bar.

Catalyst	Reaction Condition			TON (mol_{FA}/mol_{Pd})	TOF (h^{-1})
	Temperature (°C)	Pressure / CO_2:H_2 (Bar)	Time (h)		
Pd-Ni/APTES-GLU-D	30	20/20	12	47.5	3.95
Pd-Ni/APTES-GLU-D	40	20/20	12	63.2	5.3
Pd-Ni/APTES-GLU-D	50	20/20	12	60.6	5

Table 5.7. CO_2 reduction test results of Pd-Ni/APTES-GLU-D (200 μM) at different pressure and 40 °C.

Catalyst	Reaction Condition			TON (mol_{FA}/mol_{Pd})	TOF (h^{-1})
	Temperature (°C)	Pressure / CO_2:H_2 (Bar)	Time (h)		
Pd-Ni/APTES-GLU-D	40	15/15	12	56.5	4.7
Pd-Ni/APTES-GLU-D	40	20/20	12	63.2	5.3

To understand the contribution from support towards CO_2 to FA activity, the best metal combination Pd-Ni on all four supports were compared. It was seen that the best TON and TOF was exhibited by APTES-GLU-D followed by others **(Figure 5.12e** and **Table 5.8)**, which is perfectly in line with CO_2 update experiments. Thus, it was inevitably concluded that one pot synthesized APTES-GLU over silica is the best support material for the CO_2 to FA conversion. Several systems with different Pd:Ni and Pd:Ag ratio were prepared to deconvolute the influence of Pd in Pd-Ni and Pd-Ag systems. These compounds were tested at already optimized reaction conditions, and the best results were exhibited by 1:1 mole ratio of Pd-Ni and Pd-Ag systems (**Figure 5.12f** and **Table 5.9)**. Further, the effect of metal loading over APTES-GLU-D support were also compared with Pd-Ag and Pd-Ni systems. In both systems, the TON improved upon lower metal loading (20 μmol metal to 2000 μmol metal). Precisely, the TON has been increased by two times in the case of Pd-Ni system at lower loading while less than 30% improvement was seen in the case of Pd-Ag system **(Figure 5.12g** and **Table 5.10)**. To understand the effect of time, Pd-Ag and Pd-Ni systems supported on APTES-GLU-D were screened at 15 mins instead of 12 hours. Interestingly, Pd-Ni system favored 5 times higher TON than Pd-Ag system, which can be interpreted that the stability of Pd-Ni degraded with time. However, it is worth to mention that Pd-Ni system exhibits very high reactivity from t_0 producing enormous amount of FA in very short interval facilitates the reaction medium more acidic or less basic hampering the acidic CO_2 dissolution in the solvent for further conversion.[14] A proper engineering can be exploited to negate this issue by removing formic acid periodically.

Figure 5.12h and **Table 5.11** provides a comparison between the actual and expected TON with respect to time. It is evident that at a rate of 53 TON for 15 mins, Pd-Ni catalyst is expected to attain a TON above 2500 after 12 hours**,** but it saturates at 132 due to non-dissolution of CO_2 in the acidic medium**.** On the other hand, TON of 11 for Pd-Ag at 15 minutes extended to 12 hours it would result in a TON of 528 (11 TON ×4×12 hours), instead it saturates at 181.5 TON after 12 hours. Thus, it can be concluded that Pd-Ni has better active sites for CO_2 to FA compared to Pd-Ag system.

Table 5.8. CO_2 reduction test results of Pd-Ni (200 μM) on different supports at 40 ºC and 40 Bar.

Catalyst	Reaction Condition			TON (mol_{FA}/mol_{Pd})	TOF (h^{-1})
	Temperature (℃)	Pressure / CO_2:H_2 (Bar)	Time (h)		
Pd-Ni/APTES-GLU-D	40	20/20	12	63.2	5.3
Pd-Ni/APTES-GLU-Ex.	40	20/20	12	9.9	0.83
Pd-Ni/APTES-BUT-D	40	20/20	12	20.2	1.7
Pd-Ni/APTES-BUT-Ex.	40	20/20	12	28.6	2.4

Table 5.9. CO_2 reduction test results of Pd_xNi_{1-x} (Pd_3Ni, PdNi, and $PdNi_3$) and Pd_xAg_{1-x} (Pd_3Ag, PdAg and $PdAg_3$) (200 μM) on APTES-GLU-D/SBA-15 support at 40 ºC and 40 Bar.

Catalyst	Reaction Condition			TON (mol_{FA}/mol_{Pd})	TOF (h^{-1})
	Temperature (℃)	Pressure / CO_2:H_2 (Bar)	Time (h)		
Pd_3Ni/APTES-GLU-D	40	20/20	12	4.75	0.39
PdNi/APTES-GLU-D	40	20/20	12	63.2	5.3
$PdNi_3$/APTES-GLU-D	40	20/20	12	2.3	0.2
Pd_3Ag/APTES-GLU-D	40	20/20	12	7.4	0.61
PdAg/APTES-GLU-D	40	20/20	12	146	12.2
$PdAg_3$/APTES-GLU-D	40	20/20	12	4.5	0.38

Table 5.10. CO_2 reduction test results of Pd-Ni/APTES-GLU-D with different concentration at 40 ºC and 40 Bar.

Catalyst	Reaction Condition			TON (mol_{FA}/mol_{Pd})	TOF (h^{-1})
	Temperature (℃)	Pressure / CO_2:H_2 (Bar)	Time (h)		
Pd-Ni/APTES-GLU-D (20)	40	20/20	12	132.2	11.01
Pd-Ni/APTES-GLU-D (200)	40	20/20	12	63.2	5.3
Pd-Ni/APTES-GLU-D (2000)	40	20/20	12	5.53	0.46

Table 5.11. CO_2 reduction test results on Pd-Ni/APTES-GLU-D (20 µM) with different time interval at 40 ºC and 40 Bar.

Catalyst	Reaction Condition			TON (mol_{FA}/mol_{Pd})	TOF (h^{-1})
	Temperature (°C)	Pressure / CO_2:H_2 (Bar)	Time (h)		
Pd-Ni/APTES-GLU-D	40	20/20	12	132.2	3.95
Pd-Ni/APTES-GLU-D	40	20/20	0.25	53	212
Pd-Ag/APTES-GLU-D	40	20/20	12	181.5	15.1
Pd-Ag/APTES-GLU-D	40	20/20	0.25	11	44.6

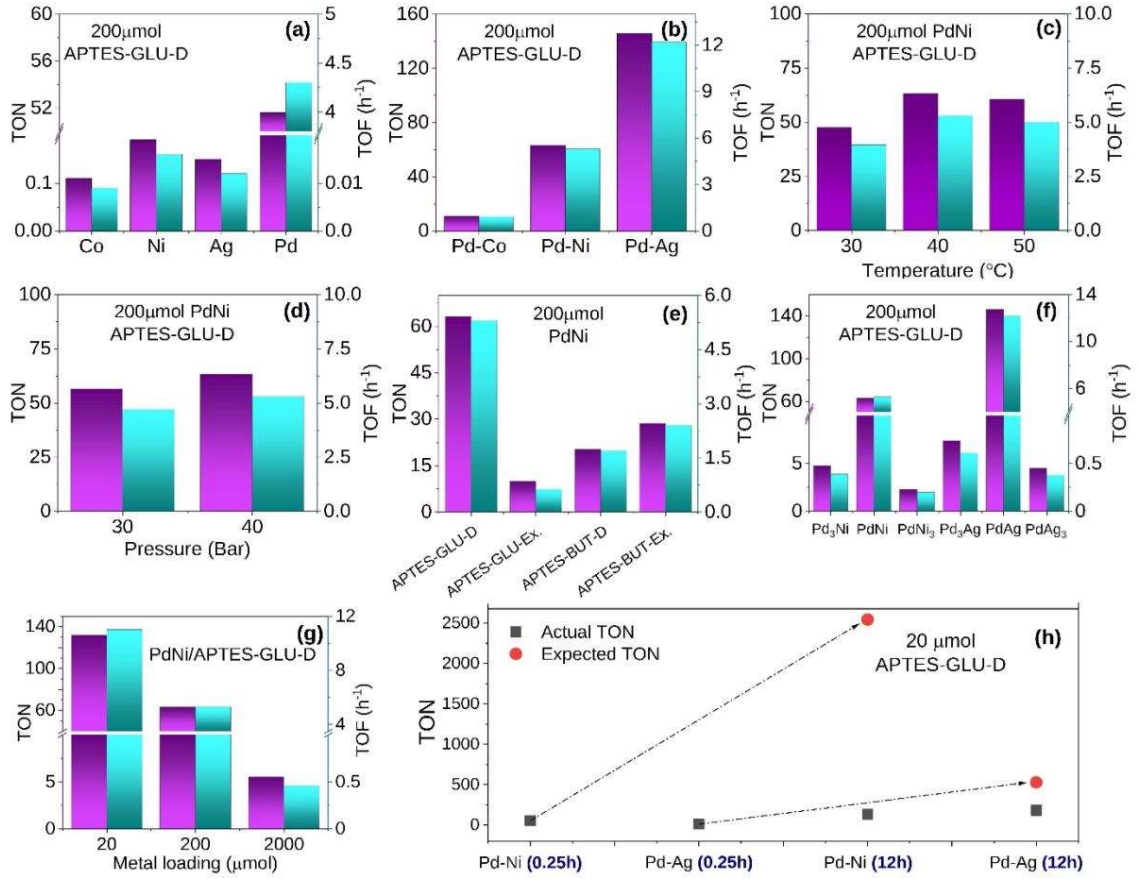

Figure 5.12. CO_2 to formic acid test: TON and TOF comparison (a) among monometallic Co, Ni, Ag and Pd supported on APTES-GLU-D (200 micro mol metal loading over 0.2g support), (b) different bimetallic system of Pd-Co, Pd-Ni and Pd-Ag over 0.2 g support in 12 hours batch process, (c) Pd-Ni/APTES-GLU-D at different temperature, (d) Pd-Ni/APTES-GLU-D at different pressure, (e) Pd-Ni/APTES-GLU-D over different support, (f) different Pd-Ni and Pd-Ag bimetallic systems supported over APTES-GLU-D, (g) Pd-Ni/APTES-GLU-D for different metal loading over 0.2 g support, (h) 20 µmol Pd-Ni Vs Pd-Ag supported on 0.2g APTES-GLU-D for 15 mins and 12 hours batch process.

5.3.4. X-ray Absorption Spectra

XAS has been used to elucidate the higher activity of Pd-Ni over Pd-Ag catalyst. The Ni K-edge XANES shows that the oxidation state of Ni is higher than 2+ in all the Pd-Ni-based catalysts as the position of the absorption edge is higher than that of the standard Ni^{2+} sample **(Figure 5.13a)** further confirmed in the white line intensity. Ni K-edge Fourier transformed (FT) EXAFS spectra of all the samples show a highly intense singlet peak at around 1.5 Å corresponding to the Ni-N or Ni-C bonds in the 1st coordination sphere **(Figure 5.13b)**.[33-35] The peak at 2.7 Å can be assigned to the Ni-Pd bond confirming the alloy formation.[36] There is no metallic Ni-Ni bonding present in the samples as there is no indication of Ni-Ni peak at 2.15 Å further confirms that Ni not crystallizing as Ni metal.[37] The XANES spectra Ag K edge shows that the white line intensity of Ag in the Pd-Ag-based catalysts is less than that of the pristine Ag/APTES-GLU-D catalyst indicating Ag has higher electron density in the bimetallic catalysts than that of monometallic Ag catalyst **(Figure 5.13c)**.[38] The Ag K-edge EXAFS spectra of all samples show an intense singlet peak corresponding to metallic bonding at approximately 2.7 Å. The little hump at about 1.8 Å may be due to C coordinated Ag bond formed on the surface (**Figure 5.13d**).[39] The XANES spectra of the Pd K-edge in Pd-Ag catalyst clearly indicate that Pd is most likely to be in the metallic state (**Figure 5.13e**).

Negligible change in the white line intensity in the Pd-Ag-based catalyst than that of Pd foil indicates the former has a similar electron density to that of elemental Pd.[40] The Pd K-edge EXAFS spectrum shows that the Pd-Ag-based catalysts have a peak at approximately 1.5 Å, which corresponds to Pd-N of Pd-C bonds in Pd-Ag/APTES-GLU-D (**Figure 5.13f**).[41] The peak at 1.8-1.9 Å in Pd-Ag/APTES-GLU-Ex (Pd_3Ag and $PdAg_3$ supported on APTES-GLU-D) is mostly due to the surface Pd-O bond present in the samples. The peak at 2.6 Å has been shifted to a higher radial distance than that of the Pd-Pd bond present in Pd foil, clearly indicating the incorporation of Pd at the crystal lattice of Ag and the formation of Ag-Pd bond in an alloy, which is in agreement with the PXRD analysis **(Figure 5.5)**.On the other hand, Pd in Pd-Ni catalysts has a slightly higher oxidation state than that of the elemental Pd **(Figure 5.13g)**. The white line intensity in the case of the PdNi/APTES-GLU-D sample is lower than that of Pd_3Ni/APTES-GLU-D and $PdNi_3$/APTES-GLU-D indicates that the former has higher electron density which is close to elemental Pd.[40] The Pd K-edge EXAFS spectrum shows that all the Pd-Ni-based catalysts have a peak of approximately 1.8-1.9 Å can be assigned as Pd-O bond, which may present at the surface of the samples can be detrimental for the catalytic activity in the long term stability testing (**Figure 5.13h**).

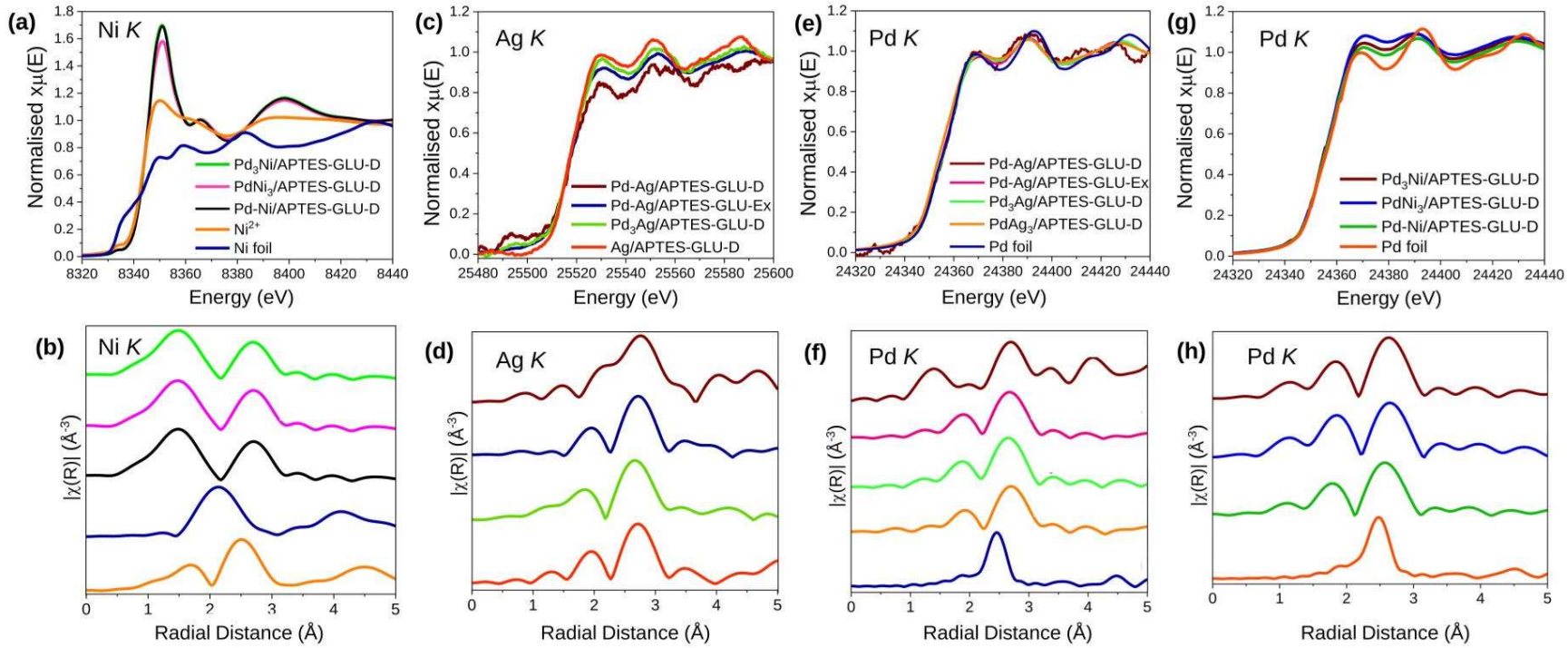

Figure 5.13. (a) Comparison of normalized XANES spectra of Ni K-edge of the synthesized samples with the respective metal foil and reference sample. (b) Fourier transformed R-space data showing the radial distances of different bonds present in the samples. (c) Comparison of normalized XANES spectra of Ag K-edge of the synthesized samples with the respective reference sample. (d) Fourier transformed R-space data showing the radial distances of different bonds present in the samples. (e) Comparison of normalized XANES spectra of Pd K-edge of Pd-Ag system with the respective reference sample. (f) Fourier transformed R-space data showing the radial distances of different bonds present in the samples. (g) Comparison of normalized XANES spectra of Pd K-edge of Pd-Ni system with the respective reference sample. (f) Fourier transformed R-space data showing the radial distances of different bonds present in the sample.

The peak at 2.6 Å, which has a higher radial distance than that of the Pd-Pd bond present in Pd foil can account for the formation Pd-Ni bond and lead into the $Pd_{1-x}Ni_x$ alloy formation. Both XANES and EXAFS analysis of Ni and Ag confirm that the oxidation state of Ni is higher than the Ni^{2+}, while electron density of Ag is higher than that of monometallic Ag loaded on APTES-GLU-D. It is apparent that the electron negativity difference between Ni/Ag and Pd plays a pivotal role in the CO_2 to FA activity.[42] The CO_2 reduction step commences with H_2 interacting with the electron rich Pd site, while the electronegative oxygen of CO_2 molecule interacts with the more electropositive site, which activates CO_2. The positively charged C atom on the CO_2 molecule is nucleophilically attacked by spilled H atom of electron rich Pd site, and FA is desorbed with the production of an OH bond as shown in **Figure 5.14.** The electron-deficient sites present along with Pd species is critical in this regard since it activates CO_2 on its surface. Ni sites in Pd-Ni system have better electron deficiency compared to that of Pd-Ag supported on APTES-GLU-D cause Pd-Ni system acts as a better catalyst than Pd-Ag.

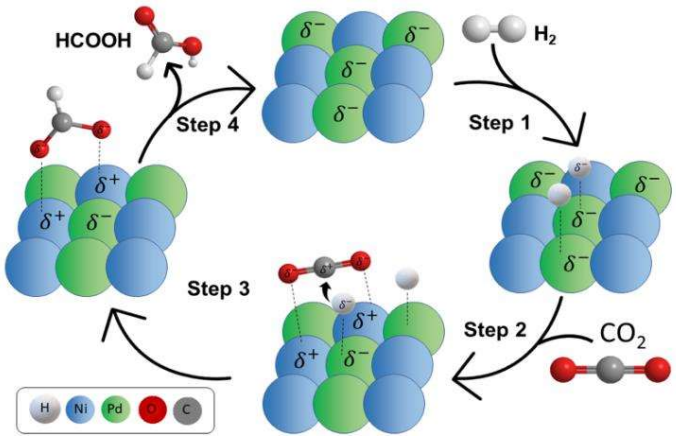

Figure 5.14. Proposed mechanism for the CO_2 to FA conversion over Pd-Ni/APTES-GLU-D.

5.4. Conclusion

In conclusion, an imine-based support material was synthesized by condensing APTES with different aldehydes over SBA-15. The condensation process induced an optimum formation of amine/imine ratio by controlling the hybridization of C and N atoms of APTES, which is very crucial for efficient CO_2 capture and its subsequent reduction. To utilize this rational design metals were impregnated to the Schiff base and optimized the best metal combination by controlled experiments. Among them, Pd-Ni and Pd-Ag alloys exhibited remarkable conversion of CO_2 to FA, which is the highest ever reported to the best of our knowledge. The superior activity Pd-Ni system compared to its second best Pd-Ag and other combination has been explained with the help of XAS. The large electronegativity difference between Pd and Ni tuned charge polarization favouring the better conversion of CO_2 to FA.

5.5. References

1. Moret, S.; Dyson, P. J.; Laurenczy, G., Direct Synthesis of Formic Acid from Carbon Dioxide by Hydrogenation in Acidic Media. *Nat. Commun.* **2014,** *5* (1), 4017.
2. Eppinger, J.; Huang, K.-W., Formic Acid as a Hydrogen Energy Carrier. *ACS Energy Lett.* **2017,** *2* (1), 188-195.
3. Álvarez, A.; Bansode, A.; Urakawa, A.; Bavykina, A. V.; Wezendonk, T. A.; Makkee, M.; Gascon, J.; Kapteijn, F., Challenges in the Greener Production of Formates/Formic Acid, Methanol, and DME by Heterogeneously Catalyzed CO_2 Hydrogenation Processes. *Chem. Rev.* **2017,** *117* (14), 9804-9838.
4. Grasemann, M.; Laurenczy, G., Formic Acid as a Hydrogen Source-Recent Developments and Future Trends. *Energy Environ. Sci.* **2012,** *5* (8), 8171-8181.
5. Sordakis, K.; Tang, C.; Vogt, L. K.; Junge, H.; Dyson, P. J.; Beller, M.; Laurenczy, G., Homogeneous Catalysis for Sustainable Hydrogen Storage in Formic Acid and Alcohols. *Chem. Rev.* **2018,** *118* (2), 372-433.
6. Cherevotan, A.; Raj, J.; Dheer, L.; Roy, S.; Sarkar, S.; Das, R.; Vinod, C. P.; Xu, S.; Wells, P.; Waghmare, U. V.; Peter, S. C., Operando Generated Ordered Heterogeneous Catalyst for the Selective Conversion of CO_2 to Methanol. *ACS Energy Lett.* **2021,** *6* (2), 509-516.
7. Tedsree, K.; Li, T.; Jones, S.; Chan, C. W. A.; Yu, K. M. K.; Bagot, P. A. J.; Marquis, E. A.; Smith, G. D. W.; Tsang, S. C. E., Hydrogen Production from Formic Acid Decomposition at Room Temperature using a Ag–Pd Core-Shell Nanocatalyst. *Nat. Nanotechnol.* **2011,** *6* (5), 302-307.
8. Hao, C.; Wang, S.; Li, M.; Kang, L.; Ma, X., Hydrogenation of CO_2 to Formic Acid on Supported Ruthenium Catalysts. *Catal. Today* **2011,** *160* (1), 184-190.
9. Masuda, S.; Mori, K.; Futamura, Y.; Yamashita, H., PdAg Nanoparticles Supported on Functionalized Mesoporous Carbon: Promotional Effect of Surface Amine Groups in Reversible Hydrogen Delivery/Storage Mediated by Formic Acid/CO_2. *ACS Catal.* **2018,** *8* (3), 2277-2285.
10. Lee, J. H.; Ryu, J.; Kim, J. Y.; Nam, S.-W.; Han, J. H.; Lim, T.-H.; Gautam, S.; Chae, K. H.; Yoon, C. W., Carbon Dioxide Mediated, Reversible Chemical Hydrogen Storage using a Pd Nanocatalyst Supported on Mesoporous Graphitic Carbon Nitride. *J. Mater. Chem. A* **2014,** *2* (25), 9490-9495.

11. Srivastava, V., In situ Generation of Ru Nanoparticles to Catalyze CO_2 Hydrogenation to Formic Acid. *Catal. Lett.* **2014,** *144* (10), 1745-1750.
12. Liu, Q.; Yang, X.; Li, L.; Miao, S.; Li, Y.; Li, Y.; Wang, X.; Huang, Y.; Zhang, T., Direct Catalytic Hydrogenation of CO_2 to Formate over a Schiff-base-mediated Gold Nanocatalyst. *Nat. Commun.* **2017,** *8* (1), 1407.
13. Mori, K.; Sano, T.; Kobayashi, H.; Yamashita, H., Surface Engineering of a Supported PdAg Catalyst for Hydrogenation of CO_2 to Formic Acid: Elucidating the Active Pd Atoms in Alloy Nanoparticles. *J. Am. Chem. Soc.* **2018,** *140* (28), 8902-8909.
14. Masuda, S.; Mori, K.; Kuwahara, Y.; Louis, C.; Yamashita, H., Additive-Free Aqueous Phase Synthesis of Formic Acid by Direct CO_2 Hydrogenation over a PdAg Catalyst on a Hydrophilic N-Doped Polymer–Silica Composite Support with High CO_2 Affinity. *ACS Appl. Energy Mater.* **2020,** *3* (6), 5847-5855.
15. Ravel, B.; Newville, M., ATHENA, ARTEMIS, HEPHAESTUS: Data Analysis for X-ray Absorption Spectroscopy using IFEFFIT. *J. Synchrotron Radiat.* **2005,** *12* (4), 537-541.
16. Chowdhury, Z.; Zain, S.; Rashid, A.; Rafique, R.; Khalid, K., Breakthrough Curve Analysis for Column Dynamics Sorption of Mn (II) Ions from Wastewater by using Mangostana Garcinia Peel-Based Granular-Activated Carbon. *J. Chem.* **2013,** *2013*.
17. Masuda, S.; Mori, K.; Futamura, Y.; Yamashita, H., PdAg Nanoparticles Supported on Functionalized Mesoporous Carbon: Promotional Effect of Surface Amine Groups in Reversible Hydrogen Delivery/Storage Mediated by Formic Acid/CO_2. *ACS Catal.* **2018,** *8* (3), 2277-2285.
18. Cherevotan, A.; Raj, J.; Peter, S. C., An Overview of Porous Silica Immobilized Amines for Direct Air CO_2 Capture. *J. Mater. Chem. A* **2021**, *9* (48), 27271-27303.
19. Didas, S. A.; Choi, S.; Chaikittisilp, W.; Jones, C. W., Amine-Oxide Hybrid Materials for CO_2 Capture from Ambient Air. *Acc. Chem. Res.* **2015,** *48* (10), 2680-2687.
20. Ray, B.; Churipard, S. R.; Peter, S. C., An Overview of the Materials and Methodologies for CO_2 Capture Under Humid Conditions. *J. Mater. Chem. A* **2021,** *9* (47), 26498-26527.
21. Goeppert, A.; Czaun, M.; May, R. B.; Prakash, G. K. S.; Olah, G. A.; Narayanan, S. R., Carbon Dioxide Capture from the Air Using a Polyamine Based Regenerable Solid Adsorbent. *J. Am. Chem. Soc.* **2011,** *133* (50), 20164-20167.

22. Lunn, J. D.; Shantz, D. F., Peptide Brush-Ordered Mesoporous Silica Nanocomposite Materials. *Chem. Mater.* **2009,** *21* (15), 3638-3648.

23. Choi, S.; Drese, J. H.; Eisenberger, P. M.; Jones, C. W., Application of Amine-Tethered Solid Sorbents for Direct CO_2 Capture from the Ambient Air. *Environ. Sci. Technol.* **2011,** *45* (6), 2420-2427.

24. Zhao, M.; Cao, Y.; Liu, X.; Deng, J.; Li, D.; Gu, H., Effect of Nitrogen Atomic Percentage on N+ Bombarded MWCNTs in Cytocompatibility and Hemocompatibility. *Nanoscale Res. Lett.* **2014,** *9* (1), 142.

25. Pozveh, A. A.; Kowsari, E.; Hashemi, M. M.; Mirjafari, Z., Preparation and Electromagnetic Wave Absorption Properties of Polymer Nanocomposites Based on New Functionalized Graphene Oxide Iron Pentacarbonyl and Ionic Liquid. *Rev. Chem. Intermed.* **2020,** *46* (2), 1329-1351.

26. Šetka, M.; Calavia, R.; Vojkůvka, L.; Llobet, E.; Drbohlavová, J.; Vallejos, S., Raman and XPS Studies of Ammonia Sensitive Polypyrrole Nanorods and Nanoparticles. *Sci. Rep.* **2019,** *9* (1), 8465.

27. Zhao, M.; Cao, Y.; Liu, X.; Deng, J.; Li, D.; Gu, H., Effect of Nitrogen Atomic Percentage on N^+-Bombarded MWCNTs in Cytocompatibility and Hemocompatibility. *Nanoscale Res. Lett.* **2014,** *9* (1), 142-142.

28. Harris, T. G.; Götz, R.; Wrzolek, P.; Davis, V.; Knapp, C. E.; Ly, K.; Hildebrandt, P.; Schwalbe, M.; Weidinger, I.; Zebger, I., Robust Electrografted Interfaces on Metal Oxides for Electrocatalysis-An In-situ Spectroelectrochemical Study. *J. Mater. Chem. A* **2018,** *6* (31), 15200-15212.

29. Barlocco, I.; Bellomi, S.; Delgado, J. J.; Chen, X.; Prati, L.; Dimitratos, N.; Roldan, A.; Villa, A., Enhancing Activity, Selectivity and Stability of Palladium Catalysts in Formic Acid Decomposition: Effect of Support Functionalization. *Catal. Today* **2021,** *382*, 61-70.

30. Liang, Y., Recent Advanced Development of Metal-Loaded Mesoporous Organosilicas as Catalytic Nanoreactors. *Nanoscale Adv.* **2021,** *3* (24), 6827-6868.

31. Xu, X.; Song, C.; Andrésen, J. M.; Miller, B. G.; Scaroni, A. W., Preparation and Characterization of Novel CO_2 "molecular basket" Adsorbents based on Polymer-Modified Mesoporous Molecular Sieve MCM-41. *Microporous Mesoporous Mater.* **2003,** *62* (1), 29-45.

32. Xu, X.; Song, C.; Andresen, J. M.; Miller, B. G.; Scaroni, A. W., Novel Polyethylenimine-Modified Mesoporous Molecular Sieve of MCM-41 Type as High-Capacity Adsorbent for CO_2 Capture. *Energy & Fuels* **2002,** *16* (6), 1463-1469.
33. Borrome, M.; Gronert, S., Gas-Phase Dehydrogenation of Alkanes: C-H Activation by a Graphene-Supported Nickel Single-Atom Catalyst Model. *Angew. Chem. Int. Ed.* **2019,** *131* (42), 15048-15052.
34. Mou, K.; Chen, Z.; Zhang, X.; Jiao, M.; Zhang, X.; Ge, X.; Zhang, W.; Liu, L., Highly Efficient Electroreduction of CO_2 on Nickel Single-Atom Catalysts: Atom Trapping and Nitrogen Anchoring. *Small* **2019,** *15* (49), 1903668.
35. Gong, Y. N.; Jiao, L.; Qian, Y.; Pan, C. Y.; Zheng, L.; Cai, X.; Liu, B.; Yu, S. H.; Jiang, H. L., Regulating the Coordination Environment of MOF-Templated Single-Atom Nickel Electrocatalysts for Boosting CO_2 Reduction. *Angew. Chem. Int. Ed.* **2020,** *132* (7), 2727-2731.
36. Zhang, F.; Ullah, M. W.; Zhao, S.; Jin, K.; Tong, Y.; Velisa, G.; Xue, H.; Bei, H.; Huang, R.; Park, C., Local Structure of NiPd Solid Solution Alloys and its Response to Ion Irradiation. *J. Alloys Compd.* **2018,** *755*, 242-250.
37. Kaiser, S. K.; Chen, Z.; Faust Akl, D.; Mitchell, S.; Pérez-Ramírez, J., Single-Atom Catalysts Across the Periodic Table. *Chem. Rev.* **2020,** *120* (21), 11703-11809.
38. Huang, Z.; Gu, X.; Cao, Q.; Hu, P.; Hao, J.; Li, J.; Tang, X. J. A. C. I. E., Catalytically Active Single-Atom Sites Fabricated from Silver Particles. *Angew. Chem. Int. Ed.* **2012,** *51* (17), 4198-4203.
39. Yang, G.; Kuwahara, Y.; Masuda, S.; Mori, K.; Louis, C.; Yamashita, H., PdAg Nanoparticles and Aminopolymer Confined within Mesoporous Hollow Carbon Spheres as an Efficient Catalyst for Hydrogenation of CO_2 to Formate. *J. Mater. Chem. A* **2020,** *8* (8), 4437-4446.
40. Liu, J.; Uhlman, M. B.; Montemore, M. M.; Trimpalis, A.; Giannakakis, G.; Shan, J.; Cao, S.; Hannagan, R. T.; Sykes, E. C. H.; Flytzani-Stephanopoulos, M., Integrated Catalysis-Surface Science-Theory Approach to Understand Selectivity in the Hydrogenation of 1-Hexyne to 1-Hexene on PdAu Single-Atom Alloy Catalysts. *ACS Catal.* **2019,** *9* (9), 8757-8765.
41. Lopes, C. W.; Cerrillo, J. L.; Palomares, A. E.; Rey, F.; Agostini, G., An in-situ XAS Study of the Activation of Precursor-Dependent Pd Nanoparticles. *Phys. Chem. Chem. Phys.* **2018,** *20* (18), 12700-12709.

42. Nguyen, L. T. M.; Park, H.; Banu, M.; Kim, J. Y.; Youn, D. H.; Magesh, G.; Kim, W. Y.; Lee, J. S., Catalytic CO_2 Hydrogenation to Formic Acid over Carbon Nanotube-graphene Supported PdNi Alloy Catalysts. *RSC Adv.* **2015,** *5* (128), 105560-105566.

SUMMARY & FUTURE OUTLOOK

The underlying motivation of this thesis is to develop cost-effective, durable, and scalable transition metal-based thermocatalysts for the efficient conversion of CO_2 to useful chemicals and fuels. This strategy can be exploited to curb global warming and the rapidly escalating energy crisis. All the catalysts designed and screened in this thesis include support dispersed with transition metal based monometallic and bimetallic systems, the later can be classified as alloys and intermetallics. Throughout the thesis inert silica-based oxide mesoporous supports have been used which are reported to offer minimum or no contribution towards any catalytic reaction besides offering surface for high dispersion of the active metal centers into nanoparticles. A plethora of catalysts were synthesized by incipient wetness impregnation of TM into mesoporous silica, and their activities are evaluated in thermocatalytic screening. A brief overview of the thesis is schematically represented below.

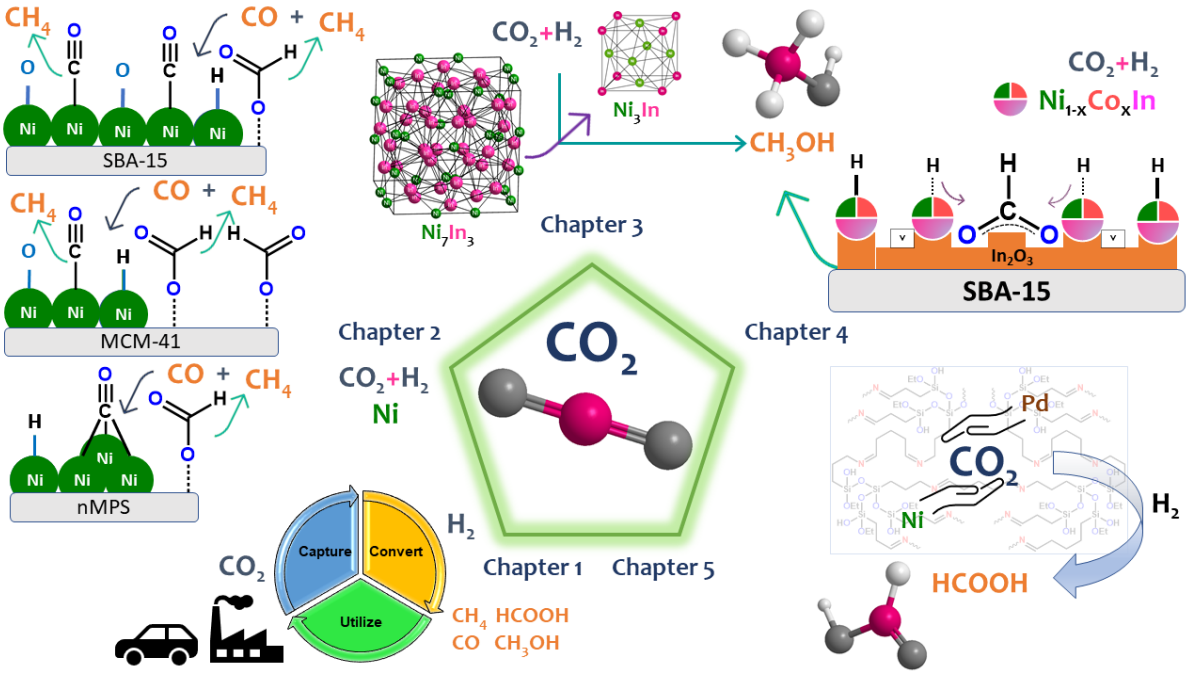

Figure 6.1. Schematic illustration describing the contents of thesis; Chapter 1 (a brief discussion of scientific solutions to curtail global warming), Chapter 2 (Describing the influence of support textural properties on CO_2 to methanation catalyst), Chapter 3 (Operando generated Ni based intermetallic improving the selective CO_2 to methanol), Chapter 4 (Enhancing the Ov of In_2O_3 catalyst by non-coinage TM to improve the CO_2 to methanol activity) and Chapter 5 (Rational tuning of hybridization and charge polarization of metal nanoparticles dispersed over Schiff Base functionalized SBA-15 to improve CO_2 capture and conversion to FA).

The thesis is divided into 5 chapters with the Chapter 1 discussed about the environmental issues associated with CO_2 emissions and its probable solutions. Chapters 2-5 highlights the discovery of novel materials as the efficient catalysts for the conversion of CO_2 to methane, methanol and formic acid. For the first time, the physicochemical textural property of the inert support material on the activity, product selectivity and deactivation of a catalyst has been studied in chapter 2. For this study, the typical CO_2 methanation catalyst, Ni on different silica supports (SBA-15, MCM-41 & non-mesoporous silica(nMPS)) were employed. The catalytic screening results revealed marked difference in the reactivity and product selectivity depending on the textural properties of the support. At 320 ^oC, Ni/SBA-15 provided best CO_2 conversion (X_{CO_2}) with 100 % methane selectivity (S_{CH_4}) followed by Ni/MCM-41 (X_{CO_2}=79 % and S_{CH_4}= 85%) and least by Ni/nMPS. For the first time, the relationship between support textural property, active metal distribution, intermediates formed, and CO_2 hydrogenation pathway were sketched with the help of operando DRIFTS. The basis of this understanding and the correlation study between CO_2 to methanation activity and textural property in depth by spectroscopic technique helped to choose SBA-15 as the support material and laid foundation for other catalyst syntheses in this thesis. These studies can be further extended to other reducible metal oxide supports such as ceria, titania and zirconia or in other words silica based mixed oxide supports (silica-ceria, silica-titania or silica-zirconia) can be synthesized with different porosity and textural property to study the enhancement in activity. These textural property-based studies can be extended to other types of heterogenous catalysis process.

In chapter 3, we strategically tuned the CO_2 hydrogenation mechanistic pathway of Ni/SBA-15 by alloying it with an inactive metal indium to produce methanol instead of methane. Several attempts were made to synthesize different Ni-In phases (different Ni to In ratio) by incipient impregnation into SBA-15 followed by reduction in flowing hydrogen, but all the attempts led into the formation of more thermodynamically stable Ni_7In_3 phase. However, under operando conditions (temperature 573 K and pressure 20-50 bar) Ni_7In_3 phase transformed into Ni_3In phase. Pressure controlled studies confirmed that this new kinetically stable Ni_3In catalyst could efficiently convert CO_2 selectively to methanol at low pressure, which is a very crucial advancement required in the industry as it can save energy cost in the economic calculation. We have performed several controlled experiments to map the mechanism on the phase transformation. The different reaction mechanistic pathways on Ni (for methane production) and Ni_3In (for methanol production) are studied by DRIFTS, XPS and

XANES (experiment) and DFT calculation (theory), which suggested the mechanistic tunability can be attributed to the ordered arrangement of Ni and In atoms and strong difference in their electronegativity, leading to interatomic charge transfer. Further the operando generated catalyst of this sample is converts CO_2 liquid methanol at much lower pressures (20 bar) than state of art catalysts (around 40-50 bar). We suggest this as one of the first steps towards the development of small-scale low-pressure devices for decentralised production of liquid fuels from CO_2. This may be realized only if the hydrogen production is also decentralised and solar generated.

The work in chapter 3 extended to Chapter 4 with the introduction of Co metal. Indium oxide-based catalysts supported on SBA-15 were studied for direct CO_2 to methanol conversion. Here the effort was to enhance the catalytically active O_v (oxygen vacancies) of In_2O_3 by co-impregnating SBA-15 with different mole ratio of low-cost abundant TM based methanation catalyst Ni and Co having high hydrogen spill-over action. The calcined catalyst was screened for CO_2 hydrogenation instead of the reduced catalyst. The spent catalyst after hydrogenation were characterized by XRD, TEM, XPS and EXAFS measurements. It was understood that the reducibility of indium oxide catalysts in a hydrogen atmosphere is directly linked to methanol production rates and selectivity. At optimized reaction condition, the MeOH activity and Ov were maximum when both Ni and Co were equally distributed over In_2O_3 catalyst, further the spent catalyst characterisation shows that the in-situ formation of medium entropy $Ni_{1-x}Co_xIn$ intermetallic along with oxygen vacant In_2O_3 are components responsible for the highest ever reported MeOH activity and STY over In_2O_3 based catalyst. Till date the Ov enhancement were done by using single metals with high methanation activity, here for the first time we co-impregnated two different 3d metals to improve the Ov of Indium oxide. There are other reducible supports with high CO_2 gas activation tendency, this study of co-impregnating 3d metals can be extended to these systems also. Further, these series of cost-effective catalysts can be directly scaled up for industrial process or further studied with other oxide modifications such as zirconia, galena to improve the activity.

In chapter 5, we have introduced capture of CO_2 in addition to conversion. SBA-15 functionalised Schiff's base is used as the support for TM based bimetallic systems and applied for CO_2 conversion in batch process. Here four different types of Schiff's base functionalised SBA-15 is synthesized by following two routes of synthesis using two different aldehydes. Direct correlation between CO_2 to formic acid reactivity and CO_2 capture ability were first time done with the help of static and dynamic CO_2 capture experiments. The condensation between

APTES and aldehydes tuned the hybridization of N in APTES from sp^3 to sp^2 favoured optimum adsorption of CO_2. The hybridization changes was quantified with the help of XPS, which is in good agreement with the CO_2 capture efficiency. Further, studies by XAS proved that the cost-effective Pd-Ni bimetallic catalyst owing to relatively larger electronegativity difference shows higher CO_2 activation and reactivity than the Pd-Ag bimetallic combination. The most important findings from this chapter are that higher conversions in batch process is hampered by formation of formic acid itself. This is because the acidic medium due to formic acid resists further dissolution of CO_2 into the reaction medium. Designing a pressurized flow process through reaction medium or engineering an effective method to timely remove the formed formic acid can improve the formic acid activity.

In conclusion, this thesis has succeeded in the development of different categories of several novel transition metal-based systems encompassing a wide variety of structural and compositional diversity. The progress of CO_2 reduction research strongly dependent on the catalysts, which dictates the CO_2 reduction activity and selectivity towards a desired product. In view of this, this content of this thesis can be used as a handbook to those who are working in this area. Various strategies used in this thesis may be exploited for developing novel catalysts, which may be a revolutionary step towards the commercial CCU research and can be a handy solution to the issues related to energy and environment.

LIST OF PUBLICATIONS

1. Thermochemical CO_2 Hydrogenation to Single Carbon Products: Scientific and Technological Challenges. **Cherevotan, A.**; Roy, S.; Peter, S. C., *ACS Energy Letters* 2018, *3* (8), 1938-1966.
2. Operando Generated Ordered Heterogeneous Catalyst for the Selective Conversion of CO_2 to Methanol. **Cherevotan, A.**; Raj, J.; Dheer, L.; Roy, S.; Sarkar, S.; Das, R.; Vinod, C. P.; Xu, S.; Wells, P.; Waghmare, U. V.; Peter, S. C., *ACS Energy Letters* 2021, *6* (2), 509-516.
3. An Overview of Porous Silica Immobilized Amines for Direct Air CO_2 Capture. **Cherevotan, A.**; Raj, J.; Peter, S. C. Cherevotan, A.; Raj, J.; Peter, S. C., *Journal of Material Chemistry A* 2021, *9* (48), 27271-27303.
4. Influence of Support Textural Property on CO_2 to Methane Activity of Ni/SiO_2 Catalysts. **Cherevotan, A.;** Ray, B.; Churipad, S. R.; Kaur, K.; Gautam, U. K.; Vinod, C. P.; Peter, S. C., **Manuscript Under Revision.**
5. Metal Substitution Induced Surface Oxygen Vacancy and Operando Generated Medium Entropy Intermetallic Compound Enhances the Conversion of Carbon Dioxide to Methanol. **Cherevotan, A.**; Yadav, A.; Singh, A. K.; Bagchi, D.; Churipad, S. R.; Ray, B.; Kaur, K.; Gautam, U. K.; Vinod, C. P.; Peter, S. C., **Manuscript Under Revision.**
6. Tuning Hybridization and Charge Polarization in Metal Nanoparticles Dispersed over Schiff Base Functionalized SBA-15 Enhances CO_2 Capture and Conversion to Formic Acid. **Cherevotan, A.**; Ray, B.; Yadav, A.; Bagchi, D.; Singh, A. K.; Churipard, S. R.; Naral, V.; Kaur, K.; Gautam, U. K.; Vinod, C. P.; Peter, S. C., **Manuscript Under Revision.**
7. Unraveling the Role of Site Isolation and Support for Semihydrogenation of Phenylacetylene. Goud, D.; **Cherevotan, A.**; Maligal-Ganesh, R.; Ray, B.; Ramarao, S. D.; Raj, J.; Peter, S. C., *Chemistry an Asian Journal* 2019, *14* (24), 4819-4827.
8. Noble-Metal-Free Heterojunction Photocatalyst for Selective CO_2 Reduction to Methane upon Induced Strain Relaxation. Das, R.; Sarkar, S.; Kumar, R.; D. Ramarao, S.; **Cherevotan, A.**; Jasil, M.; Vinod, C. P.; Singh, A. K.; Peter, S. C., *ACS Catalysis* **2022,** *12* (1), 687-697.

9. Induced Structural Ordering Enhances Highly Selective Production of Acetic Acid from CO_2 at Ultra-Low Potential. Sarkar, S.; Raj, J.; Bagchi, D.; **Cherevotan, A.**; Vinod, C. P.; Peter, S. C, **Manuscript Under Revision.**

10. Structure-Tailored Surface Oxide on Cu-Ga Intermetallics Enhances CO_2 Reduction Selectivity to MeOH at Ultra-Low Potential. Bagchi, D.; Raj, J.; Singh, A. K.; **Cherevotan, A.**; Vinod, C. P.; Peter, S. C., *Advanced Materials* **2022,** 2109426.

11. Ultra-low Loading of Atomically Dispersed Copper on WC@NGC Boosts the Conversion of CO_2 to Acetic Acid. Bagchi, D.; Raj, J.; Roy, S.; Singh, A. K.; **Cherevotan, A.**; Vinod, C. P.; Peter, S. C. **Manuscript Under Revision.**

PATENTS

1. Catalyst and Process of Preparing the Same.

   Arjun Cherevotan, Soumyabrata Roy, Manoj Kaja Sai and Sebastian C. Peter, 2018 [US Patent App. 17/298, 378]

2. Catalyst for thermochemical reduction of CO_2.

   Arjun Cherevotan, Jithu Raj, and Sebastian C. Peter, 2020 [Patent filed]

3. Metal Substitution Induced Surface Oxygen Vacancy and Operando Generated Medium Entropy Intermetallic Compound Enhances the Conversion of Carbon Dioxide to Methanol.

   Arjun Cherevotan, Anish Yadav and Sebastian C. Peter, 2022

BIOGRAPHY

Arjun Cherevotan graduated from Gurudev Arts and Science College, Mathil, Payannur affliated to Kannur University, Kerala in 2013. Arjun received his Master's degree in Chemical Science from National Institute of Technology Surathkal, Karnataka in the year of 2015. In August 2016, he joined New Chemistry Unit at Jawaharlal Nehru Centre for Advanced Scientific Research (JNCASR), Bengaluru, as a PhD student under the supervision of Prof. Sebastian C. Peter. His scientific journey at JNCASR centers around the conversion of carbon dioxide to value-added fuels and chemicals by the means of thermochemical pathway. His scientific insights are summarized as the PhD thesis entitled as "*Investigation on Thermocatalytic CO_2 Hydrogenation by High Surface Area Silica supported Transition Metal Catalysts*". Arjun was an integral part in design of high-performance catalyst and process development for thermocatalytic CO_2 conversion to methanol as a part of Breathe Applied Sciences (supported by JNCASR, Bangalore) for NRG Cosia Carbon Xprize competition. Team Breathe was one of the finalists of the competition and the developed catalyst as well as process engineering are patented. He qualified National Eligibility Test for Junior Research Fellowship in 2015 as an UGC fellow, with an All-India Rank of 64. He also cleared GATE in 2016. Arjun has attended and actively participated in several national and international conferences during past five years both in person and virtually. Notably, he has received recognition in both poster and oral section multiple times. His poster was awarded the best in *Conference on Advances in Catalysis for Energy and Environment* (CACEE), 2018 organized by TIFR Mumbai. He also received best award for poster in National Symposium in Chemistry of *Chemical Research Society of India*, organized by Vellore Institute of Technology, in 2020. He also received the best orator prize in *Virtual Conference on Materials for Energy Harvesting and Catalysis*, in 2020 jointly organized by TIFR Mumbai and IISER Kolkata. Recently, he was selected for the prestigious *Gordon Research Conference, USA* in the section of Carbon Capture, Utilization and Storage, upcoming in 2022.